diagnostics

Optical Diagnostics in Human Diseases

Edited by

Andrey Dunaev

Printed Edition of the Special Issue Published in *Diagnostics*

www.mdpi.com/journal/diagnostics

MDPI

Optical Diagnostics in Human Diseases

Optical Diagnostics in Human Diseases

Editor

Andrey Dunaev

MDPI • Basel • Beijing • Wuhan • Barcelona • Belgrade • Manchester • Tokyo • Cluj • Tianjin

Editor
Andrey Dunaev
Orel State University
Russia

Editorial Office
MDPI
St. Alban-Anlage 66
4052 Basel, Switzerland

This is a reprint of articles from the Special Issue published online in the open access journal *Diagnostics* (ISSN 2075-4418) (available at: https://www.mdpi.com/journal/diagnostics/special_issues/Optical_Diagnostics_Diseases).

For citation purposes, cite each article independently as indicated on the article page online and as indicated below:

LastName, A.A.; LastName, B.B.; LastName, C.C. Article Title. *Journal Name* **Year**, *Volume Number*, Page Range.

ISBN 978-3-0365-1617-2 (Hbk)
ISBN 978-3-0365-1618-9 (PDF)

Contents

About the Editor

Andrey Dunaev received his M.Sc. and Ph.D. degrees in instrument engineering from Orel State University (Orel, Russia) in 1999 and 2002, respectively. From 2005 to 2011, he was Associate Professor at the Department of Instrument Engineering, Metrology and Certification. From 2011 to 2013, he was a Postdoctoral Researcher (Marie Curie Research Fellow) at Photonics and Nanoscience Group, University of Dundee (Dundee, UK). Since 2014, he has been the Head of Research and Development Center of Biomedical Photonics, Orel State University. He is the author of 5 books, more than 60 papers in peer-reviewed journals, and over 10 patents. His research interests include the development of multimodal optical non-invasive diagnostic methods for microcirculatory-tissue systems. He is the leader and executor of a number of projects supported by various Russian and international foundations (RSF, RFBR, and Academy of Finland, among others).

Preface to "Optical Diagnostics in Human Diseases"

This Special Issue is devoted to the multidisciplinary studies in the field of optical non-invasive diagnostics for identifying and evaluating various diseases and pathological conditions. The purpose was to show the possibilities of using modern optical technologies in clinical practice as well as highlight the challenges, advantages, and unique aspects of optical diagnostic methods. This Special Issue is intended for medical physicists and doctors interested in the development and application of optical diagnostic techniques in medical research and practice.

Andrey Dunaev
Editor

diagnostics

MDPI

Editorial

Optical Diagnostics in Human Diseases

Andrey Dunaev

Research and Development Center of Biomedical Photonics, Orel State University, 302026 Orel, Russia; dunaev@bmecenter.ru; Tel.: +7-4862-419806

Keywords: biophotonics; optics; spectroscopy; imaging; diagnostics

Light-based technologies provide unique opportunities for the diagnosis of various pathological disorders of biological tissues. With the advancement of modern science, they allow for the non-invasive identification of diseases at early stages. The optical technologies for obtaining information on the biochemical state and morphological structure of the investigated area are based on the assessment of light-tissue interaction (including laser radiation). For this purpose, a patient's tissues and organs are probed with optical radiation, and reflected (scattered, passed through the tissue, re-emitted as fluorescence, etc.) light is recorded. The range of optical technologies applications in clinical practice is considerably wide since the optical properties of biological tissues are subject to significant changes in the course of the disease. Optical non-invasive diagnostics uses many spectroscopic and imaging techniques, including near infrared spectrophotometry, fluorescence spectroscopy (FS) and imaging, optical coherence tomography (OCT), confocal spectroscopy, optoacoustic tomography, laser Doppler flowmetry (LDF), laser speckle contrast imaging, and a number of other methods. However, despite the rapid development of optical methods in medical diagnostics, it should be borne in mind that most of them have not yet become the gold standard in clinical practice. They are mostly used in scientific research or as an additional clarifying method, increasingly using the so-called multimodal approach, where one diagnostic technology combines various optical and other physical research methods, which makes it possible to provide early diagnosis of functional changes before clinical manifestations of the disease based on the measurement results. In addition, the wider introduction of these methods into routine clinical practice is hindered by the insufficient elaboration of their methodological and technical support. This Special Issue of Diagnostics is devoted to the ideas regarding a solution to these problems.

The Special Issue highlights the challenges, advantages, and unique aspects of optical diagnostic methods for identifying and evaluating various diseases and pathological conditions. Articles focus on certain technologies, diseases, and various aspects of spectroscopy and imaging application in clinical practice.

Several studies in this Special Issue present new information relevant to surgical procedures, especially in oncology and gynecology. Zherebtsov and colleagues, according to the multimodal approach, described the development of the technical implementation and assessment of machine learning methods' efficiency for the real-time diagnosis of tumors in hepatoduodenal organs by FS and LDF. This approach is aimed at improving the effectiveness of minimally invasive surgical operations by providing additional diagnostic information online [1]. Two articles are devoted to the topical problem of breast cancer's early detection, including during surgery. Gubarkova and colleagues compared two types of optical coherence tomography–cross-polarization OCT (CP OCT) and a novel type of compressional optical coherence elastography. They confirmed the high potential of OCT-based examinations for rapid and accurate diagnostics during breast conservation surgery [2]. Iida and colleagues conducted Monte Carlo simulation of shortwave-infrared (SWIR) fluorescence photon migration in voxelized media for breast cancer detection. The obtained results showed that it is possible to predict the presence of early-stage breast

Citation: Dunaev, A. Optical Diagnostics in Human Diseases. *Diagnostics* **2021**, *11*, 873. https://doi.org/10.3390/diagnostics11050873

Received: 30 March 2021
Accepted: 10 May 2021
Published: 12 May 2021

cancer with high spatial resolution using SWIR and the phantom model in which the optical parameters are implemented in the breast structure [3]. Huang and colleagues proposed a promising method based on the gray level co-occurrence matrix (GLCM) image processing model to achieve a rapid technique with a more reliable diagnostic performance for various types of chemoresistance for the cisplatin of human ovarian adenocarcinoma cells by feature extraction of GLCM [4].

The problem of chronic or recurrent episodic pain in the urethra with unchanged urinalysis, the absence of any other clinical manifestations or somatically explainable causes, is complex and ultimately remains unresolved since the exact pathogenetic mechanisms are not yet fully understood. The article by Streltsova and colleagues is dedicated to the targeted study of female urethral tissues (their elasticity and the condition of the epithelial and connective tissue layers) in urethral pain syndrome (UPS). The results showed that the introduction of new CP OCT technology in conjunction with transvaginal compression ultrasound will allow for in vivo verification of structural changes in lower urinary tract tissues at their architectonics level and will provide more information about basic elements of the UPS pathogenesis [5].

Several studies in this Special Issue are devoted to otolaryngology and dentistry. Bryanskaya and colleagues developed a basis for instrument implementation of digital diaphanoscopy technology for the diagnosis of maxillary sinus inflammatory diseases, taking into account the anatomical, age, and gender features of patients. Their approach may be promising as a screening method for assessing the condition of maxillary sinuses both in hospitals and medical institutions, as well as remotely in the absence of otolaryngologists and diagnosticians [6].

Timchenko and colleagues studied the changes in tooth tissues in periodontitis using Raman spectroscopy for early and rapid diagnosis and the correction of treatment. The obtained results are a prerequisite for creating a device for rapid in vivo assessment of periodontitis based on changes in tooth enamel spectral values [7].

Savchenko and colleagues developed an experimental optical device for diagnosing liver diseases. The main advantages of the proposed device are its usability and fast presentation of results in real time. The device is based on optical densitometry. To determine the functional reserves of the liver, the researchers used indocyanine green. It is a non-toxic dye that binds well to blood proteins and is delivered to the liver through the bloodstream. The dye was administered intravenously to a patient, and then it was observed how long it took the liver to eliminate it from blood plasma. The concentration of indocyanine green in the blood was measured using the developed optical setup [8].

A number of articles are devoted to the study of alterations caused by diabetes mellitus (DM) and cardiovascular diseases. Kozlov and colleagues developed a new method of signal processing and data analysis in digital LDF. The main result of the study is the development of a set of classifiers that allow one to identify typical patterns of microcirculation in healthy volunteers and DM patients based on the presented diagnostic algorithm [9]. Fedorovich and colleagues studied the changes in microcirculation parameters in different body positions using a distributed system of wearable LDF devices. They demonstrated the significance of a body position influence during the monitoring of microcirculatory parameters. The results obtained may be of particular interest for further integration of an LDF channel into wearable devices for monitoring the state of cardiovascular systems [10]. Maslianitsyna and colleagues found the correspondence between in vivo and in vitro optical methods by studying the aggregation parameters in patients with cardiovascular and concomitant pathologies. Understanding the link between red blood cells (RBC) aggregation and widespread cardiovascular diseases is vital to creating new methods of diagnosis and treatment. In this work, the aggregation of RBC was studied using different optical in vivo and in vitro measurement techniques. In vivo and in vitro methods yielded correlated results: the faster the cells moved in the capillaries, the less cells aggregated in vitro. DM had an additional significant effect on the aggregation properties of coronary heart disease patients. These findings are prominent for diagnosing and monitoring the state of

patients with pathologies that affect blood properties [11]. Machikhin and colleagues reported on an in vivo stain-free blood vessel imaging technique for the analysis of zebrafish embryonic development. The developed algorithm for processing bright-field microscopy images enables detection, mapping, and quantitative characterization of cardiac activity across the whole embryo. To validate the proposed approach, the blood flow velocity and heart rate dynamics were evaluated for multiple embryos at pre-larval stages. This non-invasive technique may shed light on the mechanism of vessels' activity initiation as well as the cardiovascular system resistance to environmental stresses [12].

Finally, Batool and colleagues reviewed and compiled the optical properties of human tissues and the circulatory system, especially blood. One of the main conclusions of this review is that there are numerous physical and methodological factors important for optical properties research and that one should be aware of them before performing their own measurements. The authors pointed out the main factors that affect absorption spectra of whole blood and hence influence optical properties. Revision of available polarimetric techniques can be helpful for readers who practice biomedical optics methods [13].

Thus, the presented Special Issue reflects novel innovative research and emerging ideas in optical non-invasive diagnostics for their wider translation into clinical practice, e.g., for the development of wearable technologies, personalized medicine, and robotic surgery.

Funding: This research received no external funding.

Institutional Review Board Statement: Not applicable.

Informed Consent Statement: Not applicable.

Data Availability Statement: Not applicable.

Conflicts of Interest: The author declares no conflict of interest.

References

1. Zherebtsov, E.; Zajnulina, M.; Kandurova, K.; Potapova, E.; Dremin, V.; Mamoshin, A.; Sokolovski, S.; Dunaev, A.; Rafailov, E.U. Machine Learning Aided Photonic Diagnostic System for Minimally Invasive Optically Guided Surgery in the Hepatoduodenal Area. *Diagnostics* **2020**, *10*, 873. [CrossRef] [PubMed]
2. Gubarkova, E.V.; Kiseleva, E.B.; Sirotkina, M.A.; Vorontsov, D.A.; Achkasova, K.A.; Kuznetsov, S.S.; Yashin, K.S.; Matveyev, A.L.; Sovetsky, A.A.; Matveev, L.A.; et al. Diagnostic Accuracy of Cross-Polarization OCT and OCT-Elastography for Differentiation of Breast Cancer Subtypes: Comparative Study. *Diagnostics* **2020**, *10*, 994. [CrossRef] [PubMed]
3. Iida, T.; Kiya, S.; Kubota, K.; Jin, T.; Seiyama, A.; Nomura, Y. Monte Carlo Modeling of Shortwave-Infrared Fluorescence Photon Migration in Voxelized Media for the Detection of Breast Cancer. *Diagnostics* **2020**, *10*, 961. [CrossRef] [PubMed]
4. Huang, C.-L.; Lian, M.-J.; Wu, Y.-H.; Chen, W.-M.; Chiu, W.-T. Identification of Human Ovarian Adenocarcinoma Cells with Cisplatin-Resistance by Feature Extraction of Gray Level Co-Occurrence Matrix Using Optical Images. *Diagnostics* **2020**, *10*, 389. [CrossRef] [PubMed]
5. Streltsova, O.; Kuyarov, A.; Molvi, M.S.; Zubova, S.; Lazukin, V.; Tararova, E.; Kiseleva, E. New Approaches in the Study of the Pathogenesis of Urethral Pain Syndrome. *Diagnostics* **2020**, *10*, 860. [CrossRef] [PubMed]
6. Bryanskaya, E.O.; Novikova, I.N.; Dremin, V.V.; Gneushev, R.Y.; Bibikova, O.A.; Dunaev, A.V.; Artyushenko, V.G. Optical Diagnostics of the Maxillary Sinuses by Digital Diaphanoscopy Technology. *Diagnostics* **2021**, *11*, 77. [CrossRef] [PubMed]
7. Timchenko, E.; Timchenko, P.; Volova, L.; Frolov, O.; Zibin, M.; Bazhutova, I. Raman Spectroscopy of Changes in the Tissues of Teeth with Periodontitis. *Diagnostics* **2020**, *10*, 876. [CrossRef] [PubMed]
8. Savchenko, E.; Kolokolnikov, I.; Velichko, E.; Osovskikh, V.; Kiseleva, L.; Musakulova, Z. Design of Liver Functional Reserve Estimation Technique Based on Optical Densitometry. *Diagnostics* **2020**, *10*, 599. [CrossRef] [PubMed]
9. Kozlov, I.; Zherebtsov, E.; Masalygina, G.; Podmasteryev, K.; Dunaev, A. Laser Doppler Spectrum Analysis Based on Calculation of Cumulative Sums Detects Changes in Skin Capillary Blood Flow in Type 2 Diabetes Mellitus. *Diagnostics* **2021**, *11*, 267. [CrossRef] [PubMed]
10. Fedorovich, A.A.; Loktionova, Y.I.; Zharkikh, E.V.; Mikhailova, M.A.; Popova, J.A.; Suvorov, A.V.; Zherebtsov, E.A. Body Position Affects Capillary Blood Flow Regulation Measured with Wearable Blood Flow Sensors. *Diagnostics* **2021**, *11*, 436. [CrossRef] [PubMed]
11. Maslianitsyna, A.; Ermolinskiy, P.; Lugovtsov, A.; Pigurenko, A.; Sasonko, M.; Gurfinkel, Y.; Priezzhev, A. Multimodal Diagnostics of Microrheologic Alterations in Blood of Coronary Heart Disease and Diabetic Patients. *Diagnostics* **2021**, *11*, 76. [CrossRef] [PubMed]

12. Machikhin, A.S.; Volkov, M.V.; Burlakov, A.B.; Khokhlov, D.D.; Potemkin, A.V. Blood Vessel Imaging at Pre-Larval Stages of Zebrafish Embryonic Development. *Diagnostics* **2020**, *10*, 886. [CrossRef] [PubMed]
13. Batool, S.; Nisar, M.; Mangini, F.; Frezza, F.; Fazio, E. Scattering of Light from the Systemic Circulatory System. *Diagnostics* **2020**, *10*, 1026. [CrossRef] [PubMed]

diagnostics

MDPI

Article

Body Position Affects Capillary Blood Flow Regulation Measured with Wearable Blood Flow Sensors

Andrey A. Fedorovich [1,2], Yulia I. Loktionova [3,†], Elena V. Zharkikh [3,†], Maria A. Mikhailova [1], Julia A. Popova [2], Alexander V. Suvorov [2] and Evgeny A. Zherebtsov [3,4,*]

[1] National Medical Research Center for Therapy and Preventive Medicine of the Ministry of Healthcare of the Russian Federation, Petroverigsky 10, 101990 Moscow, Russia; faa-micro@yandex.ru (A.A.F.); marya.filina-2015@yandex.ru (M.A.M.)
[2] Russian Federation State Research Center, Institute of Biomedical Problems of the Russian Academy of Sciences, Khoroshevskoe Highway 76A, 123007 Moscow, Russia; julija.popova@gmail.com (J.A.P.); suvalex@inbox.ru (A.V.S.)
[3] Orel State University, Komsomolskaya 95, 302026 Orel, Russia; julya-loktionova@mail.ru (Y.I.L.); ev.zharkikh@gmail.com (E.V.Z.)
[4] Optoelectronics and Measurement Techniques, University of Oulu, Erkki Koiso-Kanttilankatu 3, 90014 Oulu, Finland
* Correspondence: evgenii.zherebtsov@oulu.fi
† These authors contributed equally to this work.

check for updates

Citation: Fedorovich, A.A.; Loktionova, Y.I.; Zharkikh, E.V.; Mikhailova, M.A.; Popova, J.A.; Suvorov, A.V.; Zherebtsov, E.A. Body Position Affects Capillary Blood Flow Regulation Measured with Wearable Blood Flow Sensors. *Diagnostics* **2021**, *11*, 436. https://doi.org/10.3390/diagnostics11030436

Academic Editor: Xavier Muñoz-Berbel

Received: 31 January 2021
Accepted: 24 February 2021
Published: 4 March 2021

Publisher's Note: MDPI stays neutral with regard to jurisdictional claims in published maps and institutional affiliations.

Abstract: In this study we demonstrate what kind of relative alterations can be expected in average perfusion and blood flow oscillations during postural changes being measured in the skin of limbs and on the brow of the forehead by wearable laser Doppler flowmetry (LDF) sensors. The aims of the study were to evaluate the dynamics of cutaneous blood perfusion and the regulatory mechanisms of blood microcirculation in the areas of interest, and evaluate the possible significance of those effects for the diagnostics based on blood perfusion monitoring. The study involved 10 conditionally healthy volunteers (44 ± 12 years). Wearable laser Doppler flowmetry monitors were fixed at six points on the body: two devices were fixed on the forehead, on the brow; two were on the distal thirds of the right and left forearms; and two were on the distal thirds of the right and left lower legs. The protocol was used to record three body positions on the tilt table for orthostatic test for each volunteer in the following sequence: (a) supine body position; (b) upright body position (+75°); (c) tilted with the feet elevated above the head and the inclination of body axis of 15° (−15°, Trendelenburg position). Skin blood perfusion was recorded for 10 min in each body position, followed by the amplitude–frequency analysis of the registered signals using wavelet decomposition. The measurements were supplemented with the blood pressure and heart rate for every body position analysed. The results identified a statistically significant transformation in microcirculation parameters of the average level of skin blood perfusion and oscillations of amplitudes of neurogenic, myogenic and cardiac sensors caused by the postural changes. In paper, we present the analysis of microcirculation in the skin of the forehead, which for the first time was carried out in various positions of the body. The area is supplied by the internal carotid artery system and can be of particular interest for evaluation of the sufficiency of blood supply for the brain.

Keywords: wearable blood flow sensors; blood perfusion; laser Doppler flowmetry; ortostatic test; postural changes; body position; blood perfusion in forehead; blood perfusion in wrists; blood perfusion in shins; blood perfusion oscillations; vasomotions

1. Introduction

The functional state and balance in regulation mechanisms of the cardiovascular system are some of the main factors determining the robustness in a living organism. The evolutionary development of vertebrates in a field of gravitational attraction has led to

series of adaptations in the blood supply system. Changes in hemodynamic parameters depending on the position of the body significantly assist the homeostasis in the limbs and essentially in the sufficiency of blood supply for the brain [1]. For the last two decades, laser Doppler perfusion monitoring has become an established technique capable of providing useful diagnostic information about parameters of regulation of the skin blood perfusion. The recent emergence of laser Doppler flowmetry (LDF) as a wearable device has allowed for detailed assessments of individual adaptive capabilities of the blood flow circulation system and can be of particular interest for diagnostics and sport medicine. The next decade is likely to witness a considerable rise of novel optical sensor technologies in wearable sensors, not only to be used as fitness trackers, but to provide clinicians with diagnostic information with better sensitivity and specificity.

Earlier studies have shown significant variability of the cardiovascular system's parameters (in particular, heart rate and blood pressure) associated with posture and body position [2–4]. It has also been shown that parameters of gender and age significantly affect the reactivity of blood flow in response to postural change [5]. It is known that different anatomical parts of the human body demonstrate differences in the blood flow regulation mechanisms [6]. In that respect, regional variability of the effects in microcirculation should also be taken into account. Previous studies reported that the low-frequency mechanisms of microcirculation regulation (endothelial, neurogenic and myogenic) measured with the LDF technique differ between the arm and leg regions under thermoneutral conditions [7,8]. It has also been shown that regulation of microcirculation differs in the leg and forearm under local heating [8]. The regions of glabrous and nonglabrous skin are also reported to have different responses of different types in the parameters of blood perfusion under the type of functional loading [9].

In the study of I. Tikhonova et al., it was found that a postural test (change of supine position to sitting) did not influence the forearm skin blood flow oscillations; they noted a remarkable increase in the respiratory flow and a decrease in the cardiac oscillations in the blood microcirculation in the skin of the legs [10]. The work [11] presents the results of a study of the effects of body position on oxygen consumption (VO_2) and hemodynamics. It was found that the heart rate, the blood pressure and the product of velocity pressure and oxygen consumption were highest in the sitting position compared to the lying position, and lowest in the lying position on the left side. Narayanan et al. [12] published results on a study of changes in the parameters of blood pressure (BP) and the speed of cerebral blood flow (CBFV) when changing the body position from sitting to vertical in young and old people. It is noted that in young people the linear relationship between blood pressure and the blood flow rate of the middle cerebral artery in stationary sitting conditions changes with orthostatic stress in a wide range of physiological frequencies. Nevertheless, the effects in the parameters of skin microcirculation during changes of the posture and body position were not studied comprehensively, so a lack of systematically conducted research can be identified in this area.

Multi-point measurements using recently developed wearable laser Doppler flowmetry devices [13] can be effectively used for simultaneous recordings of blood perfusion signals from arbitrary anatomical skin sites, thereby providing great potential for finding multiple applications in physiological measurements and medial diagnostics in the near future. One of the challenges that can be mitigated by the use of the distributed measuring system is the difficulty of the high spatial heterogeneity of the LDF signal. Recently, the prototypes of the measuring system have been validated by authors of the work demonstrating the effectiveness of using laser wearable Doppler analyzers for measurements of the parameters of skin blood microcirculation. It has been demonstrated that the sensitivity of the wearable 850 nm VCSEL-basedblood perfusion sensors is sufficient to reliably register physiological changes in skin blood perfusion [14–16], including high coherence of blood flow oscillation in the contralateral limbs of healthy volunteers in the basal state and during functional tests [17].

The wireless LDF sensors have been tested in the realm of pre-clinical trials in healthy volunteers of different ages and patients with type 2 diabetes [14,16,18,19]. Additionally, the dynamical changes in the blood perfusion evaluated by LDF and laser speckle contrast imaging techniques were compared, demonstrating that both techniques can be used for the recording of the blood perfusion oscillations [20].

Thus, the use of wearable LDF sensors is promising for both health monitoring, and for evaluating the effectiveness of treatment and monitoring its dynamics. While the multi-point recordings of blood perfusion have demonstrated great promise for the diagnostics of vascular complications, there is a significant gap of knowledge on the effects of the body position during measurements, which introduce systematic impact and additional variability to the recorded signals, which requires accurate systematic studies for the main cases such as measurements while standing upright and in supine position.

Thus far, to the best of our knowledge, no one has systematically studied the effects of postural changes on the skin blood flow by use of wearable LDF sensors as a prime measuring technique. A review identified only one study that used a miniaturized LDF device for the measurements of hemodynamic changes in response to changes of body position [21]. The authors reported a decrease in earlobe microcirculation in response to the squat–standing and the footstool standing tests synchronized with the decrease in blood pressure in subjects. Nevertheless, the mentioned research lacks systematic studies of the effects taking place during the transition of body position from lying supine to standing upright. Thus, the overall aim of this work was to study the reaction of the microcirculation system in skin to changes in body position using the newest wireless wearable measuring platform for the multi-point blood perfusion recordings.

2. Material and Methods

The technique of laser Doppler flowmetry (LDF) measurements with a prototyping system consisting of 6 wireless compact sensors manufactured by SPE "LAZMA" Ltd. (Moscow, Russia) has been applied in this study for the registration of the skin blood perfusion. The LDF method is based on the coherent techniques with the analysis of the laser radiation scattered by moving red blood cells in the living tissue. The output signal of blood perfusion with the LDF method (Figure 1) is a time sequence of an integral parameter that depends on the speed of red blood cells and their concentration in the diagnosed volume.

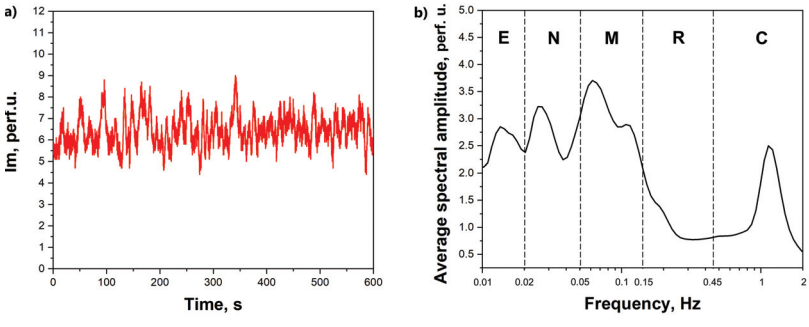

Figure 1. Representative trace of laser Doppler flowmetry (LDF) recordings by the employed measuring system (**a**), the wavelet analysis of the LDF signal with the highlighted frequency ranges for E—endothelial (e, 0.095–0.021 Hz), N—neurogenic (n, 0.021–0.052 Hz), M—myogenic (m, 0.052–0.145 Hz), R—respiratory (r, 0.145–0.6 Hz) and C—cardiac (c, 0.6–2 Hz) regions of blood flow modulation (**b**).

The distributed measuring system has built-in channels for recording microcirculation blood flow and allows for simultaneous measurements at multiple points of the human body. Every measuring device of the system employs compact VCSELs with an

emission wavelength of 850 nm and the power of output of the laser radiation of about 1 mW. Apart from the blood flow measurements, the analyzers were also equipped with a built-in accelerometer to monitor and eliminate possible motion artifacts and a skin temperature sensor.

The object of the study was a cohort of 10 conditionally healthy male volunteers, whose average age was 44 ± 12 years, height 177 ± 6 cm, weight 77 ± 6 kg, BMI 24.5 ± 1.9. All participants were staff testers of the Institute of Biomedical Problems of the Russian Academy of Sciences (IBMP RAS); twice a year they undergo a comprehensive clinical examination for admission to participate in the physiological studies. The main areas of scientific activity of the Institute are research in the fields of space biology, physiology and medicine, which is the reason for the high requirements for the physiological state of the testers. The IBMP RAS Biomedical Ethics Commission has approved the experimental studies, min number 483 dated 3 August 2018, following the rules of the Declaration of Helsinki of 1975, revised in 2013. All volunteers signed informed consent prior to the study. The LDF sensors were located at 6 points on the body: 2 devices were fixed on the forehead above the eyebrows; 2 on the distal third of the outer surface of the forearm (each arm), 2–3 cm proximal to the wrist joint; and 2-in the distal third of the shins along the anterior surface of the tibia, 10 cm proximal to the medial malleolus.

The studies were carried out in a laboratory with a maintained microclimate (air temperature $+23 \pm 1$ °C; humidity 40–60%) in the morning (from 09:00 to 12:00). The studies were carried out in the same order on all subjects (Figure 2)—(1) horizontal position; (2) orthostasis ($+75°$); (3) head-down position of the body ($-15°$, Trendelenburg position). The study was carried out on a turntable, which was developed and manufactured by the Special Design Bureau of the Institute of Biomedical Problems of the Russian Academy of Sciences. The table has a mechanical drive that allows one to change and fix the angle of inclination of the surface with a step size of 5° in the range from $-30°$ to $+90°$ with a maximum speed of position change of up to 20 °/s. The table is equipped with a leg rest, and chest and knee safety belts. Transfer of subjects from horizontal position to orthostasis took 7–10 s, from orthostasis to Trendelenburg position—9–12 s. Cutaneous perfusion was recorded for 10 min at each body position. The adaptation of the subjects to the horizontal position lasted 10–15 min, during which time the sensors were fixed and the research equipment was adjusted. During the transition to orthostasis and the Trendelenburg position, the registration of cutaneous perfusion began after 2 min of adaptation to the new body position. Immediately before the change in body position, hemodynamic parameters were recorded with an automatic tonometer "OMRON M10-IT" (OMRON HEALTHCARE Co, Ltd., Kyoto, Japan) on the right hand, due to the design features of the turntable—a technical "pocket" for placing additional research equipment is located on the right. The temperature of the skin in each area of the study was monitored continuously throughout the entire study by built-in thermal sensors. The protocol was used for recordings in three body positions for each volunteer (Figure 2): (a) horizontal body position; (b) vertical position of the body (head at the top); (c) head tilted down (15° from the horizontal, Trendelenburg position).

The applied combination of the Trendelenburg position and orthostatic probe makes it possible to characterize the functional reserve of the blood circulatory system for the volunteers, and to correlate the adaptations of peripheral hemodynamics to the body position changes. The Trendelenburg position is known to be an effective method to change cerebral perfusion, and to fill and stretch the upper central veins and the external jugular vein [22].

The measuring procedure was composed of several stages. One basal recording of blood perfusion for every body position took 10 min; then the blood pressure was measured. Thus, for each spatial position, three pairs of measurements were recorded at the corresponding symmetrical points on the forehead, wrists and shins.

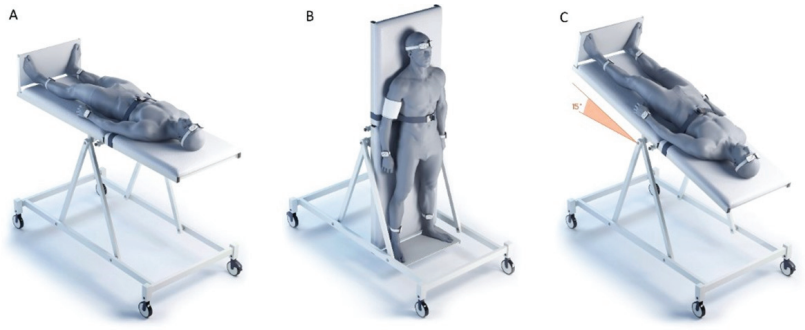

Figure 2. The measurements have been conducted and compared for three distinct body positions on a tilt table: (**A**) supine; (**B**) upright; (**C**) tilted with the feet elevated above the head and an inclination of body axis of 15 °(Trendelenburg position).

The amplitude–frequency characteristics of the skin perfusion oscillations were calculated using the mathematical apparatus of the wavelet transform. The wavelet spectrum of the signal was calculated according to the following expression:

$$W(s,\tau) = \frac{1}{\sqrt{s}} \int_{-\infty}^{\infty} x(t)\psi^*\left(\frac{t-\tau}{s}\right) \quad (1)$$

where $x(t)$ is a sample of the signal, τ is time index, s is scaling factor, * means complex conjugation. As a core wavelet, Morlet wavelet function $\psi(t) = e^{2\pi it} \cdot e^{-t^2/\sigma}$ was choosen with decay parameter $\sigma = 1$.

The time-averaged amplitude of vasomotions was assessed by the maximum values (Ai) in the corresponding frequency ranges for endothelial (e, 0.095–0.021 Hz), neurogenic (n, 0.021–0.052 Hz), myogenic (m, 0.052–0.145 Hz), respiratory (r, 0.145–0.6 Hz) and cardiac (c, 0.6–2 Hz) regions of blood flow modulation [23] (Figure 1b). The level of cutaneous perfusion (Im) and the amplitude of the units of modulation of microcirculation (Ai) were assessed as quantitative parameters measured in arbitrary (perfusion) units (p.u.). The wavelet analysis has been implemented in the MATLAB software environment. The LDF signals in this particular study were not a subject of pre-processing or filtering before the analysis. The statistical analysis was performed in Origin Pro 2019b (vers. 9.65) software. Due to the limited size of the sample, a non-parametric Mann–Whitney U test was used for the check of statistical significance of differences.

3. Results

3.1. Measurements Conducted on Wrists

The results of the amplitude analysis of cutaneous perfusion in the skin of the wrists are shown in Figure 3.

From the data obtained, it can be seen that during the transition from the horizontal position to orthostasis, the level of cutaneous perfusion has an insignificant tendency to decrease, which is accompanied by significant decreases in the amplitude of cardiac oscillations in blood flow and the amplitude of vasomotions of all tone-forming mechanisms of microcirculation—endothelial, neurogenic and myogenic. During the transition from orthostasis to the Trendelenburg position, the level of skin perfusion significantly increased, which was accompanied by significant increases in the amplitudes of cardiac and myogenic oscillations. There were no significant differences between the Trendelenburg position and the horizontal position for any of the analyzed parameters. The level of perfusion and the amplitude of the cardiac fluctuations both have a clear tendency to increase, but we did not find significant differences.

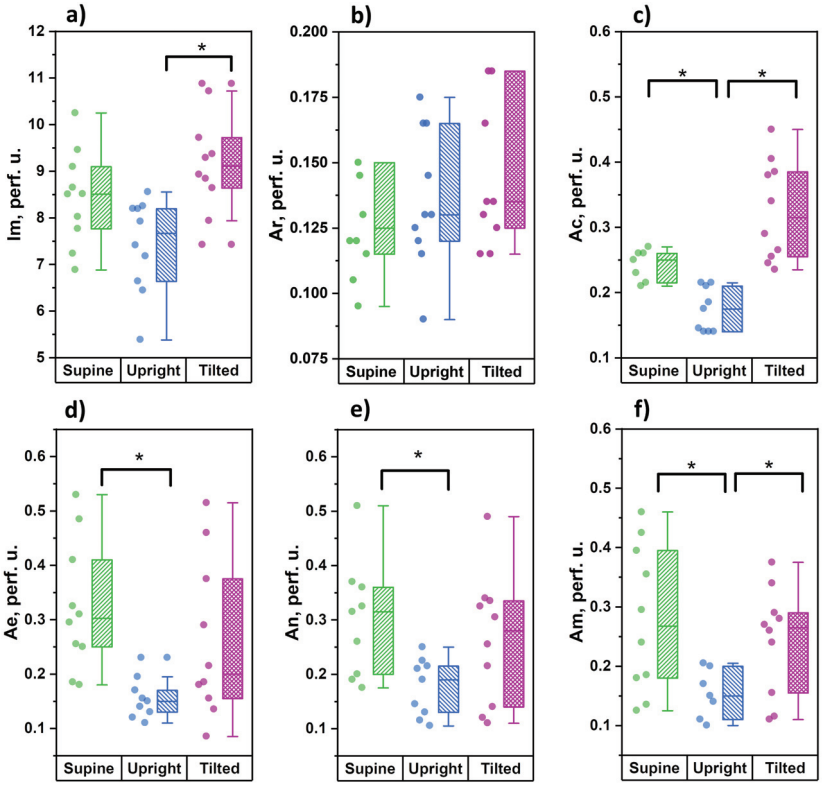

Figure 3. Analysis of average blood perfusion parameters on the wrists for three tested body positions: supine, upright and tilted (Trendelenburg position): (**a**) average blood perfusion; (**b**) cardiac oscillations; (**c**) respiratory oscillations; (**d**) endotelial oscillations; (**e**) neurogenic oscillations; (**f**) myogenic oscillations (* the significance of a difference between values was confirmed with $p < 0.05$ using the the Mann–Whitney test).

3.2. Measurements on Lower Legs

Figure 4 demonstrates the distribution of the studied parameters during measurements in the lower third of shin.

The parameters of microcirculatory blood flow demonstrated a significant decrease in the average level of tissue perfusion and the amplitude of cardiac oscillations during the transition to orthostasis. During the change from orthostasis to the Trendelenburg position, these parameters significantly increased and were comparable with those measured in the horizontal position. In contrast to the measurements conducted in forearms, the functional state of the tone-forming mechanisms of microcirculation modulation in shins (parameters Ae, An and Am) did not demonstrate any significant changes during all three stages of the study.

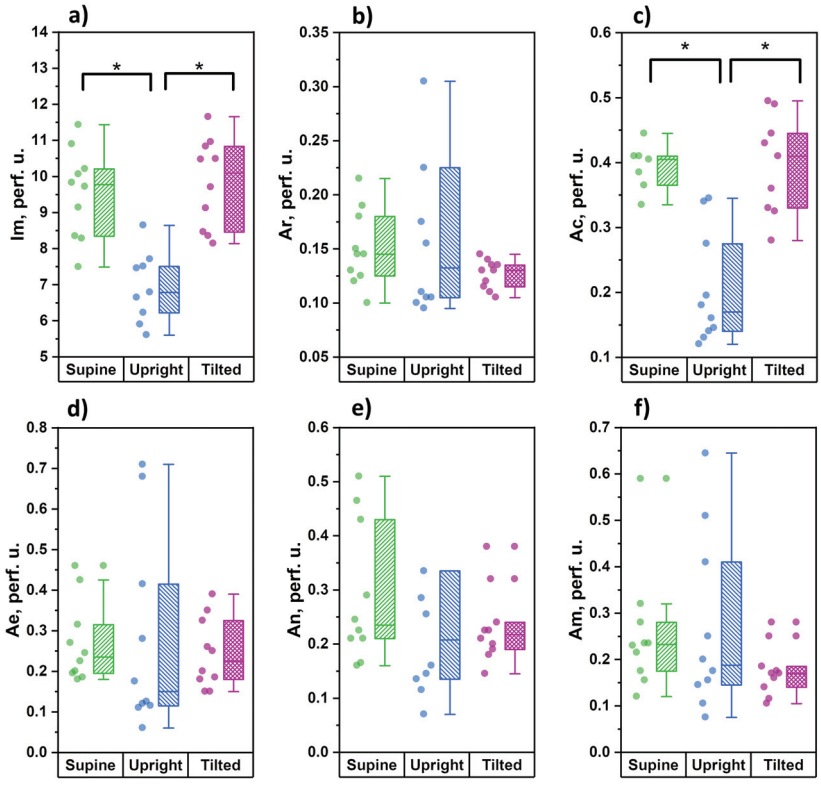

Figure 4. Analysed blood perfusion parameters measured on the shins for three body positions: supine, upright and tilted (Trendelenburg position): (**a**) average blood perfusion; (**b**) cardiac oscillations; (**c**) respiratory oscillations; (**d**) endotelial oscillations; (**e**) neurogenic oscillations; (**f**) miogenic oscillations (* the significance of a difference between values was confirmed with $p < 0.05$ using the Mann–Whitney test)

3.3. Measurements on the Forehead

Figure 5 shows the results of the measurements of the cutaneous blood perfusion dynamics on the forehead.

During measurements on the forehead, we did not register any significant changes in the index of microcirculation caused by postural changes. With unchanged tissue perfusion, however, significant increases in the amplitudes of neurogenic and myogenic oscillations were recorded when changing from a supine to an upright position, which is the opposite of the results obtained in the shins. Despite the presence of a tendency towards moderate increases in the amplitudes of endothelial and neurogenic oscillations in the Trendelenburg position, these changes did not reach statistically significant levels.

3.4. Blood Pressure and Heart Rate

Before each stage of the study, for every tested subject the parameters of blood pressure and heart rate were recorded via the right arm. The results of these measurements are shown in Figure 6.

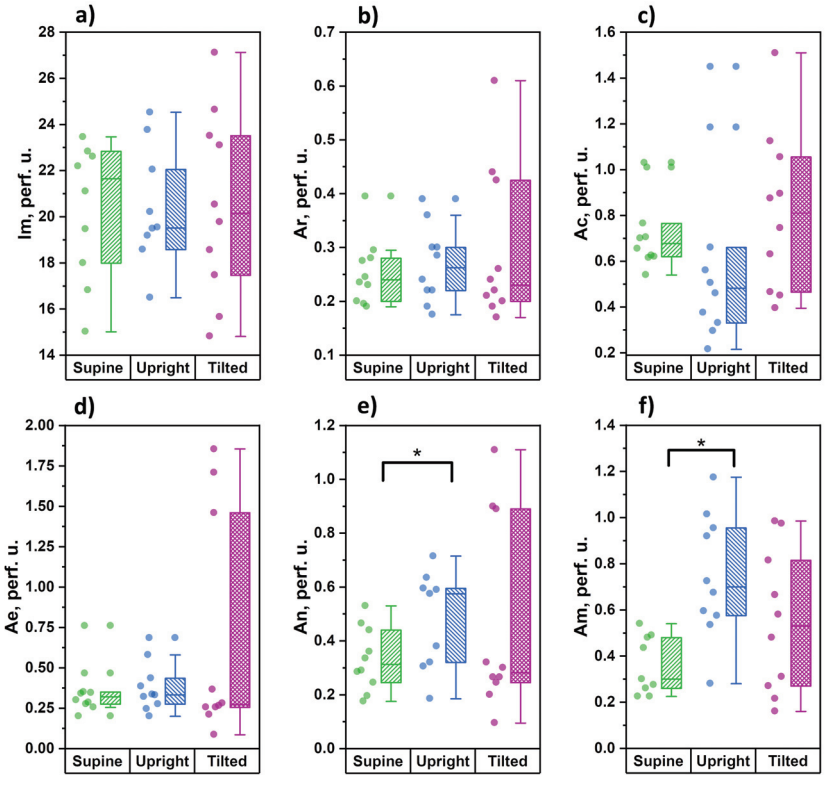

Figure 5. Analysis of blood perfusion parameters in the skin of the brow of the forehead for three tested body positions: supine, upright and tilted (Trendelenburg position): (**a**) average blood perfusion; (**b**) cardiac oscillations; (**c**) respiratory oscillations; (**d**) endotelial oscillations; (**e**) neurogenic oscillations; (**f**) miogenic oscillations (* the significance of a difference between values was confirmed with $p < 0.05$ using the Mann–Whitney test).

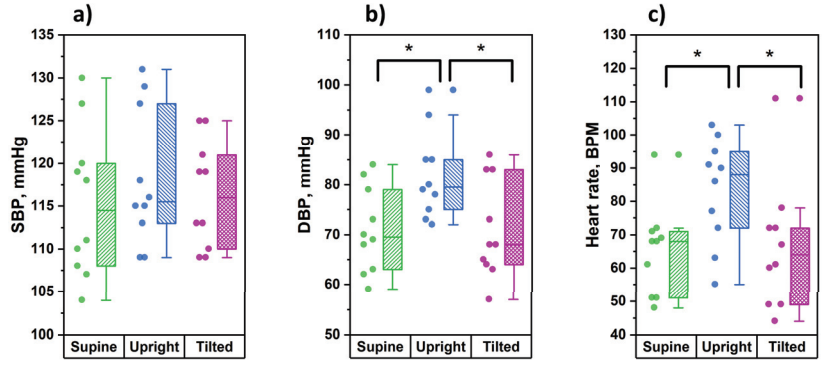

Figure 6. Analysis of parameters of blood pressure and hear rate measured in the tested body positions: supine, upright and tilted (Trendelenburg position): (**a**) systolic blood pressure; (**b**) diastolic blood pressure; (**c**) heart rate (* the significance of a difference between the values was confirmed with $p < 0.05$ using the Mann–Whitney test).

From the data obtained, it can be seen that in the position of orthostasis, significantly higher values of diastolic pressure and heart rate were observed compared to the supine and the Trendelenburg positions. At the same time, the values of systolic blood pressure did not undergo significant changes during postural changes.

4. Discussion

The value of the skin microvascular bed as an object of research for identifying the patterns of the cardiovascular system functioning is under discussion nowadays. In a review work, based on the results of LDF amplitude–frequency wavelet analysis, Martini R. and Bagno A. showed that changes in the parameters of the skin microcirculation are detected in the widest range of diseases [24]. This includes studies of diabetes complications [25], peripheral arterial disease [26] and arterial hypertension [27] among other conditions.

It is known that the microvascular bed of the skin is not subject to baroreflex regulation [28,29], and the results we obtained on the forearm are very interesting. During the transition to orthostasis, when the measurement area was below the height of the heart, we noted decreases in the amplitudes of endothelial, neurogenic and myogenic vasomotions. A decrease in the vasomotions' amplitude indicates a decrease in the lumen size of resistive precapillary arterioles, which can be regarded as an increase in the vascular tone. It can be assumed that a decrease in the lumen of resistive precapillary arterioles leads to a decrease in the amplitude of cardiac oscillations in microvessels, which, in turn, indicates a decrease in arterial blood flow to the capillaries. A decrease in the amplitude of cardiac oscillations at the level of precapillary arterioles can be caused by several mechanisms: (1) An increase in hydrostatic pressure in the venular link of the vascular bed amidst the difficulty in the blood outflow from the capillaries leads to an increase in the capacitive vessels tone, which, through the mechanisms of venulo-arteriolar communication, can lead to an increase in the tone of the bringing arterioles [30]. (2) Activation of the sympathoadrenal system due to weakening of the depressor effects on it from the baroreceptors of the carotid sinus. Amidst that, the subjects showed a significant increase in diastolic blood pressure and heart rate. We did not find a significant correlation between these parameters, which may have been due to a small sample size, but it can be assumed that there is a relationship between the amplitude of vasomotions of the tone-forming mechanisms of skin microvessels and the level of blood pressure. If this hypothesis is correct, then the LDF technique can be a useful additional tool for interpreting the results of 24-h blood pressure monitoring when patients are in an upright position for most of the day, and for monitoring the functional state of resistive skin microvessels when prescribing antihypertensive therapy.

When the head is lowered 15° below the horizontal line, the measurement point on the forearms is slightly above the heart level, which does not affect the functional state of the tone-forming regulatory mechanisms of skin microcirculation in the upper extremities. Amidst this, there is a significant increase in the amplitude of the cardiac oscillations, which can be explained by the opposite mechanisms observed in orthostasis: (1) the precapillary arterioles' tone is restored through the mechanisms of venulo-arteriolar communication against the background of a decrease in pressure in the venous vessels; (2) a decrease in the activity of the sympathoadrenal system amidst the restoration of the depressor activity of the carotid sinuses. An increase in the arterial blood inflow into the microvasculature is accompanied by a significant increase in the level of tissue perfusion (Figure 3a). For the lower extremities, a change in body position leads to a decrease in the amplitude of cardiac oscillations (a decrease in inflow), and a corresponding decrease in the level of tissue perfusion without changing the activity of tone-forming mechanisms at the level of resistive precapillary arterioles. This is most likely due to regional features of the tissue perfusion regulation of the skin in the legs and is of a compensatory nature aimed at maintaining nutritive blood flow in conditions of decreased tissue perfusion. In a non-physiological position for the legs, when they are above the heart, the outflow of venous blood is significantly facilitated, but the perfusion pressure decreases. Amidst this, we see an insignificant tendency towards a decrease in the amplitude of neurogenic and myogenic

vasomotions (increased tone), which can also be regarded as a compensatory response aimed at maintaining perfusion pressure in the skin capillaries.

The results of the study of skin perfusion in the forehead can be of particular interest in connection with the brain's blood supply. It is known that the scalp receives nutrition from the external carotid artery system, and only the skin of the forehead is supplied with blood from the a.supratrochlearis and a.supraorbitalis, which are the final branches of the supraorbital arteries that are part of the internal carotid artery system [31]. The researchers' interest in the basin of the a.supraorbitalis is due to the fact that disorders of microcirculatory blood flow in the eye area (fundus and bulbar conjunctiva) are associated with various variants of cerebral circulatory disorders [32–34]. As was shown in the pilot study [35], the nature of skin microcirculation in the forehead significantly differs in the level of skin perfusion and in the activity of regulatory mechanisms, depending on the side and volume of ischemic brain damage, and during thrombolytic therapy, these parameters showed significant changes.

The higher level of average blood perfusion in skin of the forehead, relative to the skin of the upper and lower extremities, and the stability of cutaneous blood perfusion in any position of the body (Figure 5a), draw attention. This may indicate a high potential of the mechanisms of autoregulation of cerebral blood flow. Significant changes in the regulatory mechanisms at the level of precapillary arterioles are observed only in orthostasis and are expressed in an increase of amplitude of neurogenic and myogenic vasomotations. When the head is higher than the heart, the neurogenic and myogenic mechanisms of microvascular tone-forming are reduced.

In the Trendelenburg position, when not only the outflow of venous blood from the head is hindered, but also the pressure in the arterial bed increases, the functional state of the tone-forming mechanisms changes in a very wide range. We assume that this is due to the high potential of the mechanisms of regulation of cerebral hemodynamics. For the tone-forming mechanisms of microcirculation regulation (Ae, An and Am), changing their functional activity according to the principle of positive and negative responses, modulates the volume and speed of arterial blood flowing to the capillaries (Ac) to the optimal values for transcapillary exchange in the vascular volume at the time, and in our study—depending on the position of the body in space.

The facial skin, as an object of research, is also interesting due to its features of innervation. The system of innervation of skin microvessels is mainly represented by somatic sensitive (afferent) and vegetative sympathetic (efferent) systems of regulation. The direct involvement of the parasympathetic nervous system in the regulation of cutaneous microvessels is considered proven only for the skin of the face [32,36]. Thus, the study of microcirculatory blood flow in the area of the facial skin opens up opportunities for studying almost all mechanisms of neurogenic control of the vasomotor activity of resistive microvessels at the opposite end to the heart pole of the great circle of blood circulation [37].

5. Conclusions

The novel wearable sensors implementing the measuring principles of laser Doppler and dynamic light scattering techniques for blood perfusion monitoring significantly extend the capabilities of researchers and practical clinicians in terms of monitoring parameters of skin blood perfusion. The analysis of signals recorded by the wearable LDF devices can be effectively realized using machine learning algorithms. Nevertheless, practical applications of the sensors for medical diagnostics require taking into account a considerable number of details. Some of the factors greatly influencing the patterns of the blood perfusion behavior are the posture and body position. In this study, we demonstrate what kind of relative changes can be expected in average perfusion and blood flow oscillations during postural changes being measured on skin of the limbs and on the brow of forehead. We show the importance of taking into account the position of the body in space during the monitoring of physiological parameters interrelated with blood perfusion. Presented findings of the amplitude–frequency analysis of LDF signals measured in different body

positions confirm the early promise of the measurement technique for the orthostatic test and diagnostic procedures based on it, and more specifically, for the use of this particular type of wearable device together with the physiological tests. The results obtained can be of particular interest for the development of new protocols for the study of microcirculation, including those related to daily monitoring. The vast majority of modern fitness trackers use the method of photoplethysmography to record physiological parameters. In this and previous works, we have shown that the LDF method can also be of significant interest for wearable applications, opening up new opportunities for the diagnostics of the microcirculation and cardiovascular systems.

6. Patents

1. E.A. Zherebtsov, I.O. Kozlov, A.I. Zherebtsova, E.V. Zharkikh, Y.I. Loktionova and A.V. Dunaev, "Software for data analysis of multi-channel wearable device for recording the level of capillary blood flow." Software patent RU 2019665950 (2019).
2. I.O. Kozlov and E.A. Zherebtsov, "Software for recording the distribution of blood perfusion by Doppler shift frequencies." Software patent RU 2019616389 (2019).

Author Contributions: Conceptualization, methodology, investigation, discussion, writing—review and editing, A.A.F.; writing—original draft preparation, formal analysis, Y.I.L.; writing—original draft preparation, discussion, E.V.Z.; investigation, data curation, M.A.M.; investigation, J.A.P.; methodology, investigation, A.V.S.; discussion, funding acquisition, project administration, formal analysis, E.A.Z. All authors edited the manuscript. All authors have read and agreed to the published version of the manuscript.

Funding: The reported study was funded by the Russian Foundation for Basic Research (RFBR), grant number 20-08-01153. A. Fedorovich, J. Popova and A. Suvorov were funded in the framework of the research topic 64.1 by the Russian Academy of Science (RAS). E. Zherebtsov acknowledges the funding from the Academy of Finland, grant number 318281.

Institutional Review Board Statement: The study was conducted according to the guidelines of the Declaration of Helsinki, and approved by the Ethics Committee of Institute of Biomedical Problems of the Russian Academy of Sciences (protocol code 483, 3 August 2018).

Informed Consent Statement: Informed consent was obtained from all subjects involved in the study.

Data Availability Statement: The data presented in this study are available on request from the corresponding author.

Acknowledgments: The authors express their acknowledgements to all the volunteers who contributed to the present study.

Conflicts of Interest: The authors declare no conflict of interest. The funders had no role in the design of the study; in the collection, analyses, or interpretation of data; in the writing of the manuscript, or in the decision to publish the results.

References

1. Cooke, W.H.; Pellegrini, G.L.; Kovalenko, O.A. Dynamic cerebral autoregulation is preserved during acute head-down tilt. *J. Appl. Physiol.* **2003**, *95*, 1439–1445. [CrossRef]
2. Borst, C.; Wieling, W.; Van Brederode, J.; Hond, A.; De Rijk, L.; Dunning, A. Mechanisms of initial heart rate response to postural change. *Am. J. Physiol. Heart Circ. Physiol.* **1982**, *243*, H676–H681. [CrossRef] [PubMed]
3. Borst, C.; Van Brederode, J.; Wieling, W.; Van Montfrans, G.; Dunning, A. Mechanisms of initial blood pressure response to postural change. *Clin. Sci.* **1984**, *67*, 321–327. [CrossRef] [PubMed]
4. Klijn, E.; Niehof, S.; Groeneveld, A.J.; Lima, A.P.; Bakker, J.; van Bommel, J. Postural change in volunteers: Sympathetic tone determines microvascular response to cardiac preload and output increases. *Clin. Auton. Res.* **2015**, *25*, 347–354. [CrossRef]
5. Barantke, M.; Krauss, T.; Ortak, J.; Lieb, W.; Reppel, M.; Burgdorf, C.; Pramstaller, P.P.; Schunkert, H.; Bonnemeier, H. Effects of gender and aging on differential autonomic responses to orthostatic maneuvers. *J. Cardiovasc. Electrophysiol.* **2008**, *19*, 1296–1303. [CrossRef]
6. Thiriet, M. *Biology and Mechanics of Blood Flows: Part II: Mechanics and Medical Aspects*; Springer: New York, NY, USA, 2008. [CrossRef]

7. Del Pozzi, A.T.; Carter, S.J.; Collins, A.B.; Hodges, G.J. The regional differences in the contribution of nitric oxide synthase to skin blood flow at forearm and lower leg sites in response to local skin warming. *Microvasc. Res.* **2013**, *90*, 106–111. [CrossRef] [PubMed]
8. Hodges, G.J.; Del Pozzi, A.T. Noninvasive examination of endothelial, sympathetic, and myogenic contributions to regional differences in the human cutaneous microcirculation. *Microvasc. Res.* **2014**, *93*, 87–91. [CrossRef]
9. Sorelli, M.; Stoyneva, Z.; Mizeva, I.; Bocchi, L. Spatial heterogeneity in the time and frequency properties of skin perfusion. *Physiol. Meas.* **2017**, *38*, 860. [CrossRef] [PubMed]
10. Tikhonova, I.V.; Grinevich, A.A.; Guseva, I.E.; Tankanag, A.V. Effect of orthostasis on the regulation of skin blood flow in upper and lower extremities in human. *Microcirculation* **2020**, e12655. [CrossRef]
11. Alice Y.M.; Jones, E.D. Body position change and its effect on hemodynamic and metabolic status. *Heart Lung* **2004**, *33*, 281–290. [CrossRef]
12. Narayanan, K.; James, J.C.; Hamner, J.; Mukai, S.; Lipsitz, L.A. Predicting cerebral blood flow response to orthostatic stress from resting dynamics: Effects of healthy aging. *Am. J. Physiol. Regul. Integr. Comp. Physiol.* **2001**, *281*, 716–722. [CrossRef] [PubMed]
13. Zherebtsov, E.; Sokolovski, S.; Sidorov, V.; Rafailov, I.; Dunaev, A.; Rafailov, E. Novel wearable VCSEL-based blood perfusion sensor. *Proc. SPIE* **2018**, 564. [CrossRef]
14. Zherebtsov, E.; Zharkikh, E.; Kozlov, I.; Loktionova, Y.; Zherebtsova, A.; Rafailov, I.; Sokolovski, S.; Sidorov, V.; Dunaev, A.; Rafailov, E. Wearable sensor system for multipoint measurements of blood perfusion: Pilot studies in patients with diabetes mellitus. *Proc. SPIE* **2019**, 62. [CrossRef]
15. Loktionova, Y.; Zharkikh, E.; Kozlov, I.; Zherebtsov, E.; Bryanskaya, S.; Zherebtsova, A.; Sidorov, V.; Sokolovski, S.; Dunaev, A.; Rafailov, E. Pilot studies of age-related changes in blood perfusion in two different types of skin. *Proc. SPIE* **2019**, 37. [CrossRef]
16. Loktionova, Y.; Zherebtsov, E.; Zharkikh, E.; Kozlov, I.; Zherebetsova, A.; Sidorov, V.; Sokolovski, S.; Rafailov, I.; Dunaev, A.; Rafailov, E. Studies of age-related changes in blood perfusion coherence using wearable blood perfusion sensor system. *Proc. SPIE* **2019**, *11075*, 1107507. [CrossRef]
17. Zherebtsov, E.; Zharkikh, E.; Kozlov, I.; Zherebtsova, A.; Loktionova, Y.; Chichkov, N.; Sidorov, V.; Dunaev, A.; Rafailov, E.; Sokolovski, S.; et al. Novel wearable VCSEL-based sensors for multipoint measurements of blood perfusion. *Proc. SPIE* **2019**, 6. [CrossRef]
18. Loktionova, Y.; Zharkikh, E.; Zherebtsov, E.; Kozlov, I.; Sidorov, V.; Zherebtsova, A.; Sokolovski, S.; Dunaev, A.; Rafailov, E. Wearable laser Doppler sensors for evaluating the nutritive and shunt blood flow. *Proc. SPIE* **2020**. [CrossRef]
19. Zharkikh, E.; Loktionova, Y.; Kozlov, I.; Zherebtsova, A.; Sidorov, V.; Zherebtsov, E.; Dunaev, A.; Rafailov, E. Wearable Laser Doppler Flowmetry for the Analysis of Microcirculatory Changes during Intravenous Infusion in Patients with Diabetes Mellitus. *Proc. SPIE* **2020**, 57. [CrossRef]
20. Mizeva, I.; Dremin, V.; Potapova, E.; Zherebtsov, E.; Kozlov, I.; Dunaev, A. Wavelet Analysis of the Temporal Dynamics of the Laser Speckle Contrast in Human Skin. *IEEE Trans. Biomed. Eng.* **2020**. [CrossRef]
21. Goma, M.; Kimura, Y.; Shimura, H.; Kaneshige, M.; Kobayashi, T.; Kikuchi, M.; Terada, N. Orthostatic response of cephalic blood flow using a mini laser Doppler blood flowmeter and hemodynamics of a new active standing test. *Eur. J. Appl. Physiol.* **2015**, *115*, 2167–2176. [CrossRef] [PubMed]
22. Bivins, H.; Knopp, R.; dos Santos, P.A. Blood volume distribution in the Trendelenburg position. *Ann. Emerg. Med.* **1985**, *14*, 641–643. [CrossRef]
23. Shiogai, Y.; Stefanovska, A.; McClintock, P.V.E. Nonlinear dynamics of cardiovascular ageing. *Phys. Rep.* **2010**, *488*, 51–110. [CrossRef] [PubMed]
24. Martini, R.; Bagno, A. The wavelet analysis for the assessment of microvascular function with the laser Doppler fluxmetry over the last 20 years. Looking for hidden informations. *Clin. Hemorheol. Microcirc.* **2018**, *70*, 213–229. [CrossRef] [PubMed]
25. Hu, H.F.; Hsiu, H.; Sung, C.J.; Lee, C.H. Combining laser-Doppler flowmetry measurements with spectral analysis to study different microcirculatory effects in human prediabetic and diabetic subjects. *Lasers Med. Sci.* **2017**, *32*, 327–334. [CrossRef]
26. Schabauer, A.M.; Rooke, T.W. Cutaneous laser Doppler flowmetry: Applications and findings. In *Mayo Clinic Proceedings*; Elsevier: Amsterdam, The Netherlands, 1994; Volume 69, pp. 564–574. [CrossRef]
27. Farkas, K.; Kolossváry, E.; Járai, Z.; Nemcsik, J.; Farsang, C. Non-invasive assessment of microvascular endothelial function by laser Doppler flowmetry in patients with essential hypertension. *Atherosclerosis* **2004**, *173*, 97–102. [CrossRef] [PubMed]
28. Ninomiya, I.; Fujita, S. Reflex effects of thermal stimulation on sympathetic nerve activity to skin and kidney. *Am. J. Physiol. Leg. Content* **1976**, *230*, 271–278. [CrossRef] [PubMed]
29. Malpas, S.C. Neural influences on cardiovascular variability: Possibilities and pitfalls. *Am. J. Physiol. Heart Circ. Physiol.* **2002**, *282*, H6–H20. [CrossRef] [PubMed]
30. Tigno, X.T.; Ley, K.; Pries, A.R.; Gaehtgens, P. Venulo-arteriolar communication and propagated response. *PflÜGers Arch.* **1989**, *414*, 450–456. [CrossRef]
31. Goltsov, A.; Anisimova, A.V.; Zakharkina, M.; Krupatkin, A.I.; Sidorov, V.V.; Sokolovski, S.G.; Rafailov, E. Bifurcation in blood oscillatory rhythms for patients with ischemic stroke: A small scale clinical trial using laser doppler flowmetry and computational modeling of vasomotion. *Front. Physiol.* **2017**, *8*, 160. [CrossRef]
32. Ikram, M.K.; De Jong, F.J.; Van Dijk, E.J.; Prins, N.D.; Hofman, A.; Breteler, M.M.B.; De Jong, P.T.V.M. Retinal vessel diameters and cerebral small vessel disease: The Rotterdam Scan Study. *Brain* **2006**, *129*, 182–188. [CrossRef]

33. Sharrett, A.R. A Review of Population-Based Retinal Studies of the Microvascular Contribution to Cerebrovascular Diseases. *Ophthalmic Epidemiol.* **2007**, *14*, 238–242. [CrossRef] [PubMed]
34. Cheung, N.; Mosley, T.; Islam, A.; Kawasaki, R.; Sharrett, A.R.; Klein, R.; Coker, L.H.; Knopman, D.S.; Shibata, D.K.; Catellier, D.; et al. Retinal microvascular abnormalities and subclinical magnetic resonance imaging brain infarct: A prospective study. *Brain* **2010**, *133*, 1987–1993. [CrossRef] [PubMed]
35. Anisimova, A.; Krupatkin, A.; Sidorov, V.; Zacharkina, M.; Yutskova, E.; Galkin, S. Laser Doppler flowmetry in the assessment of the microcirculation in patients with acute and chronic cerebrovascular insufficiency. *Reg. Blood Circ. Microcirc.* **2014**, *13*, 31–37. [CrossRef]
36. Izumi, H. Nervous control of blood flow in the orofacial region. *Pharmacol. Ther.* **1999**, *81*, 141–161. [CrossRef]
37. Fedorovich, A.A. Functional State of the Microvascular Bed of the Skin in Essential Arterial Hypertension Assessed by Laser Doppler Flowmetry with Amplitude-Frequency Wavelet Analysis of Blood Flow Oscillations. In *Basic and Clinical Understanding of Microcirculation*; IntechOpen: London, UK, 2019.

diagnostics

MDPI

Article

Laser Doppler Spectrum Analysis Based on Calculation of Cumulative Sums Detects Changes in Skin Capillary Blood Flow in Type 2 Diabetes Mellitus

Igor Kozlov [1,*], Evgeny Zherebtsov [1,2], Galina Masalygina [3], Konstantin Podmasteryev [1] and Andrey Dunaev [1]

[1] Research and Development Center of Biomedical Photonics, Orel State University, 302026 Orel, Russia; evgenii.zherebtsov@oulu.fi (E.Z.); asms-orel@mail.ru (K.P.); inohvat@yandex.ru (A.D.)
[2] Optoelectronics and Measurement Techniques Unit, University of Oulu, 90570 Oulu, Finland
[3] Orel Regional Clinical Hospital, 302028 Orel, Russia; kovalina68@ya.ru
* Correspondence: igor57_orel@mail.ru; Tel.: +7-(4862)-41-98-06

Abstract: In this article, we introduce a new method of signal processing and data analysis for the digital laser Doppler flowmetry. Our approach is based on the calculation of cumulative sums over the registered Doppler power spectra. The introduced new parameter represents an integral estimation for the redistribution of moving red blood cells over the range of speed. The prototype of the device implementing the technique is developed and tested in preliminary clinical trials. The methodology was verified with the involvement of two age groups of healthy volunteers and in a group of patients with type 2 diabetes mellitus. The main practical result of the study is the development of a set of binary linear classifiers that allow the method to identify typical patterns of the microcirculation for the healthy volunteers and diabetic patients based on the presented diagnostic algorithm.

Keywords: laser Doppler flowmetry; non-invasive optical diagnostics; cumulative sum; power spectrum; heating test; diabetes mellitus type 2

Citation: Kozlov, I.; Zherebtsov, E.; Masalygina, G.; Podmasteryev, K.; Dunaev, A. Laser Doppler Spectrum Analysis Based on Calculation of Cumulative Sums Detects Changes in Skin Capillary Blood Flow in Type 2 Diabetes Mellitus. *Diagnostics* **2021**, *11*, 267. https://doi.org/10.3390/diagnostics11020267

Academic Editor: Xavier Muñoz-Berbel
Received: 1 December 2020
Accepted: 3 February 2021
Published: 9 February 2021

1. Introduction

The blood microcirculation (BM) performs a crucial role for the life support of every type of living tissue in the human body. The BM supports gases and nutrients exchange, delivering of immune cells, and temperature regulation. The BM makes a major contribution to the overall flow resistance of the blood vessels, being the main actor in the regulation of the blood pressure. The functional state of human tissues directly depends on the state of elementary BM units (capillaries, plexus, minor arterioles, and venules). It is well-known [1] that the microcirculatory bed is composed of blood vessels of the certain types with a particular specialisation: arterioles, capillaries, venules and arterio-venular anastomoses (AVA). AVA, together with the smooth muscle structures acts as a physiological valve that redirects the micro blood flow either through the capillary plexus or bypassing one. The process orchestrated by the physiological regulation from the endothelium, neural activity, myogenic contraction and relaxation, as well as by the modulation from the breathing and heart activity creates characteristic patterns of the blood perfusion fluctuations [2,3].

The disruptions in BM significantly contribute to the development of many diseases and syndromes. One of the most common and widespread diseases with a plethora of severe complications affecting BM is diabetes mellitus type 2 (T2DM). According to forecasts, the number of patients with T2DM is projected to constantly grow in the near future to achieve 500 million people by 2030 [4,5]. Common complications of T2DM are ulcers and lesions on the feet and toes, as well as the development of necrosis due to the trophic disorders of the affected tissues. Optical, non-invasive diagnostics offer a good

range of methods for the evaluation of the functional insufficiency in the components of tissue vitality including blood microcirculation system. The methods are based on such approaches as fluorescence spectroscopy [6], diffuse reflectance spectrocopy [7–9], speckle contrast imaging [10], photopletismography [11], videocapillaroscopy [12] and methods based on coherent light scattering and optical coherence tomography [13,14].

One well-established method for the non-invasive measurements of the blood perfusion in vivo is the laser Doppler flowmetry (LDF). The theoretical basis for the technique is based on the statistical analysis of the laser radiation scattered in the scattering medium with the moving light-scattering elements. For the case of the measurements in the living tissue, the static scattering structures are the cells and static tissue layers, whereas the moving particles are the locomotive blood cells in the flowing capillaries and blood microvessels. The subtle frequency shift caused by an optical Doppler effect is usually detected by the couple of photodiodes operating in the photomixing regime [15,16]. This method has a sufficient time resolution and depth of probing (about 1 mm [17]) to register the blood microflow fluctuations of different origin, as well as the average level of blood perfusion. The range of applications of the non-invasive diagnostics by the LDF method covers the topics of relationship between oxygen saturation and blood flow [18], dental pulp blood flow [19], blood flow analysis in cases of type 1 diabetes mellitus [20] and rheumatic diseases [21], combining LDF and endoscopy during surgery interventions [22,23], nonlinear blood flow dynamics analysis in a various application [24,25], analysis of transdermal transport of drugs [26] and registration of arterial hypertension associated changes in microcirculation [27]. Numerically, the resulting value for the blood perfusion in the LDF technique is commonly given by the expression:

$$PU = \int_{f_{min}}^{f_{max}} f \cdot S(f) df, \tag{1}$$

where $S(f)$ is the power spectrum of the photocurrent given as a function of the frequency, f; f_{min}, f_{max} are the limits of integration over the region of the power spectrum corresponding to the physiological range of the RBC speed in the blood capillaries. In several recent studies, more advanced techniques on the LDF signal processing were presented [28,29]. The power spectrum analysis within selected ranges of integration allowed Fredriksson et al., to estimate the three ranges of RBC speed in the diagnostic volume of a fibre optical probe. Taking into account the RBC speed distribution and light scattering phase function, a similar approach has been applied for the laser Doppler spectrum decomposition [30,31].

From the very early studies on the LDF technique development, it has been revealed that the distribution of the power spectrum amplitudes over the dimension of frequency changes to a considerable degree, and represents the frequency distribution of intensities for the Doppler shifted optical components scattered on moving RBC [32,33]. In many clinical studies, it has been demonstrated that the information is of substantial diagnostic value for the quantitative characterisation of the microcirculation disorders [34–38]. As an example, the LDF signal recorded with the power spectrum integration up to the frequency of 3000 Hz demonstrated a better signal-to-noise ratio and presented overall quality of diagnostics of the dental pulp vitality than using the full range of the bandwidth [39]. The power spectrum properties for the purposes of the verification of the LDF technique were also studied in liquid phantoms where the interrelation between the distribution of the speed of scattering particles with the registered power spectrum of photocurrent from the detector was also confirmed [40]. Also, the effects of local pressure on the optical probe to the skin surface [34] and breath-holding test [41] on the broadening of the Doppler spectra were studied. Despite the recent interest several research groups on the diagnostic potential of LDF measurements with a more sophisticated analysis of the detector power spectrum, the topic has still not been well understood and dealt with in depth.

In that respect, the aim of this study was to elaborate the concept of a new feature space extracted from the Doppler power spectrum that will increase the diagnostic capability of the LDF method for analysis of blood microcirculation disorders in patients with T2DM.

2. Materials and Methods

To implement the LDF signal registration, an in-house built setup was designed and tested (Figure 1). The block diagram of the device is shown in Figure 2. Infra-red laser diode (LPS-785-FC, Thorlabs, USA) (1) with a central radiation wavelength of 785 nm was used for the local illumination of the area of interest (AOI) with 2 mW of output light power. The channel of the electronic signal processing consisted of light-to-current converting and amplifying modules (2, 3), low-frequency (4, 5) and high-frequency (6, 7) filters and a unit for the stabilised power supply.

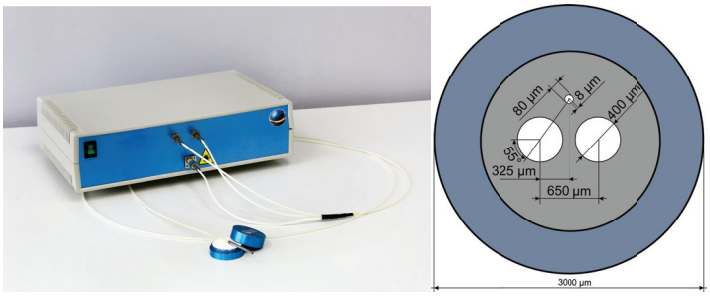

(**a**) (**b**)

Figure 1. In-house built prototype of laser Doppler flowmeter with 2 mW of output light power, a signal amplifying, filtration unit, 50 kHz sample rate per channel (**a**) and fibre geometrical configuration (**b**).

The analog-to-digital conversion was implemented by a USB 6211 (National Instruments™,Austin, Texas, USA) data acquisition board (8) with a sampling rate of 50 kHz per channel. LabVIEW™-based PC application (9) was developed for the device control, data acquisition and pre-processing. The period of cycle with the recording of time series containing 2500 data points of photocurrent and the power spectrum calculation was set to be 0.05 s, with the corresponding sampling rate of 20 Hz for the output calculated perfusion. The cut-off frequency for the calculation of the power spectrum was set to 12,800 Hz with the possible increase of this parameter up to the Nyquist frequency limit.

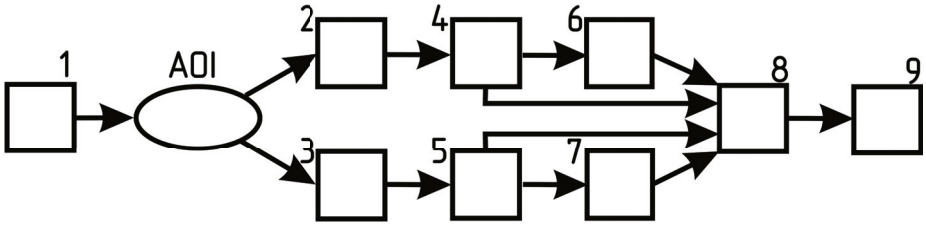

Figure 2. The schematic diagram of the developed laser Doppler flowmetry measuring setup. 1— infrared laser diode; 2, 3—light-to-current conversion and amplification modules; 4, 5—low-frequency filters; 6, 7—high-frequency filters; 8—data acquisition board; 9—PC with LabVIEW-based application.

For the blood perfusion calculations over the sub-regions of the power spectrum, the following expression has been used:

$$PU = \frac{K}{i_{dc}^2} \int_{f_{min}}^{f_{max}} f \cdot S(i_{ac2}(t) - i_{ac1}(t))df, \tag{2}$$

where K—the static coefficient of gain; $i_{dc}(t)$—the d.c. component of the photocurrent; $i_{ac1}(t)$, $i_{ac2}(t)$—the a.c. components of the photocurrents in the two input photo-detecting sub-channels (the implementation of the differential measuring technique with the subtraction of $i_{ac1}(t)$ and $i_{ac2}(t)$ significantly reduces the motion artefacts from the fibre optical probe); S—the procedure of the power spectrum calculation from the accumulated array of the subtracted values of $i_{ac1}(t)$ and $i_{ac2}(t)$. The key functionality of the developed software was the ability to save on disk the calculated power spectra for every sample for further post-processing.

In addition to conventional perfusion units, an estimation of the blood cell speed $\langle v \rangle$ [42] was conducted during the data analysis. The parameters were calculated according to the following equation:

$$\langle v \rangle = \frac{\int_{f_{min}}^{f_{max}} f \cdot S(i_{ac2}(t) - i_{ac1}(t))df}{\int_{f_{min}}^{f_{max}} S(i_{ac2}(t) - i_{ac1}(t))df}. \tag{3}$$

Parameter $\langle v \rangle$ is described as the ratio of conventional perfusion parameter to concentration of moving red blood cells (CMBC) [43] estimated by the Doppler power spectrum, and is general expressed in arbitrary units.

For the validation of the experimental setup, preliminary measurements have been done with the participation of healthy volunteers. The developed and implemented signal processing approach allowed us to reliably register and visualise (Figure 3) the effect of redistribution of the power spectrum signal due to the changes in the distribution of the RBCs speed in blood capillaries during a breath-holding test (BHT) [44]. In the middle of a deep breath, the level of the skin blood perfusion evaluated in the low-frequency range (60–400 Hz) increased prominently, while the overall blood perfusion figured out by the integration in the range of 60–6400 Hz decreased. The result is explained by the slowing down of the bulk of RBC during the procedure of the deep breath-holding causing the shift of the power spectrum to the region of the lower frequencies.

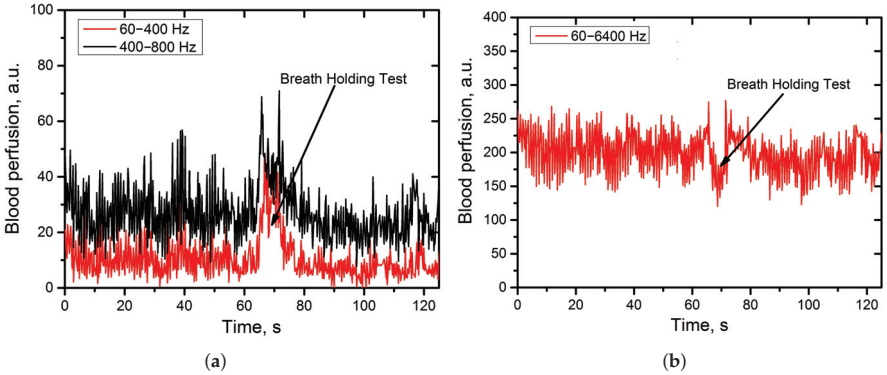

(**a**) (**b**)

Figure 3. Registered skin blood perfusion during the breath-holding test evaluated by the integration in the sub-ranges of the photocurrent power spectrum. (**a**): blood perfusion from the low frequency range (60–400 Hz: red; 400–800 Hz-black); (**b**): blood perfusion from the broader frequency range (60–6400 Hz).

2.1. Research Protocol

The developed measuring setup has been validated in the frame of limited clinical studies with the involvement of patients with diabetic disorders. Thermal stimuli applied to the skin has been used to implement a study protocol, benefiting the most from the developed signal processing approach. The heat test is widely used in diagnostics of disorders associated with the regulation of blood perfusion. Moderate heating of the skin to the temperatures between 41–43 °C provokes activation of nociceptive C-fibres [45] and induces the release of nitric oxide [46] from the endothelial layer of vessels. The effect of the stimuli results in the increase of the skin blood perfusion and modulation of its oscillations. T2DM is often associated with an impairment in the response of blood perfusion on the thermal stimuli. The provocation test can also be applied together with a multi-modal approach that combines several measuring techniques such as laser Doppler flowmetry, diffuse reflectance measurements, or fluorescence spectroscopy [6]. Skin temperature dynamics during the skin heating has a significant diagnostic value, being supplemented with the blood perfusion measurements [47]. The fibre optic probe of the developed prototype of laser Doppler flowmeter with the bespoke signal processing algorithm was placed on the dorsal surface of the foot, and coaxially combined with attachment Figure 4 for the heating and cooling tests containing Peltier element with water cooling.

Reliable fixation on the probe on the foot was carried out using several mesh bandages. The measurements were taken 2 h after a meal and caffeine intake. The volunteers were acclimatised for at least 15 min to the conditions of the room where the measurements were conducted.

At the first stage (further on referred as stage 1), blood perfusion was recorded at a temperature of 33 °C for 10 min, to equalise the temperature conditions of the experiment for all subjects. At the second stage (in the text referred to as stage 2), the temperature was increased sequentially at a rate of 2 °C per min to 42 °C for 5 min. At the third stage (referred to below as stage 3), blood perfusion and effects occurring in the capillary blood flow due to heating were recorded for 3 min (Figure 5).

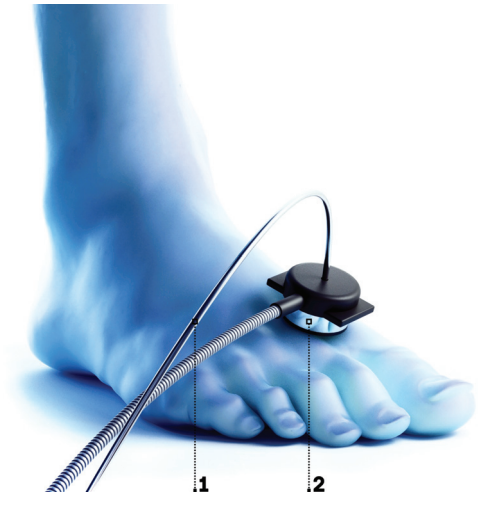

Figure 4. Allocation of the fibre optical probe combined with the attachment for the heat and cooling tests on the dorsal surface of foot. 1—fibre optical probe; 2—the attachment for the heating and cooling tests (contains Peltier element with water cooling).

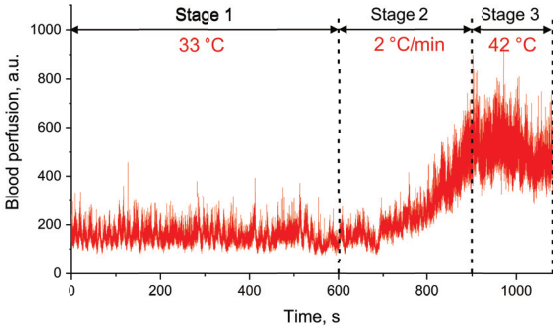

Figure 5. An exemplary trace of the blood perfusion during the implemented research protocol.

The cohort of conditionally healthy volunteers was divided into two groups consisting of 7 non-smoking volunteers aged 22 ± 0.5 years and (referred to as group 1) 6 volunteers (with 1 smoking person) aged 51 ± 6 (referred to as group 2), respectively. The group of patients comprised of 10 non-smoking volunteers aged 61 ± 7 with type 2 diabetes confirmed during for at least 5 years , but without diabetic foot, necrosis and visible lesions and characteristics described in Table 1.

All experiments were carried out at a temperature of 21–23 degrees, at a distance of 1 m from heat sources. Studies in patients and volunteers were conducted with the mandatory obtaining of informed consent for the participation in the study. The research protocol was approved by the Institutional ethical committee of Orel State University (Minutes No. 15 dated 21 February 2019).

Table 1. Characteristics of T2DM patients and volunteers.

Parameters	Patients	Group 1	Group 2
Age (y)	61 ± 7 *	22 ±0.5 *	51 ± 6 *
Sex (M/F)	3/7	2/5	3/3
Systolic BP (mmHg)	125 ± 11	122 ± 8	120 ± 5
Diastolic BP (mmHg)	75 ± 7	70 ± 3	77 ± 4
Body mass index (kg/m^2)	31 ± 4.5 *	24 ± 3.5	25 ± 3.8
Fasting glucose (mmol/L)	10.4 ± 3	-	-
Diabetes duration (y)	11.5 ± 4	-	-
HbA1c (%)	7.1 ± 0.2	-	-
Total cholesterol (mmol/L)	5.2 ± 0.8	-	-
Creatinine (μmol/L)	78.6 ± 7.6	-	-
Urea (mmol/L)	6 ± 0.9	-	-
ALT (IU/L)	24.9 ± 5.4	-	-
AST (IU/L)	19.9 ± 4.3	-	-

Note: Data in the columns is represented as mean ± SD except Sex parameter. Reference values of the laboratory: HbA1c 4.0% to 6.0%, total cholesterol 3.5 to 5.0 mmol/L, urea 2.5 to 7.5 mmol/L, creatinine 70 to 110 μmol/L, ALT 10 to 38 IU/L, and AST 10 to 40 IU/L. *—denotes a statistical difference identified by Mann-Whitney test between two other groups, $p < 0.05$.

2.2. Data Processing

For the study, a novel approach was applied that previously was not used for signal processing in LDF. The implemented LDF channel (Figure 1) during the measuring procedure recorded the raw data with the power spectra from the photodiodes and performed blood perfusion calculation based on those measurements. To analyse the changes in a response to the applied functional tests, cumulative sum curves were calculated at the stage of post-processing by the following steps. Firstly, power spectra weighted by the

frequency were calculated. Secondly, cumulative sum curves for every weighted power spectrum in samples were calculated according to the following recursive expression:

$$C_n = C_{n-1} + \frac{f_n \cdot S(f_n)}{\sum f_i \cdot S(f_i)}, \tag{4}$$

where C_n—a cumulative sum of the series from one to n; $C_0 = 0$; $f_n \cdot S(f_n)$—perfusion calculated for the frequency bin n; $\sum f_i \cdot S(f_i)$—perfusion calculated over all frequencies; n is changed in range from 1 to 640 that equals a frequency range from 0 to 12,800 Hz. Thirdly, the average cumulative sum curve is calculated for a specified period of the perfusion recording. C_n is a value that represents what part of the signal is localised before the certain frequency. The shape of the cumulative sum curve depends on the distribution of the signal over the frequencies of Doppler broadening. The expression (3) can be expressed in an integral form that resembles Equation (1):

$$C_n = \frac{\int_{f_{min}}^{f_n} f \cdot S(f) df}{\int_{f_{min}}^{f_{max}} f \cdot S(f) df}, \tag{5}$$

where f_n is the frequency of the n-th frequency bin. The processing of the data obtained in the standard occlusion test demonstrates the sensitivity of the calculated C_n parameter to the changes in skin blood perfusion during the occlusion stage and stage of post-occlusive reactive hyperaemia (Figure 6).

The cumulative sum curve for the signal recording when occlusion is applied is growing faster. During the occlusion, there is a shift of the localisation of the signal to the low frequency band. Also the overall shape of the cumulative sum curve changes. To quantify the redistribution of the signal over the frequency subbands before and after provocative test, we calculate the parameter of the area enclosed between the two cumulative sum curves.

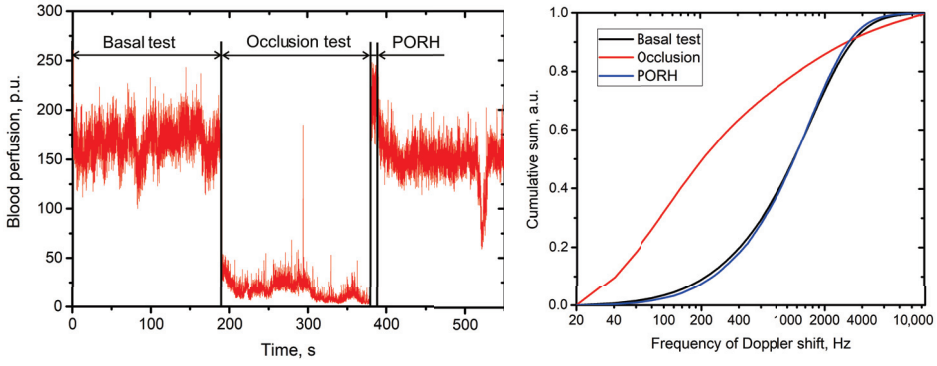

Figure 6. Cumulative sum curves calculated for the main stages of occlusion test. (**a**)—representative trace of the evaluated blood perfusion during the occlusion test; (**b**)—cumulative sum curves calculated for the stages of the occlusion test.

An example of the two curves calculated for stage 1 and stage 3 of the described protocol (Figure 5) implemented in patients is shown in Figure 7, where the purple highlighted area represents the introduced parameter, further called Area between Curves (AbC). The AbC parameter is calculated for the area between the curves from starting frequency

to the first intersection of the curves. The area after the intersection is not included in the calculation.

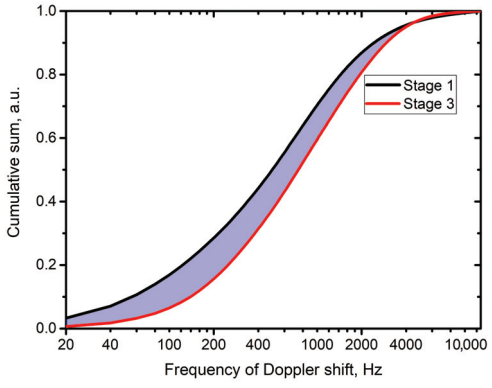

Figure 7. Representative example of cumulative sum curves and analysed area between them (highlighted in purple) for the stages 1 and 3 of the implemented research protocol with thermal stimuli applied to the skin

It is known that the shape of a first moment of the power spectrum depends on the speed of moving red blood cells. However, it remains unclear which mechanisms are more responsible for perfusion alterations during functional tests—a proportional increase in amplitude or changes in the shape of weighted power spectra.

The second informative parameter used in the data analysis was the difference between averaged blood perfusion values calculated for stage 3 and stage 1 (subsequently called the DBP parameter):

$$DBP = \langle PU \rangle_{stage3} - \langle PU \rangle_{stage1}, \tag{6}$$

where $\langle \dots \rangle$—symbol of averaging by time. The DBP parameter is often used in studies as a parameter characterising functional state of the microvascular regulation [20,48]. Also, the average RBC speed calculated according the expression (4) was estimated for the analysed stages 1 and 3:

$$\langle v \rangle_{31} = \langle v \rangle_3 - \langle v \rangle_1, \tag{7}$$

where $\langle v \rangle_1$ and $\langle v \rangle_3$ — average estimation of blood cell speed calculated by whole duration of stage 1 and stage 3 correspondingly.

3. Results

The approach of the cumulative sum curve analysis is intended to demonstrate that mean perfusion changes under thermal stimuli may have different characteristics from volunteer to volunteer in the context of power spectral distribution. Using the two parameters AbC and DBP as a feature space, two binary linear classifiers based on linear discriminant analysis (LDA) were implemented to distinguish the group of patients and the group of volunteers 2, ($Y1$) as well as the groups of volunteers 1 and 2 ($Y2$) (Figure 8).

The calculated discriminant functions have been identified to have the following form:

$$Y1 = -5.0622 + 0.84 \cdot X1_{2p} + 0.0177 \cdot X2_{2p}$$
$$Y2 = -4.28022 + 0.86 \cdot X1_{12} + 0.0076 \cdot X2_{12}$$

Table 1 shows the area under curve (AUC) values for the classifiers based on the discriminant functions calculated using only one of the two input parameters and for their combined use.

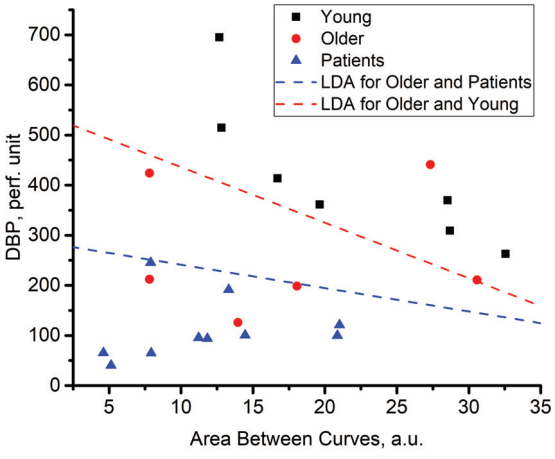

Figure 8. Scatter plots for analysed groups of patients and volunteers with the dividing lines of the LDA classifiers.

The scatter plots for the collected data in Figure 8 are divided into three areas. The first one, the lower-left corner of Figure 8 is represented by the group of patients. Group 1 and group 2 occupied the intermediate position and the upper-right corner, respectively. Group 2 and some individuals from the patient group are characterised by a high DPB parameter. Other individuals showed a relatively high value of the AbC parameter.

4. Discussion

The observed effects are potentially connected with the presence of two ways of mean blood perfusion increase. One of them occurs when the value of the AbC parameter is relatively high. Apparently, the increase in mean blood perfusion is connected with the redistribution of the spectrum amplitude to higher frequencies of Doppler broadening. Whereas, if the DBP parameter increases and the AbC parameter is small, then the blood perfusion changes due to a proportional amplification in the spectrum amplitudes, which will not drastically change the shape of the cumulative sum curves. Thus, the shape of the cumulative sum curve calculated during stage 3 is changed weakly. Consequently, the AbC parameter does not substantially increase. Group 1 is characterised by both mechanisms: a sufficient broadening of the spectrum, and a significant DBP parameter. In the case of group 2, the trend is not recognised. However, group 2 is characterised by reduced values of the DBP and significantly high scattering values relative to the AbC parameter. As for the patient group, both parameters are significantly reduced.

Variations in the AbC parameter can be associated with various factors. The article [49] presents the results of modelling the distribution of photons over the Doppler shift frequencies taking into account changes in both the speed of scattering particles and their concentration. The simulation results show that both of these parameters simultaneously influence the shape of the Doppler spectra. Indeed, during the thermal test, both an increase in the RBC concentration and a change in their average rate can occur. Moreover, article [30] described that the shape of power spectra depends on a distribution characteristic of RBC speed. It is difficult to say with complete certainty which of the described factors is decisive for a particular functional test in healthy volunteers.Further research and modelling is required since Figure 8 shows a substantial variation of the results from healthy volunteers. However, for patients with type 2 diabetes mellitus, it is important to note that changes in the shape of the power spectra in response to the heat test are weak in comparison with cohorts of healthy volunteers, which is demonstrated by the AbC.

Power spectrum shape-changing (consequently, changes in cumulative sum curves) can occur for several reasons. It was previously described that severe geometric shape

changing in capillary loops happens in patients with T2DM [50]. On the example of nailfold capillaroscopy, giant capillaries, and an increase of the distance between capillaries, the appearance of convoluted and intersecting capillaries are shown. The article [51] described the speed of distribution in a healthy capillary loop. To the best of our knowledge, such a numerical experiment for pathological capillaries did not perform. However, in the presence of sharp turns, bends and intersections in a capillary loop, the blood flow will differ substantially from laminar flow. The diameter of capillaries and its influence on power spectra is also considered by Fredriksson et al. [52]. Possibly, the cross-section of capillary loops in patients with T2DM is larger than in healthy volunteers. Thus, a change in the geometric shape of the capillaries, the cross-section and a decrease in their number [53] lead to phenomena where an increase in blood perfusion occurs only due to a proportional increase in the power spectrum amplitudes with relatively constant overall shape of the function. From a clinical point of view, the low-values of parameters AbC and DBP in the cohort of patients can be observed due to the decreasing of capillary loop quantity and pathological changes in the capillaries where the RBC speed profile changes slightly during the applied thermal stimuli.

Thus, introduced in this study, AbC parameter is a novel approach for LDF signal processing. As seen for group 1 and 2 in Table 2, combined use of the parameters significantly increases the prediction value in comparison with the classifiers built using the parameters separately.

To date, there are several methods for recording speed-resolved blood perfusion. For example, PeriFlux 6000 EPOS (Perimed, Järfälla, Sweden) enable simultaneously registering blood perfusion in the frame of three speed ranges. This approach is based on a mathematical model that takes into account the concentration of RBC, blood oxygenation, the potential geometric shapes of capillaries, as well as the optical properties of biological tissues under study. These capabilities are achieved by combining the LDF with the diffuse reflectance spectroscopy measuring channel. A series of studies were made using that technique, for example by Wang et al. [54]. Nevertheless, the current study approach can be implemented using hardware of both classical LDF devices and ones implementing more advanced techniques with recording speed-resolved blood perfusion, supplementing the present arsenal of the signal processing methods in the field.

Calculated AUC-scores of $\langle v \rangle$-based classifiers and classifier with extended feature space for three involved parameters for group 2 vs. patients and group 1 vs. group 2 is shown in Table 2. The combined use of the three parameters augmented with parameter of blood perfusion improves the classification between the compared groups. The proposed estimates represent different aspects of blood perfusion and complement each other.

Thus, the introduced AbC parameter can be used for the interpretation of the origin of observing alterations in mean blood perfusion indicating whether the changes are due to the RBC speed redistribution, or due to the proportional increase in all components of blood perfusion. The AUC-score for the classifier between aged healthy volunteers and patients is of almost the same value as for using a single DBP parameter, which can also be explained by the limited size of the tested cohort of volunteers. Identification of factors, which affect the shape of perfusion distribution by Doppler frequencies, can be of particular interest in the diagnostics of disorders characterised by changes in blood perfusion. It is important to note that the cumulative sum-based estimations such as Area between Curves can be combined with conventional perfusion measurements (CMBC and blood cell speed $\langle v \rangle$). As is shown on Table 2, the combination of the proposed and conventional parameters is better suited for classification for both considered pairs.

The proposed approach can find applications in clinical practice and diagnostics without significant modifications of the standard configuration of LDF channel, facilitating the translation of the study results in routine diagnostics procedures.

Table 2. AUC-scores for the tested classifiers for the groups of volunteers and patients.

Classifiers	AUC
Group 1 vs. Group 2	
DBP classifier	0.76
AbC classifier	0.64
$\langle v \rangle_{31}$ classifier	0.79
Linear classifier (DBP and AbC together)	0.86
Linear classifier (DBP and $\langle v \rangle_{31}$ together)	0.91
Complex classifier (DBP, AbC, $\langle v \rangle_{31}$)	0.928
Group 2 vs. Patients	
DBP classifer	0.92
AbC classifer	0.65
$\langle v \rangle_{31}$ classifier	0.71
Linear classifier (DBP and AbC together)	0.9
Linear classifier (DBP and $\langle v \rangle_{31}$ together)	0.91
Complex classifier (DBP, AbC, $\langle v \rangle_{31}$)	0.933

5. Conclusions

In the study, the measurement of perfusion is complemented by a new parameter based on the calculation of cumulative sums from the power spectrum of the photodetector signals. The described diagnostic approach allows for revising the known protocols for characterising blood microcirculation parameters based on LDF measurements. In the context of the proposed signal processing technique, a new feature space can be added to the set of known diagnostic parameters expanding the range of applications for the LDF. The translation of the study results suggests that routine diagnostics procedures do not require significant modifications of the standard configuration of LDF channel. Also, the method does not involve any additional measurement channels (fluorescence, diffuse reflectance spectroscopy, and others) that still demonstrate relatively high accuracy of classification for the diagnostics of impaired blood microcirculation, even being tested in a limited size of the cohort of patients with T2DM.

Author Contributions: I.K.: experimental studies, data processing, signal processing, drafting the manuscript. E.Z.: co-supervising, the concept and implementation of the measuring setup, drafting the manuscript, data analysis, funding acquisition. G.M.: the research protocol, experimental studies in hospital. K.P.: finalizing the article; A.D.: supervising, study conceptualisation, discussion, funding acquisition. All authors edited manuscript. All authors have read and agreed to the published version of the manuscript.

Funding: The reported study was funded by the Russian Foundation for Basic Research (RFBR), project numbers 19-32-90253. E. Zherebtsov acknowledges the funding from the Academy of Finland (grant number 318281, data analysis) and Russian Science Foundation (grant number 20-75-00123, development of the experimental setup).

Institutional Review Board Statement: The study was conducted according to the guidelines of the Declaration of Helsinki, and approved by the Ethics Committee of Orel State University (Minutes No. 15 dated 21 February 2019).

Informed Consent Statement: Informed consent was obtained from all subjects involved in the study.

Conflicts of Interest: The authors declare no conflict of interest.

References

1. Braverman, I.M. The Cutaneous Microcirculation: Ultrastructure and Microanatomical Organization. *Microcirculation* **1997**, *4*, 329–340. [CrossRef]
2. Stefanovska, A.; Bracic, M.; Kvernmo, H.D. Wavelet analysis of oscillations in the peripheral blood circulation measured by laser Doppler technique. *IEEE Trans. Biomed. Eng.* **1999**, *46*, 1230. [CrossRef]
3. Kvandal, P.; Landsverk, S.; Bernjak, A.; Stefanovska, A.; Kvernmo, H.; Kirkebøen, K. Low-frequency oscillations of the laser Doppler perfusion signal in human skin. *Microvasc. Res.* **2006**, *72*, 120. [CrossRef]
4. Rowley, W.R.; Bezold, C.; Arikan, Y.; Byrne, E.; Krohe, S. Diabetes 2030: Insights from Yesterday, Today, and Future Trends. *Popul. Health Manag.* **2017**, *20*, 6–12. [CrossRef]
5. Ogurtsova, K.; da Rocha Fernandes, J.D.; Huang, Y.; Linnenkamp, U.; Guariguata, L.; Cho, N.H.; Cavan, D.; Shaw, J.E.; Makaroff, L.E. IDF Diabetes Atlas: Global estimates for the prevalence of diabetes for 2015 and 2040. *Diabetes Res. Clin. Pract.* **2017**, *128*, 40–50. [CrossRef]
6. Dremin, V.V.; Zherebtsov, E.A.; Sidorov, V.V.; Krupatkin, A.I.; Makovik, I.N.; Zherebtsova, A.I.; Zharkikh, E.V.; Potapova, E.V.; Dunaev, A.V.; Doronin, A.A.; et al. Multimodal optical measurement for study of lower limb tissue viability in patients with diabetes mellitus. *J. Biomed. Opt.* **2017**, *22*, 1–10. [CrossRef]
7. Potapova, E.V.; Dremin, V.V.; Zherebtsov, E.A.; Makovik, I.N.; Zherebtsova, A.I.; Dunaev, A.V.; Podmasteryev, K.V.; Sidorov, V.V.; Krupatkin, A.I.; Khakhicheva, L.S.; et al. Evaluation of microcirculatory disturbances in patients with rheumatic diseases by the method of diffuse reflectance spectroscopy. *Hum. Physiol.* **2017**, *43*. [CrossRef]
8. Jonasson, H.; Fredriksson, I.; Bergstrand, S.; Östgren, C.J.; Larsson, M.; Strömberg, T. In vivo characterization of light scattering properties of human skin in the 475- to 850-nm wavelength range in a Swedish cohort. *J. Biomed. Opt.* **2018**, *23*. [CrossRef] [PubMed]
9. Fredriksson, I.; Larsson, M.; Strömberg, T. Machine learning for direct oxygen saturation and hemoglobin concentration assessment using diffuse reflectance spectroscopy. *J. Biomed. Opt.* **2020**, *25*, 1–16. [CrossRef] [PubMed]
10. Hultman, M.; Larsson, M.; Strömberg, T.; Fredriksson, I. Real-time video-rate perfusion imaging using multi-exposure laser speckle contrast imaging and machine learning. *J. Biomed. Opt.* **2020**, *25*, 1–15. [CrossRef] [PubMed]
11. Volkov, M.V.; Margaryants, N.B.; Potemkin, A.V.; Volynsky, M.A.; Gurov, I.P.; Mamontov, O.V.; Kamshilin, A.A. Video capillaroscopy clarifies mechanism of the photoplethysmographic waveform appearance. *Sci. Rep.* **2017**, *7*, 13298. [CrossRef] [PubMed]
12. Dremin, V.; Kozlov, I.; Volkov, M.; Margaryants, N.; Potemkin, A.; Zherebtsov, E.; Dunaev, A.; Gurov, I. Dynamic evaluation of blood flow microcirculation by combined use of the laser Doppler flowmetry and high-speed videocapillaroscopy methods. *J. Biophotonics* **2019**, *12*, e201800317. [CrossRef]
13. de Carlo, T.E.; Romano, A.; Waheed, N.K.; Duker, J.S. A review of optical coherence tomography angiography (OCTA). *Int. J. Retin. Vitr.* **2015**, *1*, 5. [CrossRef]
14. Shu, X.; Beckmann, L.J.; Zhang, H.F. Visible-light optical coherence tomography: A review. *J. Biomed. Opt.* **2017**, *22*, 1–14. [CrossRef] [PubMed]
15. Forrester, A.T. Photoelectric Mixing As a Spectroscopic Tool. *J. Opt. Soc. Am.* **1961**, *51*, 253–259. [CrossRef]
16. Cummins, H.Z.; Swinney, H.L. III light beating spectroscopy. In *Progress in Optics*; Wolf, E., Ed.; Elsevier: Amsterdam, The Netherlands, 1970; Volume 8, pp. 133–200.
17. Humeau-Heurtier, A.; Mahe, G.; Durand, S.; Abraham, P. Skin perfusion evaluation between laser speckle contrast imaging and laser Doppler flowmetry. *Opt. Commun.* **2013**, *291*, 482–487. [CrossRef]
18. Wang, G.; Jia, S.; Liu, M.; Song, X.; Li, H.; Chang, X.; Zhang, W. Impact of local thermal stimulation on the correlation between oxygen saturation and speed-resolved blood perfusion. *Sci. Rep.* **2020**, *10*. [CrossRef]
19. Dzeletovic, B.; Stratimirovic, D.; Stojic, D.; Djukic, L. Linear and nonlinear analysis of dental pulp blood flow oscillations in ageing. *Int. Endod. J.* **2020**, *53*, 1033–1039. [CrossRef]
20. Sorelli, M.; Francia, P.; Bocchi, L.; De Bellis, A.; Anichini, R. Assessment of cutaneous microcirculation by laser Doppler flowmetry in type 1 diabetes. *Microvasc. Res.* **2019**, *124*, 91–96. [CrossRef] [PubMed]
21. Mizeva, I.; Makovik, I.; Dunaev, A.; Krupatkin, A.; Meglinski, I. Analysis of skin blood microflow oscillations in patients with rheumatic diseases. *J. Biomed. Opt.* **2017**, *22*, 1–3. [CrossRef]
22. Berge, S.T.; Safi, N.; Medhus, A.W.; Ånonsen, K.; Sundhagen, J.O.; Hisdal, J.; Kazmi, S.S.H. Gastroscopy assisted laser Doppler flowmetry and visible light spectroscopy in patients with chronic mesenteric ischemia. *Scand. J. Clin. Lab. Investig.* **2019**, *79*, 541–549. [CrossRef]
23. Zherebtsov, E.; Zajnulina, M.; Kandurova, K.; Potapova, E.; Dremin, V.; Mamoshin, A.; Sokolovski, S.; Dunaev, A.; Rafailov, E.U. Machine Learning Aided Photonic Diagnostic System for Minimally Invasive Optically Guided Surgery in the Hepatoduodenal Area. *Diagnostics* **2020**, *10*. [CrossRef] [PubMed]
24. Liao, F.; Jan, Y.K. Nonlinear dynamics of skin blood flow response to mechanical and thermal stresses in the plantar foot of diabetics with peripheral neuropathy. *Clin. Hemorheol. Microcirc.* **2017**, *66*, 197–210. [CrossRef] [PubMed]

25. Sorelli, M.; Perrella, A.; Francia, P.; De Bellis, A.; Anichini, R.; Bocchi, L. Multi-gaussian Decomposition of the Microvascular Pulse Detects Alterations in Type 1 Diabetes BT. In Proceedings of the World Congress on Medical Physics and Biomedical Engineering 2018, Prague, Czech Republic, 3–8 June 2018; Lhotska, L., Sukupova, L., Lacković, I., Ibbott, G.S., Eds.; Springer: Singapore, 2019; pp. 173–176.
26. Vandersee, S.; Erdmenger, U.; Patzelt, A.; Beyer, M.; Meinke, M.; Darvin, M.; Koscielny, J.; Lademann, J. Significance of the follicular pathway for dermal substance penetration quantified by laser Doppler flowmetry. *J. Biophotonics* **2016**, *9*, 276–281. [CrossRef] [PubMed]
27. Yuan, X.; Wu, Q.; Shang, F.; Li, B.; Liu, M.; Wang, B.; Sheng, Y.; Zhang, H.; Xiu, R. A comparison of the cutaneous microvascular properties of the Spontaneously Hypertensive and the Wistar-Kyoto rats by Spectral analysis of Laser Doppler. *Clin. Exp. Hypertens.* **2019**, *41*, 342–352. [CrossRef] [PubMed]
28. Fredriksson, I.; Larsson, M.; Strömberg, T. Model-based quantitative laser Doppler flowmetry in skin. *J. Biomed. Opt.* **2010**, *15*, 57002–57012. [CrossRef]
29. Jonasson, H.; Fredriksson, I.; Larsson, M.; Strömberg, T. Validation of speed-resolved laser Doppler perfusion in a multimodal optical system using a blood-flow phantom. *J. Biomed. Opt.* **2019**, *24*, 1–8. [CrossRef]
30. Wojtkiewicz, S.; Liebert, A.; Rix, H.; Maniewski, R. Evaluation of algorithms for microperfusion assessment by fast simulations of laser Doppler power spectral density. *Phys. Med. Biol.* **2011**, *56*, 7709. [CrossRef]
31. Liebert, A.; Zolek, N.; Wojtkiewicz, S.; Maniewski, R. Estimation of Speed Distribution of Particles Moving in an Optically Turbid Medium Using Decomposition of a Laser-Doppler Spectrum. In Proceedings of the 2007 29th Annual International Conference of the IEEE Engineering in Medicine and Biology Society, Lyon, France, 23–26 August 2007; pp. 4080–4082.
32. Bonner, R.; Nossal, R. Model for laser Doppler measurements of blood flow in tissue. *Appl. Opt.* **1981**, *20*, 2097–2107. [CrossRef]
33. Nilsson, G.E.; Tenland, T.; Oberg, P.A. Evaluation of a Laser Doppler Flowmeter for Measurement of Tissue Blood Flow. *IEEE Trans. Biomed. Eng.* **1980**, *BME-27*, 597–604. [CrossRef]
34. Zherebtsov, E.; Kandurova, K.; Seryogina, E.; Kozlov, I.; Dremin, V.; Zherebtsova, A.; Dunaev, A.; Meglinski, I. The influence of local pressure on evaluation parameters of skin blood perfusion and fluorescence. In *Progress in Biomedical Optics and Imaging—Proceedings of SPIE*; SPIE: Bellingham, WA, USA, 2017; Volume 10336. [CrossRef]
35. Kozlov, I.O.; Zherebtsov, E.A.; Dremin, V.V.; Zherebtsova, A.I.; Zharkikh, E.V.; Dunaev, A.V.; Rafailov, E.U. Laser doppler spectrum decomposition applied in diagnostics of microcirculatory disturbances. In *Biophotonics: Photonic Solutions for Better Health Care VI*; Popp, J., Tuchin, V.V., Pavone, F.S., Eds.; International Society for Optics and Photonics (SPIE): Bellingham, WA, USA, 2018; Volume 10685, pp. 735–738. [CrossRef]
36. Kozlov, I.; Zherebtsov, E.; Zherebtsova, A.; Dremin, V.; Dunaev, A. Investigation of Doppler spectra of laser radiation scattered inside hand skin during occlusion test. *J. Phys. Conf. Ser.* **2017**, *929*, 012063. [CrossRef]
37. Fredriksson, I.; Hultman, M.; Strömberg, T.; Larsson, M. Machine learning in multiexposure laser speckle contrast imaging can replace conventional laser Doppler flowmetry. *J. Biomed. Opt.* **2019**, *24*, 1–11. [CrossRef] [PubMed]
38. Wojtkiewicz, S.; Wojcik-Sosnowska, E.; Jasik, M.; Maniewski, R.; Karnafel, W.; Liebert, A. Assessment of speed distribution of red blood cells in the microvascular network in healthy volunteers and type 1 diabetes using laser Doppler spectra decomposition. *Physiol. Meas.* **2014**, *35*, 283–295. [CrossRef]
39. Qu, X.; Ikawa, M.; Shimauchi, H. Improvement of the detection of human pulpal blood flow using a laser Doppler flowmeter modified for low flow velocity. *Arch. Oral Biol.* **2014**, *59*, 199–206. [CrossRef]
40. Chen, Y.Y.; Lin, Y.H.; Jan, I.C.; Liu, R.S.; Chou, N.K.; Jan, G.J. Adaptive processing bandwidth adjustment for laser Doppler flowmetry. *Med. Biol. Eng. Comput.* **2004**, *42*, 277–281. [CrossRef]
41. Dremin, V.V.; Zherebtsov, E.A.; Makovik, I.N.; Kozlov, I.O.; Sidorov, V.V.; Krupatkin, A.I.; Dunaev, A.V.; Rafailov, I.E.; Litvinova, K.S.; Sokolovski, S.G.; et al. Laser Doppler flowmetry in blood and lymph monitoring, technical aspects and analysis. *Proc. SPIE* **2017**, *10063*, 1006303–1006308.
42. Malanin, K.; Havu, V.K.; Kolari, P.J. Dynamics of Cutaneous Laser Doppler Flux with Concentration of Moving Blood Cells and Blood Cell Velocity in Legs with Venous Ulcers and in Healthy Legs. *Angiology* **2004**, *55*, 37–42. [CrossRef] [PubMed]
43. Karlsson, D.M.G.; Larsson, M.; Stroemberg, T.; Wardell, K. Influence of tissue movements on laser Doppler perfusion imaging. In *Optical Diagnostics and Sensing of Biological Fluids and Glucose and Cholesterol Monitoring II*; Priezzhev, A.V., Cote, G.L., Eds.; International Society for Optics and Photonics (SPIE): Bellingham, WA, USA, 2002; Volume 4624, pp. 106–114. [CrossRef]
44. Bodo, M.; Mahon, R.; Razumovsky, A.; Kouperberg, E.; Crimmins, M.; Armonda, R.; Baruch, M. Comparison of cerebrovascular reactivity tests: A pilot human study. *J. Electr. Bioimpedance* **2019**, *8*, 25–33. [CrossRef]
45. Lenoir, C.; Plaghki, L.; Mouraux, A.; van den Broeke, E.N. Quickly responding C-fibre nociceptors contribute to heat hypersensitivity in the area of secondary hyperalgesia. *J. Physiol.* **2018**, *596*, 4443–4455. [CrossRef]
46. Filina, M.A.; Potapova, E.V.; Makovik, I.N.; Zharkih, E.V.; Dremin, V.V.; Zherebtsov, E.A.; Dunaev, A.V.; Sidorov, V.V.; Krupatkin, A.I.; Alimicheva, E.A.; et al. Functional Changes in Blood Microcirculation in the Skin of the Foot during Heating Tests in Patients with Diabetes Mellitus. *Hum. Physiol.* **2017**, *43*, 693–699. [CrossRef]
47. Zherebtsova, A.I.; Zherebtsov, E.A.; Dunaev, A.V.; Podmasteryev, K.V.; Pilipenko, O.V.; Krupatkin, A.I.; Khakhicheva, L.S.; Muradyan, V.F. Study of the functional state of peripheral vessels in fingers of rheumatological patients by means of laser Doppler flowmetry and cutaneous thermometry measurements. *Proc. SPIE* **2016**, *9917*, 99170M–99170M-7.

48. Nieuwenhoff, M.; Wu, Y.; Huygen, F.; Schouten, A.; van der Helm, F.; Niehof, S. Reproducibility of axon reflex-related vasodilation assessed by dynamic thermal imaging in healthy subjects. *Microvasc. Res.* **2016**, *106*, 1–7. [CrossRef]
49. Liebert, A.; Zołek, N.; Maniewski, R. Decomposition of a laser-Doppler spectrum for estimation of speed distribution of particles moving in an optically turbid medium: Monte Carlo validation study. *Phys. Med. Biol.* **2006**, *51*. [CrossRef] [PubMed]
50. Maldonado, G.; Guerrero, R.; Paredes, C.; Ríos, C. Nailfold capillaroscopy in diabetes mellitus. *Microvasc. Res.* **2017**, *112*. [CrossRef] [PubMed]
51. Shih, T.C.; Zhang, G.; Wu, C.C.; Hsiao, H.D.; Wu, T.H.; Lin, K.P.; Huang, T.C. Hemodynamic analysis of capillary in finger nail-fold using computational fluid dynamics and image estimation. *Microvasc. Res.* **2011**, *81*, 68–72. [CrossRef] [PubMed]
52. Fredriksson, I.; Larsson, M. Vessel packaging effect in laser speckle contrast imaging and laser Doppler imaging. *J. Biomed. Opt.* **2017**, *22*, 1–7. [CrossRef]
53. Chang, C.H.; Tsai, R.K.; Wu, W.C.; Kuo, S.L.; Yu, H.S. Use of dynamic capillaroscopy for studying cutaneous microcirculation in patients with diabetes mellitus. *Microvasc. Res.* **1997**, *53*. [CrossRef]
54. Wang, G.; Jia, S.; Li, H.; Song, X.; Zhang, W. Exploring the relationship between the speed-resolved perfusion of blood flux and HRV following different thermal stimulations using MSE and MFE analyses. *PLoS ONE* **2019**, e0217973. [CrossRef]

diagnostics

MDPI

Article

Optical Diagnostics of the Maxillary Sinuses by Digital Diaphanoscopy Technology

Ekaterina O. Bryanskaya [1,*], Irina N. Novikova [1], Viktor V. Dremin [1,2], Roman Yu. Gneushev [1], Olga A. Bibikova [3], Andrey V. Dunaev [1] and Viacheslav G. Artyushenko [3]

[1] R & D Center of Biomedical Photonics, Orel State University, Orel 302026, Russia; irina.makovik@gmail.com (I.N.N.); dremin_viktor@mail.ru (V.V.D.); tef312@yandex.ru (R.Y.G.); dunaev@bmecenter.ru (A.V.D.)
[2] College of Engineering and Physical Sciences, Aston University, Birmingham B4 7ET, UK
[3] Art Photonics GmbH, 12489 Berlin, Germany; olga.a.bibikova@gmail.com (O.A.B.); sa@artphotonics.com (V.G.A.)
* Correspondence: bryanskayae@mail.ru; Tel.: +7-980-366-29-12

Abstract: The work is devoted to the development of a scientific and technical basis for instrument implementation of a digital diaphanoscopy technology for the diagnosis of maxillary sinus inflammatory diseases taking into account the anatomical features of patients (differences in skin structure, skull bone thickness, and sinus size), the optical properties of exercised tissues, and the age and gender characteristics of patients. The technology is based on visualization and analysis of scattering patterns of low-intensity radiation as it passes through the maxillary sinuses. The article presents the experimental data obtained using the digital diaphanoscopy method and the results of numerical simulation of the optical radiation passage through the study area. The experimental setup has been modernized through the installation of a a device for controlling the LED applicator brightness. The approach proposed may have considerable promise for creating diagnostic criteria for various pathological changes and can be used to assess the differences in the optical and anatomical features of males and females.

Keywords: optical diagnostics; digital diaphanoscopy; magnetic resonance imaging; paranasal sinuses; inflammatory diseases; Monte Carlo simulation

Citation: Bryanskaya, E.O.; Novikova, I.N.; Dremin, V.V.; Gneushev, R.Y.; Bibikova, O.A.; Dunaev, A.V.; Artyushenko, V.G. Optical Diagnostics of the Maxillary Sinuses by Digital Diaphanoscopy Technology. *Diagnostics* **2021**, *11*, 77. https://doi.org/10.3390/diagnostics11010077

Received: 19 November 2020
Accepted: 31 December 2020
Published: 6 January 2021

1. Introduction

Sinusitis is a common disease with worldwide prevalence and one of the leading causes of antibiotic prescription [1]. In 2018, 28.9 million people in the United States reported a sinusitis diagnosis in the previous 12-month period, which accounted for 11.6% of the adult population [2]. In Europe, sinusitis affects 10.9% of the population [3]. Delay in diagnosis and treatment of sinusitis may cause serious effects such as immune sensitivities to medication, development of different complications, including intracranial complications (50% of deaths). Therefore, an accurate, painless, and timely diagnosis of maxillary sinus pathology is one of the key problems of modern otolaryngology. Diagnostic imaging techniques, such as radiography, computed tomography, magnetic resonance imaging, ultrasound diagnostics (including assessment of stiffness and echogenicity), and rhinoscopy, are important tools to detect this kind of disorder, but they are not recommended for pregnant women and children due to the use of carcinogenic roentgen radiation during the study, painfulness of the diagnostic procedures, and a high level of false-negative results.

Radiography is based on the high penetrating power of radiation and its absorption ability. It allows assessing the general condition of the paranasal sinuses and makes it possible to detect the presence of liquid content (along with formed cysts or polyps) in them, as well as the changes in the mucous membrane. If there is a pathological change in sinus pneumatization, then the resulting image will show significant darkening along the

upper horizontal level, asymmetry of the inflamed sinuses, narrowing of the nasal passages, and mucosal thickening [4]. Despite the advantages of this technique, its application in clinical practice is limited to assessments that help to identify the degree of development of a pathological process which already has pronounced signs to determine further treatment tactics and the need for surgical interventions. It should also be noted that a high dose of radiation exposed to pregnant women raises the risk of hypertension, may slow down the growth of the fetus, and cause the worsening of the health indicators of newborns.

The major contribution of computed tomography (CT) is in providing additional useful information. The CT method, similar to other imaging techniques, uses X-ray radiation and its distribution in tissues depending on their density. CT provides the differentiation of soft tissues and can distinguish between density differences of no more than 0.1%. However, it is also associated with significant radiation exposure [5].

Magnetic resonance imaging (MRI), endoscopy (rhinoscopy), or ultrasound are used as alternative methods. The MRI method consists in registering the excitation of hydrogen atomic nuclei by a certain combination of electromagnetic waves in a constant magnetic field of high intensity [5]. MRI can be useful in assessing lesions in nasal bones, inflammatory processes in the paranasal sinuses, formed cysts or polyps, chronic diseases, and changes in bone structure resulting from injury. However, this method is characterized by a high level of false positive results, poor visualization of bone tissue, and is contraindicated in the presence of implants, prostheses, and obesity. The disadvantages of this method are the cost and high microwave load on the patient.

Rhinoscopy is performed by placing a flexible fiber-optic tube into the nasal passage to assess the color of the mucous membrane, its humidity, the shape of the nasal septum, the caliber of vessels, the condition of the nasal shell, and the size and content of the nasal passages. Although rhinoscopy yields important information and adequate sample collection, it also has some disadvantages which include its high cost and discomfort to the patient.

Ultrasound makes it possible to diagnose inflammatory processes in the sinuses, cysts, polyps, and traumatic damage to the walls of the paranasal sinuses, as well as to detect foreign bodies. Normally, the paranasal sinuses contain air, which serves as an obstacle to the propagation of ultrasonic waves. In the absence of pathological changes, the echo signal from the sinus is not detected due to its complete reflection from the air contained in it. If the walls of the sinuses are thickened, for example, due to edema of the mucosa, or they contain pathological contents, then there occur conditions for the propagation of ultrasound waves. When passing through the sinus, ultrasound waves are reflected from its posterior parts and are fixed by an ultrasound device. The results of ultrasound scanning do not always correspond to reality, which can be attributed to deficiencies in equipment design or incorrect interpretation of the results.

Non-invasive optical technologies are increasingly used in various fields of medicine to diagnose pathological conditions. The digital diaphanoscopy method has the potential to separate normal and pathological conditions (inflammation, cystic, and tumor tissues) of the maxillary sinuses. It is based on the visualization of scattering patterns of low-intensity radiation as it passes through the maxillary sinuses [6–8]. Although the method of diaphanoscopy or transillumination has a long history of usage [9,10], especially in ophthalmology [11] and urology [12], it is of limited use in otolaryngology. First examinations of tissue parameters in the near infrared were performed by Beuthan in 1982. Relying on these tests, infrared transillumination seems to be a promising tool for the rapid diagnosis of sinusitis, but white light spectrum radiation is a limiting factor influencing the application of this approach in otolaryngology [13,14]. White light does not provide a complete diagnostic picture because it is absorbed and dispersed by tissues to a great extent; no informative features and algorithms capable of separating normal and pathological conditions exist. At present, there are no clinically justified classifying features, developed classification models, and diagnostic criteria that can differentiate pathological changes in the maxillary sinuses (inflammation, cysts, and tumor tissues) by digital diaphanoscopy.

The purpose of this study was to develop a scientific and technical basis for instrument implementation of the technology proposed for diagnosing maxillary sinus pathology, taking into account the anatomical features of the study area (skin structure, bone thickness of the facial part of the skull, sinus size, and asymmetry), its optical properties, and age and gender characteristics.

2. Materials and Methods

2.1. Experimental Setup

For the realization of this approach, the experimental setup was designed and assembled (Figure 1a). Low-intensity radiation of the visible (650 nm) and NIR (850 nm) ranges was used for translucence of the paranasal sinuses. The CMOS-camera was applied to visualize the light scattering pattern [15]. To minimize the external illumination influence, a protective screen was designed which facilitated research under various external conditions. To suppress movement artifacts, the volunteers were asked to place their head on a chin rest.

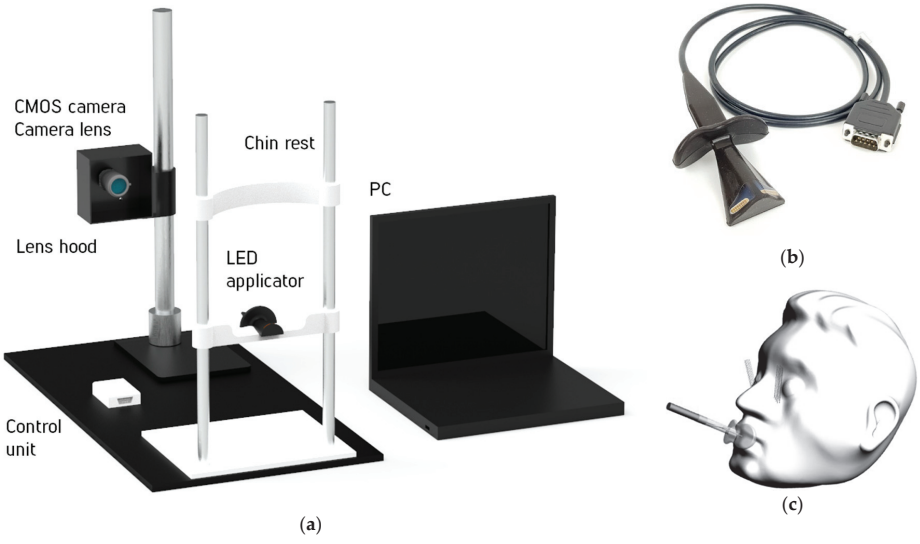

Figure 1. General view of the experimental setup (**a**); the LED applicator (the working part) (**b**); and the position of the applicator during measurement with the propagation of probing rays (3D model) (**c**).

The LED applicator takes into account the anatomical features of the study area, namely, the features of the oral cavity and maxillary sinuses (Figure 1b). During the diagnostic procedure, the applicator was placed in the oral cavity, and then the measurements were performed (Figure 1c). Before each use, the surface of the applicator was cleaned with wipes impregnated with a disinfecting solution. The solution composition included purified water, isopropanol, ethanol, didetsildimetilammonium chloride, and dodecyl dipropylene triamine.

The micro-LEDs OSRAM Opto Semiconductors GmbH (Regensburg, Germany) with wavelengths of 650 (C4L-H12T5) and 850 nm (F3453) and 8 pieces on the right and left sides for each wavelength were used as radiation sources for the applicator. The CMOS-camera UI-3240CP-NIR-GL Rev.2 IDS GmbH (Obersulm, Germany) and the lens Pentax C1614-M (Tokyo, Japan) were applied to register diagnostic information in the prototype device. The camera provides high-speed image acquisition, high quality, and maximum quantum efficiency (light sensitivity) in the selected spectral range. The control unit provides the

LEDs sequential switching on and off at wavelengths of 650 and 850 nm, as well as their performance in the setting mode (LEDs flashing at a wavelength of 650 nm).

The specially designed software assists us in analyzing the obtained scattering pattern. It allows for trial control (selection of a radiation source and a camera operation mode), gathering of personal patient data, and recording of diaphanoscopic images and their quantitative (visualization) and qualitative processing (pseudo-color image segmentation). The software also provides the function of uploading a diaphanoscopic examination report, which contains information about the patient, diaphanoscopic images, diagnostic assessments, and quantitative values (the percentage of light passed through the sinus).

2.2. Study Design

The study groups were formed taking into account the differences in age, gender parameters, and anatomical features of the study area, as well as the existing pathological changes and inflammatory processes of the maxillary sinuses. Preliminary experimental studies were conducted in 20 conditionally healthy volunteers and 15 patients with suspected maxillary sinus inflammation at the medical diagnostic center "MediScan" (Orel, Russia).

The study was approved by the Ethics committee of the Orel State University (record of meeting No. 15 of 21 February 2019) and carried out in accordance with the 2013 Declaration of Helsinki by the World Medical Association. After receiving the description of the protocol, the volunteers signed an informed consent indicating their voluntary willingness to participate in the study.

The experiments were conducted under established protocols. The subjects were in a sitting position. After the pre-disinfected LED-applicator was inserted into the oral cavity of the subject, the subject head was placed in a precision positioning unit and, then, together with the CMOS-camera, it was covered with a protective screen. To account for the effect of the camera exposure time on the light scattering patterns, images were recorded at 40 different camera exposure times in the range from 0 to 40 ms (increment of 1 ms). In the patient study, the measurement results were additionally compared with the T2 weighted images by MRI studies, which were performed using the 1T MRI Scanner of the Magnetom series, Siemens (Munich, Germany).

3. Results

3.1. Results of Preliminary Experimental Studies

The data obtained in trials with healthy volunteers showed that changing the camera exposure time does not significantly affect the diagnostic result. Therefore, further analysis of the experimental data was carried out at the camera exposure time of 20.7 ms.

Figures 2 and 3 present the registered and processed images for two conditionally healthy volunteers (a man and a woman of the same age group) with the same camera exposure time of 20.7 ms for probing radiation wavelengths of 650 nm (a) and 850 nm (b).

Preliminary experimental studies using the relevant method MRI have confirmed the sensitivity of the digital diaphanoscopy method in detecting pathological changes in the maxillary sinuses [6]. Figure 4 gives examples of the T2 weighted MRI images (Figure 4a) and the images registered and processed by diaphanoscopy (Figure 4b).

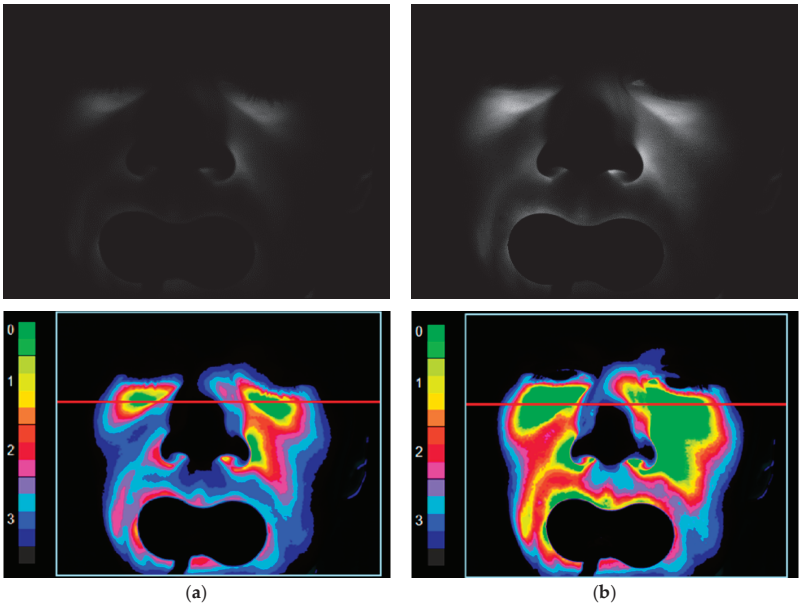

(**a**) (**b**)

Figure 2. Registered (**top**) and processed (**bottom**) images for a conditionally healthy volunteer 1 (male) at a camera exposure time of 20.7 ms for probing radiation wavelengths of: 650 nm (**a**); and 850 nm (**b**). The red line is the selection of the area for analyzing the transmitted light.

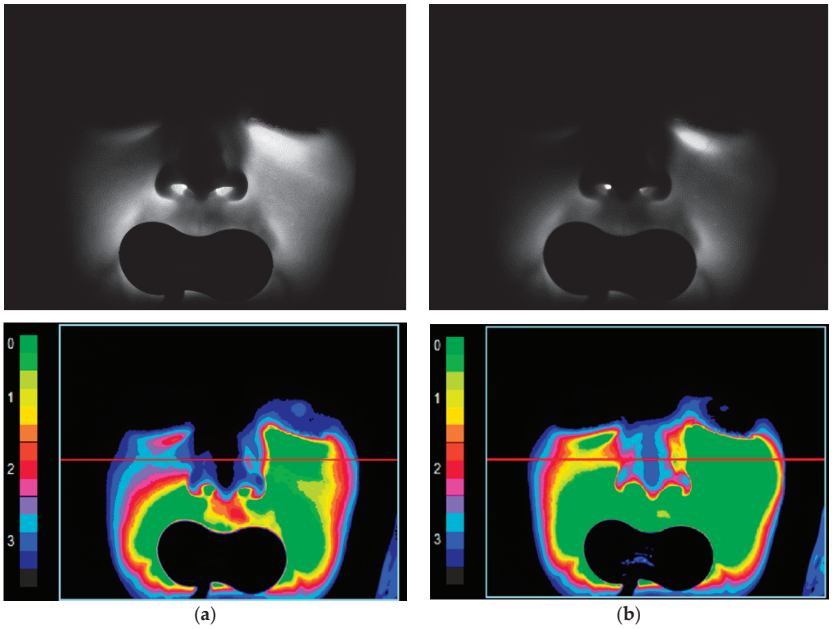

(**a**) (**b**)

Figure 3. Registered (**top**) and processed (**bottom**) images for a conditionally healthy volunteer 2 (female) at a camera exposure time of 20.7 ms for probing radiation wavelengths of: 650 nm (**a**); and 850 nm (**b**).

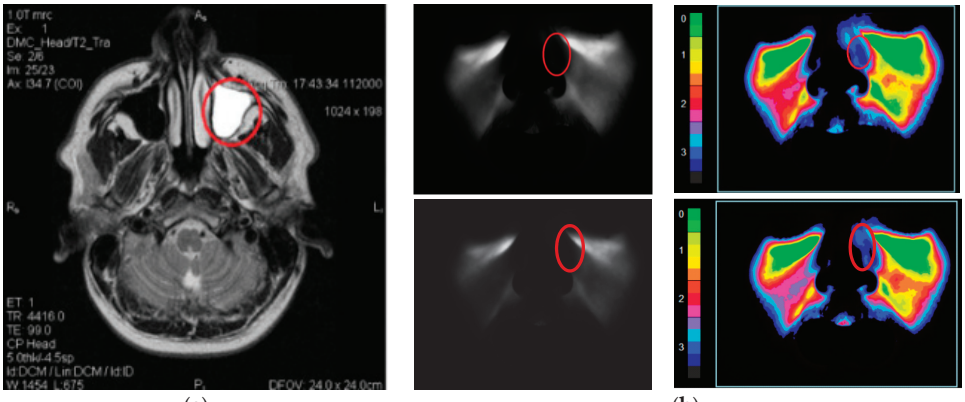

(**a**) (**b**)

Figure 4. The T2 weighted MRI image (**a**); and the images registered and processed by diaphanoscopy (**b**) for a patient (male) at radiation wavelengths of 650 nm (**top**) and 850 nm (**bottom**).

Analysis of the registered and processed images obtained by digital diaphanoscopy revealed that the cyst area is characterized by the lowest intensity compared to other structures, which can be explained by the strong absorbing properties of the cystic fluid in the near-infrared range [6]. The results of digital diaphanoscopy are determined by the optical properties of the study area [16–23] and their changes in various anatomical and gender features [24,25]. In our study, we applied Monte Carlo simulation to take into account the effect of the anatomical and gender characteristics of patients on the scattering pattern of light, to justify the medical and technical requirements for the instrument, and to adjust the parameters of the LED applicator.

3.2. Monte Carlo Simulation

Since the object of research has a rather complex organization, a simplified model of the maxillary sinus was developed to establish the regularity of the weakening of the probing signal from the anatomical and gender features of the studied area (differences in the skin structure, the thickness of the skull bone tissue, and the size of the sinuses). The Monte Carlo methodology was used for the construction of the 3D model. This method is one of the most effective simulation tools when dealing with biological tissues [26,27]. Figure 5 shows a scheme of the developed model.

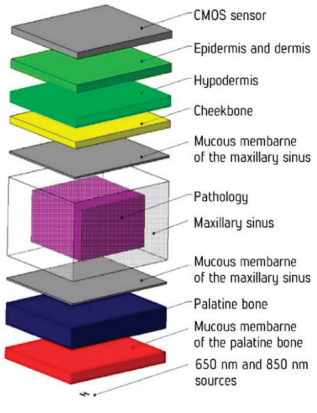

Figure 5. Full 3D view of the developed model.

In the model, the environment is represented by 8 main layers, as well as by an additional layer in the form of a pathological change (cystic fluid or tumor). The optical characteristics of the biological tissues used in the simulation are presented in Table 1.

Table 1. The optical characteristics of biological tissues.

Biological Tissue Layer	Wavelength λ, nm	Absorption Coefficient μ_a, mm^{-1}	Scattering Coefficient μ_s, mm^{-1}
Mucous membrane (sinus/palatine bone) [18]	650	0.05	0.8
	850	0.075	1.2
Zygomatic/Palatine bone [19,20]	650	0.011	1.873
	850	0.007	2.113
Cystic fluid [16,17]	650	0.022	1.34
	850	0.027	0.95
Tumor [21]	650	0.0391	2.17
	850	0.0522	2.67
Hypodermis [22]	650	0.18	2
	850	0.1	2.7
Epidermis and dermis [23]	650	0.17	3
	850	0.2	3.7

The thickness and size of the layers and their absorption and scattering coefficients were set for both females and males. Since the sizes and thicknesses of the layers depend on gender and age [18,19], the layer thicknesses were averaged within one gender to simplify the developed model. The thicknesses of the simulated layers are given in Table 2.

Table 2. The thickness of the simulated layers, mm.

Layer	Male	Female
Mucous membrane of a palatine bone [25,28]	2	3
Palatine bone [24,25,29]	3.1	3.1
Mucous membrane of a sinus [17]	0.5	0.5
Sinus [29,30]	6.7	6.2
Zygomatic bone [31,32]	26	23
Hypodermis [33]	3	3
Epidermis and dermis [33]	1.5–3	1–2

Analysis of the optical properties of the research area indicates high absorbing properties of the hypodermis at the selected wavelengths of probing radiation. In addition, the results of the preliminary experimental studies demonstrate that the changes in the hypodermis thickness strongly affect the diagnostic result.

The Monte Carlo simulation involving a simplified model of the research area was performed for 650 and 850 nm radiation sources in the TracePro software environment (Lambda Research Corporation) [34–36]. The number of simulated photons was 10^6. The power of probing radiation in the simulation for the wavelengths of 650 and 850 nm was 8 mW.

Figures 6–8 show the simulation results of the probe radiation propagation (the photons path through the biological tissue and the irradiance map) for the maxillary sinus of female (a) and male (b) without pathology (Figure 6), with cystic fluid (Figure 7) and with tumor (Figure 8).

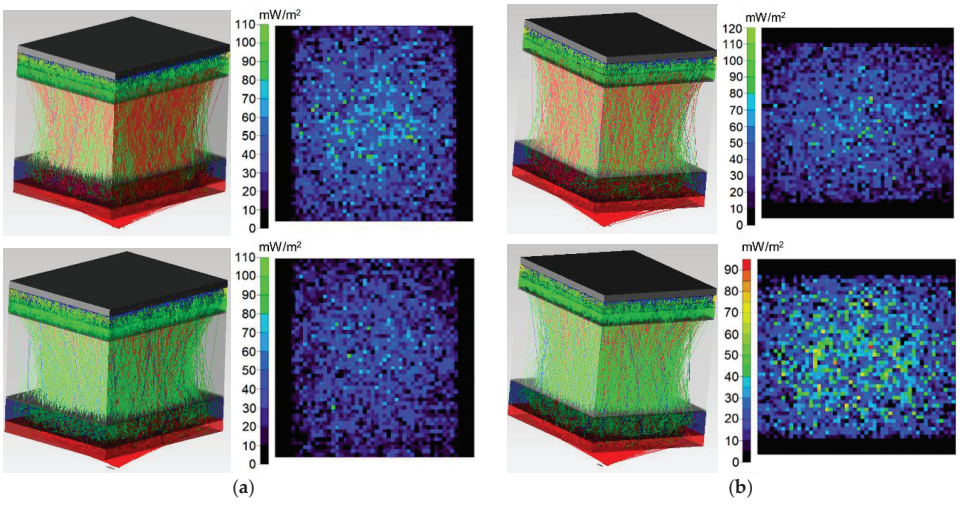

Figure 6. Simulation results for the probe radiation propagation through the maxillary sinus of female (**a**) and male (**b**) without pathology at a wavelength of 650 nm (**top**) and 850 nm (**bottom**).

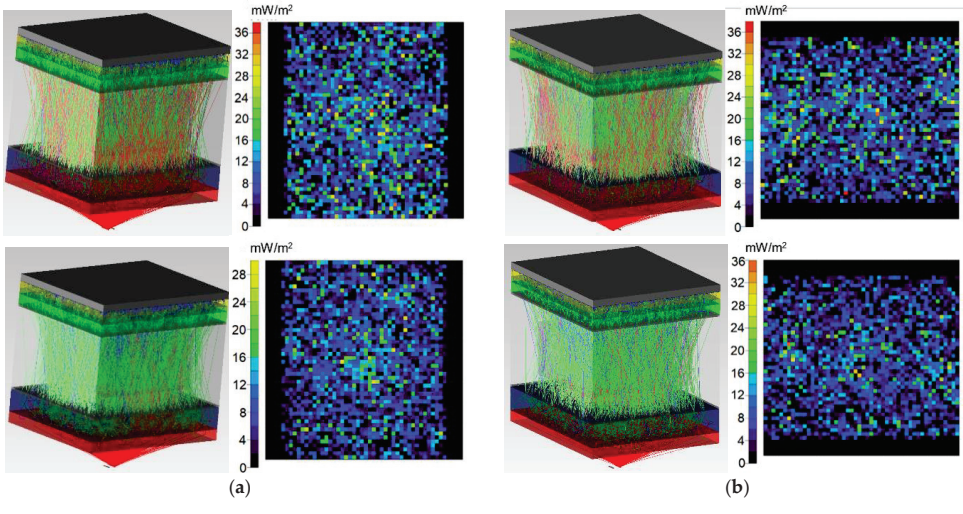

Figure 7. Simulation results for the probe radiation propagation through the maxillary sinus of female (**a**) and male (**b**) with cystic fluid at a wavelength of 650 nm (**top**) and 850 nm (**bottom**).

Figure 9 illustrates the difference in radiation power (intensity) reduction in males and females. This decrease has a more pronounced character when the pathology in the sinuses is observed in the NIR range (850 nm) and can be attributed to the optical features of pathological tissues, namely, the high absorption properties at selected wavelength [16,17].

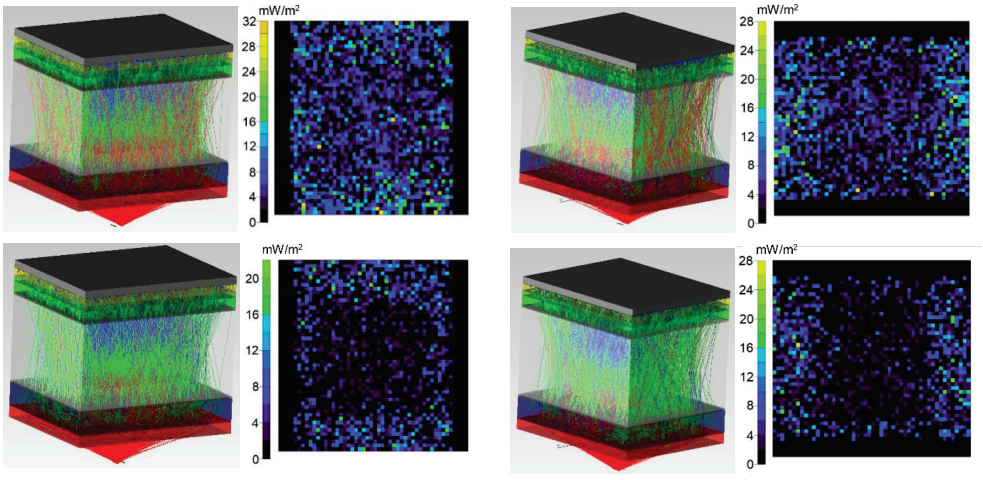

Figure 8. Simulation results for the probe radiation propagation through the maxillary sinus of female (**a**) and males (**b**) with tumor at a wavelength of 650 nm (**top**) and 850 nm (**bottom**).

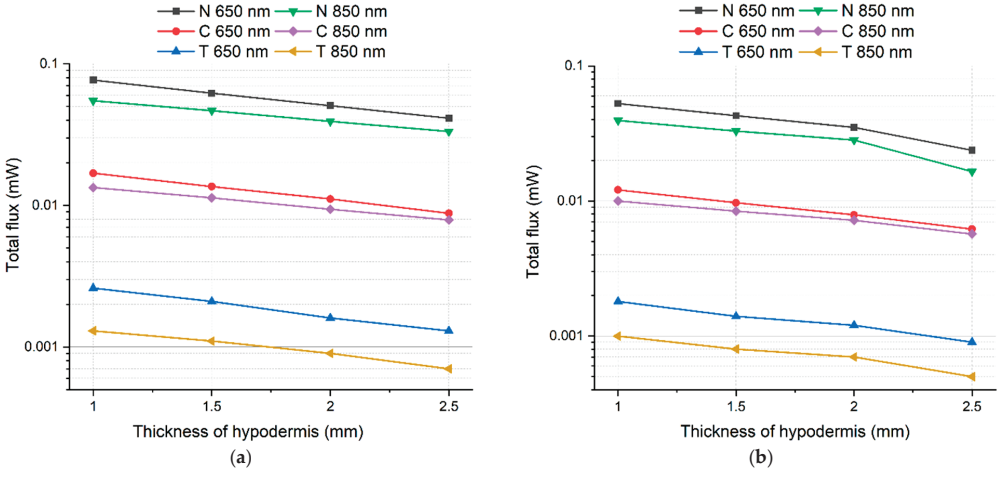

Figure 9. Dependence of the change in the total flux (power) of radiation coming to the camera detector on the change in the hypodermis thickness and on the presence of pathology in the sinuses of female (**a**) and males (**b**) for wavelengths of 650 and 850 nm. The following labels are used: "N" for healthy tissues, "C" for tissues with cyst, and "T" for tissues with tumor.

Besides, the results demonstrate a decrease in the intensity of radiation at the detector (radiant power) when it passed through the biological tissues at different values of the bone tissue and skin, the sinus size [22,23].

The revealed regularity confirmed the results of the experimental studies. It was also found that the adjustment of the parameters of the probing and measuring parts of the device for implementation of the proposed technology is necessary to ensure similar scattering light patterns for different patients and their further comparison.

3.3. Upgrade of the Experimental Setup

Based on the simulation results, the experimental setup was upgraded; the block scheme of the setup is shown in Figure 10.

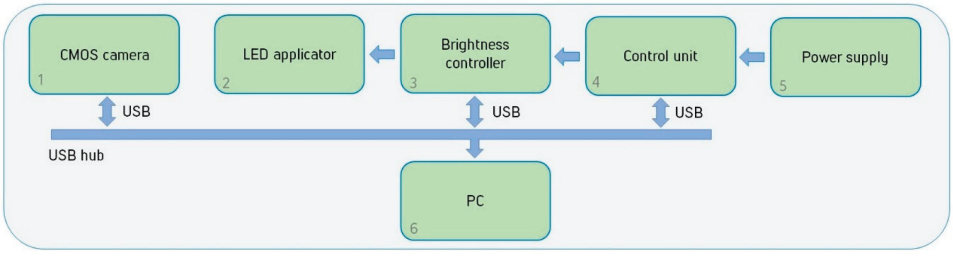

Figure 10. The block scheme of a modernized experimental setup.

A controller of the LED applicator brightness was designed and installed in the setup in addition to the unit controlling the output power of the probing applicator. It is positioned in the gap between the LED control unit of the applicator and the LED applicator itself. To control the operation of the controller of the LED applicator, an additional software has been developed, which allows one to change the voltage supplied to the LEDs, as well as to measure the current flow in real time and to calculate the power consumption. The software makes it possible to save many brightness profiles and switch them immediately before starting the measurements, thereby automatically selecting the desired range of radiation power of the applicator for specific volunteers and patients in accordance with their anatomical features.

The experimental studies, which were conducted using the modernized installation, allowed the detection of changes in the power consumption of the LEDs applicator. To identify the values of power consumption specific to each patient based on their gender and anatomical features, the study involved conditionally healthy volunteers; the power consumption of the LEDs applicator varied from 0 to 750 mW in increments of 50 mW. The camera exposure time remained unchanged. It was established that, in healthy male volunteers, the maximum power consumption of the LEDs applicator was insufficient to obtain an adequate scattering pattern of light passing through the sinuses, which is associated with their anatomical features (bone thickness, skin, and size of the sinuses). In female volunteers, the maxillary sinuses were visualized in the range of LEDs power consumption equal to 300–500 mW.

The ranges of changes in the radiation flux for the two radiation sources were also revealed. Thus, it was found that at 850 nm the radiation flux varies in the range from 0 to 200 mW, whereas for the 650 nm radiation source this parameter changes in the range from 0 to 18 mW.

In the future, the elements of the controller of the LED applicator brightness will be adjusted and replaced, and a new applicator will be designed to increase the radiated light power.

4. Discussion

In this study, we tested a device designed to implement the digital diaphanoscopy technology, which is based on visualization and analysis of the low-intensity radiation scattering pattern in the maxillary sinuses.

The review and analysis of existing methods (CT and MRI) for the diagnosis of inflammatory diseases of maxillary sinuses diseases showed their limitation either for the repeated conduct of studies due to radiation or microwave exposure or for the conduct of studies in general, for example, for pregnant women or children. In otolaryngology, the standard methods for diagnosing such pathologies (ultrasound and rhinoscopy tech-

niques) sometimes yield false positive results due to complexity in interpreting the results, or due to trauma-related aspects. In comparison with the considered methods, the method of digital diaphanoscopy allows one to overcome these drawbacks.

In addition, the review of the literature in the field of non-invasive optical diagnosis of paranasal pathology demonstrates that our technology has the advantage over the previously published results, as it provides a foundation for the assessement of the condition of the sinuses for all categories of patients, based on their anatomical and gender features. For this purpose, we designed the original brightness controller of the LED applicator and developed a specialized adjustment software for the probing mode, which makes it possible to select an effective radiation dose for each patient.

Currently, further experimental studies are being conducted to form an appropriate database and identify diagnostic criteria for various pathological changes, taking into account the range of the optical power of probing radiation, that have the greatest sensitivity to visualization of pathological changes in the maxillary sinuses in different study groups divided by gender.

5. Conclusions

Preliminary trials were conducted in 20 conditionally healthy volunteers and 15 patients with suspected maxillary sinus inflammation. The influence of anatomical and gender features of the study area on the diagnostic results (differences in skin structure, skull bone thickness, and sinus size) was revealed. The sensitivity of the prototype device to detect pathological changes was confirmed by the results of MRI studies.

The simulation results show the regularity of changes in the light scattering and parameters of the probing and measuring parts of the experimental setup. The mathematical model developed via Monte Carlo simulation made it possible to take into account the anatomical and gender features of the study area, as well as the absorption and scattering of optical radiation.

The prototype of the device was upgraded to obtain similar scattering patterns of light for different patients and to ensure their comparison. To adjust the output power of the probing applicator, a device for controlling the LED applicator brightness was designed, and additional software was developed.

The obtained results can be used to create modern diagnostic devices for the diagnosis of maxillary sinus pathology based on visualization and analysis of the low-intensity radiation scattering pattern. The application of the developed digital diaphanoscopy technology will make it possible to conduct timely, reliable, and painless diagnostics of maxillary sinus pathology, assess the dynamics of changes in the pathological processes within the framework of the therapy, and analyze its effectiveness. It is important to note that, due to the portability and simplicity of its instrument implementation, the technology can be used as a screening method for assessing the condition of the maxillary sinuses both in hospital and medical institutions and remotely in the absence of otolaryngologists and diagnosticians.

Author Contributions: Original draft preparation and, measurements, E.O.B. and I.N.N.; data acquisition setup, methodology, and numerical simulation, V.V.D.; numerical simulation, R.Y.G.; experiments at the Diagnostic Medical Center "MediScan" (Orel, Russia), E.O.B.; funding acquisition, supervision, and project administration, A.V.D.; and original development of the project idea and supervision, O.A.B. and V.G.A. All authors edited the manuscript. All authors have read and agreed to the published version of the manuscript.

Funding: The reported study was funded by RFBR according to the research project No. 20-32-90147 (original draft preparation, measurements, numerical simulation). The work was also supported by the grant of the President of the Russian Federation for state support of young Russian scientists No. MK-2634.2019.8 (development of experimental setup and data acquisition). V.D. kindly acknowledges personal support from the European Union's Horizon 2020 research and innovation programme under the Marie Skłodowska-Curie grant agreement No. 839888.

Institutional Review Board Statement: The study was conducted according to the guidelines of the Declaration of Helsinki by the World Medical Association and approved by the Ethics committee of the Orel State University (record of meeting No. 15 of 21 February 2019).

Informed Consent Statement: Informed consent was obtained from all subjects involved in the study.

Data Availability Statement: The data that support the findings of this study are available upon reasonable request request from the corresponding author.

Acknowledgments: Thanks for assistance in project realization are given to Olaf Minet (Charité Universitätsmedizin Berlin, Berlin, Germany) and Urszula Zabarylo (Charité—Universitätsklinikum Berlin, Berlin, Germany). Special thanks are extended to the head doctor of Diagnostic Medical Center "MediScan" (Orel, Russia) Boris Shuraev for assistance in conducting experiments and conceptualization.

Conflicts of Interest: The authors declare no conflict of interest. The funders had no role in the design of the study; in the collection, analyses, or interpretation of data; in the writing of the manuscript, or in the decision to publish the results.

Abbreviations

CT	computed tomography
MRI	magnetic resonance imaging
NIR	near infrared
CMOS	complementary metal oxide semiconductor
LED	light-emitting diode

References

1. Battisti, A.S.; Pangia, J. *Sinusitis. StatPearls—NCBI Bookshelf*; StatPearls Publishing: Treasure Island, FL, USA, 2018.
2. Villarroel, M.; Blackwell, D.; Jen, A. Tables of Summary Health Statistics for U.S. Adults: 2018 National Health Interview Survey. National Center for Health Statistics; NCHS: National Health Interview Survey. 2019. Available online: http://www.cdc.gov/nchs/nhis/SHS/tables.htm (accessed on 19 November 2020).
3. Hastan, D.; Fokkens, W.J.; Bachert, C.; Newson, R.B.; Bislimovska, J.; Bockelbrink, A.; Bousquet, P.J.; Brozek, G.; Bruno, A.; Dahlén, S.E.; et al. Chronic rhinosinusitis in Europe—An underestimated disease. A GA 2LEN study. *Allergy* **2011**, *66*, 1216–1223. [CrossRef] [PubMed]
4. Mafee, M.F.; Farid, N.; Lim, W.Y. Imaging of the Paranasal Sinuses: Plain-Film Radiography, Computed Tomography, and Magnetic Resonance Imaging. In *Diseases of the Sinuses*; Springer Science and Business Media LLC: Berlin/Heidelberg, Germany, 2014; pp. 295–322.
5. Kanwar, S.S.; Mital, M.; Gupta, P.K.; Saran, S.; Parashar, N.; Singh, A. Evaluation of paranasal sinus diseases by computed tomography and its histopathological correlation. *J. Oral Maxillofac. Radiol.* **2017**, *5*, 46–52. [CrossRef]
6. Bryanskaya, E.; Makovik, I.; Bukin, A.; Bibikova, O.; Shuraev, B.M.; Minet, O.; Zabarilo, U.; Dunaev, A.; Artyushenko, V. Diagnosis of inflammatory diseases of the paranasal sinuses using digital diaphanoscopy. In Proceedings of the Clinical and Preclinical Optical Diagnostics II, Munich, Germany, 23–25 June 2019; p. 11073.
7. Bryanskaya, E.O.; Gneushev, R.Y.; Makovik, I.N.; Dremin, V.V.; Bukin, A.G.; Bibikova, O.A.; Shuraev, B.M.; Minet, O.; Zabarilo, U.; Dunaev, A.V.; et al. Monte Carlo simulation of signals in digital diaphanoscopy of the maxillary sinuses. In *Saratov Fall Meeting 2019: Optical and Nano-Technologies for Biology and Medicine*; SPIE: Saratov, Russia, 2020; Volume 11457, p. 114571K.
8. Stölzel, K.; Szczepek, A.J.; Olze, H.; Koß, S.; Minet, O.; Zabarylo, U. Digital diaphanoscopy of the maxillary sinuses: A revival of optical diagnosis for rhinosinusitis. *Am. J. Otolaryngol.* **2020**, *41*, 102444. [CrossRef] [PubMed]
9. Beuthan, J. IR-diaphanoscopy in medicine. *Med Opt. Tomogr. Funct. Imaging Monit.* **1993**, 103110H. [CrossRef]
10. Feldmann, H. Die Geschichte der Diaphanoskopie. *Laryngo-Rhino-Otologie* **1998**, *77*, 297–304. [CrossRef]
11. Koch, F.H.J.; Deuchler, S.; Hessling, M.; Singh, P. Diaphanoskopie am Auge Ophthalmic diaphanoscopy. *Der Ophthalmol.* **2017**, *11*, 331–864. [CrossRef]
12. Schips, L.; Lipsky, K.; Hebel, P.; Hutterer, G.; Gidaro, S.; Petritsch, P.H.; Zigeuner, R.E. Laparoscopic fenestration of lymphoceles after kidney transplantation with diaphanoscopic guidance. *Urology* **2005**, *66*, 185–187. [CrossRef]
13. Linnarz, M.; Hopf, J.U.G.; Prapavat, V.; Beuthan, J. *Die IR-Diaphanoskopie—Eine Neue Methode in der Diagnostik der Nasennebenhöhlen-Erkrankungen*; Springer Science and Business Media LLC: Berlin/Heidelberg, Germany, 1994; p. 252.
14. Hopf, M.; Hopf, J.U. Near Infrared Transillumination in Acute Maxillary Sinusitis: Theoretical Background—Clinical Application—Diagnostic Potential—Limitations. *Med. Laser Appl.* **2003**, *18*, 217–231. [CrossRef]
15. Bellemann, V. Digitale Diaphanoskopie der Nasennebenhöhlen. *Med. Bildgeb. Master* **2012**, *1*, 30–31.
16. Jacques, S.L. Optical properties of biological tissues: A review. *Phys. Med. Biol.* **2013**, *58*, R37–R61. [CrossRef]
17. Peters, V.G.; Wymant, D.R.; Patterson, M.S.; Frank, G.L. Optical properties of normal and diseased human breast tissues in the visible and near infrared in the visible and near infrared. *Phys. Med. Biol. Relat. Content* **1990**, *35*, 1317–1334. [CrossRef] [PubMed]

18. Bashkatov, A.N.; Genina, É.A.; Kochubey, V.I.; Tuchin, V.V.; Chikina, E.É.; Knyazev, A.B.; Mareev, O.V. Optical properties of mucous membrane in the spectral range 350–2000 nm. *Opt. Spectrosc.* **2004**, *97*, 978–983. [CrossRef]
19. Bashkatov, A.N.; Genina, E.A.; Kochubey, V.I.; Tuchin, V.V. Optical properties of human cranial bone in the spectral range from 800 to 2000 nm. *SPIE Proc.* **2006**, 616310. [CrossRef]
20. Genina, E.A.; Bashkatov, A.N.; Tuchin, V.V. Optical Clearing of Cranial Bone. *Adv. Opt. Technol.* **2008**, *2008*, 1–8. [CrossRef] [PubMed]
21. Van Veen, R.L.P.; Sterenborg, H.J.C.M.; Marinelli, A.W.K.S.; Menke-Pluymers, M. Intraoperatively assessed optical properties of malignant and healthy breast tissue used to determine the optimum wavelength of contrast for optical mammography. *J. Biomed. Opt.* **2004**, *9*, 1129–1136. [CrossRef]
22. Bashkatov, A.N.; Genina, E.A.; Tuchin, V.V. Optical properties of skin, subcutaneous, and muscle tissues: A review. *J. Innov. Opt. Health Sci.* **2011**, *4*, 9–38. [CrossRef]
23. Teke, H.Y.; Duran, S.; Canturk, N.; Canturk, G. Determination of gender by measuring the size of the maxillary sinuses in computerized tomography scans. *Surg. Radiol. Anat.* **2006**, *29*, 9–13. [CrossRef]
24. Gracco, A.; Lombardo, L.; Cozzani, M.; Siciliani, G. Quantitative evaluation with CBCT of palatal bone thickness in growing patients. *Prog. Orthod.* **2006**, *7*, 164–174.
25. Kang, S.; Lee, S.-J.; Ahn, S.-J.; Heo, M.-S.; Kim, T.-W. Bone thickness of the palate for orthodontic mini-implant anchorage in adults. *Am. J. Orthod. Dentofac. Orthop.* **2007**, *131*, S74–S81. [CrossRef]
26. Dremin, V.; Zherebtsov, E.; Bykov, A.; Popov, A.; Doronin, A.; Meglinski, I. Influence of blood pulsation on diagnostic volume in pulse oximetry and photoplethysmography measurements. *Appl. Opt.* **2019**, *58*, 9398–9405. [CrossRef]
27. Zherebtsov, E.; Dremin, V.; Popov, A.; Doronin, A.; Kurakina, D.; Kirillin, M.Y.; Meglinski, I.; Bykov, A. Hyperspectral imaging of human skin aided by artificial neural networks. *Biomed. Opt. Express* **2019**, *10*, 3545–3559. [CrossRef] [PubMed]
28. Wara-Aswapati, N.; Pitiphat, W.; Chandrapho, N.; Rattanayatikul, C.; Karimbux, N. Thickness of Palatal Masticatory Mucosa Associated With Age. *J. Periodontol.* **2001**, *72*, 1407–1412. [CrossRef] [PubMed]
29. Genina, E.A.; Zubkova, E.A.; Korobko, A.A.; Yanina, I.Y.; Bashkatov, A.N.; Kamenskikh, T.G.; Galanzha, V.A.; Tuchin, V.V. Diffusion of Cortexin and Retinalamin in eye sclera. In Proceedings of the Saratov Fall Meeting 2006: Optical Technologies in Biophysics and Medicine VIII, Saratov, Russia, 26–29 September 2006; Volume 65351.
30. Barghouth, G.; Prior, J.; Lepori, D.; Duvoisin, B.; Schnyder, P.; Gudinchet, F. Paranasal sinuses in children: Size evaluation of maxillary, sphenoid, and frontal sinuses by magnetic resonance imaging and proposal of volume index percentile curves. *Eur. Radiol.* **2002**, *12*, 1451–1458. [CrossRef] [PubMed]
31. Uchida, Y.; Goto, M.; Katsuki, T.; Akiyoshi, T. Measurement of the maxilla and zygoma as an aid in installing zygomatic implants. *J. Oral Maxillofac. Surg.* **2001**, *59*, 1193–1198. [CrossRef] [PubMed]
32. Xu, X.; Zhao, S.; Liu, H.; Sun, Z.; Wang, J.; Zhang, W. An Anatomical Study of Maxillary-Zygomatic Complex Using Three-Dimensional Computerized Tomography-Based Zygomatic Implantation. *BioMed Res. Int.* **2017**, *2017*, 1–8. [CrossRef] [PubMed]
33. De Greef, S.; Claes, P.; Vandermeulen, D.; Mollemans, W.; Suetens, P.; Willems, G. Large-scale in-vivo Caucasian facial soft tissue thickness database for craniofacial reconstruction. *Forensic Sci. Int.* **2006**, *159*, S126–S146. [CrossRef] [PubMed]
34. Dremin, V.; Dunaev, A. How the melanin concentration in the skin affects the fluorescence-spectroscopy signal formation. *J. Opt. Technol.* **2016**, *83*, 43. [CrossRef]
35. Rafailov, I.E.; Dremin, V.V.; Litvinova, K.S.; Dunaev, A.V.; Sokolovski, S.G.; Rafailov, E.U. Computational model of bladder tissue based on its measured optical properties. *J. Biomed. Opt.* **2016**, *21*, 025006. [CrossRef]
36. Rafailov, I.; Palmer, S.; Litvinova, K.; Dremin, V.; Dunaev, A.; Nabi, G. A novel excitation-emission wavelength model to facilitate the diagnosis of urinary bladder diseases. *Photonic Ther. Diagn. XI* **2015**, *9303*, 93030W. [CrossRef]

diagnostics

MDPI

Article

Multimodal Diagnostics of Microrheologic Alterations in Blood of Coronary Heart Disease and Diabetic Patients

Anastasia Maslianitsyna [1,*], Petr Ermolinskiy [1], Andrei Lugovtsov [1,2], Alexandra Pigurenko [3], Maria Sasonko [4], Yury Gurfinkel [5] and Alexander Priezzhev [1,2]

[1] Physics Department, Lomonosov Moscow State University, 119991 Moscow, Russia; peter.ermolinskiy@biomedphotonics.ru (P.E.); anlug@biomedphotonics.ru (A.L.); avp@biomedphotonics.ru (A.P.)
[2] International Laser Center, Lomonosov Moscow State University, 119991 Moscow, Russia
[3] Faculty of Fundamental Medicine, Lomonosov Moscow State University, 119991 Moscow, Russia; pigurenko-alexandra-101-16-17@yandex.ru
[4] Research Clinical Center of JSC "Russian Railways", 123567 Moscow, Russia; msasonko@yandex.ru
[5] Medical Research and Educational Center, Lomonosov Moscow State University, 119991 Moscow, Russia; yugurf@yandex.ru
* Correspondence: stasyazavr2000@biomedphotonics.ru

Abstract: Coronary heart disease (CHD) has serious implications for human health and needs to be diagnosed as early as possible. In this article in vivo and in vitro optical methods are used to study blood properties related to the aggregation of red blood cells in patients with CHD and comorbidities such as type 2 diabetes mellitus (T2DM). The results show not only a significant difference of the aggregation in patients compared to healthy people, but also a correspondence between in vivo and in vitro parameters. Red blood cells aggregate in CHD patients faster and more numerously; in particular the aggregation index increases by 20 ± 7%. The presence of T2DM also significantly elevates aggregation in CHD patients. This work demonstrates multimodal diagnostics and monitoring of patients with socially significant pathologies.

Keywords: blood rheology; red blood cell aggregation; laser tweezers; laser aggregometry; digital capillaroscopy; coronary heart disease; diabetes mellitus

Citation: Maslianitsyna, A.; Ermolinskiy, P.; Lugovtsov, A.; Pigurenko, A.; Sasonko, M.; Gurfinkel, Y.; Priezzhev, A. Multimodal Diagnostics of Microrheologic Alterations in Blood of Coronary Heart Disease and Diabetic Patients. *Diagnostics* **2021**, *11*, 76. https://doi.org/10.3390/diagnostics11010076

Received: 4 November 2020
Accepted: 30 December 2020
Published: 6 January 2021

1. Introduction

Blood flow and circulation inside vessels in vivo are defined by many interconnected parameters, such as blood viscosity, hematocrit, and plasma protein composition, so to properly study them a complex approach is required [1]. There are many methods allowing for in vivo and in vitro measurements of different blood properties [1,2].

The main focus of this study is the aggregation of red blood cells (RBCs), which significantly influences the viscosity of blood [3]. RBC aggregation is the reversible process of the formation of linear and more complex structures of RBCs. It promotes the formation of peripheral cell-poor fluid layer that lowers the hydrodynamic vessel resistance to blood flow [3]. The process of in vitro as well as in vivo RBC aggregation can be described in several ways: by the number of cells aggregating during a given time interval, by how many aggregates are observed, by how fast a couple of RBCs can form a doublet, etc. [3]. These parameters require specialized tools in order to be measured, so they are not used widely in clinical conditions. RBC aggregation depends on many internal and external factors. For example, blood plasma composition, temperature, RBC shapes, and the age, state of health of an individual, and his or her medicine intake determine in part the aggregation parameters of RBCs [3–5].

Many methods can be applied to studying RBCs, including micropipette aspiration [6], etc., but among all methods it would be worth highlighting the optical techniques as far as they have several advantages: non-invasiveness and lack of direct mechanical contact with

the cells, the option to study both individual cells and their ensembles, and the possibility of in vivo and in vitro application [4,7]. The last point can pose a challenge in terms of comparing results for these different conditions—in vitro measurements require anticoagulants for stabilizing the blood samples and storing blood during sample preparation, which can influence the measured parameters, whereas in vivo methods allow for measuring a different set of parameters that may be difficult to correlate with those measured in vitro.

The aim of this work was to find correspondence between in vivo and in vitro optical methods by studying patients with cardiovascular and associated pathologies. Understanding the link between RBC aggregation and widespread cardiovascular diseases is vital to create new methods of diagnosis and treatment. In this article, we look at coronary heart disease (CHD) and type 2 diabetes mellitus (T2DM), which are known to have a significant effect on microvasculature [8].

2. Materials and Methods

2.1. Patients

The study enrolled 81 adults, including 25 healthy volunteers and 56 patients with CHD and arterial hypertension (Table 1). The patients with CHD were divided into two groups depending on the presence of T2DM. The first group included 42 CHD patients without T2DM, and second group included 14 CHD patients with T2DM. We did not find any statistically significant differences in the clinical background for these two groups of patients. The study was conducted during the period from July 2015 to July 2020.

Table 1. The clinical backgrounds for each group of patients, mean ± standard deviation or number (%).

Parameter	Overall Patient Data (n = 56)	Patients with CHD and without T2DM (n = 42)	Patients with CHD and T2DM (n = 14)
Number (percentage) of males	38 (68%)	29 (69%)	9 (64%)
Number (percentage) of females	18 (32%)	13 (31%)	5 (36%)
Mean age (range), years	69.2 (51–92)	70.5 (51–92)	65.3 (52–81)
Number (percentage) of smokers	10 (18%)	6 (14%)	4 (29%)
Body mass index, kg/m^2	29 ± 5	28 ± 5	31 ± 5
Systolic blood pressure, mm Hg	139 ± 27	142 ± 22	137 ± 20
Diastolic blood pressure, mm Hg	82 ± 12	82 ± 13	83 ± 9
Heart rate, bpm	71 ± 9	72 ± 9	69 ± 10
LV ejection fraction, %	57 ± 7	56 ± 6	58 ± 8
Previous myocardial infarction	22 (39%)	18 (43%)	4 (29%)
Angina pectoris	48 (86%)	36 (86%)	12 (86%)
Bypass grafts	5 (9%)	4 (9%)	1 (7%)
Stents	17 (30%)	12 (29%)	4 (31%)
Antiaggregants	39 (70%)	29 (69%)	10 (71%)
Anticoagulants	12 (23%)	10 (24%)	3 (21%)
Diuretics	28 (50%)	19 (45%)	9 (64%)

CHD—coronary heart disease; T2DM—type 2 diabetes mellitus; LV ejection fraction—left ventricular ejection fraction.

Criteria for exclusion from the study were the following: chronic heart disease insufficiency, heart rhythm and conduction disorders, renal and hepatic insufficiency, type 1 diabetes mellitus, vascular or other pathology of the brain, or oncological diseases in the medical history.

The study included several procedures for the patients. The measurements of blood pressure and heart rate were conducted for each patient between 8:00 and 8:30 a.m. before their medicine intake on the day following their hospitalization in the cardiological unit. In addition to the standard medical check-up, all patients underwent a non-invasive study of microcirculatory parameters in the nail bed capillaries using the method of digital capillaroscopy. For the in vitro study, the blood was drawn from the patients' cubital veins on an empty stomach, stabilized with EDTA K2 anticoagulant and was used for the experiments within the first three hours.

Twenty-five healthy volunteers (16 males and 9 females) had an average age 27.5 and body mass index (BMI) of 22.1, were non-smokers, and had not taken any medication. These people were divided into two control groups (n = 10 (4 males and 6 females) and 15 (12 males and 3 females)) that were studied independently at different time intervals with different parameters measured.

The study design was approved by the local ethics committee of medical research and educational center of M.V. Lomonosov Moscow State University, Moscow, Russia (protocol code: 1/19, date of approval: 18 February 2019). The experiment design took into account the latest recommendations for laboratories made by the international expert team for the standardization of hemorheological methods [9]. The patients and healthy volunteers participating in the research were informed on the purpose of the study and gave written informed consent in accordance with the Declaration of Helsinki.

2.2. Laser Aggregometry Method

The laser aggregometry method implemented in a microchip stirring type RheoScan aggregometer (RheoMedTech, Seoul, Korea) was used to measure the aggregation parameters of RBCs in vitro in whole blood samples [10]. Laser aggregometry is based on the diffused light scattering of a laser beam by the blood sample [11]. To perform the measurements 8 μL of whole blood were placed inside a flat reservoir and heated up to 37 °C. Then the sample was illuminated by a laser beam (633 nm, 2.5 mW), which was scattered by the RBCs and their aggregates mostly in the forward direction—the scattering particles were much larger than the light wavelength. The larger the size of the scattering particle the more intensity was scattered forward [12,13].

The time course of measured intensity of light scattered forward is presented in Figure 1. In the beginning of the measurement the RBCs were in a state of maximum aggregation and therefore the scattered intensity was also at its maximum. Then, a small magnetic bar inside the reservoir started stirring the sample, causing shear stress-induced destruction of the aggregates. After the stirring process (t = 0 in Figure 1), all aggregates were dispersed and none of the RBCs were in the aggregated state and therefore the scattered intensity was at its minimum; the cells themselves suffered no permanent damage from this. The stirring stopped and so the RBCs started to aggregate again, the average size of a scattering particle in the sample grew, and the scattered intensity increased. The aggregation process lasted approximately two minutes; after that the intensity reached its maximum, indicating that the cells were in a state of complete aggregation.

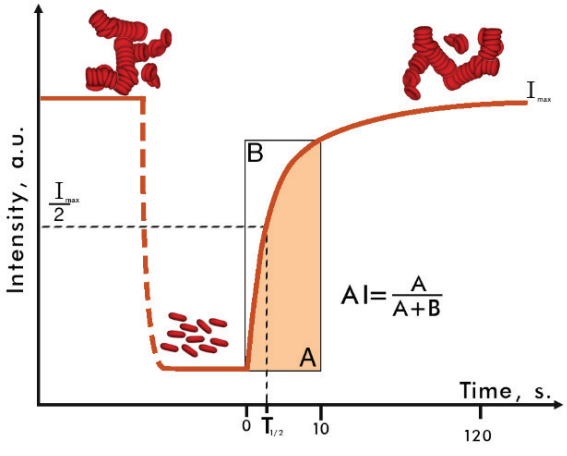

Figure 1. The kinetics of the RheoScan aggregometer output signal (intensity of light scattered forward as a function of time). The meaning of $T_{1/2}$ and AI is indicated. 'A' is the area below the intensity curve inside the rectangle; 'B' is the area above the intensity curve inside the rectangle.

The aggregation kinetics were reflected in the dependence of the scattered intensity on time and several parameters were calculated based on it. Firstly, the characteristic time of aggregate formation ($T_{1/2}$) characterized the time interval, during which the signal (scattered light intensity) reached half of the maximum value (see Figure 1). A smaller $T_{1/2}$ indicated greater curve slope and faster aggregation of the cells. Secondly, the aggregation index (AI) characterized the fraction of cells aggregated during the first 10 s of measurement. It was calculated as a ratio between the area under the intensity curve to the total area above and below it (see Figure 1). Higher AI values corresponded to more numerous RBC aggregation in the sample.

2.3. Laser Tweezers

Laser tweezers (LT) are scientific tools that allow for the trapping and manipulation of microobjects (such as living cells, etc.) using a highly focused laser beam [14]. LT are essential instruments in single-cell studies. The physical principle of optical trapping is described in more detail in [15].

In our study, LT were used to measure the duration of the process of spontaneous aggregation of two individual RBCs [16]. Two beams from the Nd:YAG lasers (1064 nm, 200 mW) propagated through a system of lenses and polarizers and reached the dichroic mirror where they were split in two parts: The first one was directed to the aperture of the Olympus objective (×100, NA = 1.00, water immersion) and into the sample, and the second one to the photodetector in order to evaluate its power. One laser beam was always stationary whereas the other one could be moved by rotating the movable mirror—this allowed for two laser traps in the sample to be obtained: one stationary and one movable.

The measurements were carried out at room temperature (22 °C) in a highly diluted blood suspension inside a glass microcuvette with a 100 µm gap [17]. Patients' autological platelet-poor plasma was used as the suspension medium. The plasma was acquired by centrifuging all the blood for 10 min at 170 g, removing the platelet-rich plasma, then centrifuging the platelet-rich plasma for 10 min at 3000 g and removing the buffy coat. Lastly, the RBCs were added to the plasma to achieve the final hematocrit of about 0.1%. Due to such a high dilution of the suspension the hematocrit did not affect the measurements.

In LT the trapped RBCs oriented themselves vertically, so the cells were observed edge-on [18]. The time of doublet aggregate formation T_{agg} was measured by orienting two trapped RBCs parallel to each other and creating a single point of contact between their membranes using the movable laser trap (see Figure 2a) [16]. Then, the laser traps were disabled and the time of the doublet formation as a result of spontaneous aggregation was measured (see Figure 2b,c). Smaller values of T_{agg} corresponded to faster aggregate formation.

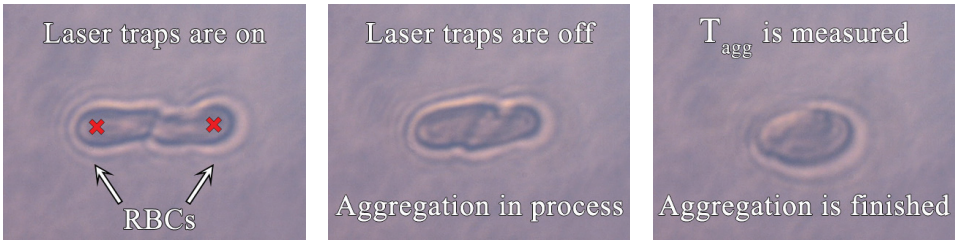

Figure 2. Three steps of T_{agg} measurement. Red crosses indicate the laser traps. (**a**) Two separate RBCs are brought together until the state of a "point contact"; (**b**,**c**) RBCs start to aggregate (overlap) after the laser beams are shut off.

For the interpretation of the results, it needs to be emphasized that the T_{agg} parameter corresponds to the initial stage of the aggregation process, whereas the laser aggregometry parameters ($T_{1/2}$ and AI) represent the whole aggregation process, including the later formation of complex 3D aggregate structures.

2.4. Digital Capillaroscopy

Digital capillaroscopy was used to evaluate capillary blood flow parameters in vivo. Using the Kapillaroskan-1 device (AET, Moscow, Russia) a quantitative assessment of the blood flow characteristics was carried out in the nail bed capillaries. This method is described in more detail in [19,20]. Several nail bed capillaries of each patient were recorded at the high frame rate and then used to assess the average capillary blood flow velocity (CBV), which was calculated by frame-by-frame analysis.

Before the start of the measurements, the temperature of the skin of the studied finger was measured using an AND DT-635 skin thermometer (A&D, Tokyo, Japan). On average, the temperature of the skin of the finger in the patients included in the study was 33.6 ± 1.3 °C. There were no statistically significant differences between the groups considering the finger temperature.

2.5. Statistical Analysis

For each blood sample, the parameters AI $T_{1/2}$, and T_{agg} were measured 5 times. The calculation of the CBV and the presence of aggregates for the DC method was carried out using original software that analyzed recordings of the nail bed capillaries. Videos of at least 6 good reading capillaries were used for calculations with a video duration of 3 to 5 s (at a recording rate of 100 frames per second, i.e., from 1800 to 3000 frames per patient). In the Results section the averaged values and the standard errors of the mean are presented. They were chosen over the standard deviations because they show the precision of the mean value. Statistical difference was calculated with a two-tailed Student *t*-test with unequal variance. The difference between the two values was considered statistically significant if the *p*-value according to the *t*-test was less than 0.05.

3. Results

3.1. Comparison of CHD Patients and Healthy Volunteers

The parameters assessed with the methods described above for all the CHD patients were different from the control values (Table 2). The first and second control group did not show statistically significant differences between themselves.

Table 2. The comparison of CHD patients and the control groups. The averaged values and the standard errors are presented. The *p*-value was calculated by a two-tailed *t*-test with unequal variance.

Parameter/Group	Control Group A (n = 15)	Control Group B (n = 10)	CHD Patients (n = 56)
AI, %	41.0 ± 1.3	44 ± 3	49.0 ± 1.2 *
$T_{1/2}$, s	5.9 ± 0.4	5.6 ± 1.0	4.2 ± 0.4 *
T_{agg}, s	6.6 ± 0.4	-	4.8 ± 0.2 *
CBV, mcm/s	-	1290 ± 230	850 ± 100

CHD—coronary heart disease; AI—aggregation index; CBV—capillary blood velocity; * $p < 0.05$ for control group A.

The values for control groups A and B did not show statistically significant differences for AI and $T_{1/2}$ (see Table 2), which proves the consistency of the laser aggregometry method. Unfortunately, other parameters (T_{agg} and CBV) could not be measured for both control groups, but they were consistent with our previous work [11]. Control group A was studied more recently and had a greater number of subjects than group B, so we used it in the analysis.

In CHD patients compared to the control group A, AI was higher by 20 ± 7% ($p < 0.05$), meaning more numerous aggregation, $T_{1/2}$ was lower by 14 ± 9% ($p < 0.05$), meaning faster

aggregation, and T_{agg} was lower by 27 ± 7% ($p < 0.05$), showing faster doublet formation. As for CBV, it was smaller than the control, but significant only at $p = 0.1$ level due to high variation from person to person.

The CHD patients were divided into two groups by the presence of T2DM and they showed significant ($p < 0.05$) differences in some parameters (Table 3).

Table 3. The comparison of CHD patients with and without T2DM. The averaged values and the standard errors of the sample mean are presented. The *p*-value was calculated by a two-tailed *t*-test with unequal variance.

Parameter/Group	CHD Patients (n = 42)	CHD + T2DM Patients (n = 14)
AI, %	48.6 ± 1.0	53.0 ± 1.1 *
$T_{1/2}$, s	4.1 ± 0.2	3.1 ± 0.2 *
T_{agg}, s	5.0 ± 1.2	4.6 ± 0.4
CBV, mcm/s	750 ± 90	1150 ± 300

CHD—coronary heart disease; T2DM—type 2 diabetes mellitus; AI—aggregation index; CBV—capillary blood velocity; * $p < 0.05$.

3.2. Digital Capillaroscopy Results Matched with In Vitro Parameters

Figure 3a–c shows the RBC aggregation parameters plotted as functions of CBV and the Pearson's r coefficient for each trend. AI for all the presented groups decreased with the increase of CBV, as indicated by the negative r. $T_{1/2}$, on the other hand, increased and had positive r values. T_{agg} remained constant for the whole CBV range. These results show that for patients with high CBV the aggregation process in vitro was weaker compared to the patients with low CBV: The aggregation was less numerous and the doublet formation took longer.

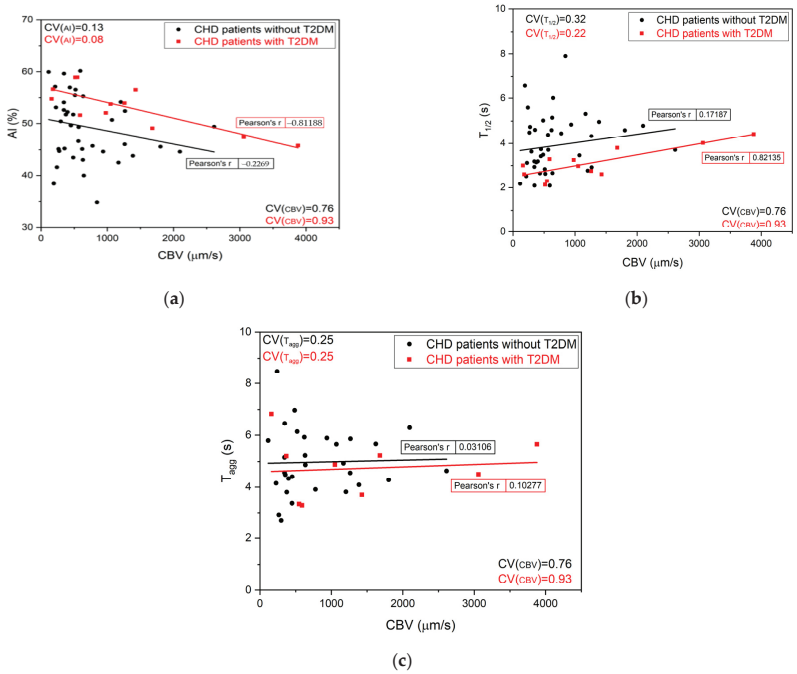

Figure 3. The individual values of AI (**a**), $T_{1/2}$ (**b**), and T_{agg} (**c**) for groups of patients with and without T2DM versus the CBV. The linear fit and the Pearson's r coefficient are shown. CHD—coronary heart disease; T2DM—type 2 diabetes mellitus; CBV—capillary blood velocity.

No statistically significant difference in aggregation was found between several patient subgroups, including the division by gender and smoking habits. AI weakly correlated with BMI (Pearson's r = 0.29) and did not correlate with age (r = −0.05).

4. Discussion

In vitro and in vivo aggregation conditions are, of course, different due to the channel shape, presence, or absence of an endothelium layer, surrounding medium, etc. [21]. Moreover, in vivo aggregation in big vessels differs from the aggregation in capillaries [3]. In this study, we investigated in vivo RBC aggregation in nailfold capillaries, therefore excluding effects that can be observed in big vessels, such as axial migration of RBC, etc. [3]. Hemorheological parameters (including blood flow in capillaries) show alterations in pathophysiological processes in a complex way [22]. That is why our data could have provided contradictory results if we had not used criteria for exclusion (mentioned above in Section 2. Materials and Methods 2.1. Patients).

We found correlations between blood flow parameters measured in vitro and in vivo, as well as significant differences between the control group and CHD patients with and without T2DM. Firstly, the RBC aggregation in CHD patients was enhanced compared to the healthy volunteers (see Table 2). The increase in RBC aggregation has already been linked to cardiovascular diseases, including CHD and arterial hypertension using different techniques [23–25]. However, the relationship between aggregation and pathologies is yet to be established—article [26] suggests that aggregation and pathologies are not linked directly but rather share the same factors, such as obesity and cigarette smoking, among others. We found only a weak correlation for these factors and aggregation in CHD patients.

Secondly, the presence of T2DM had a significant effect on aggregation properties: Both AI and $T_{1/2}$ were higher ($p < 0.05$) compared to the patients without it (see Table 3). Of course, the effect of T2DM on RBC aggregation is already established [27], but being able to detect it specifically for CHD patients opens many doors in terms of diagnostics and monitoring the discussed pathologies. Two other parameters (T_{agg} and CBV) did not show significant differences; this could be in part due to the methodology. Both LT and capillaroscopy study a limited number of RBCs, whereas laser aggregometry analyzes ensembles of tens of thousands. A high uncertainty in T_{agg} and CBV demonstrated a great variation of RBC properties for each individual patient, which could have been caused by his or her health status. It could also mean that the effect of elevated aggregation was clearer during the later stages of aggregate formation (3D aggregate structures) than in the initial doublet formation.

Higher CBV means lower friction in the vessels and therefore weaker RBC aggregation [2]. This was clearly manifested for patients with T2DM in Figure 3 by the negative correlation with AI (r = −0.81) and positive correlation of $T_{1/2}$ (r = 0.82). For patients with a high CBV it was more likely that their RBC aggregation be more numerous and take less time for a large ensemble. T_{agg} measured with LT did not correlate with CBV for all groups.

Additionally, it is important to mention the differences of blood temperature during measurement of different in vitro parameters. RheoScan parameters (AI and $T_{1/2}$) were measured at 37 °C, whereas the LT parameter (T_{agg}) was measured at room temperature at 22 °C. Because the aggregation depends on the temperature, these different conditions might have influenced the obtained data [3,28]. For example, RheoScan parameters (AI and $T_{1/2}$) greatly depend on temperature [28]. However, in our previous work [29] it was shown that for LT measurements the temperature-dependent change of the RBC aggregation was nearly absent for the temperatures of 20 °C and 38 °C. This means that we could compare all in vitro parameters between each other as if they were measured at the same temperatures.

The novelty of the presented work consists of a complex analysis of in vitro and in vivo parameters for different pathologies. The results of studies performed by alternative methods do not contradict our conclusions and show increased aggregation of RBCs in patients with CHD (including various complications) compared to healthy donors [3,30–32].

One of the limitations of the study is the small number of patients with both CHD and T2DM; in the future, we plan to increase this number. This will allow for grouping the patients by specific medication used, such as antiaggregants and anticoagulants. Another point that can be improved is the observation of additional factors that influence the blood flow, for example plasma components [3,33]. In addition, BMI and other factors influence platelet activation and aggregation [34], which can indirectly affect the aggregation of RBCs; this was not accounted for in this article.

5. Conclusions

In this work, the aggregation of red blood cells was studied using different optical in vivo and in vitro measurement techniques. The aggregation for patients with coronary heart disease was statistically significantly enhanced compared to the control group. In vivo and in vitro methods yielded correlated results: The faster the cells moved in the capillaries, the less cells aggregated in vitro. Type 2 diabetes mellitus had an additional significant effect on the aggregation properties of coronary heart disease patients. These findings are prominent for diagnosing and monitoring the state of patients with pathologies that affect blood properties.

Author Contributions: This paper is a result of the cooperation and contribution of all authors. Conceptualization, A.P. (Alexander Priezzhev), and Y.G.; investigation, P.E., A.M., and Y.G.; methodology, M.S., supervision, A.P. (Alexandra Pigurenko) and A.L. All authors have read and approved the published version of the manuscript.

Funding: This research was funded by RFBR, grant number 19-52-51015.

Institutional Review Board Statement: The study was conducted according to the guidelines of the Declaration of Helsinki, and approved by the Ethics Committee of the medical research and educational center of M.V. Lomonosov Moscow State University, Moscow, Russia (protocol code: 1/19, date of approval: 18 February 2019).

Informed Consent Statement: Informed consent was obtained from all subjects involved in the study.

Data Availability Statement: The data presented in this study are available on request from the corresponding author. The data are not publicly available due to the ethical and privacy issues.

Acknowledgments: The authors would like to extend thanks for the financial support provided to this study by RFBR (19-52-51015).

Conflicts of Interest: The authors declare no conflict of interest. The funders had no role in the design of the study; in the collection, analyses, or interpretation of data; in the writing of the manuscript, or in the decision to publish the results.

References

1. Tuchin, V. (Ed.) *Handbook of Optical Biomedical Diagnostics*; SPIE: Bellingham, WA, USA, 2016; Volume 2.
2. Patrícia, S.; Fernando, P.; Manuel, A.; Mónica, O. A review of hemorheology: Measuring techniques and recent advances. *Korea-Aust. Rheol. J.* **2016**, *28*, 1–22. [CrossRef]
3. Baskurt, O.; Neu, B.; Meiselman, H. *Red Blood Cell Aggregation*; CRC Press: Boca Raton, FL, USA, 2012.
4. Priezzhev, A.; Lee, K.; Firsov, N.; Lademann, J. Optical Study of RBC Aggregation in Whole Blood Samples and Single Cells. In *Handbook on Optical Biomedical Diagnostics*, 2nd ed.; Tuchin, V., Ed.; SPIE Press: Bellingham, WA, USA, 2016; pp. 5–36.
5. Muravyov, A.; Tikhomirova, I.; Maimistova, A.; Bulaeva, S.; Mikhailov, P.; Kislov, N. Red blood cell aggregation changes are dependent on its initial value: Effect of long-term drug treatment and short-term cell incubation with drug. *Clin. Hemorheol. Microcirc.* **2011**, *48*, 231–240. [CrossRef] [PubMed]
6. Hochmuth, R. Micropipette aspiration of living cells. *J. Biomech.* **2000**, *33*, 15–22. [CrossRef]
7. Kyriacou, P.; Budidha, K.; Abay, T.Y. Optical Techniques for Blood and Tissue Oxygenation. *Ref. Modul. Biomed. Sci.* **2019**, *3*, 461–472. [CrossRef]
8. Gurfinkel, Y.; Suchkova, O.; Sasonko, M.; Priezzhev, A. Implementation of digital optical capillaroscopy for quantifying and estimating the microvascular abnormalities in diabetes mellitus. *Proc. SPIE SFM 2015* **2015**, *9917*, 991703. [CrossRef]
9. Baskurt, O.; Boynard, M.; Cokelet, G.; Connes, P.; Cooke, B.; Forconi, S.; Liao, F.; Hardeman, M.; Jung, F.; Meiselman, H.; et al. New guidelines for hemorheological laboratory techniques. *Clin. Hemorheol. Microcirc.* **2009**, *42*, 75–97. [CrossRef] [PubMed]

10. Shin, S.; Yang, Y.; Suh, J. Measurement of erythrocyte aggregation in a microchip stirring system by light transmission. *Clin. Hemorheol. Microcirc.* **2009**, *41*, 197–207. [CrossRef]
11. Lopatin, V.V.; Priezzhev, A.V. Multiple light scattering by suspensions of erythrocytes in geometrical optics approximation. *Proc. SPIE* **2002**, *4749*, 267–274. [CrossRef]
12. Lopatin, V.N.; Priezzhev, A.V.; Aponasenko, A.D.; Shepelevich, N.V.; Lopatin, V.V.; Pozhilenkova, P.V.; Prostakova, I.V. *Metody Svetorassejanija v Analize Dispersnykh Biologicheskikh Sred*; Fizmatlit: Moscow, Russia, 2004. (In Russian)
13. Mauer, J.; Peltomäki, M.; Poblete, S.; Gompper, G.; Fedosov, D.A. Static and dynamic light scattering by red blood cells: A numerical study. *PLoS ONE* **2017**, *12*, e0176799. [CrossRef]
14. Ashkin, A.; Dziedzic, J. Optical trapping and manipulation of single living cells using infra-red laser beams. *Berichte der Bunsen-Gesellschaft für Physikalische Chemie* **1989**, *98*, 254–260. [CrossRef]
15. Arne, G. (Ed.) *Optical Tweezers. Methods and Protocols*; Humana Press: New York, NY, USA, 2017.
16. Ermolinskiy, P.; Lugovtsov, A.; Maslyanitsina, A.; Semenov, A.; Dyachuk, L.; Priezzhev, A. Interaction of erythrocytes in the process of pair aggregation in blood samples from patients with arterial hypertension and healthy donors: Measurements with laser tweezers. *J. Biomed. Photonics Eng.* **2018**, *4*, 030303. [CrossRef]
17. Lee, K.; Kinnunen, M.; Khokhlova, M.; Lyubin, E.; Priezzhev, A.; Meglinski, I.; Fedyanin, A. Optical tweezers study of red blood cell aggregation and disaggregation in plasma and protein solutions. *J. Biomed. Opt.* **2016**, *21*, 035001. [CrossRef] [PubMed]
18. Grover, S.; Gauthier, P.; Skirtach, A. Analysis of the behaviour of erythrocytes in an optical trapping system. *Opt. Express* **2000**, *7*, 533–539. [CrossRef]
19. Gurfinkel, Y.; Sasonko, M. Potentialities of Digital Capillaroscopy in the Diagnostics of Oedema Syndrome. *J. Biomed. Photonics Eng.* **2017**, *3*, 030401. [CrossRef]
20. Parker, M.J.S.; McGill, N.W. *The Established and Evolving Role of Nailfold Capillaroscopy in Connective-Tissue Disease. Chapter in book Connective-Tissue Disease, Connective Tissue Disease—Current State of the Art, Akira Takeda*; IntechOpen: Rijeka, Croatia, 2018.
21. Baskurt, O.K. In vivo correlates of altered blood rheology. *Biorheology* **2008**, *45*, 629–638. [CrossRef] [PubMed]
22. Nemeth, N.; Deak, A.; Szentkereszty, Z.; Peto, K. Effects and influencing factors on hemorheological variables taken into consideration in surgical pathophysiology research. *Clin. Hemorheol. Microcirc.* **2018**, *69*, 133–140. [CrossRef] [PubMed]
23. Hahn, R.; Müller-Seydlitz, P.M.; Jöckel, K.H.; Hubert, H.; Heimburg, P. Viscoelasticity and red blood cell aggregation in patients with coronary heart disease. *Angiology* **1989**, *40*, 914–920. [CrossRef]
24. Cicco, G.; Pirrelli, A. Red Blood Cell (RBC) Deformability, RBC Aggregability and Tissue Oxygenation in Hypertension. *Clin. Hemorheol. Microcirc.* **1999**, *21*, 169–177.
25. Arbel, Y.; Banai, S.; Benhorin, J.; Finkelstein, A.; Herz, I.; Halkin, A.; Keren, G.; Yedgar, S.; Barshtein, G.; Berliner, S. Erythrocyte aggregation as a cause of slow flow in patients of acute coronary syndromes. *Int. J. Cardiol.* **2011**, *154*, 322–327. [CrossRef]
26. Bogar, L. Hemorheology and hypertension: Not "chicken or egg" but two chickens from similar eggs. *Clin. Hemorheol. Microcirc.* **2002**, *26*, 81–83.
27. Li, Q.; Li, L.; Li, Y. Enhanced RBC Aggregation in Type 2 Diabetes Patients. *J. Clin. Lab. Anal.* **2015**, *29*, 387–389. [CrossRef] [PubMed]
28. Ermolinkiy, P.B.; Semenov, A.N.; Lugovtsov, A.E.; Poeschl, C.; Windberger, U.; Kaliviotis, E.; Priezzhev, A.V. Effect of different macromolecules on viscous and microrheologic properties of blood at various temperatures. *Proc. SPIE* **2019**, *11065*, 1106507.
29. Lee, K.; Priezzhev, A.; Shin, S.; Yaya, F.; Meglinsky, I. Characterization of shear stress preventing red blood cells aggregation at the individual cell level: The temperature dependence. *Clin. Hemorheol. Microcirc.* **2016**, *64*, 853–857. [CrossRef] [PubMed]
30. Yang, Q.; Wang, J.H.; Huang, D.D.; Li, D.G.; Chen, B.; Zhang, L.M.; Yuan, C.L.; Cai, L.J. Clinical significance of analysis of the level of blood fat, CRP and hemorheological indicators in the diagnosis of elder coronary heart disease. *Saudi J. Biol. Sci.* **2018**, *25*, 1812–1816. [CrossRef] [PubMed]
31. Brun, J.F.; Varlet-Marie, E.; Raynaud de Mauverger, E.; Mercier, J. Both overall adiposity and abdominal adiposity increase blood viscosity by separate mechanisms. *Clin. Hemorheol. Microcirc.* **2011**, *48*, 257–263. [CrossRef] [PubMed]
32. Koscielny, J.; Jung, E.M.; Mrowietz, C.; Kiesewetter, H.; Latza, R. Blood fluidity, fibrinogen, and cardiovascular risk factors of occlusive arterial disease: Results of the Aachen study. *Clin. Hemorheol. Microcirc.* **2004**, *31*, 185–195.
33. Kwaan, H.C. Role of plasma proteins in whole blood viscosity: A brief clinical review. *Clin. Hemorheol. Microcirc.* **2010**, *44*, 167–176. [CrossRef]
34. Haszon, I.; Papp, F.; Kovács, J.; Bors, M.; Németh, I.; Bereczki, C.; Túri, S. Platelet aggregation, blood viscosity and serum lipids in hypertensive and obese children. *Eur. J. Pediatr.* **2003**, *162*, 385–390. [CrossRef]

diagnostics

MDPI

Article

Diagnostic Accuracy of Cross-Polarization OCT and OCT-Elastography for Differentiation of Breast Cancer Subtypes: Comparative Study

Ekaterina V. Gubarkova [1,*], Elena B. Kiseleva [1], Marina A. Sirotkina [1], Dmitry A. Vorontsov [2], Ksenia A. Achkasova [1], Sergey S. Kuznetsov [3], Konstantin S. Yashin [4], Aleksander L. Matveyev [5], Aleksander A. Sovetsky [6], Lev A. Matveev [6], Anton A. Plekhanov [1], Alexey Y. Vorontsov [2], Vladimir Y. Zaitsev [6] and Natalia D. Gladkova [1]

1 Institute of Experimental Oncology and Biomedical Technologies, Privolzhsky Research Medical University, 603950 Nizhny Novgorod, Russia; kiseleva84@gmail.com (E.B.K.); sirotkina_m@mail.ru (M.A.S.); achkasova.k@bk.ru (K.A.A.); strike_gor@mail.ru (A.A.P.); natalia.gladkova@gmail.com (N.D.G.)
2 Department of Oncology, Nizhny Novgorod Regional Oncologic Hospital, 603126 Nizhny Novgorod, Russia; dr.vorontsovdmitriy@rambler.ru (D.A.V.); doctorvorontsov@mail.ru (A.Y.V.)
3 Department of Pathology, Privolzhsky Research Medical University, 603950 Nizhny Novgorod, Russia; zunek@mail.ru
4 University Clinic, Privolzhsky Research Medical University, 603950 Nizhny Novgorod, Russia; jashinmed@gmail.com
5 Laboratory of Multidimensional Signal Processing, Institute of Applied Physics of the Russian Academy of Sciences, 603950 Nizhny Novgorod, Russia; matveyev@appl.sci-nnov.ru
6 Laboratory of Wave Methods for Studying Structurally Inhomogeneous Media, Institute of Applied Physics of the Russian Academy of Sciences, 603950 Nizhny Novgorod, Russia; alex.sovetsky@mail.ru (A.A.S.); lionnn52rus@mail.ru (L.A.M.); vyuzai@ipfran.ru (V.Y.Z.)
* Correspondence: kgybarkova@mail.ru

Received: 1 October 2020; Accepted: 19 November 2020; Published: 24 November 2020

Abstract: The possibility to assess molecular-biological and morphological features of particular breast cancer types can improve the precision of resection margin detection and enable accurate determining of the tumor aggressiveness, which is important for treatment selection. To enable reliable differentiation of breast-cancer subtypes and evaluation of resection margin, without performing conventional histological procedures, here we apply cross-polarization optical coherence tomography (CP-OCT) and compare it with a novel variant of compressional optical coherence elastography (C-OCE) in terms of the diagnostic accuracy (Ac) with histological verification. The study used 70 excised breast cancer specimens with different morphological structure and molecular status (Luminal A, Luminal B, Her2/Neo+, non-luminal and triple-negative cancer). Our first aim was to formulate convenient criteria of visual assessment of CP-OCT and C-OCE images intended (i) to differentiate tumorous and non-tumorous tissues and (ii) to enable more precise differentiation among different malignant states. We identified such criteria based on the presence of heterogeneities and characteristics of signal attenuation in CP-OCT images, as well as the presence of inclusions/mosaic structures combined with visually feasible assessment of several stiffness grades in C-OCE images. Secondly, we performed a blinded reader study of the Ac of C-OCE versus CP-OCT, for delineation of tumorous versus non-tumorous tissues followed by identification of breast cancer subtypes. For tumor detection, C-OCE showed higher specificity than CP-OCT (97.5% versus 93.3%) and higher Ac (96.0 versus 92.4%). For the first time, the Ac of C-OCE and CP-OCT were evaluated for differentiation between non-invasive and invasive breast cancer (90.4% and 82.5%, respectively). Furthermore, for invasive cancers, the difference between invasive but low-aggressive and highly-aggressive subtypes can be detected. For differentiation between non-tumorous tissue and low-aggressive breast-cancer subtypes, Ac was 95.7% for C-OCE and 88.1% for CP-OCT. For differentiation between non-tumorous tissue and highly-aggressive breast cancers, Ac was found to be 98.3% for C-OCE and

97.2% for CP-OCT. In all cases C-OCE showed better diagnostic parameters independently of the tumor type. These findings confirm the high potential of OCT-based examinations for rapid and accurate diagnostics during breast conservation surgery.

Keywords: breast cancer; cross-polarization optical coherence tomography (CP-OCT); compressional optical coherence elastography (C-OCE); image assessment

1. Introduction

Intraoperative detection of breast malignancy margins would allow minimization of the risk of tumor recurrence in patients undergoing breast conservation surgery (BCS). Intraoperative pathological estimation can be performed through frozen section analysis and imprint cytology [1]; however, these techniques are characterized by several restrictions such as resource intensity, sampling only a small percentage of the surgical margins and limited efficacy, especially for ductal carcinoma in situ (DCIS) [2]. Consequently, these methods have not been widely adopted [3]. Fluorescent techniques that utilize molecular contrast, potentially affording surgeons to visualize tumor in the cavity, are currently in the development [4,5]. Ultrasound elastography has been developed for a number of applications, and specifically for preoperative diagnosis of breast lesions [6–8]. However, its relatively low spatial resolution makes it inappropriate to use this method for intraoperative tumor margin assessment.

Optical coherence tomography (OCT) presents a very promising method for surgical tasks solving due to the clear benefits of this method such as: safety (using a near infrared light source does not risk tissue damage); accuracy (high resolution ~10–15 micron); there being no need for contrast agents; and the short duration of image attainment. OCT can be used both in the resected specimen of tumor and in the surgical cavity. OCT can be added to biopsy needle probes and can be used to guide correct sampling of tumor biopsies [9–11]. OCT is a promising method for intraoperative guidance during the resection of breast cancer and for identifying positive margins in specimens from BCS [12–15]. Recently, OCT has been proposed for intraoperative use in distinguishing tumorous and non-tumorous tissues using handheld probes [16,17]. To overcome the limited imaging depth ~2 mm typical for OCT (which usually requires sufficiently close approaching of the OCT probe towards the studied tissue), utilization of endoscopic and/or needle OCT probes are considered [11]. Moreover, it is known that structural OCT scans exhibit low contrast between tumor and uninvolved dense stromal tissue, which makes it challenging to accurately assess margin status [18]. In view of this, improvements in several aspects of OCT attract much attention, in particular, the development of functional OCT extensions based on polarization effects and stiffness analysis as considered below.

Based on the birefringence of the tissue structure, polarization-sensitive (PS) OCT provides advanced imaging of collagen fibers in the breast tissue and enhances intraoperative differentiation of breast cancer [19–21]. Stroma state assessment is fundamentally important, because tumor collagen matrix plays a crucial role in breast cancer invasion and metastatic spreading [22]. Several studies have developed quantitative diagnosis algorithms for intraoperative assessing breast cancer margins and validated them against OCT, both alone and in combination with other modalities [23]. Cross-polarization OCT (CP-OCT) is a variant of PS OCT that allows imaging of the initial polarization state changes due to both birefringence and cross-scattering in biological tissues [24]. Only orthogonally polarized backscattered light, which is mutually coherent with the incident wave, contributes to the cross-polarized (CP) OCT image. CP-OCT is a promising method for differentiating tumorous from non-tumorous tissues in human breast tissues [25], human brain tissues [26,27], as well as for diagnosis of bladder cancer [28–31]. OCT can also measure attenuation, which can be helpful for improving contrast of breast imaging research [32,33].

Attention to the problem of determining tissue stiffness (elastographic mapping) by optical coherence elastography (OCE) methods has been increasing in recent years [34–37]. Sufficiently high

resolution of quantitative stiffness maps enabled by compressional OCE opened the possibility to perform morphological segmentations of tumor tissue constituents very similar to morphological segmentation of conventional histological images [25,38,39]. In these studies of experimental tumor models on animals, this technique allowed in vivo monitoring of morphological variation in tumor tissue during tumor growth and response to therapies. In studies [25,40–42], application of compressional OCE (C-OCE) for characterization of mechanical properties of excised human breast cancer specimens was demonstrated. New possibilities for intraoperative assessment of the breast cancer borders by means of optical coherence micro-elastography (OCME) were reported in a recent study [43,44]. It has been demonstrated that OCME provides additional contrast of tumor compared to OCT alone. Additionally, the potential of OCME images for evaluation of tumor margins in specimens excised during BCS was demonstrated in [41,43]. In our previous paper it was shown that CP-OCT and C-OCE can be helpful in breast cancer margin identification, as well as for grading breast cancer subtypes [25].

For more accurate evaluation of the resection margin, it is advantageous to take into account the genetic heterogeneity of breast cancer, as well as the variety of molecular-biological and morphological features influencing prognosis of the disease course (degree of aggressiveness) and treatment selection [45,46]. Indeed, it was demonstrated that probability of tumor recurrence mainly depends on molecular-biological characteristic of the tumor [47,48], while an increase in the size of the removed tissue, free of cancer cells, is not associated with a decrease in the recurrence rate [49].

Various molecular-biological and morphological features of breast cancer are anticipated to differently influence the polarizing and elastic tumor and peritumoral tissue qualities. This stimulates interest in evaluation of the clinical potential of polarization-sensitive and elastographic OCT techniques for determining breast cancer subtypes (malignancy grade) and improving tumor boundary detection based on the ability of these methods to identify different tumor subtypes. In this way, surgeons are expected to be provided with essential information that can improve reliability of the positive resection margin detection during BCS, at least for some breast cancer subtypes.

The goals of this research are (1) to define the visual assessment criteria required for the CP-OCT and C-OCE images in order to enable differentiation among various breast cancer subtypes; (2) to determine the diagnostic accuracy (sensitivity and specificity) of C-OCE in comparison with CP-OCT, for delineation of tumorous and non-tumorous breast tissues and subsequent identification of breast cancer subtypes in a blinded reader study.

2. Materials and Methods

2.1. Human Breast Specimens

This study was approved by the institutional review board of the Privolzhsky Research Medical University (Protocol #10 from 28 September 2018). All of the patients included in the study provided written informed consent. A total of 70 breast tumor tissue specimens were taken from 50 patients post partial (n = 35) or complete (n = 15) mastectomy with different diagnosis (Table 1). To minimize the effect tissue degrading, the excised specimens were immediately placed in gauze saturated with phosphate buffer and closed to prevent dehydration. CP-OCT and C-OCE images of the fresh, un-fixed breast tissue were acquired within 2 h after surgical excision. The studies were done on specimens with sizes from 0.5 × 1 cm to 1 × 2 cm. Specimens were taken from central zone of tumors for diagnostics of breast cancer subtypes and in the peritumoral area for visualization of normal (non-tumorous) breast tissue. A special motorized table for convenient positioning the specimen under the OCT probe was used. The entire CP-OCT and C-OCE study of each specimen was no longer than 20 min (including preliminary sample preparation and orientation).

Table 1. Clinical specimens' characteristics and number of imaged specimens.

Diagnosis	Number of Specimens	Age of Patients (Range)	Tumor Size
Benign breast conditions			
Non-tumorous breast tissue	20	43–68	-
Fibroadenoma/fibroadenomatosis	4	35–48	≤1 cm
Malignant breast lesions			
Ductal carcinoma in situ (DCIS)	5	44–63	≤1 cm
Invasive ductal carcinoma (IDC) of scirrhous structure	24	41–82	≤2 cm
Invasive ductal carcinoma (IDC) of solid structure	10	41–82	≤2 cm
Invasive lobular carcinoma (ILC) of solid structure	7	48–72	≤2 cm

2.2. Multimodal OCT Device

This study used a common path spectral domain multimodal OCT system with a central wavelength of 1310 nm and spectral width of 100 nm, with an axial resolution of 10 μm, lateral resolution is 15 μm, a scanning depth of 2 mm in air, a scanning speed of 20,000 A-scans per second. The OCT-system acquired 3D blocks of OCT data, 2 mm in depth (in air) over 2.4 × 2.4 mm^2 area and 2D lateral scanning with a similar field of view were acquired in 26 s. The CP-OCT and C-OCE images were generated in real time during the acquisition process. For living tissues, real-time angiographic imaging was also possible by processing the same data [50]. For the described OCT studies, the total scanning time along a 1–2 cm trajectory on a biopsy sample was 3–5 min depending on the number of stitched images.

Structural 2D (cross-sectional images) CP-OCT images were constructed in two virtual channels, one of which was co-polarized with the incident polarization (co-polarization channel) and the other one was orthogonal (cross-polarization channel) to the incident polarization, respectively [24]. CP-OCT aims to obtain the information contained in the cross-polarization channel, which allows one to form cross-polarization images caused by birefringence of the tissue from optically anisotropic structures (evaluate the state of connective tissue component), as well as due to contribution of coherent cross-polarization backscattering on non-spherical particles and particles with dimensions much larger than the wavelength. In view of low informativity of the co-polarization images (as found in previous studies [25]), only cross-polarization images were used for diagnostic conclusions in this study.

An advanced variant of phase-sensitive compression OCE [37,39,51–55] was used to visualize inter-frame strains in the tissue and subsequently map the Young modulus. The probe was slightly pressed onto the studied sample surface, and strain distribution in the probe vicinity was reconstructed. Strain mapping was based on estimation of axial gradients of interframe phase variations of the OCT signal using the "vector" method [51,53]. The name "vector" is due to the fact that, without explicitly singling out amplitude and phase, the complex-valued OCT signals in this method are considered as vectors in the complex plane, and the phase is singled out at the very last step of the processing. Such vector representation allows one to perform flexibly-tuned amplitude-weighted averaging over the processing-window area. As a result, noisy contributions of small-amplitude pixels and, at the same time, especially strong phase errors (by ~π rad.) are very efficiently suppressed. This allows obtaining strain maps with fairly high quality even without periodic averaging (which is very important for the one-directional single-step loading of the tissue used in the described studies). In addition to the exceptionally high tolerance to various measurement noises, the vector method is very efficient computationally, so that the elastographic processing of the acquired sequence of several hundreds of OCT scans requires ~5–10 s using a "typical" PC without the necessity of GPU computations.

Another important point is that the estimated interframe phase-variation gradient is averaged over a processing window, the dimensions of which being the main factor determining the resolution of the resultant OCE scans. For a rectangular processing window with comparable axial and lateral

sizes, the resolution in strain maps is also comparable in these directions and corresponds to ~$\frac{1}{2}$ of the window size. For the described system, the window size was ~90–100 μm, which defined the strain-mapping resolution ~45–50 μm. Such a window size was chosen empirically as a compromise between worse quality of the OCE-images for smaller windows (because of insufficiently averaged noise) and too-strong smoothing of spatial inhomogeneities for larger windows.

The next important point is quantification of the tissue Young's modulus, to enable which a reference silicone layer with preliminary calibrated stiffness (with the Young's modulus in the range 50–100 kPa) was used as described in [42,54–56]. Of key importance in the used variant of C-OCE technique is that all OCE images are formed using a pre-selected pressure level (4 kPa in the described study) standardized over the entire image area, despite the fact that for real OCE scans, the local pressure over the lateral coordinate usually varies several times because of the non-ideally planar boundary of the sample, its mechanical inhomogeneity, etc. The pressure standardization technique is based on the usage of the reference silicone layer as a sensor of local pressure as described in detail in [55]. To synthesize such a single "standardized OCE image", a series of initial structural OCT-scans acquired during monotonic compression of the sample was first processed to obtain a series of cumulative-strain maps as described in [54,57,58]. Then vertical A-scans corresponding to the selected pressure were picked up from the initial series of cumulative-strain maps and reassembled to synthesize a single cumulative-strain image in which all A-scans now correspond to the same preselected pressure onto the tissue [55]. To be sure that the strain in silicone can be considered linearly proportional to stress (pressure), high linearity of silicone was specially verified as described in [42,54,55]. Real biological tissues usually demonstrate a pronouncedly nonlinear stress–strain law. The described C-OCE method allows one to determine this law by plotting the strain in the linear precalibrated silicone against strain in any region of interest in the tissue beneath the silicone. The elasticity of the tissue can then be estimated as the tangent Young's modulus (the slope of the stress-strain curve) corresponding to the desired pre-selected pressure. It was empirically found that for breast-cancer tissue the sought tangent modulus could be conveniently estimated as the slope of the chorde corresponding to the pressure range 4 ± 1 kPa. At lower pressures, very small strain of stiffer regions was difficult to estimate, whereas at higher pressures, the elasticity contrast among various tumor components became worse because of strong nonlinearity-induced stiffening of the initially softer components of the tumor (see examples in [55]). Without such standardization the intrinsic elastic nonlinearity of breast-cancer tissues may result in uncontrollable variability of the estimated elastic modulus in different measurements and even different parts of the same image. This unpredictable variability may be rather significant (several times and greater) even for apparently moderate strains within a few percent [42,55]. Thus, the developed pressure-standardization procedures were critically important for enabling meaningful quantitative comparisons of elastographic data obtained from different measurements.

The so-obtained OCE-images were represented in the color-coded form, such that stiffer areas (those with weaker strain) are shown in blue, and soft areas, where deformation is greater, are shown in red.

2.3. Histological Study

After CP-OCT and C-OCE imaging of the freshly-excised sample with yet non-modified optical and biomechanical properties, the scanned area was marked on the specimen with histological ink. Then the specimen was fixed in 10% formalin for 48 h and resectioned through the marked area, so that the plane of the histological sections coincided to the cross-sectional CP-OCT and C-OCE images. For the histological evaluation, haematoxylin and eosin (H&E) staining was used. Two independent histopathologists interpreted the histological slices photographed in transmitted light with a Leica DM2500 DFC (Leica Microsystems, Wetzlar, Germany) microscope, equipped with a digital camera. Based on histopathological analysis, all samples were classified into tumorous and non-tumorous breast tissues. The revealed histological types of breast tissue include: adipose tissue with streaks of

connective tissue (number of specimens $n = 20$); fibroadenomatosis/fibroadenoma ($n = 4$); DCIS ($n = 5$); invasive lobular carcinoma (ILC) ($n = 7$); invasive ductal carcinoma (IDC) of scirrhous ($n = 24$) and solid ($n = 10$) structure (Table 1). In addition, to assess tumor aggressiveness (prognosis of the disease course) immunohistochemistry (for $n = 46$ samples) was performed, identifying five molecular subtypes of the tumors: Luminal A, Luminal B (Her2/Neo-), Her2/Neo+, Non-luminal, Triple-negative cancer (TNC). Luminal A and Luminal B (Her2/Neo-) are reported to be low-aggressive tumors characterized by predominantly favorable prognosis of disease course and treatment in comparison with Her2/Neo+, Non-luminal and TNC [24]. Furthermore, it should be noted that Luminal A and Luminal B subtypes were characterized by scirrhous architectonics, while Her2/Neo+, Non-luminal, TNC had solid structure.

The results of histopathology were compared with the corresponding CP-OCT-based and C-OCE-based findings. For the blinded reader study, all images were divided into 4 groups: adipose and normal stromal breast tissue, benign breast tissue (fibroadenoma/fibroadenomatosis), non-invasive DCIS, and images portraying cancerous features of invasive low and highly-aggressive breast cancer.

2.4. Reader Analysis of CP-OCT and C-OCE Images

A blinded reader study was performed to evaluate the statistical performance of assessing tumorous and non-tumorous breast tissues based on the CP-OCT imaging (first test) and C-OCE visualization (second test). In the study, 115 CP-OCT and 115 C-OCE images from 50 patients were interpreted by 6 readers specially trained for this OCT-based assessment (2 biologists experienced in optical imaging, but unskilled in recognizing breast cancer pathology; 2 post-graduate students of the Medical University unexperienced both in optical imaging and in recognizing breast cancer pathology; 2 surgeons skilled in detecting breast cancer pathology, but without work experience in optical imaging) who were unaware whether the image contained cancer or not. The readers were given a training set of sample CP-OCT and C-OCE images (3 images of each histological type of breast tissue).

The criteria evaluated by the readers are summarized in Tables 2 and 3. Each image group had its own set of visual criteria. The reader's goal was to distinguish between tumorous and non-tumorous breast tissues. If an image was considered to represent non-tumorous breast tissue, the reader indicated a score of "0" whether it was normal breast tissue or fibroadenoma. If the reader identified malignant lesion marks, a score from "1" to "3" was assigned to the sample depending on the estimated tumor aggressiveness. The score of "1" means that the reader thinks that the image represents non-invasive DCIS; a score of "2" means that the reader considers the cancer to be invasive, but less aggressive; a score of "3" means that the reader thinks that invasive cancer is more aggressive.

The first test was based on assessment of signal architecture in cross- polarization images (Table 2). The cross-polarization channel enables more contrast visualization of the presence and state of connective tissue in comparison with the co-polarization OCT images.

Structural features in the CP-OCT images were distinguished by the following features of the scattering intensity and lateral uniformity of the signal attenuation (Table 2):

(i) the average level of the CP-OCT signal throughout the image is visually estimated as "low" like in Figure 1(b5) or "high" for the used 0–50 dB signal range, where "low" corresponded to intensities below 25 dB, i.e., the noise range in the used scale, and "high" related to the level above 25 dB on the used scale like in Figure 1(b2);

(ii) the presence of structures with a sharp boundary between contrasting-in-brightness regions with well-circumscribed boundary architecture like in Figure 1(b3) (which was graded as "yes"/"no");

(iii) the attenuation rate as estimated by the penetration depth of the probing radiation ("high" attenuation like in Figure 1(b5) and "low" like in Figure 1(b2));

(iv) the uniformity of attenuation along the interior border of the structural CP-OCT image ("uniform" like in Figure 1(b2)/"non-uniform" like in Figure 1(b4)).

Table 2. Visual assessment criteria of cross-polarization optical coherence tomography (CP-OCT) images for distinguishing between non-tumorous and tumorous breast tissue.

	Normal (Non-Tumorous) Breast Tissue (*n* = 20)	**Fibroadenoma/ Fibroadenomatosis (*n* = 13)**	**DCIS (*n* = 10)**	**Low-Aggressive Invasive Breast Cancer (*n* = 47)**	**Highly-Aggressive Invasive Breast Cancer (*n* = 25)**
Main criterion:					
Typical architecture	honeycomb structure, areas of high intensity signal	predominance of areas with high signal intensity	alternating signal of high, medium and low intensity; the presence of structures with no signal with clear boundaries (ducts)	alternating signal of medium and low intensity	homogenous low intensity signal
Additional criteria:					
Signal penetration depth	high	high	high	high	low
Structures with clear (contrasting) boundaries	no	no	yes	no	no
Uniformity of the OCT signal attenuation along the inferior border of the image	uniform	uniform	highly uneven	non-uniform	uniform
Final score	0	0	1	2	3

n—number of images.

Table 3. Visual assessment criteria of compressional optical coherence elastography (C-OCE) images for distinguishing between non-tumorous and tumorous breast tissue.

	Normal (Non-Tumorous) Breast Tissue (*n* = 20)	**Fibroadenoma/ Fibroadenomatosis (*n* = 13)**	**DCIS (*n* = 10)**	**Low-Aggressive Invasive Breast Cancer (*n* = 47)**	**Highly-Aggressive Invasive Breast Cancer (*n* = 25)**
Main criterion:					
Typical stiffness pattern	uniform low stiffness level over the C-OCE image		low stiffness level of the stiffness throughout the image with high-contrast zones with strongly increased stiffness	non-uniform high stiffness level over the C-OCE image	
Additional criteria:					
Predominance of uniform distribution of high stiffness values (>500 kPa)	no	no	no	no	yes
Presence of multiple moderately contrast inclusions of high stiffness (Mosaic structure)	no	no	no	yes	no
Final score	0	0	1	2	3

n—number of images.

The second test was based on the analysis of stiffness values distributions on C-OCE images. Stiffness maps are presented in a color palette, where hard areas (blue—above 500 kPa) indicate the presence of tumor cells, and soft regions (red—below 100 kPa) represent adipose and connective tissues. At the same time, tissues with intermediate stiffness (the predominance of orange and yellow colors corresponding to ~200–400 kPa) correspond to the presence of such degenerative changes of breast-tissue stroma as fibrosis or hyalinosis of collagen fibers. The threshold values for stiffness (Table 3) of the main types of breast-tissue components were identified as described in detail in our previous work [25], in which accurate comparison of histological and OCE images was performed.

Main and additional criteria of subsuming the images to one or another group were formulated for cross-polarization and C-OCE images, the additional criteria of visual assessment being needed for more precise differentiation among different malignant states (Tables 2 and 3).

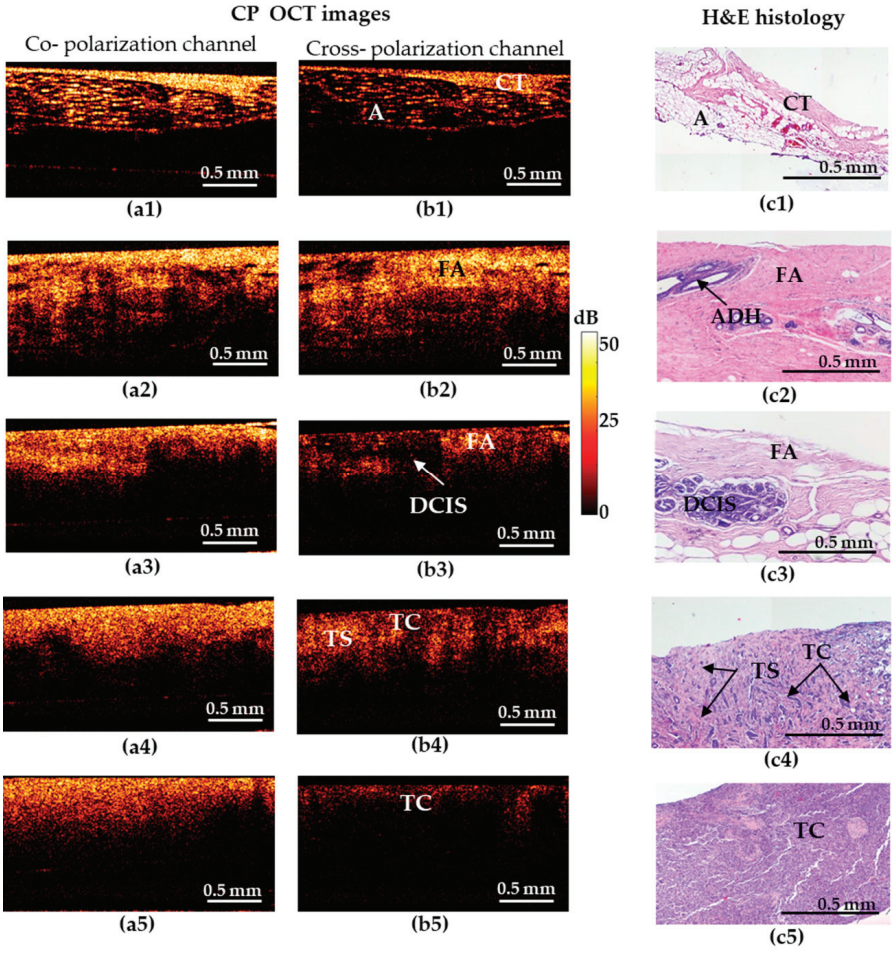

Figure 1. Representative depth-wise co- and cross-polarization OCT images (**a**,**b**) of non-tumorous and tumorous breast tissue with the corresponding histology (**c**). (**a1**–**c1**) Adipose tissue with streaks of connective tissue; (**a2**–**c2**) fibroadenomatosis/fibroadenoma; (**a3**–**c3**) DCIS; (**a4**–**c4**) invasive ductal carcinoma (IDC) of scirrhous structure (low-aggressive breast cancer subtype); (**a5**–**c5**) IDC of solid structure (highly-aggressive breast cancer subtype). (**a1**–**a5**) OCT images in co-polarization channel; (**b1**–**b5**) OCT images in cross-polarization channel; (**c1**–**c5**) histological images, haematoxylin and eosin (H&E) staining. Abbreviations: A—adipose, CT—connective tissue, FA—fibroadenomatosis, ADH—atypical ductal hyperplasia, DCIS—ductal carcinoma in situ, TS—tumor stroma, TC—cluster of tumor cells.

2.5. Statistical Analysis

The results of the blinded reader study of CP-OCT and C-OCE images analysis were collected for determining the diagnostic accuracy for distinguishing: (1) non-tumorous breast tissues (n = 33) from tumor (n = 82); (2) non-invasive DCIS (n = 10)) from invasive breast cancer (n = 72); (3) low-aggressive invasive tumors (Luminal A, Luminal B (Her2/Neo-)) (n = 47) with favorable prognosis from highly aggressive invasive tumors (Her2/Neo+, Non-luminal, TNC) (n = 25) with unfavorable prognosis;

(4) non-tumorous breast tissues (n = 33) from low-aggressive invasive tumors (n = 47), and (5) non-tumorous breast tissues (n = 33) from highly-aggressive invasive tumors (n = 25).

The statistical analysis was performed using Statistica 10.0 and IBM SPSS Statistics software.

The assessment of the informative value and diagnostic capabilities of the studied methods (CP-OCT and C-OCE) was carried out with an estimation of their sensitivity (Se), specificity (Sp), and diagnostic accuracy (Ac). Based on the sensitivity and specificity values, Receiver operating characteristic (ROC) curves were constructed, which show the dependence of the number of true positive rate (TP) on the number of false positive rate (FN). For quantitative characterization of the ROC curves, we evaluated the area under the ROC curve (AUC), i.e., the area bounded by the ROC curve and the axis of the false positive rate [59]. The higher the AUC, the better the classifier is.

The inter-reader agreement was calculated using Cohen's kappa coefficient (k): $k \geq 0.81$—perfect agreement; $0.61 \leq k < 0.80$—substantial agreement; $k < 0.6$—poor agreement [60].

3. Results

3.1. Visual Assessment of the CP-OCT and C-OCE Images for Distinguishing between Non-Tumorous and Tumorous Breast Tissue

The results based on the CP-OCT and C-OCE images for representative cases of the non-tumorous and tumorous breast tissue and differentiation among highly-aggressive breast-cancer subtypes are shown in Figures 1 and 2.

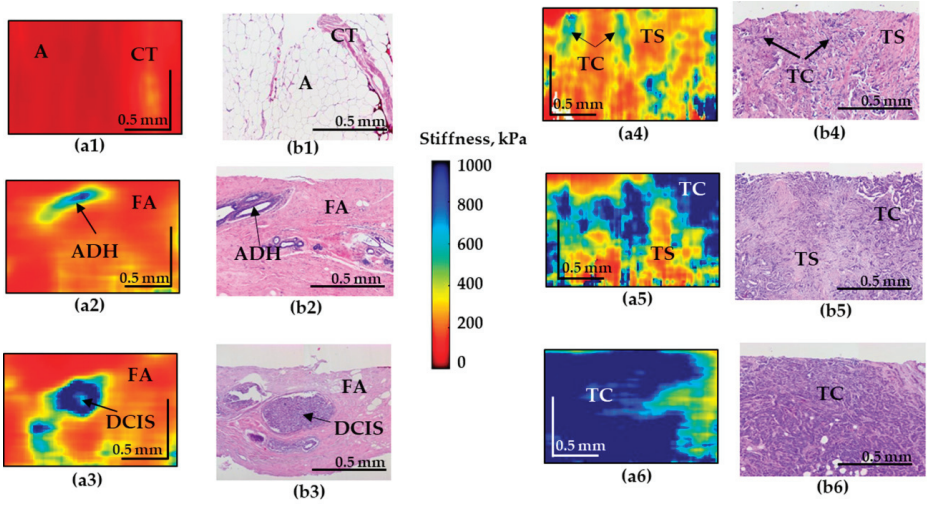

Figure 2. Representative depth-wise C-OCE images (**a1**–**a6**) of non-tumorous and tumorous breast tissue with corresponding histological images (**b1**–**b6**). (**a1**–**b1**) Adipose tissue with streaks of connective tissue; (**a2**–**b2**) fibroadenomatosis/fibroadenoma; (**a3**–**b3**) DCIS; (**a4**,**a5**–**b4**,**b5**) IDC of scirrhous structure (low-aggressive breast cancer subtypes); (**a6**–**b6**) IDC of solid structure (highly-aggressive breast cancer subtype). Abbreviations: A—adipose, CT—connective tissue, ADH—atypical ductal hyperplasia, FA—fibroadenomatosis, DCIS—ductal carcinoma in situ, TS—tumor stroma, TC—cluster of tumor cells.

Figure 1 shows five types of representative CP-OCT and histological images: "adipose tissue with streaks of connective tissue" (a1–c1)/"fibroadenomatosis/fibroadenoma" (a2–c2)/"DCIS" (a3–c3)/invasive low-aggressive breast cancer of scirrhous structure (a4–c4)/invasive highly-aggressive breast cancer of solid structure (a5–c5).

Benign breast tissue states are characterized by high signal-penetration depth and uniformity of the signal attenuation along the inferior border in co- and cross-polarized structural OCT images (Figure 1). The hallmark of normal adipose (fatty) tissue is a "honeycomb" structure with low sparse scattering, while fibrous structures are characterized by high uniform scattering in co- and cross-polarized structural OCT images (Figure 1(a1–c1)). Fibroadenoma is characterized by a predominance of high-intensity OCT signal in co- and cross-polarization channels (Figure 1(a2–c2)) in comparison with normal breast tissue that has a dense structure due to the presence of large fibrous collagen fibers (Figure 1(c2)).

Cases suspicious for malignancy are characterized by general reduction in signal intensity and its penetration depth, irregular inferior border. All these features cause heterogeneity of the image. In particular, DCIS (Figure 1(c3)) is characterized by the presence of localized structures with low signal intensity and clear boundaries in the surrounding fibrous stroma with a high signal intensity in the cross-polarization channel (Figure 1(b3)). In co-polarization channels DCIS is not detectable (Figure 1(a3)).

In case of invasive breast cancer, the OCT signal in the cross-polarization channel for highly-aggressive (Figure 1(b5)) and less-aggressive (Figure 1(b4)) cancer subtypes is greatly different. IDC of solid structure (highly-aggressive) demonstrates a uniform low-level OCT signal, which is associated with an increased density of tumor cells and an almost total absence of anisotropic (fibrous) structures in this tumor subtype (Figure 1(b5)). For IDC of scirrhous structure (less-aggressive subtype), the heterogeneity of the OCT signal was observed: an alternating signal of medium and low intensity was revealed (Figure 1(b4)). On the corresponding histological images, there were clusters of tumor cells surrounded by connective tissue in a state of fibrosis and hyalinosis (Figure 1(c4)), which clearly leads to an increase in the level of OCT signal in these areas. It should be noted that in these cases, there is no pronounced contrast between low-aggressive (Figure 1(a4)) and highly-aggressive (Figure 1(a5)) breast cancer subtypes in the co-polarization channel.

Thus, in the structural OCT images, the most informative is the cross- polarization channel showing both regions with fairly high cross-polarization backscattering and (corresponding to the presence of connective tissue) and regions with a reduced cross-polarization signal (corresponding to the clusters of tumor cells), see Figure 1(b1–b5)). Therefore, in view of low informativity of the co-polarization images, only cross- polarization images were used for diagnostic accuracy analysis in this study.

The C-OCE image of the normal mammary gland (normal connective tissue and adipose tissue) is characterized by the lowest stiffness (Figure 2(a1)). However, fibroadenomatosis/fibroadenoma is characterized by a slight overall increase in stiffness (Figure 2(a2)) and the presence of well-localized areas with an increased elastic modulus in the regions of atypical ductal hyperplasia (ADH).

C-OCE images of malignancy demonstrate the appearance of regions with pronouncedly increased stiffness. Moreover, for IDC of solid structure (highly-aggressive), these areas occupy up to 90% of the entire image, which sharply distinguishes this breast cancer subtype (Figure 2(a6)). The ducts filled with tumor cells for DCIS are visualized as high-contrast zones with strongly increased stiffness (Figure 2(a3)) which coincide well with the histological image. The surrounding fibrous tissue is characterized by fairly low stiffness values (Figure 2(a3)). The OCE images of IDC of scirrhous structure demonstrate an increased stiffness in the regions of the clusters of tumor cells and significantly lower stiffness in the regions of the tumor stroma, causing multiple moderately contrast inclusions with elevated stiffness, which represents a feature of low-aggressive tumor subtype (Figure 2(a4–a5)).

In addition, it is necessary to mention that images of IDC of scirrhous structure and fibroadenoma may have similar patterns that may be challenging to differentiate for the reader. To solve this problem an additional criteria (Table 3) of "presence the numerous and less contrasting inclusions of increased stiffness" was included in cases of IDC (Figure 2(a4)) in contrast to single inclusions in cases of fibroadenoma (Figure 2(a2)) and DCIS (Figure 2(a3)).

3.2. Diagnostic Accuracy of CP-OCT and C-OCE Based on Visual Assessment of Images

The results of the two tests, using the identified main and additional criteria, separately in CP-OCT images and C-OCE images demonstrate their great agreement among the readers. The concordance coefficient in the determination of tumorous or non-tumorous breast tissue in the analysis of CP-OCT images between two researchers was k = 0.68, between two post-graduate students k = 0.93, between the two surgeons k = 0.80. The concordance coefficient in the detection of tissue type in the analysis of C-OCE images between two researchers was k = 0.86, between two post-graduate students k = 0.93, between the two surgeons k = 0.82.

To demonstrate the variability of the test results, ROC-curves were presented for each reader (Figures 3 and 4). ROC-curves analysis confirmed that visual assessment of CP-OCT and C-OCE images has a high diagnostic value for differentiating non-tumorous and tumorous breast tissue (AUC values for all readers were 0.90–0.97 and 0.93–0.99, respectively) and also for distinguishing between low- and highly-aggressive invasive breast-cancer subtypes (AUC values for all readers were 0.84–0.90 and 0.80–1.00, respectively) (Figure 3c, Figure 4c). Slightly lower values were obtained for differentiation between non-invasive breast lession and invasive breast cancer (AUC values for all readers were 0.74–0.93 and 0.86–0.95, respectively) (Figure 3b, Figure 4b). The ROC-curves show that the best results were demonstrated by the researches experienced in optical imaging.

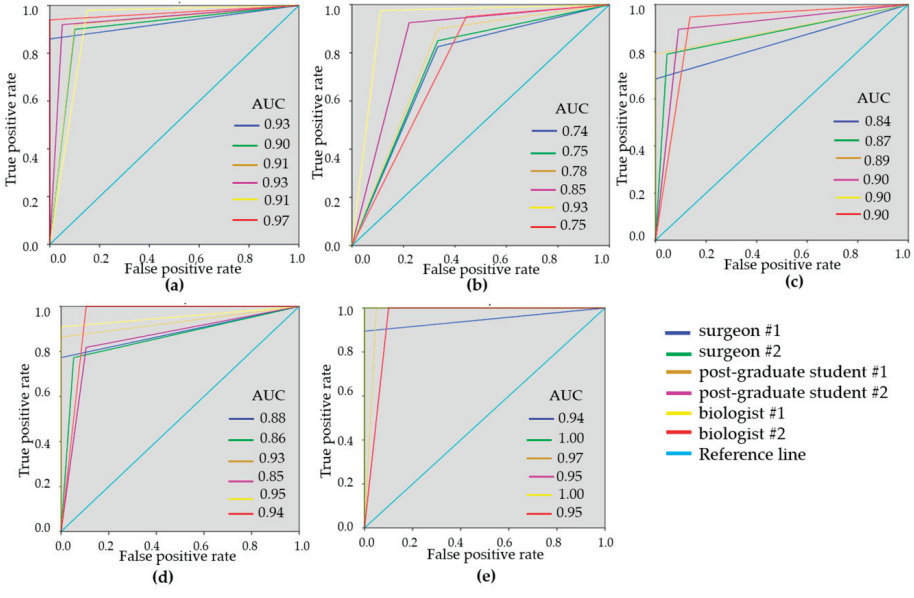

Figure 3. Receiver operating characteristic (ROC)-curves showing the results of visual assessment CP-OCT images for distinguishing non-tumorous breast tissue from tumor (**a**), DCIS from invasive breast cancer (**b**), low-aggressive invasive breast cancer from highly aggressive (**c**), non-tumorous breast tissue from low-aggressive breast cancer (**d**), non-tumorous breast tissue from highly aggressive breast cancer (**e**) for six "blinded" readers.

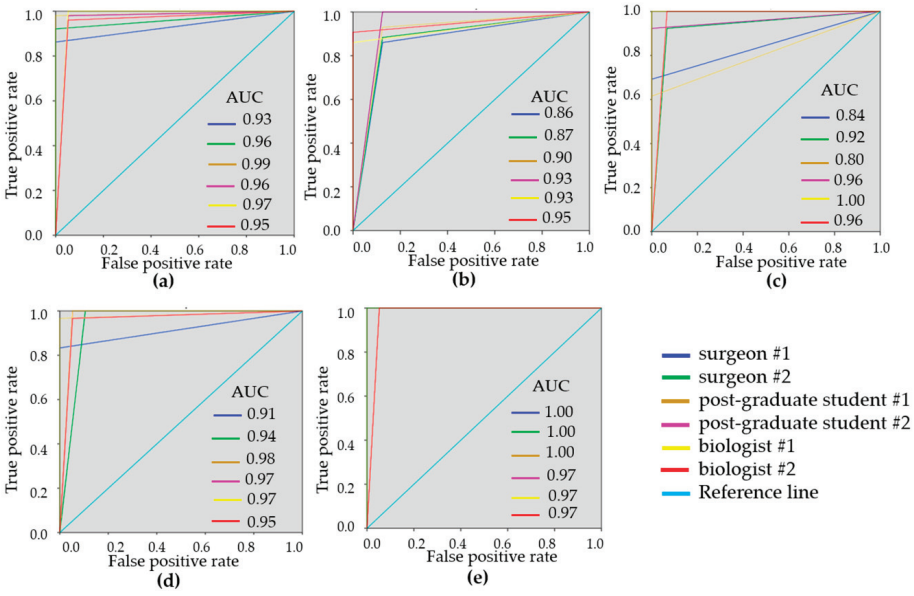

Figure 4. ROC-curves showing the results of visual assessment of C-OCE images for distinguishing non-tumorous from tumorous breast tissue (**a**), DCIS from invasive breast cancer (**b**), low-aggressive invasive breast cancer from highly-aggressive (**c**), non-tumorous breast tissue from low-aggressive breast cancer (**d**), non-tumorous breast tissue from highly-aggressive breast cancer (**e**) for six "blinded" readers.

The results of the blinded reader analysis are summarized in Table 4, showing the sensitivity, specificity and diagnostic accuracy. Each diagnostic index was averaged among all six readers. High diagnostic values were obtained for the differential diagnosis of all analyzed groups. The diagnostic accuracy of distinguishing non-tumorous tissue from tumor was 92.4 ± 2.3% for CP-OCT and 96.0 ± 3.3% for OCE, which determines the OCE method as more specific for detecting tumorous tissue.

For the first time, the diagnostic efficiency of CP-OCT and C-OCE methods for the differential diagnosis of non-invasive from invasive breast cancer was established (Se = 90.1 ± 5.7%, Sp = 70.6 ± 11.3%, Ac = 82.5 ± 7.1% and Se = 90.5 ± 5.3%, Sp = 92.0 ± 6.1%, Ac = 90.4 ± 2.7%, respectively). Furthermore, we demonstrated the possibility to differentiate invasive low-aggressive breast cancer subtypez with a favorable prognosis from highly-aggressive breast cancer subtypes with a poor prognosis for treatment and the course of the disease (Se-83.5 ± 10.5%, Sp-93.5 ± 6.0%, Ac-87.8 ± 6.5% and Se-87.3 ± 13.8 ± 6.5%, Sp-98.0 ± 3.1%, Ac-89.5 ± 10.0%, respectively). In both cases, it was demonstrated that C-OCE showed the best diagnostic indicators (Table 4).

Additionally, we performed a diagnostic analysis of the possibility to distinguish non-tumorous breast tissue from low- and highly-aggressive breast cancer subtypes. It has been shown that the diagnostic accuracy of the difference between non-tumorous breast tissue and a low-aggressive subtype of cancer is 88.1 ± 6.0% for CP-OCT and 95.7 ± 4.1% for C-OCE. The diagnostic accuracy of the difference between non-tumorous breast tissue and highly-aggressive cancer is 97.2 ± 2.8% for CP-OCT and for C-OCE—98.3 ± 2.2%.

Thus, we demonstrated the possibility to use CP-OCT and C-OCE methods for detecting different breast cancer subtypes on the resection margin which would minimize the risk of recurrence and reoperations.

Table 4. The results of diagnostic test for visual assessment of the CP-OCT and C-OCE images.

	AUC (Range)	Sensitivity (Se), %	Specificity (Sp), %	Diagnostic Accuracy (Ac), %
CP-OCT imaging				
Non-tumorous versus tumorous breast tissue	0.90–0.97	92.0 ± 4.0	93.3 ± 6.0	92.4 ± 2.3
DCIS versus invasive breast cancer	0.74–0.93	90.1 ± 5.7	70.6 ± 11.3	82.5 ± 7.1
Low-aggressive versus highly-aggressive breast cancer	0.84–0.90	83.5 ± 10.5	93.5 ± 6.0	87.8 ± 6.5
Non-tumorous breast tissue versus low-aggressive breast cancer	0.85–0.95	85.1 ± 8.8	95.8 ± 4.9	88.1 ± 6.0
Non-tumorous breast tissue versus highly-aggressive breast cancer	0.94–1.00	98.1 ± 4.4	95.8 ± 4.9	97.2 ± 2.8
C-OCE imaging				
Non-tumorous versus tumorous breast tissue	0.93–0.99	95.0 ± 5.1	97.5 ± 2.7	96.0 ± 3.3
DCIS versus invasive breast cancer	0.86–0.95	90.5 ± 5.3	92.0 ± 6.1	90.4 ± 2.7
Low-aggressive versus highly-aggressive breast cancer	0.80–1.00	87.3 ± 13.8	98.0 ± 3.1	89.5 ± 10.0
Non-tumorous breast tissue versus low-aggressive breast cancer	0.91–0.98	95.8 ± 6.5	95.8 ± 3.7	95.7 ± 4.1
Non-tumorous breast tissue versus highly-aggressive breast cancer	0.97–1.00	98.6 ± 3.2	97.5 ± 2.7	98.3 ± 2.2

3.3. Assessment of Human Breast Cancer Margins

The tests performed in this study demonstrated that, in distinguishing the norm from low-aggressive cancers (and, moreover, highly aggressive ones), the analysis of both CP-OCT and C-OCE images the both methods enable high diagnostic accuracy. However, when searching for the transition between IDC of scirrhous structure and non-cancerous tissue, the C-OCE-based stiffness mapping (Figure 5c) visualizes the tumor margin much more clearly in comparison with the cross-polarization images (Figure 5b).

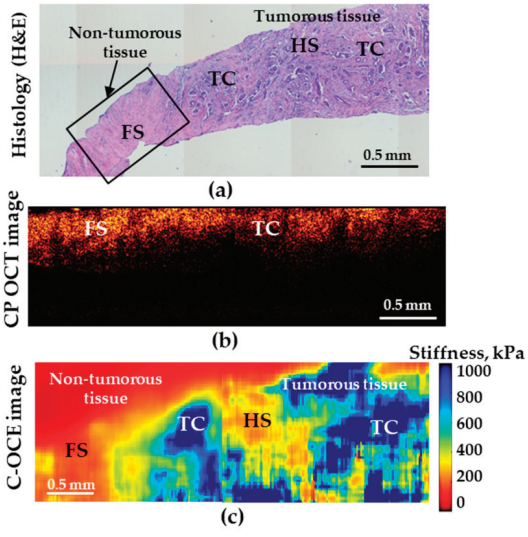

Figure 5. Histological image (**a**) demonstrating transition between non-tumorous (fibrous stroma—FS) and tumorous breast tissues (low-aggressive IDC of scirrhous structure); (**b**) is the corresponding CP-OCT image in the cross-polarization channel and (**c**) is the C-OCE images of the same area. HS denotes hyalinized stroma, and TC—clusters of tumor cells.

4. Discussion

The results presented here show the high diagnostic value and efficiency of CP-OCT and C-OCE methods for differential diagnosis of non-tumorous and tumorous breast tissue, with the further prospect of intraoperative determination of the "positive" margin of tumor resection during breast-conserving surgery in real time. In addition, the diagnostic efficiency of CP-OCT and C-OCE methods for differentiation between non-invasive and invasive breast cancers, as well as between invasive low-aggressive breast cancer subtype with a favorable prognosis (Luminal A, Luminal B (Her2/Neo-)) and highly aggressive breast cancer subtypes with a poor prognosis for course of the disease (Her2/Neo+, Non-luminal, TNC).

In previous studies, only standard visual imaging criteria, such as signal intensity and high/low stiffness, were used for differentiation between tumorous and non-tumorous breast tissues. In this study, additional analysis criteria were proposed, which made it possible to increase the diagnostic sensitivity and specificity, significantly reducing the number of erroneous diagnoses. We identified such additional analysis criteria as the presence of structures and the characteristics of signal attenuation in depth on cross-polarization images, as well as the presence of inclusions and mosaic structure on C-OCE images with visually feasible assessment of several stiffness grades.

Previous works have demonstrated that conventional, intensity-based OCT can provide differentiation between tumorous and non-tumorous breast tissues through both quantitative [18,61–63] and qualitative [32,61,63] assessment of the OCT signal. Several studies demonstrated that OCE has the high potential to delineate tumor in breast tissue based on elevated elasticity on a microscale [33,40,41,44]. A recent study [16] demonstrated the ability of structural OCT to identify positive margins in specimens from BCS. The qualitative assessment of OCT images showed the high diagnostic accuracy of structural OCT for distinguishing normal and cancerous tissue within the resection bed following wide local excision of the human breast: sensitivity of 91.7% and specificity of 92.1% [16]. Additionally, visual assessment of C-OCE images for evaluation of tumor margins in specimens excised during breast-conserving surgery also provides high sensitivity of (92.9%) and specificity (96.4%) [43].

Breast cancer is a highly heterogeneous disease, both morphologically and genetically. The surgical approach and the amount of resection depend on the subtype of breast cancer, which, as this study has shown, can be determined in rapid OCT-based tests, including the possibility of intraoperative use. The C-OCE and CP-OCT images provide additional contrast between tumor and normal tissue in comparison with structural OCT. C-OCE and CP-OCT analysis of excised tissue specimens can distinguish between normal and cancerous tissues by identifying the heterogeneous and disorganized connective tissue structures indicative for malignancy. We have demonstrated that differences in the microstructural features of cross-polarization and stiffness images enable differentiation between highly and low-aggressive breast cancer subtypes confirmed by histopathology. For this purpose, the main and additional criteria for assigning an image to a particular group were formulated, which are necessary for a more accurate differentiation of malignant conditions among themselves. For example, a uniform low-intensity in CP-OCT images and a uniform high level of stiffness in C-OCE images characterize tumor of a solid structure, while tumor tissue of a scirrhous structure in the immediate vicinity of non-tumorous breast tissue can also retain homogeneity, or it can lose it and may be represented by different levels of signal intensity and stiffness.

ROC curves were constructed as a measure of overall accuracy for each reader when non-cancerous tissue was distinguished from tumor by CP-OCT and C-OCE methods (Figure 3). In this case, C-OCE showed higher specificity (97.5 ± 2.7% vs. 93.3 ± 6.0%) and diagnostic accuracy (96.0 ± 3.3% vs. 92.4 ± 2.3%) compared to cross-polarized images. This fact may be caused by the difficulty in interpreting qualitative OCT criteria based on signal intensity by readers, in comparison with the criteria for interpreting quantitative OCE images that usually have more contrast and visually easier assessable differences. Overall, for differentiation between tumorous and non-tumorous tissues, the C-OCE method has proved to be more efficient.

Additionally, for more specific differentiation between non-invasive breast cancer and invasive breast cancer, the following diagnostic parameters were determined for CP-OCT and C-OCE methods: Se = 90.1 ± 5.7%, Sp = 70.6 ± 11.3%, Ac = 82.5 ± 7.1% and Se = 90.5 ± 5.3%, Sp = 92.0 ± 6.1%, Ac = 90.4 ± 2.7%, respectively. For distinguishing between invasive low-aggressive and highly-aggressive breast cancer subtypes, the CP-OCT and C-OCE gave the following results: Se = 83.5 ± 10.5%, Sp = 93.5 ± 6.0%, Ac = 87.8 ± 6.5% and Se = 87.3 ± 13.8 ± 6.5%, Sp = 98.0 ± 3.1%, Ac = 89.5 ± 10.0%, respectively. Therefore, in both cases, C-OCE showed better diagnostic indicators (Table 4).

The diagnostic accuracy of the difference between non-tumorous breast tissue and low-aggressive breast cancer for CP-OCT and C-OCE was found to be fairly high, 88.1 ± 6.0% and 95.7 ± 4.1%, respectively. Even higher was the Ac of CP-OCT and C-OCE for the difference between non-tumorous breast tissue and highly-aggressive breast cancer (97.2 ± 2.8% and 98.3 ± 2.2%, respectively).

Accurate determining of the boundaries of tumor resection is more feasible for tumors of a solid structure in comparison with tumors of scirrhous structure that may resemble fibroadenomas in OCT-based images. However, the performed targeted histological examination has given a clue for better understanding of the causes of stiffness increase or decrease and made it possible to define additional criteria that improved the diagnostic accuracy of C-OCE for various breast cancer subtypes detection, including non-invasive and low-aggressive tumors.

Thus, the formulated additional (clarifying) criteria for visual assessment of CP-OCT and C-OCE images provided a higher diagnostic accuracy in differentiation between tumorous and non-tumorous breast tissues with various grades of aggressiveness. In the future, this will increase the value of these OCT-based methods in detecting the boundaries of tumor resection during BCS.

5. Conclusions

Both CP-OCT and C-OCE data may be helpful to a surgeon–oncologist for more accurate detection of a "clean" resection margin during breast-conserving surgery. The test based on assessment of C-OCE images has shown higher diagnostic accuracy (96%) and sensitivity (95%) in comparison with CP-OCT images (Se—92%, Ac—92.4%) for breast cancer detection. Furthermore, the preformed study demonstrated high potential of CP-OCT and C-OCE for differentiating particular molecular-biological and morphological subtypes of breast cancer with assessment of the tumor aggressiveness, which is important for subsequent treatment selection.

Author Contributions: Conceptualization, N.D.G. and M.A.S.; images analysis, M.A.S., E.B.K., K.A.A., A.A.P., K.S.Y. and D.A.V.; C-OCE methodology and software, A.L.M., L.A.M., A.A.S. and V.Y.Z.; histological analysis, S.S.K., D.A.V.; data curation, E.V.G., E.B.K.; writing—original draft preparation, E.V.G.; writing—review and editing, N.D.G., A.Y.V. and V.Y.Z.; visualization, E.V.G.; supervision, N.D.G. All authors have read and agreed to the published version of the manuscript.

Funding: The study was funded by the Russian Science Foundation under grant No. 18-75-10068. The development of software for plotting OCE scans was supported by RFBR grant No. 19-32-90110.

Conflicts of Interest: The authors declare no conflict of interest. The funders/sponsors had no role in the design of the study; in the collection, analyses, or interpretation of data; in the writing of the manuscript, or in the decision to publish the results.

References

1. Esbona, K.; Li, Z.; Wilke, L.G. Intraoperative imprint cytology and frozen section pathology for margin assessment in breast conservation surgery: A systematic review. *Ann. Surg. Oncol.* **2012**, *19*, 3236–3245. [CrossRef] [PubMed]
2. Decker, M.R.; Trentham-Dietz, A.; Loconte, N.K.; Neuman, H.B.; Smith, M.A.; Punglia, R.S.; Greenberg, C.C.; Wilke, L.G. The Role of Intraoperative Pathologic Assessment in the Surgical Management of Ductal Carcinoma In Situ. *Ann. Surg. Oncol.* **2016**, *23*, 2788–2794. [CrossRef] [PubMed]
3. Harness, J.K.; Giuliano, A.E.; Pockaj, B.A.; Downs-Kelly, E. Margins: A status report from the Annual Meeting of the American Society of Breast Surgeons. *Ann Surg Oncol Ann. Surg. Oncol.* **2014**, *21*, 3192–3197. [CrossRef] [PubMed]

4. Lamberts, L.E.; Koch, M.; de Jong, J.S.; Adams, A.L.L.; Glatz, J.; Kranendonk, M.E.G.; van Scheltinga, A.G.T.T.; Jansen, L.; de Vries, J.; Lub-de Hooge, M.N.; et al. Tumor-Specific Uptake of Fluorescent Bevacizumab-IRDye800CW Microdosing in Patients with Primary Breast Cancer: A Phase I Feasibility Study. *Clin. Cancer Res.* **2017**, *23*, 2730–2741. [CrossRef]
5. Tummers, Q.R.; Verbeek, F.P.; Schaafsma, B.E.; Boonstra, M.C.; van der Vorst, J.R.; Liefers, G.J.; van de Velde, C.J.; Frangioni, J.V.; Vahrmeijer, A.L. Real-time intraoperative detection of breast cancer using near-infrared fluorescence imaging and Methylene Blue. *Eur. J. Surg. Oncol.* **2014**, *40*, 850–858. [CrossRef]
6. Wojcinski, S.; Farrokh, A.; Weber, S.; Thomas, A.; Fischer, T.; Slowinski, T.; Schmidt, W.; Degenhardt, F. Multicenter study of ultrasound real-time tissue elastography in 779 cases for the assessment of breast lesions: Improved diagnostic performance by combining the BI-RADS®-US classification system with sonoelastography. *Ultraschall. Med.* **2010**, *31*, 484–491. [CrossRef]
7. Dua, S.M.; Gray, R.J.; Keshtgar, M. Strategies for localisation of impalpable breast lesions. *Breast* **2011**, *20*, 246–253. [CrossRef]
8. Xu, H.; Varghese, T.; Jiang, J.; Zagzebski, J.A. In vivo classification of breast masses using features derived from axial-strain and axial-shear images. *Ultrason. Imaging* **2012**, *4*, 222–236. [CrossRef]
9. Wang, J.; Xu, Y.; Boppart, S.A. Review of optical coherence tomography in oncology. *J. Biomed. Opt.* **2017**, *22*, 1–23. [CrossRef]
10. Curatolo, A.; McLaughlin, R.A.; Quirk, B.C.; Kirk, R.W.; Bourke, A.G.; Wood, B.A.; Robbins, P.D.; Saunders, C.M.; Sampson, D.D. Ultrasound-guided optical coherence tomography needle probe for the assessment of breast cancer tumor margins. *AJR Am. J. Roentgenol.* **2012**, *199*, W520–W522. [CrossRef]
11. Kennedy, K.M.; McLaughlin, R.A.; Kennedy, B.F.; Tien, A.; Latham, B.; Saunders, C.M.; Sampson, D.D. Needle optical coherence elastography for the measurement of microscale mechanical contrast deep within human breast tissues. *J. Biomed. Opt.* **2013**, *18*, 121510. [CrossRef] [PubMed]
12. Nguyen, F.T.; Zysk, A.M.; Chaney, E.J.; Kotynek, J.G.; Oliphant, U.J.; Bellafiore, F.J.; Rowland, K.M.; Johnson, P.A.; Boppart, S.A. Intraoperative evaluation of breast tumor margins with optical coherence tomography. *Cancer Res.* **2009**, *69*, 8790–8796. [CrossRef] [PubMed]
13. Ha, R.; Friedlander, L.C.; Hibshoosh, H.; Hendon, C.; Feldman, S.; Ahn, S.; Schmidt, H.; Akens, M.K.; Fitzmaurice, M.; Wilson, B.C.; et al. Optical Coherence Tomography: A Novel Imaging Method for Post-lumpectomy Breast Margin Assessment-A Multi-reader Study. *Acad. Radiol.* **2018**, *25*, 279–287. [CrossRef] [PubMed]
14. Schmidt, H.; Connolly, C.; Jaffer, S.; Oza, T.; Weltz, C.R.; Port, E.R.; Corben, A. Evaluation of surgically excised breast tissue microstructure using wide-field optical coherence tomography. *Breast J.* **2020**, *26*, 917–923. [CrossRef] [PubMed]
15. Savastru, D.; Chang, E.W.; Miclos, S.; Pitman, M.B.; Patel, A.; Iftimia, N. Detection of breast surgical margins with optical coherence tomography imaging: A concept evaluation study. *J. Biomed. Opt.* **2014**, *19*, 056001. [CrossRef]
16. Erickson-Bhatt, S.J.; Nolan, R.M.; Shemonski, N.D.; Adie, S.G.; Putney, J.; Darga, D.; McCormick, D.T.; Cittadine, A.J.; Zysk, A.M.; Marjanovic, M.; et al. Real-time Imaging of the Resection Bed Using a Handheld Probe to Reduce Incidence of Microscopic Positive Margins in Cancer Surgery. *Cancer Res.* **2015**, *75*, 3706–3712. [CrossRef]
17. Zysk, A.M.; Chen, K.; Gabrielson, E.; Tafra, L.; May Gonzalez, E.A.; Canner, J.K.; Schneider, E.B.; Cittadine, A.J.; Scott Carney, P.; Boppart, S.A.; et al. Intraoperative Assessment of Final Margins with a Handheld Optical Imaging Probe During Breast-Conserving Surgery May Reduce the Reoperation Rate: Results of a Multicenter Study. *Ann. Surg. Oncol.* **2015**, *22*, 3356–3362. [CrossRef]
18. Zhou, C.; Cohen, D.W.; Wang, Y.; Lee, H.C.; Mondelblatt, A.E.; Tsai, T.H.; Aguirre, A.D.; Fujimoto, J.G.; Connolly, J.L. Integrated optical coherence tomography and microscopy for ex vivo multiscale evaluation of human breast tissues. *Cancer Res.* **2010**, *70*, 10071–10079. [CrossRef]
19. de Boer, J.F.; Hitzenberger, C.K.; Yasuno, Y. Polarization sensitive optical coherence tomography—A review [Invited]. *Biomed. Opt. Express* **2017**, *8*, 1838–1873. [CrossRef]
20. Wang, J.; Xu, Y.; Mesa, K.J.; South, F.A.; Chaney, E.J.; Spillman, D.R.; Barkalifa, R., Jr.; Marjanovic, M.; Carney, P.S.; Higham, A.M.; et al. Complementary use of polarization-sensitive and standard OCT metrics for enhanced intraoperative differentiation of breast cancer. *Biomed. Opt. Express* **2018**, *9*, 6519–6528. [CrossRef]

21. South, F.A.; Chaney, E.J.; Marjanovic, M.; Adie, S.G.; Boppart, S.A. Differentiation of ex vivo human breast tissue using polarization-sensitive optical coherence tomography. *Biomed. Opt. Express* **2014**, *5*, 3417–3426. [CrossRef]
22. Provenzano, P.P.; Eliceiri, K.W.; Campbell, J.M.; Inman, D.R.; White, J.G.; Keely, P.J. Collagen reorganization at the tumor-stromal interface facilitates local invasion. *BMC Med.* **2006**, *4*, 1741–7015. [CrossRef]
23. Patel, R.; Khan, A.; Quinlan, R.; Yaroslavsky, A.N. Polarization-sensitive multimodal imaging for detecting breast cancer. *Cancer Res.* **2014**, *74*, 4685–4693. [CrossRef] [PubMed]
24. Gelikonov, V.M.; Romashov, V.N.; Shabanov, D.V.; Ksenofontov, S.Y.; Terpelov, D.A.; Shilyagin, P.A.; Gelikonov, G.V.; Vitkin, I.A. Cross-polarization optical coherence tomography with active maintenance of the circular polarization of a sounding wave in a common path system. *Radiophys. Quantum Electron.* **2018**, *60*, 897–911. [CrossRef]
25. Gubarkova, E.V.; Sovetsky, A.A.; Zaitsev, V.Y.; Matveyev, A.L.; Vorontsov, D.A.; Sirotkina, M.A.; Matveev, L.A.; Plekhanov, A.A.; Pavlova, N.P.; Kuznetsov, S.S.; et al. OCT-elastography-based optical biopsy for breast cancer delineation and express assessment of morphological/molecular subtypes. *Biomed. Opt. Express* **2019**, *10*, 2244–2263. [CrossRef] [PubMed]
26. Yashin, K.S.; Kiseleva, E.B.; Gubarkova, E.V.; Moiseev, A.A.; Kuznetsov, S.S.; Shilyagin, P.A.; Gelikonov, G.V.; Medyanik, I.A.; Kravets, L.Y.; Potapov, A.A.; et al. Cross-Polarization Optical Coherence Tomography for Brain Tumor Imaging. *Front. Oncol.* **2019**, *9*, 201. [CrossRef] [PubMed]
27. Yashin, K.S.; Kiseleva, E.B.; Moiseev, A.A.; Kuznetsov, S.S.; Timofeeva, L.B.; Pavlova, N.P.; Gelikonov, G.V.; Medyanik, I.A.; Kravets, L.Y.; Zagaynova, E.V.; et al. Quantitative nontumorous and tumorous human brain tissue assessment using microstructural co- and cross-polarized optical coherence tomography. *Sci. Rep.* **2019**, *9*, 2024. [CrossRef] [PubMed]
28. Kiseleva, E.; Kirillin, M.; Feldchtein, F.; Vitkin, A.; Sergeeva, E.; Zagaynova, E.; Streltzova, O.; Shakhov, B.; Gubarkova, E.; Gladkova, N. Differential diagnosis of human bladder mucosa pathologies in vivo with cross-polarization optical coherence tomography. *Biomed. Opt. Express* **2015**, *6*, 1464–1476. [CrossRef]
29. Gladkova, N.; Kiseleva, E.; Streltsova, O.; Prodanets, N.; Snopova, L.; Karabut, M.; Gubarkova, E.; Zagaynova, E. Combined use of fluorescence cystoscopy and cross-polarization OCT for diagnosis of bladder cancer and correlation with immunohistochemical markers. *J. Biophotonics* **2013**, *6*, 687–698. [CrossRef]
30. Gladkova, N.; Streltsova, O.; Zagaynova, E.; Kiseleva, E.; Gelikonov, V.; Gelikonov, G.; Karabut, M.; Yunusova, K.; Evdokimova, O. Cross-polarization optical coherence tomography for early bladder-cancer detection: Statistical study. *J. Biophotonics* **2011**, *4*, 519–532. [CrossRef]
31. Gladkova, N.; Kiseleva, E.; Robakidze, N.; Balalaeva, I.; Karabut, M.; Gubarkova, E.; Feldchtein, F. Evaluation of oral mucosa collagen condition with cross-polarization optical coherence tomography. *J. Biophotonics* **2013**, *6*, 321–329. [CrossRef] [PubMed]
32. Foo, K.Y.; Chin, L.; Zilkens, R.; Lakhiani, D.D.; Fang, Q.; Sanderson, R.; Dessauvagie, B.F.; Latham, B.; McLaren, S.; Saunders, C.M.; et al. Three-dimensional mapping of the attenuation coefficient in optical coherence tomography to enhance breast tissue microarchitecture contrast. *J. Biophotonics* **2020**, *13*, e201960201. [CrossRef]
33. Gubarkova, E.V.; Moiseev, A.A.; Kiseleva, E.B.; Vorontsov, D.A.; Kuznetsov, S.S.; Vorontsov, A.Y.; Gelikonov, G.V.; Sirotkina, M.A.; Gladkova, N.D. Tissue optical properties estimation from cross-polarization OCT data for breast cancer margin assessment. *Laser Phys. Lett.* **2020**, *17*, 075602. [CrossRef]
34. Kennedy, K.M.; Chin, L.; McLaughlin, R.A.; Latham, B.; Saunders, C.M.; Sampson, D.D.; Kennedy, B.F. Quantitative micro-elastography: Imaging of tissue elasticity using compression optical coherence elastography. *Sci. Rep.* **2015**, *5*, 15538. [CrossRef] [PubMed]
35. Kennedy, B.F.; Wijesinghe, P.; Sampson, D.D. The emergence of optical elastography in biomedicine. *Nat. Photonics* **2017**, *11*, 215–221. [CrossRef]
36. Larin, K.V.; Sampson, D.D. Optical coherence elastography—OCT at work in tissue biomechanics [Invited]. *Biomed. Opt. Express* **2017**, *8*, 1172–1202. [CrossRef]
37. Zaitsev, V.Y.; Matveyev, A.L.; Matveev, L.A.; Sovetsky, A.A.; Hepburn, M.S.; Mowla, A.; Kennedy, B.F. Strain and elasticity imaging in compression optical coherence elastography: The two-decade perspective and recent advances. *J. Biophotonics* **2020**, e202000257. [CrossRef] [PubMed]

38. Sirotkina, M.A.; Gubarkova, E.V.; Plekhanov, A.A.; Sovetsky, A.A.; Elagin, V.V.; Matveyev, A.L.; Matveev, L.A.; Kuznetsov, S.S.; Zagaynova, E.V.; Gladkova, N.D.; et al. In vivo assessment of functional and morphological alterations in tumors under treatment using OCT-angiography combined with OCT-elastography. *Biomed. Opt. Express* **2020**, *11*, 1365–1382. [CrossRef]
39. Plekhanov, A.A.; Sirotkina, M.A.; Sovetsky, A.A.; Gubarkova, E.V.; Kuznetsov, S.S.; Matveyev, A.L.; Matveev, L.A.; Zagaynova, E.V.; Gladkova, N.D.; Zaitsev, V.Y. Histological validation of in vivo assessment of cancer tissue inhomogeneity and automated morphological segmentation enabled by Optical Coherence Elastography. *Sci. Rep.* **2020**, *10*, 11781. [CrossRef]
40. Kennedy, B.F.; McLaughlin, R.A.; Kennedy, K.M.; Chin, L.; Wijesinghe, P.; Curatolo, A.; Tien, A.; Ronald, M.; Latham, B.; Saunders, C.M.; et al. Investigation of Optical Coherence Microelastography as a Method to Visualize Cancers in Human Breast Tissue. *Cancer Res.* **2015**, *75*, 3236–3245. [CrossRef]
41. Allen, W.M.; Foo, K.Y.; Zilkens, R.; Kennedy, K.M.; Fang, Q.; Chin, L.; Dessauvagie, B.F.; Latham, B.; Saunders, C.M.; Kennedy, B.F. Clinical feasibility of optical coherence micro-elastography for imaging tumor margins in breast-conserving surgery. *Biomed. Opt. Express* **2018**, *9*, 6331–6349. [CrossRef] [PubMed]
42. Zaitsev, V.Y.; Matveyev, A.L.; Matveev, L.A.; Gubarkova, E.V.; Sovetsky, A.A.; Sirotkina, M.A.; Gelikonov, G.V.; Zagaynova, E.V.; Gladkova, N.D.; Vitkin, A. Practical obstacles and their mitigation strategies in compressional optical coherence elastography of biological tissues *J. Innovative Opt. Health Sci.* **2017**, *10*, 1742006. [CrossRef]
43. Kennedy, K.M.; Zilkens, R.; Allen, W.M.; Foo, K.Y.; Fang, Q.; Chin, L.; Sanderson, R.W.; Anstie, J.; Wijesinghe, P.; Curatolo, A.; et al. Diagnostic Accuracy of Quantitative Micro-Elastography for Margin Assessment in Breast-Conserving Surgery. *Cancer Res.* **2020**, *80*, 1773–1783. [CrossRef] [PubMed]
44. Allen, W.M.; Kennedy, K.M.; Fang, Q.; Chin, L.; Curatolo, A.; Watts, L.; Zilkens, R.; Chin, S.L.; Dessauvagie, B.F.; Latham, B.; et al. Wide-field quantitative micro-elastography of human breast tissue. *Biomed. Opt. Express.* **2018**, *9*, 1082–1096. [CrossRef]
45. Aleskandarany, M.A.; Vandenberghe, M.E.; Marchiò, C.; Ellis, I.O.; Sapino, A.; Rakha, E.A. Tumour Heterogeneity of Breast Cancer: From Morphology to Personalised Medicine. *Pathobiology* **2018**, *85*, 23–34. [CrossRef]
46. Iwao, K.; Matoba, R.; Ueno, N.; Ando, A.; Miyoshi, Y.; Matsubara, K.; Noguchi, S.; Kato, K. Molecular classification of primary breast tumors possessing distinct prognostic properties. *Hum. Mol. Genet.* **2002**, *11*, 199–206. [CrossRef]
47. Lowery, A.J.; Kell, M.R.; Glynn, R.W.; Kerin, M.J.; Sweeney, K.J. Locoregional recurrence after breast cancer surgery: A systematic review by receptor phenotype. *Breast Cancer Res. Treat.* **2012**, *133*, 831–841. [CrossRef]
48. Cancello, G.; Maisonneuve, P.; Rotmensz, N.; Viale, G.; Mastropasqua, M.G.; Pruneri, G.; Montagna, E.; Dellapasqua, S.; Iorfida, M.; Cardillo, A.; et al. Prognosis in women with small (T1mic,T1a,T1b) node-negative operable breast cancer by immunohistochemically selected subtypes. *Breast Cancer Res. Treat.* **2011**, *127*, 713–720. [CrossRef]
49. Houssami, N.; Macaskill, P.; Marinovich, M.L.; Morrow, M. The association of surgical margins and local recurrence in women with early-stage invasive breast cancer treated with breast-conserving therapy: A meta-analysis. *Ann. Surg. Oncol.* **2014**, *21*, 717–730. [CrossRef]
50. Moiseev, A.; Ksenofontov, S.; Sirotkina, M.; Kiseleva, E.; Gorozhantseva, M.; Shakhova, N.; Matveev, L.; Zaitsev, V.; Matveyev, A.; Zagaynova, E.; et al. Optical coherence tomography-based angiography device with real-time angiography B-scans visualization and hand-held probe for everyday clinical use. *J. Biophotonics* **2018**, *11*, e201700292. [CrossRef]
51. Zaitsev, V.Y.; Matveyev, A.L.; Matveev, L.A.; Gelikonov, G.V.; Sovetsky, A.A.; Vitkin, A. Optimized phase gradient measurements and phase-amplitude interplay in optical coherence elastography. *J. Biomed. Opt.* **2016**, *21*, 116005. [CrossRef] [PubMed]
52. Zaitsev, V.Y.; Matveyev, A.L.; Matveev, L.A.; Gelikonov, G.V.; Gubarkova, E.V.; Gladkova, N.D.; Vitkin, A. Hybrid method of strain estimation in optical coherence elastography using combined sub-wavelength phase measurements and supra-pixel displacement tracking. *J. Biophotonics* **2016**, *9*, 499–509. [CrossRef] [PubMed]
53. Matveyev, A.L.; Matveev, L.A.; Sovetsky, A.A.; Gelikonov, G.V.; Moiseev, A.A.; Zaitsev, V.Y. Vector method for strain estimation in phase-sensitive optical coherence elastography. *Laser Phys. Lett.* **2018**, *15*, 065603. [CrossRef]

54. Sovetsky, A.A.; Matveyev, A.L.; Matveev, L.A.; Shabanov, D.V.; Zaitsev, V.Y. Manually-operated compressional optical coherence elastography with effective aperiodic averaging: Demonstrations for corneal and cartilaginous tissues. *Laser Phys. Lett.* **2018**, *15*, 85602. [CrossRef]
55. Sovetsky, A.A.; Matveyev, A.L.; Matveev, L.A.; Gubarkova, E.V.; Plekhanov, A.A.; Sirotkina, M.A.; Gladkova, N.D.; Zaitsev, V.Y. Full-optical method of local stress standardization to exclude nonlinearity-related ambiguity of elasticity estimation in compressional optical coherence elastography. *Laser Phys. Lett.* **2020**, *17*, 065601. [CrossRef]
56. Sovetsky, A.A.; Matveev, L.A.; Gubarkova, E.V.; Matveyev, A.L.; Gladkova, N.D.; Zaitsev, V.Y. Characterization of elastic nonlinear properties of the tissues using compressional optical coherence elastography. *Proc. SPIE* **2020**, *11359*, 113590H. [CrossRef]
57. Zaitsev, V.Y.; Matveyev, A.L.; Matveev, L.A.; Gelikonov, G.V.; Omelchenko, A.I.; Shabanov, D.V.; Baum, O.I.; Svistushkin, V.M.; Sobol, E.N. Optical coherence tomography for visualizing transient strains and measuring large deformations in laser-induced tissue reshaping. *Laser Phys. Lett.* **2016**, *13*, 115603. [CrossRef]
58. Zaitsev, V.Y.; Matveyev, A.L.; Matveev, L.A.; Gelikonov, G.V.; Omelchenko, A.I.; Baum, O.I.; Avetisov, S.E.; Bolshunov, A.V.; Siplivy, V.I.; Shabanov, D.V.; et al. Optical coherence elastography for strain dynamics measurements in laser correction of cornea shape. *J. Biophotonics* **2017**, *10*, 1450–1463. [CrossRef]
59. Feuerman, M.; Miller, A.R. Relationships between statistical measures of agreement: Sensitivity, specificity and kappa. *J. Eval. Clin. Pract.* **2008**, *14*, 930–933. [CrossRef]
60. Viera, A.J.; Garrett, J.M. Understanding interobserver agreement: The kappa statistic. *Fam. Med.* **2005**, *37*, 360–363.
61. Yao, X.; Gan, Y.; Chang, E.; Hibshoosh, H.; Feldman, S.; Hendon, C. Visualization and tissue classification of human breast cancer images using ultrahigh-resolution OCT. *Lasers Surg. Med.* **2017**, *49*, 258–269. [CrossRef] [PubMed]
62. Assayag, O.; Antoine, M.; Sigal-Zafrani, B.; Riben, M.; Harms, F.; Burcheri, A.; Grieve, K.; Dalimier, E.; Le Conte de Poly, B.; Boccara, C. Large field, high resolution full-field optical coherence tomography: A pre-clinical study of human breast tissue and cancer assessment. *Technol. Cancer Res. Treat.* **2014**, *13*, 455–468. [CrossRef] [PubMed]
63. Zysk, A.M.; Boppart, S.A. Computational methods for analysis of human breast tumor tissue in optical coherence tomography images. *J. Biomed. Opt.* **2006**, *11*, 054015. [CrossRef] [PubMed]

diagnostics

MDPI

Article

Monte Carlo Modeling of Shortwave-Infrared Fluorescence Photon Migration in Voxelized Media for the Detection of Breast Cancer

Tatsuto Iida [1], Shunsuke Kiya [1], Kosuke Kubota [1], Takashi Jin [2], Akitoshi Seiyama [3] and Yasutomo Nomura [1,2,*]

[1] Department of Systems Life Engineering, Maebashi Institute of Technology, Maebashi 371-0816, Japan; m1956001@maebashi-it.ac.jp (T.I.); m1771013@maebashi-it.ac.jp (S.K.); m1771014@maebashi-it.ac.jp (K.K.)
[2] Laboratory for Nano-Bio Probes, RIKEN Center for Biosystems Dynamics Research, Suita 565-0874, Japan; tjin@riken.jp
[3] Human Health Sciences, Graduate School of Medicine, Kyoto University, Kyoto 606-8507, Japan; seiyama.akitoshi.7x@kyoto-u.ac.jp
* Correspondence: ynomura@maebashi-it.ac.jp; Tel.: +81-27-265-7389

Received: 30 September 2020; Accepted: 15 November 2020; Published: 17 November 2020

Abstract: Recent progress regarding shortwave-infrared (SWIR) molecular imaging technology has inspired another modality of noninvasive diagnosis for early breast cancer detection in which previous mammography or sonography would be compensated. Although a SWIR fluorescence image of a small breast cancer of several millimeters was obtained from experiments with small animals, detailed numerical analyses before clinical application were required, since various parameters such as size as well as body hair differed between humans and small experimental animals. In this study, the feasibility of SWIR was compared against visible (VIS) and near-infrared (NIR) region, using the Monte Carlo simulation in voxelized media. In this model, due to the implementation of the excitation gradient, fluorescence is based on rational mechanisms, whereas fluorescence within breast cancer is spatially proportional to excitation intensity. The fluence map of SWIR simulation with excitation gradient indicated signals near the upper surface of the cancer, and stronger than those of the NIR. Furthermore, there was a dependency on the fluence signal distribution on the contour of the breast tissue, as well as the internal structure, due to the implementation of digital anatomical data for the Visible Human Project. The fluorescence signal was observed to become weaker in all regions including the VIS, the NIR, and the SWIR region, when fluorescence-labeled cancer either became smaller or was embedded in a deeper area. However, fluorescence in SWIR alone from a cancer of 4 mm diameter was judged to be detectable at a depth of 1.4 cm.

Keywords: shortwave-infrared light; near-infrared light; visible light; fluorescence; breast cancer; duct; visible human project; Monte Carlo simulation; voxelized media

1. Introduction

Ductal carcinoma is the most common type of breast cancer and tends to progress to invasive cancer. Breast conservation therapy should be considered when the cancer is less than 2.0 cm [1,2]. However, it was shown by the accuracy of the same MRI(magnetic resonance imaging)-sonography co-registration system that the mean lesion size correlated well on MRI (11.4 mm; range 6–28 mm) compared with that of sonography (10.3 mm; range 6–28 mm) [3]. Therefore, early breast cancers of only several millimeters have occasionally failed to be detected by the use of such noninvasive methods alone. However, shortwave-infrared (SWIR) fluorescence imaging for the detection of small cancers offers a higher contrast and sensitivity with deeper penetration depths in comparison with

the conventional visible (VIS) and the near-infrared (NIR) fluorescence imaging, thus it has attracted much attention recently [4,5]. As radiation exposure due to SWIR is much less than that from X-rays in mammography and gamma-rays in PET, SWIR fluorescence imaging can be used repetitively, which suggests its suitability in the case of young subjects. Furthermore, it would have a higher spatial resolution than the sentinel lymph-node biopsy with VIS (Patent blue) or NIR fluorescence (Indocyanine green, ICG) because of the lower scattering property [6–9]. Indeed, a fluorescent image of a small breast cancer of several millimeters was obtained from small animal experiments [10].

Before clinical application, detailed numerical analyses of the behavior of excitation and emission photons are required, since optical parameters such as scattering and absorption coefficients differ between humans and small experimental animals. In our previous study, as the first step for the detection of early breast cancer, Monte Carlo modeling in a multi-layered media (MCML) for fluorescence photon migration of the ICG in the NIR was proposed [11]. In contrast to the VIS fluorescence of fluorescein, the NIR fluorescence of the ICG showed effectiveness in detecting a cancer of 1.0 cm in diameter at a depth of 1.0 cm. This suggests that smaller cancers are probably detected when SWIR fluorescence is utilized. However, the analytical model was composed of a spherical cancer with fluorescence in the fat layer below the flat skin surface. The results of the analysis in the approximate model of the layered structure are not always correct, because actual breast tissue has a complex three-dimensional structure, e.g., the mammary gland. Therefore, taking the high spatial resolution of the SWIR fluorescence imaging into account, an analytical model which reflected the contour of the breast surface and its internal structure was pursued. Recently, Monte Carlo modeling in voxelized media (MCVM), by which the authors could track photon migration in realistic brain tissue structure, was reported by Li et al. [12,13], where a digital anatomical dataset of the voxelized media of the Monte Carlo model was implemented in which optical parameters were set specific to regions of the human tissue. Here we developed their method to apply to a breast cancer model, as follows.

The authors predicted distribution within the tissue of light absorption in the VIS and the NIR. In this study, we developed MCVM for the analysis of excitation and emission. The intensity of fluorescence is proportional to the concentration of the fluorescent molecules as well as the excitation efficiency. The accumulation of fluorescent probes in the cancer is dependent on the expression level of the marker protein. The concentration of fluorescent molecules located in the cancer was assumed to be spatially constant. On the other hand, it was quite difficult to set the excitation efficiency to be spatially constant. When incident photons reached the cancerous cell, the fluorescent molecules within it partially absorbed the energy. Therefore, the excitation efficiency was influenced by the optical properties surrounding the cancer and its depth. When optical parameters were set, specific to the regions of the duct with a complex morphology and the fat tissue, photon migration in association with excitation and emission would reflect the internal structure faithfully. Thus, the feasibility of detecting early breast cancer was examined by analyzing the SWIR fluorescence, which was emitted by several mechanisms, using MCVM with exact distribution of the optical parameters.

2. Materials and Methods

2.1. Breast Model

Digital anatomical data in which the internal structure of the breast was reflected were pursued for the improvement of our previous Monte Carlo model [11,14–16]. In the previous studies, Li et al. used a dataset of cross-sectional cryosection images which was provided by the Visible Chinese Human (VCH) [12,13]. However, due to limited access, there was a difficulty in obtaining the dataset from VCH. Therefore we used a public-domain library of cross-sectional cryosection, CT, as well as MRI images provided by the Visible Human Project (VHP) of the US National Library of Medicine [17]. Because 3D tomography of the breast was obtained from the dataset, it permitted us to analyze photon behaviors in the Monte Carlo model set to a complex internal structure identical to the human breast. In this study, the thoracic part of an anatomical dataset built from a cadaver of an American woman who had

died of heart disease at the age of 59 was used. With the permission of her husband, the body was frozen, thinly sliced more than 5000 times, and photographed. The thickness of each slice was 0.33 mm. The three-dimensional reconstruction of the thoracic part, built from thin slices as in Figure 1A, is shown in (B). When images of the slice were processed based on the anatomy of the breast as described in the next section, the mammary gland (green structure with complex morphology) was included within the thoracic part (C). As shown in (D), fluorescence-labeled cancer (red sphere) was set in the duct of the structure. To indicate the structure observed from a different angle, rotating (D) $\pi/2$ clockwise on the x-axis was performed to obtain (E). Furthermore, (F) was obtained by rotating (D) $\pi/2$ once more.

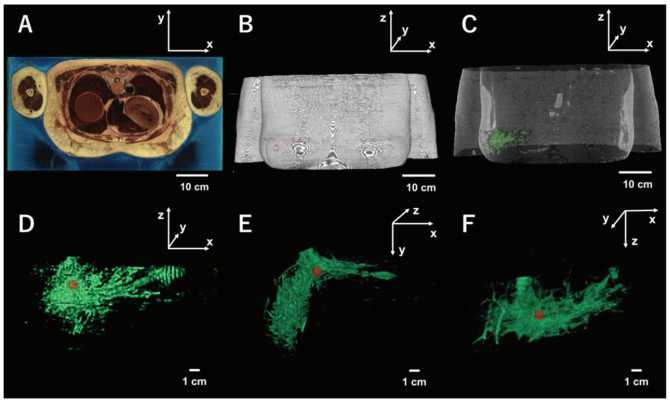

Figure 1. Visualization of the internal structure of the female breasts from the Visible Human Project (VHP). (**A**) Slice of the upper body. (**B**) Three-dimensional reconstruction of the upper body. (**C**) Internal structure in the reconstruction. (**D**) Enlarged internal structure with fluorescence-labeled cancer with 1 cm diameter. (**E**) The 3-D vision of the enlarged structure is observed from a different angle. (**F**) 3-D vision from another different angle. See text.

2.2. Image Processing and Implementation of the Model

250 slices were used from the thoracic part, with 2048 × 1216 pixels for each slice provided by the VHP, where the breast area of 500 × 220 pixels was cropped using an image processing software (ImageJ). A cropped breast image (24-bit RGB color) from the original VHP image is shown in Figure 2A. Regarding the pixel values, the cropped image in Figure 2B was allocated to areas of fat of more than 180, as well as to areas of the breast duct between 80 and 120, respectively, after conversion to an 8-bit grayscale image. The boundary between the outside and inside tissue area was extracted and the border of two pixels width was assumed to be the skin layer. Previous studies were used to set the optical parameters specific to the three areas in Table 1 [18–22]. In this study, taking medical applications into account, the excitation and emission wavelengths of the fluorescein (excitation max (Ex) 488 nm, emission max (Em) 520 nm, quantum yield (QY): 0.95, concentration (C): 0.75 mM, absorption coefficient (εC): 12 cm^{-1}) were selected, which were used for the examination of the fundus in the VIS region, as well as those of the ICG (Ex 780 nm/Em 820 nm, QY: 0.09, C: 0.2 mM, εC: 20 cm^{-1}) for the sentinel lymph-node biopsy in the NIR region [6–9,23,24]. Fluorescence imaging in the VIS region is an effective diagnostic method for transparent media such as the eyeball, but it is difficult to use in turbid media which is characteristic of the optical properties of breast tissue. For SWIR imaging, we employed lead sulfide (PbS) quantum dots (QDs) (Ex 970 nm/Em 1100 nm, QY: 0.40, C: 1.0 μM, εC: 0.63 cm^{-1}) as fluorescent probes which have been used in prior animal experiments despite the lack of medical applications of QDs [5]. As shown in Figures 2C and 3A, the optical parameters were implemented in the voxel of the 3-dimensional matrix (500, 250, 220). Each voxel was of 0.033 × 0.033 × 0.033 cm^3. The fluorescence-labeled cancers with a diameter of 1, 4, 7, and 10 mm were embedded at a depth of 1 to 3 cm (Figure 2D).

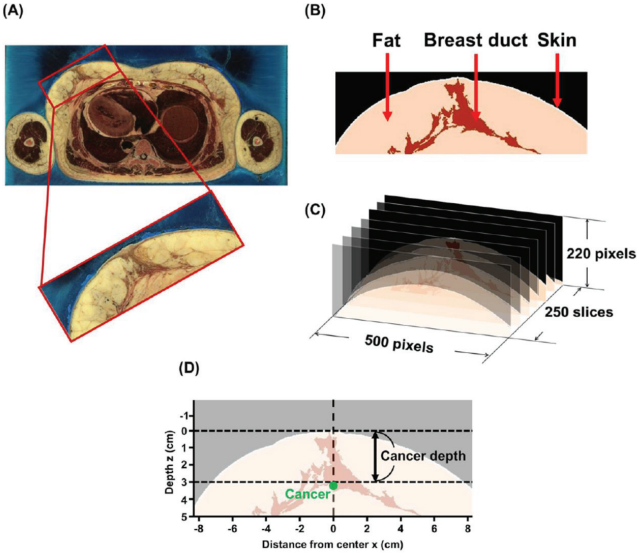

Figure 2. Implementation of the contour and the internal structures derived from breast anatomical data of the Visible Human Project (VHP). (**A**) Cropped image from a slice. (**B**) Allocation of the fat, the duct and the skin based on pixel value. (**C**) Reconstruction of a 3-D voxel model. (**D**) Setting of coordinate system in the slice containing the center and top of nipple ($x = 0$, $z = 0$). The depth denotes the distance from $z = 0$ to the upper surface of the cancer.

Table 1. Optical parameters specific to tissues in the visible (VIS), the near-infrared (NIR), and the shortwave-infrared (SWIR).

	Wavelength (nm)	Tissue	μ_a (cm^{-1})	μ_s (cm^{-1})	n
VIS	Ex 488	Skin	6.0	625	1.37
		Fat	6.0	310	1.45
		Duct	0.2	317	1.42
		Cancer	1.0	300	1.45
	Em 520	Skin	5.8	450	1.37
		Fat	4.0	300	1.45
		Duct	0.2	268	1.42
		Cancer	1.0	230	1.45
NIR	Ex 780	Skin	2.0	241	1.37
		Fat	1.4	136	1.45
		Duct	0.2	169	1.42
		Cancer	1.0	150	1.45
	Em 820	Skin	1.2	228	1.37
		Fat	1.2	132	1.45
		Duct	0.2	198	1.42
		Cancer	0.7	140	1.45
SWIR	Ex 970	Skin	1.0	210	1.37
		Fat	0.9	76.6	1.45
		Duct	0.3	122	1.42
		Cancer	0.9	75.5	1.45
SWIR	Em 1100	Skin	0.7	176	1.37
		Fat	0.6	72.3	1.45
		Duct	0.3	122	1.42
		Cancer	1.0	80.0	1.45

2.3. The Monte Carlo Simulation

The software for Monte Carlo modeling of fluorescence was developed with the use of the C programing language within the Microsoft Visual Studio program. As shown in Figure 3B, this simulation was executed by the input of an excited photon in the voxelized media, where each voxel had optical parameters specific to the three areas of the skin, duct, and fat. In Figure 3C, the computation routines described by Wang et al. were used [25]. In brief, each pathlength was considered to be the distance traveled by a photon from the original position to the next interaction site between the photon and the tissue, due to scattering and absorption. The pathlength and the direction were calculated using a random number, anisotropy g, as well as the total attenuation coefficient μ_t, which is the sum of the scattering coefficient μ_s and the absorption coefficient μ_a. Although each excitation photon had an initial weight of unity, the original weight of the photon was reduced by μ_a/μ_t during movement of the photon to the next site. Pseudo-random numbers generated using the Mersenne twister method were used [26]. Photons were reflected or transmitted based on Fresnel reflectance, calculated using refractive indices n of each layer when they crossed the boundary between two layers [25]. Random paths for photons were computed until the weight of each photon was absorbed to less than a threshold, or the photon left the medium.

The photon weight absorbed within each voxel was scored after completion in order to calculate the behavior of a million excitation photons. This was divided by μ_a of the voxel to obtain the fluence. The fluence can be considered as the weight of photons passed and the amount of energy passed per unit area (W/cm^2). Furthermore, since the fluence yielded a response to a light source 1 W/cm^2, it was converted into the response to 50 mW/cm^2 of light source, generally used in tissue spectroscopy [13,27]. The fluence was inherited by the emission photon in two ways as shown in Figure 3D. In the previous study, without the excitation gradient [14], the weight of the emission photon was set as spatially constant by the use of excitation fluency in the center of the cancer. In the present study with an excitation gradient, the emission photon had an initial weight dependent on excitation fluency in each voxel. A million emission photons were generated isotopically in a random position within the cancer.

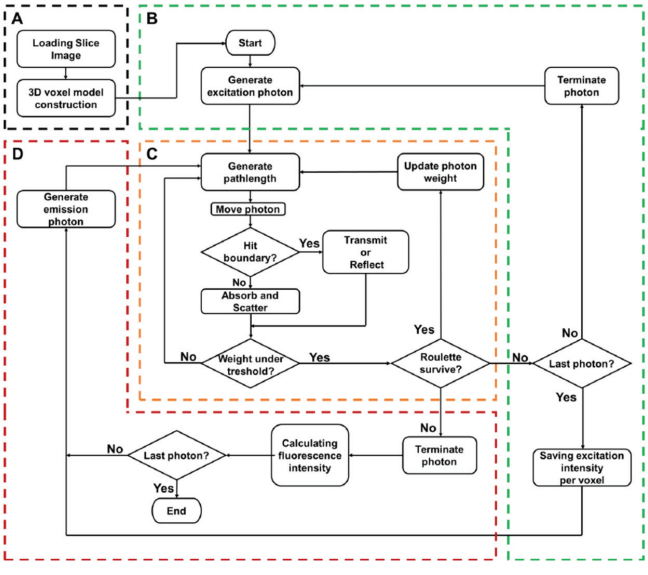

Figure 3. Flowchart of the Monte Carlo simulation in voxelized media for breast tissue. (**A**) Implementation of the breast anatomical data of the VHP. (**B**) Excitation part of the simulation. (**C**) Computation routines were based on Wang et al. [25]. (**D**) Emission part.

3. Results and Discussion

3.1. Excitation Gradient

In the previous study [11], we used the fluorescence Monte Carlo model in which spherical cancer was embedded in the fat layer below the flat skin surface for detecting of early breast cancer. Fluorescence was based on two assumptions. (1) The fluorescent probes were distributed within cancer homogeneously. (2) All probes were excited by the same intensity as the light which reached the center of the cancer. Compared with cancer near the body surface, weaker excitation light reached cancer embedded deeply. There may have been a difference in excitation light intensity between cancer in shallow and deep regions.

In this study, the Monte Carlo model was developed with or without the excitation gradient (Figure 3). The effect of the excitation gradient on VIS, NIR, and SWIR was examined. Fluence maps without and with excitation gradient are shown in Figure 4 when fluorescence-labeled cancer of 1 cm diameter in the duct was embedded $x = 0$ at a depth of 2 cm. Because high μ_s and μ_a were obstructive against reaching fluorescence-labeled cancer for VIS excitation, there was little fluorescence, with and without excitation gradient. In contrast, since the excitation of NIR and SWIR reached the fluorescence-labeled cancer, there was fluorescence with and without excitation gradient. Furthermore, taking the excitation gradient into account, the upper area of cancer shows strong signals in both NIR and SWIR. Without excitation gradient, homogeneous signals in NIR and SWIR were distributed within the entire cancer. The fluence map of SWIR simulation with excitation gradient indicated near-surface signals stronger than those of the NIR. Therefore, the previous model was improved by the use of rational mechanisms for fluorescence, further confirmed in three regions, the VIS, the NIR, and the SWIR, in this study.

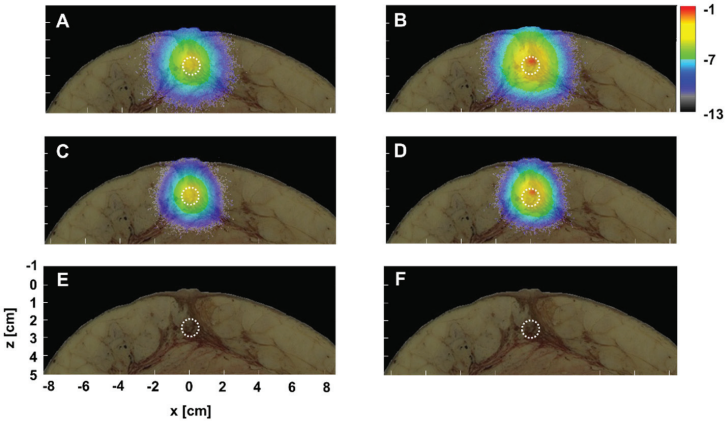

Figure 4. Effect of the excitation gradient in the SWIR (**A**,**B**), the NIR (**C**,**D**) and the VIS (**E**,**F**). Fluence maps without excitation gradient (**A**,**C**,**E**) and with gradient (**B**,**D**,**F**). Fluorescence-labeled cancer with a diameter of 1 cm in the duct were embedded $x = 0$ at a depth of 2 cm, denoted by circles of the white broken line. All maps share the values on the x and the z-axis of (**E**) and the scale bar, which shows the logarithmic scale of intensity (W/cm^2) in (**B**).

3.2. Setting Optical Parameters Faithful to Duct Morphology

In the previous model, spherically fluorescence-labeled cancer was embedded in the fat layer which had homogeneous optical parameters. However, the model was too simple as the actual breast tissue structure was complex. Breast cancer is frequently developed in the duct and progresses invasively. Thus, it is quite important to set optical parameters for ducts with complex morphology (Figure 1) when photon migration in the breast tissue is examined. Furthermore, the excitation and

emission would be influenced by the various locations of fluorescence-labeled cancer within the duct, outside of the duct, or between the duct and the fat, due to the different optical properties that can be characteristic of each location (see Table 1).

In this study, optical parameters specific to various regions such as skin, duct, and fat were provided for the analytical model based on the breast structure data of the VHP. When the fluorescence-labeled cancer of 1 cm diameter was embedded in the duct at a depth of 2 cm, the fluorescent fluence signals from the spherical cancer had a small and vertically long shape in both the NIR and the SWIR, probably due to a higher μ_s and a lower μ_a of the duct shown in Figure 4A–D. The distortion from the perfect circle in the SWIR fluorescence signals was smaller than that in the NIR due to the low μ_s. Moreover, the signal shape on the fluence map can be attributed to the distribution of the optical parameters.

To confirm this possibility, the fluence map of excitation and emission were examined in detail when the spherical cancer of 1 mm diameter was embedded in the duct at a depth of 3 cm. Although there was no emission fluence of the VIS in Figure 4, we confirmed the effect on excitation of the faithful distribution of the optical parameters due to a higher μ_s and μ_a of the VIS than the NIR and the SWIR. As shown in Figure 5E, the VIS excitation fluence signals along the duct appeared due to the migration of photons, impeded by fat with a higher μ_a. However, no photons reached the fluorescence-labeled cancer (1 mm) embedded in the deep region of the duct at a depth of 3 cm. Then, no fluorescence probes within cancer were excited by the incident photon in Figure 5F.

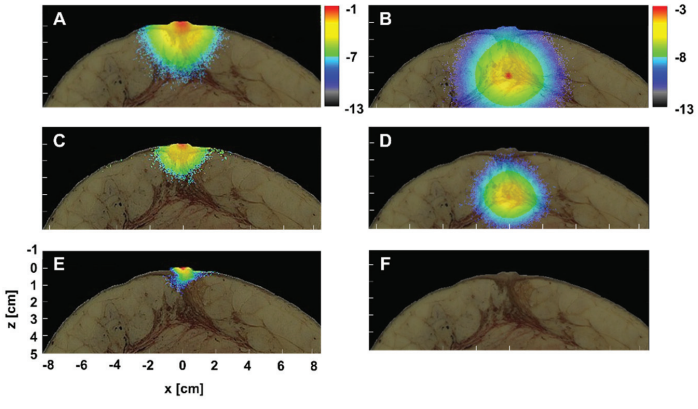

Figure 5. Fluence maps of photons associated with excitation (**A**,**C**,**E**) and emission (**B**,**D**,**F**) in the SWIR (**A**,**B**), the NIR (**C**,**D**), and the VIS (**E**,**F**). Fluorescence-labeled cancer with a diameter of 1 mm in the duct was embedded $x = 0$ at a depth of 3 cm. All maps share values on the x and z-axis of (**E**). (**A**,**C**,**E**) share the scale bar which shows the logarithmic scale in (**A**) and (**B**,**D**,**F**) share the scale bar in (**B**).

The excitation fluence signals of the NIR are distributed more widely than those of the VIS in Figure 5C. The signal shape of the excitation fluence of NIR was not isotropic and the signals were distributed a little downward. Although the incident photons excited the fluorescent probes within the cancer, the breast surface was not reached by any emission photon in Figure 5D. The distribution of the emission fluence signals was not isotropic either. In contrast to the excitation, the distribution was a little upward.

The excitation fluence signals of the SWIR were distributed widely than those of the NIR in Figure 5A. The distribution was downward and similar to that of the NIR. Sufficient incident photons from the SWIR reached the fluorescent probes within the cancer and emission photons reached the breast surface in Figure 5B. Therefore, the previous model was improved by a fluence signal distribution dependent on the contour of the breast tissue and the internal structure, and we confirmed this in three regions, VIS, NIR, and SWIR.

3.3. SWIR for the Detection of Small Breast Cancer in Deep Tissue

By the use of the improved Monte Carlo model improved above, photon behaviors in association with excitation and emission were examined in detail. Fluorescence-labeled cancer with a diameter of 1, 4, 7, and 10 mm was embedded at a depth of 1 to 2 cm. The fluorescence intensity detected on the tissue surface when the fluorescence-labeled cancer with a 1–10 mm diameter was embedded at a depth of 1 cm is shown in Figure 6A. In this study, a fluorescence intensity of more than 10 nW/cm^2 was detectable and the sensitivity of fluorescence image sensors reported previously was taken as the basis of the assessment [28,29]. Fluorescence from cancerous cells with a diameter of 10 mm was detectable in all regions of the VIS, the NIR, and the SWIR. The SWIR signal was the strongest; the VIS was 5.9% of the SWIR, and the NIR it was 23.5% of the SWIR. In the case of the 7 mm diameter, there was almost no VIS signal and the NIR signal was 17.2% that of the SWIR. As shown in the insert, the signal of the NIR in the 4 mm diameter was under the detection limit and was 12.6% of the SWIR. In the case of the 1 mm diameter, only the SWIR signal was detectable.

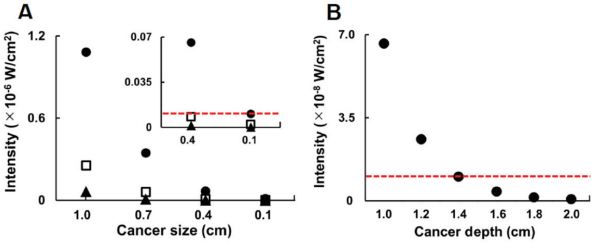

Figure 6. Effect on the detected fluorescence intensity of cancer size (**A**, 0.1–1.0 cm) and cancer depth (**B**, 1–2 cm). Insert is enlarged on the axis of the intensity. Closed circles: SWIR, Open squares: NIR, Closed triangles: VIS. The red broken line denotes the detectable intensity of 10 nW/cm^2.

Finally, as shown in Figure 6B, the detectable depth of the fluorescence from cancerous cells with a diameter of 4 mm was examined in detail. Due to the fact that no fluorescence from the VIS or the NIR from the depth of 1 cm was detectable, fluorescence-labeled cancer with SWIR alone was embedded deeper than 1 cm. At a depth of 1.2 cm, the fluorescence became weaker by 39.4% of that for 1 cm. The deepest position for cancer of a 4 mm diameter to be detectable was 1.4 cm. When the cancer was embedded deeper, the fluorescence was under the detection limit. Therefore, when the fluorescence-labeled cancer became smaller or was embedded in a deeper area, the fluorescence signal in all regions, the VIS, the NIR, and the SWIR, became weaker. However, fluorescence in the SWIR alone from cancerous cells with a diameter of 4 mm was detectable at a depth of 1.4 cm. The results show that SWIR fluorescence molecular imaging can be expected to detect breast cancer (4 mm), which is smaller than the cancer size (6 mm) detectable by MRI and sonography so far reported. Compared to the depth at which the diagnostic accuracy of sonography can be maintained (4 cm) [30], SWIR fluorescence molecular imaging may be more limited in detecting cancer, due to the depth. However, SWIR fluorescence molecular imaging has the potential advantage of distinguishing between benign and malignant tumors by the use of markers for the cancer. Furthermore, compared to MRI-sonography, the SWIR imaging system is expected to be the more practical diagnostic instrument with small size at a low running cost.

In addition to our SWIR molecular imaging for detecting early breast cancer, recently there have been remarkable advances in diagnostic methods. One of these was the early detection of circulating tumor cells in blood, an eagerly awaited noninvasive diagnosis or prognosis method [31]. In vitro assays confirmed the real time detection of cancer cells at 49 cells/mL [32]. Using a DNA biosensor based on gold nanoparticles-modified graphene oxide, breast cancer markers in the early stage were detected at a sub-nanomolar level [33]. Furthermore, when the ensemble discrete wavelet transformation as a new image processing technology was introduced to conventional mammography,

the benign/malignant ROIs (regions of interest) were predicted at a precision rate of more than 97% by microcalcification cluster classification [34]. When the SWIR molecular imaging proposed in this study is applied clinically, it can be regarded as a noninvasive diagnostic method for primary breast cancer in women, without radiation exposure.

4. Conclusions and Perspectives

In the Monte Carlo model where optical parameters were set faithfully to the internal structure of the breast tissue, photon migration in association with excitation and emission was examined in detail based on the rational mechanisms for fluorescence. SWIR fluorescence molecular imaging proved the promising for the detection of small breast cancer (4 mm) at a depth of 1.4 cm, which was difficult for MRI and sonography to detect. Our results show that it is possible to predict the presence of early-stage breast cancer with high spatial resolution using SWIR and a phantom model in which the optical parameters are accurately set in the breast structure. The SWIR molecular imaging proposed in this study is suitable as a noninvasive diagnostic method for primary breast cancer in women, without radiation exposure.

Author Contributions: Conceptualization, Y.N., T.J. and A.S.; methodology, T.J.; software, T.I.; validation, T.I. and Y.N.; data curation, T.I.; writing—original draft preparation, T.I. and Y.N.; writing—review and editing, T.J. and A.S. All authors have read and agreed to the published version of the manuscript.

Funding: This research received no external funding And The APC was funded by Nakatani Foundation for Advancement of Measuring Technologies in Biomedical Engineering.

Acknowledgments: The authors would like to thank Enago (www.enago.jp) for the English language review.

Conflicts of Interest: The authors have no conflicts of interest with any company or commercial organization.

References

1. van Dongen, J.A.; Voogd, A.C.; Fentiman, I.S.; Legrand, C.; Sylvester, R.J.; Tong, D.; van der Schueren, E.; Helle, P.A.; van Zijl, K.; Bartelink, H. Long-Term Results of a Randomized Trial Comparing Breast-Conserving Therapy with Mastectomy: European Organization for Research and Treatment of Cancer 10801 Trial. *J. Natl. Cancer Inst.* **2000**, *92*, 1143–1150. [CrossRef]
2. Silverstein, M.J.; Cohlan, B.F.; Gierson, E.D.; Furmanski, M.; Gamagami, P.; Colburn, W.J.; Lewinsky, B.S.; Waisman, J.R. Duct Carcinoma in Situ: 227 Cases without Microinvasion. *Eur. J. Cancer* **1992**, *28*, 630–634. [CrossRef]
3. Causer, P.A.; Piron, C.A.; Jong, R.A.; Plewes, D.B. Preliminary In Vivo Validation of a Dedicated Breast MRI and Sonographic Coregistration Imaging System. *Am. J. Roentgenol.* **2008**, *191*, 1203–1207. [CrossRef]
4. Wilson, R.H.; Nadeau, K.P.; Jaworski, F.B.; Tromberg, B.J.; Durkin, A.J. Review of Short-Wave Infrared Spectroscopy and Imaging Methods for Biological Tissue Characterization. *J. Biomed. Opt.* **2015**, *20*, 030901. [CrossRef] [PubMed]
5. Tsukasaki, Y.; Morimatsu, M.; Nishimura, G.; Sakata, T.; Yasuda, H.; Komatsuzaki, A.; Watanabe, T.M.; Jin, T. Synthesis and Optical Properties of Emission-Tunable PbS/CdS Core/Shell Quantum Dots for In Vivo Fluorescence Imaging in the Second Near-Infrared Window. *RSC. Adv.* **2014**, *4*, 41164–41171. [CrossRef]
6. Tong, M.; Guo, W.; Gao, W. Use of Fluorescence Imaging in Combination with Patent Blue Dye versus Patent Blue Dye Alone in Sentinel Lymph Node Biopsy in Breast Cancer. *J. Breast Cancer* **2014**, *17*, 250–255. [CrossRef] [PubMed]
7. Sugie, T.; Kassim, K.A.; Takeuchi, M.; Hashimoto, T.; Yamagami, K.; Masai, Y.; Toi, M. A Novel Method for Sentinel Lymph Node Biopsy by Indocyanine Green Fluorescence Technique in Breast Cancer. *Cancers* **2010**, *2*, 713–720. [CrossRef] [PubMed]
8. Pitsinis, V.; Wishart, G.C. Comparison of Indocyanine Green Fluorescence and Blue Dye Methods in Detection of Sentinel Lymph Nodes in Early-Stage Breast Cancer. *Ann. Surg. Oncol.* **2017**, *24*, 581–582. [CrossRef] [PubMed]
9. Kitai, T.; Inomoto, T.; Miwa, M.; Shikayama, T. Fluorescence Navigation with Indocyanine Green for Detecting Sentinel Lymph Nodes in Breast Cancer. *Breast Cancer* **2005**, *12*, 211–215. [CrossRef]

10. Tsuboi, S.; Jin, T. Shortwave-infrared (SWIR) Fluorescence Molecular Imaging Using Indocyanine Green–Antibody Conjugates for the Optical Diagnostics of Cancerous Tumours. *RSC. Adv.* **2020**, *10*, 28171–28179. [CrossRef]
11. Iida, T.; Jin, T.; Nomura, Y. Monte Carlo Modeling of Near-Infrared Fluorescence Photon Migration in Breast Tissue for Tumor Prediction. *Adv. Biomed. Eng.* **2020**, *9*, 100–105. [CrossRef]
12. Li, T.; Li, Y.; Sun, Y.; Duan, M.; Peng, L. Effect of Head Model on Monte Carlo Modeling of Spatial Sensitivity Distribution for Functional Near-Infrared Spectroscopy. *J. Innov. Opt. Health Sci.* **2015**, *8*, 1550024. [CrossRef]
13. Li, T.; Xue, C.; Wang, P.; Li, Y.; Wu, L. Photon Penetration Depth in Human Brain for Light Stimulation and Treatment: A Realistic Monte Carlo Simulation Study. *J. Innov. Opt. Health Sci.* **2017**, *10*, 1743002. [CrossRef]
14. Iida, T.; Yamato, H.; Jin, T.; Nomura, Y. Optimal Focus Evaluated Using Monte Carlo Simulation in Non-Invasive Neuroimaging in the Second near-Infrared Window. *MethodsX* **2019**, *6*, 2367–2373. [CrossRef] [PubMed]
15. Yamato, H.; Iida, T.; Jin, T.; Nomura, Y. Monte Carlo Evaluation of In Vivo Neuroimaging Using Quantum Dots with Fluorescence in the Second Window of Near Infrared Region. *Adv. Biomed. Eng.* **2019**, *8*, 105–109. [CrossRef]
16. Hasegawa, Y.; Yamada, Y.; Tamura, M.; Nomura, Y. Monte Carlo Simulation of Light Transmission through Living Tissues. *Appl. Opt.* **1991**, *30*, 4515–4520. [CrossRef]
17. Visible Human Project. Available online: https://www.nlm.nih.gov/research/visible/visible_human.html (accessed on 15 August 2020).
18. Salomatina, E.; Jiang, B.; Novak, J.; Yaroslavsky, A.N. Optical Properties of Normal and Cancerous Human Skin in the Visible and Near-Infrared Spectral Range. *J. Biomed. Opt.* **2006**, *11*, 064026. [CrossRef]
19. Jacques, S.L. Optical Properties of Biological Tissues: A Review. *Phys. Med. Biol.* **2013**, *58*, R37–R61. [CrossRef]
20. Troy, T.L.; Page, D.L.; Sevick-Muraca, E.M. Optical Properties of Normal and Diseased Breast Tissues: Prognosis for Optical Mammography. *J. Biomed. Opt.* **1996**, *1*, 342–355. [CrossRef]
21. Ding, H.; Lu, J.Q.; Wooden, W.A.; Kragel, P.J.; Hu, X.H. Refractive Indices of Human Skin Tissues at Eight Wavelengths and Estimated Dispersion Relations between 300 and 1600 nm. *Phys. Med. Biol.* **2006**, *51*, 1479–1489. [CrossRef]
22. Prince, S.; Malarvizhi, S. Monte Carlo Simulation of NIR Diffuse Reflectance in the Normal and Diseased Human Breast Tissues. *BioFactors* **2007**, *30*, 255–263. [CrossRef] [PubMed]
23. Hayreh, S.S. Recent Advances in Fluorescein Fundus Angiography. *Br. J. Ophthalmol.* **1974**, *58*, 391–412. [CrossRef]
24. Altan-Yaycioglu, R.; Akova, Y.A.; Akca, S.; Yilmaz, G. Inflammation of the Posterior Uvea: Findings on Fundus Fluorescein and Indocyanine Green Angiography. *Ocul. Immunol. Inflamm.* **2006**, *14*, 171–179. [CrossRef] [PubMed]
25. Wang, L.; Jacques, S.L.; Zheng, L. MCML—Monte Carlo Modeling of Light Transport in Multi-Layered Tissues. *Comput. Methods Programs Biomed.* **1995**, *47*, 131–146. [CrossRef]
26. Matsumoto, M.; Nishimura, T. Mersenne Twister: A 623-Dimensionally Equidistributed Uniform Pseudo-Random Number Generator. *ACM Trans. Model. Comput. Simul.* **1998**, *8*, 3–30. [CrossRef]
27. Jacques, S.L. Light Distributions from Point, Line and Plane Sources for Photochemical Reactions and Fluorescence in Turbid Biological Tissues. *Photochem. Photobiol.* **1998**, *67*, 23–32. [CrossRef]
28. Nan, L.; Zhiliang, H.; Ran, L. A CMOS Detector System for Fluorescent Bio-Sensing Application. In Proceedings of the 2008 IEEE Asian Solid-State Circuits Conference (ASSCC), Fukuoka, Japan, 3–5 November 2008.
29. Murari, K.; Ralph, E.C.; Nitish, V.T.; Cauwenberghs, G. A CMOS In-Pixel CTIA High-Sensitivity Fluorescence Imager. *IEEE. Trans. Biomed. Circuits Syst.* **2011**, *5*, 449–458. [CrossRef]
30. Guo, R.; Lu, G.; Qin, B.; Fei, B. Ultrasound Imaging Technologies for Breast Cancer Detection and Management: A Review. *Ultrasound Med. Biol.* **2018**, *44*, 37–70. [CrossRef]
31. De Mattos-Arruda, L.; Cortes, J.; Santarpia, L.; Vivancos, A.; Tabernero, J.; Jorge S Reis-Filho, J.S.R.; Seoane, J. Circulating Tumour Cells and Cell-free DNA as Tools for Managing Breast Cancer. *Nat. Rev. Clin. Oncol.* **2013**, *10*, 377–389. [CrossRef]

32. Loyez, M.; Hassan, E.M.; Lobry, M.; Liu, F.; Caucheteur, C.; Wattiez, R.; DeRosa, M.C.; Willmore, W.G.; Albert, J. Rapid Detection of Circulating Breast Cancer Cells using a Multiresonant Optical Fiber Aptasensor with Plasmonic Amplification. *ACS Sens.* **2020**, *5*, 454–463. [CrossRef]
33. Saeed, A.A.; Sánchez, J.L.A.; O'Sullivan, C.K.; Abbas, M.N. DNA biosensors based on gold nanoparticles-modified graphene oxide for the detection of breast cancer biomarkers for early diagnosis. *Bioelectrochemistry* **2017**, *118*, 91–99. [CrossRef] [PubMed]
34. Fanizzi, A.; Basile, T.M.; Losurdo, L.; Bellotti, L.; Bottigli, U.; Campobasso, F.; Didonna, V.; Fausto, A.; Massafra, R.; Tagliafico, A.; et al. Ensemble Discrete Wavelet Transform and Gray-Level Co-Occurrence Matrix for Microcalcification Cluster Classification in Digital Mammography. *Appl. Sci.* **2019**, *9*, 5388. [CrossRef]

diagnostics

MDPI

Article

Blood Vessel Imaging at Pre-Larval Stages of Zebrafish Embryonic Development

Alexander S. Machikhin [1], Mikhail V. Volkov [2], Alexander B. Burlakov [3], Demid D. Khokhlov [1,*] and Andrey V. Potemkin [2]

[1] Laboratory of Acousto-optical Spectroscopy, Scientific and Technological Center of Unique Instrumentation, Russian Academy of Sciences, 117342 Moscow, Russia; machikhin@ntcup.ru
[2] Department of Applied Optics, University ITMO, 190000 Saint Petersburg, Russia; ph-m.volkov@yandex.ru (M.V.V.); appanpotemkin@gmail.com (A.V.P.)
[3] Department of Ichthyology, Faculty of Biology, Lomonosov Moscow State University, 119991 Moscow, Russia; alexander_burl08@rambler.ru
* Correspondence: khokhlov.dd@ntcup.ru

Received: 31 August 2020; Accepted: 28 October 2020; Published: 30 October 2020

Abstract: The zebrafish (*Danio rerio*) is an increasingly popular animal model biological system. In cardiovascular research, it has been used to model specific cardiac phenomena as well as to identify novel therapies for human cardiovascular disease. While the zebrafish cardiovascular system functioning is well examined at larval stages, the mechanisms by which vessel activity is initiated remain a subject of intense investigation. In this research, we report on an in vivo stain-free blood vessel imaging technique at pre-larval stages of zebrafish embryonic development. We have developed the algorithm for the enhancement, alignment and spatiotemporal analysis of bright-field microscopy images of zebrafish embryos. It enables the detection, mapping and quantitative characterization of cardiac activity across the whole specimen. To validate the proposed approach, we have analyzed multiple data cubes, calculated vessel images and evaluated blood flow velocity and heart rate dynamics in the absence of any anesthesia. This non-invasive technique may shed light on the mechanism of vessel activity initiation and stabilization as well as the cardiovascular system's susceptibility to environmental stressors at early developmental stages.

Keywords: zebrafish; embryonic development; cardiovascular system; in vivo imaging; optical mapping; non-invasive measurements

1. Introduction

The zebrafish has emerged to become a common and useful vertebrate animal model for cardiovascular research in recent years [1–4]. It is a powerful genetic system to study cardiac function due to several advantages. The ability to implement the main modern genome editing tools and techniques, including engineered nucleases (meganucleases, zinc-finger nucleases, transcription activator-like effector nucleases) and CRISPR gene editing, have been demonstrated for *Danio rerio* [5–8]. Various zebrafish transgenic lines can be used to enhance the visualization contrast of different transformation processes [9–11]. The use of the zebrafish as a model organism is of particular interest for the analysis of innate immunity [12] and for the study of viral [13–15], bacterial [16,17] and fungal infections [18,19].

Small size, ease of maintenance, short reproduction cycle with multiple (up to 2000) embryos and short period (3 days) of embryonic development make *Danio rerio* a convenient object for continuous observation and experimental research of the mechanisms by which genetic and disease-related modifications are being passed to the offspring.

Cardiovascular system functional characteristics of zebrafish are well studied in various conditions and in the whole life cycle. Their accurate analysis and patterning may indicate developmental disorders and presence of pathology at the very early stages. Detailed studies of cardiovascular system function are of great value for understanding cardiac failures and identifying novel therapies for human cardiovascular disease [20–22].

Zebrafish embryos develop in the external environment and are relatively small-sized and transparent in the optical wavelength range. These features allow one to easily visualize the circulatory system structure [23,24], observe heart and blood vessel formation and development, and simulate cardiovascular diseases [25–28]. While the zebrafish cardiovascular system functioning is well examined at larval stages [24,29–31], the mechanisms by which the vessel activity is initiated under natural conditions remain a subject of intense investigation. At the pharyngula stage (24–40 hpf) that precedes hatching [32], invasive procedures (excising, fixation, sectioning and staining) are not effective for real-time monitoring due to the fast-changing and vulnerable state of the emerging cardiovascular system.

Thus, biomedical optical imaging techniques are remaining promising in the field of in vivo zebrafish studies [2,33]. Though heart function analysis from bright field time-lapse image sequences [31,33–35] as well as quantitative research of zebrafish heartbeat initiation and stabilization [36] have been reported, blood vessel imaging during early embryonic development has not been carried out. Due to constant embryo motion within the shell, conventional processing algorithms based on image subtraction are inefficient and require precise initial image stabilization. In this research, we show that a combination of time-lapse bright-field microscopy and an advanced image processing technique represents an effective approach to in vivo stain-free cardiac activity mapping across the whole specimen and quantitative analysis of cardiovascular performance even at pre-larval developmental stages in the absence of any anesthesia.

2. Materials and Methods

2.1. Experimental Animals

Zebrafish embryos were from an existing stock at the Biological Faculty of Lomonosov Moscow State University. Before embryo collection, single species groups of males and females were kept by local aquarists in isolated 10 L glass aquaria at a temperature of 26 °C with the aquaria illumination turned on for 12 h daily. The selected groups were fed three times a day ad libitum on flake and *Artemia*. For embryo collection, males and females were placed together in a breeding tank and the embryos were collected immediately post-fertilization. A mixture of individuals from several different breeding groups was used during the experiment to maximize genetic variation among embryos. The two-cell development stage was used as initial time point during observation because the exact time of fertilization was difficult to determine. The development, survival rate and morphology of the collected embryos was not affected in comparison to the control group not subjected to the study.

2.2. Experimental Setup

The conventional off-the-shelf trinocular transmitted light bright-field microscope is the basis of the experimental setup (Figure 1). A Koehler system was implemented to achieve uniform illumination of the object. Images were formed by an optical system assembled of a flat field corrected apochromatic objective (10× NA 0.25) and a standard tube lens. To acquire the digital images, the complementary metal-oxide-semiconductor active-pixel image sensor (IDS uEye UI-3060CP-M-GL Rev.2, 1/1.2″, 1936 × 1216 pixels) was installed onto the camera tube. The image sensor was connected to the PC for raw data acquisition and storage. The image processing and data analysis pipeline is described in Section 2.3.

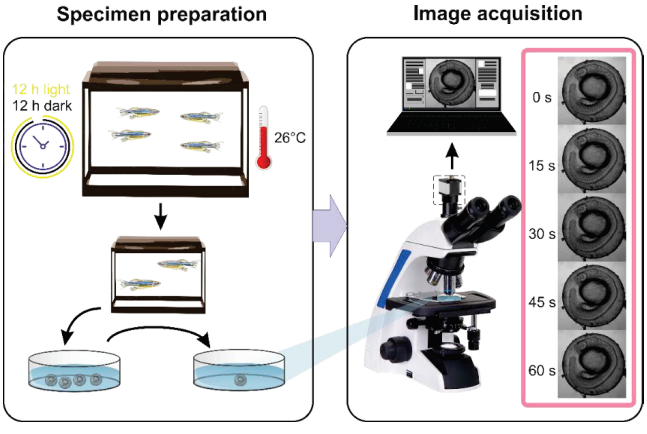

Figure 1. Experimental protocol.

2.3. Experimental Protocol

The single experimental dataset contained 3000 12-bit grayscale digital images with 1200 × 1200 pixel resolution obtained during a 60-s time series (50 fps). For preliminary geometrical calibration of the imaging setup, the images of the test chart were captured before the experimental dataset acquisition. The geometrical calibration procedure is an essential step for the magnification determining and estimation of the real image distortions. During image acquisition, the inspected embryo may move and rotate within the shell, and illumination conditions and background characteristics may also vary. Data analysis procedures require pre-processing of raw images to crop the region of interest, compensate for movement and eliminate the illumination non-uniformity (Figure 2). After these procedures, we obtained the well-matched and intensity-corrected spatiotemporal data cube $I(x,y,t)$ including time-domain dependences $I(t)$ for each image pixel with spatial coordinates x,y.

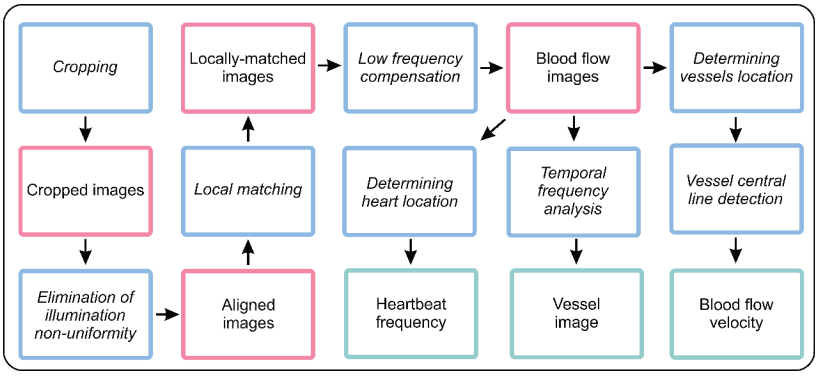

Figure 2. Image processing pipeline.

Figure 3 illustrates the main image pre-processing stages shown in pink color in Figure 2. First, the microscopic images of 26 hpf unhatched zebrafish embryo in a lateral position were to be cropped down to the embryo dimensions (Figure 3a). Second, to compensate for illumination non-uniformity and align the average intensity of all images in a series, we subtracted a smoothed image and constant term 127 (Figure 3b). Third, to ensure pixel-to-pixel matching of all images, we calculated local motion vectors and matched the images with respect to their directions and lengths. Figure 3c shows a locally matched image with crosses indicating the positions of each grid knot in the first (black) and

the last (white) image of the sequence. Shape and intensity of the temporal signal $I(t)$ in each pixel of the obtained data cube $I(x,y,t)$ characterizes morphogenetic events occurring during embryonic development. The blood flow changes may be detected by the periodic variations of the transmitted light intensity since blood cells absorb light more strongly than the surrounding tissues [37]. Plotting the spectrum of the temporal signal using Fourier transform allowed detection of the dominant frequencies, which corresponded to the cardiovascular activity. After obtaining the intensity deviation values in each image pixel, we could subtract the blood-free background and consider only the pixels with blood flow related to significant intensity oscillations. Thus, we obtained a series of well-matched blood flow images ready for cardiac activity analysis (Figure 3d). The blood circulation was clearly visible throughout the full cardiac cycle (Supplementary Video).

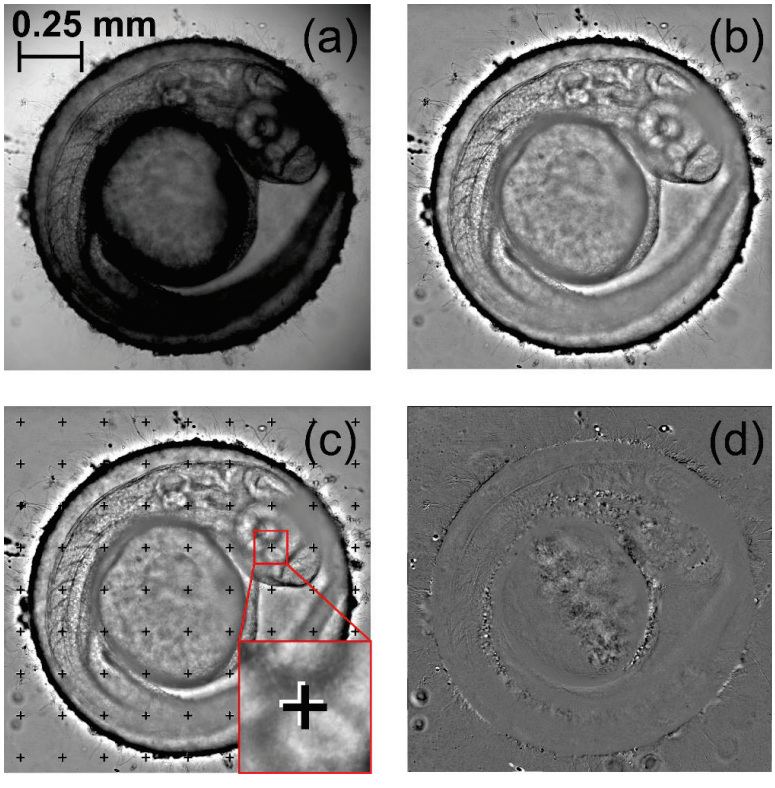

Figure 3. Stages of image pre-processing: (**a**) cropped image, (**b**) aligned image, (**c**) locally matched image and (**d**) blood flow image.

3. Results

From the series of blood flow images (Figure 4a), we could calculate the intensity of blood volume changes as the ratio of high- and low-frequency spectral components in the Fourier spectrum. Thus, we obtained the vessel image. It vividly depicts the tissues associated with cardiac activity, i.e., the spatial structure of the cardiovascular system existing at this developmental stage (Figure 4b). The heart and the system of vessels that carry blood throughout the embryo's body may be clearly identified on the blood-free background [32,38,39]. The calculated vessel image in Figure 4b demonstrates the efficiency of the proposed processing algorithm and shows the main elements of the existing cardiovascular system. Vessels are named according to commonly used classification [40]: ACeV—anterior cerebral

vein; BA—basilar artery; CA—caudal artery; CaDI—caudal division of the internal carotid artery; CCV—common cardinal vein; CV—caudal vein; DA—dorsal aorta; MsA—mesencephalic artery; MsV—mesencephalic vein; PCV—posterior cardinal vein; PHBC—primordial hindbrain channel; PHS—primary head sinus; PICA—primitive internal carotid artery; PMBC—primordial midbrain channel; PMsA—primitive mesencephalic artery; PPrA—primitive prosencephalic artery.

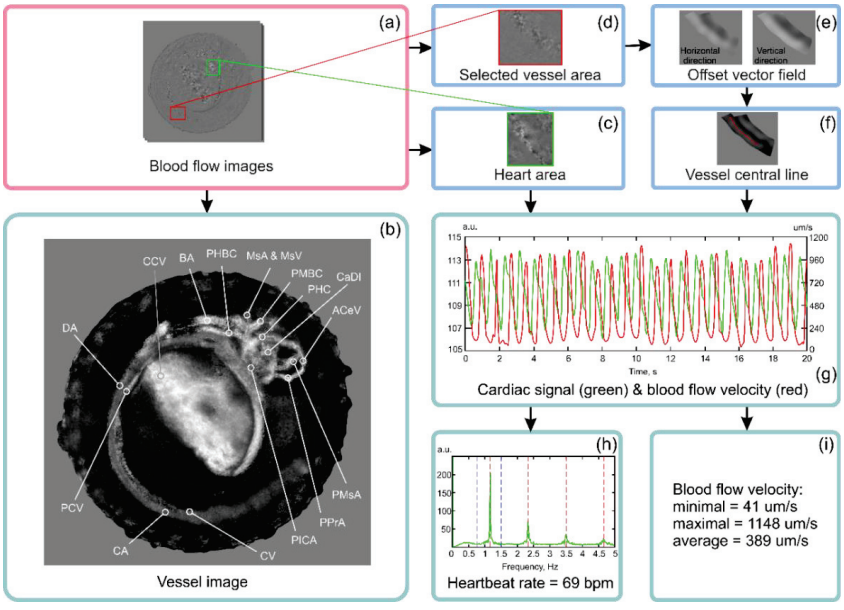

Figure 4. Example of cardiovascular data extraction using the proposed algorithm: (**a**) blood flow images, (**b**) vessel image, (**c**) the selected heart area, (**d**) the selected vessel area, (**e**) offset vector field examples, (**f**) the detected vessel central line, (**g**) cardiac signal and blood flow velocity examples, (**h**) cardiac signal spectrum, (**i**) blood flow velocity range and average value.

Besides the two-dimensional mapping of cardiac activity, the obtained spatiotemporal data cube $I(x,y,t)$ allowed calculation of the heartbeat rate and blood flow velocity—quantitative parameters characterizing cardiovascular functioning. The heart location (Figure 4c) could be detected automatically as the image pixel group demonstrating the most intensive and constant oscillations. Heart area detection in the blood flow images allowed accurate cardiac beat detection and heart rate monitoring. The obtained temporal signals in the heart area had the correct shape and spectrum [30,34]. In the experiment shown in Figure 4, the measurement result for the heart rhythm was 69 bpm (Figure 4h), which is in good agreement with the values obtained in other studies for this stage of zebrafish development [36,41].

Pulsatile flow of blood cells could be easily detected in zebrafish embryo blood vessels from the beginning of circulation at 24 hpf. To demonstrate blood flow velocity measurement, we selected one of the vessel areas (Figure 4d) and carried out its morphological analysis in order to detect the offset vector field (Figure 4e) and central line of the vessel (Figure 4f) and to calculate normal direction at each point. Implementation of this procedure allowed the alignment of the pixels corresponding to the blood vessel into a straight line [42] to calculate the blood flow velocity. Since the blood vessel pixels were aligned, the relative shift between consequent images could be estimated. Then the blood flow velocity could be determined as the ratio of this shift to the time interval between the moments of image acquisition. The obtained blood flow velocity signal was compared with the temporal signal in the heart area to validate the proposed velocity measurement technique. In the diagram in Figure 4g,

the curves corresponding to these signals are superimposed so that their mean values are equal. Heart area temporal signal and blood flow velocity signal had the same period of 0.86 s and a constant relative temporal shift of 0.35 s. Average blood flow velocity was 389 μm/s, which is close to the value measured using quantitative fluorescent imaging at the larval stage (Figure 4i) [24].

We implemented the described image processing algorithms in C++ using parallel computing on multiple CPU cores. The software includes modules for camera control and image acquisition, preprocessing and data analysis. The total processing time of 3000 12-bit monochrome images with 1200 × 1200 resolution was about 12 min using Intel's 8th generation 4-core processor. The most time-consuming processes were local matching (18 min) and vessel image calculation (1 min). Further optimization may be related to GPU computing.

Figure 5 illustrates the vessel activity across the whole embryo and the heart rate at the stages from 22 hpf to 27 hpf. Due to the absence of anesthesia, embryos moved and were randomly oriented in chorions. For this reason, the viewing angle and orientation of the embryos differed. Figure 5 shows temporal dynamics of the key features indicating the state of the embryos and suitability for non-invasive measurements at early developmental stages. The experiments demonstrated a continuous increase of the heartbeat rate and gradual activation of vasculature initiated by the heart functioning. Such measurements are important for predicting the further development of the embryo, in particular the time of its hatching.

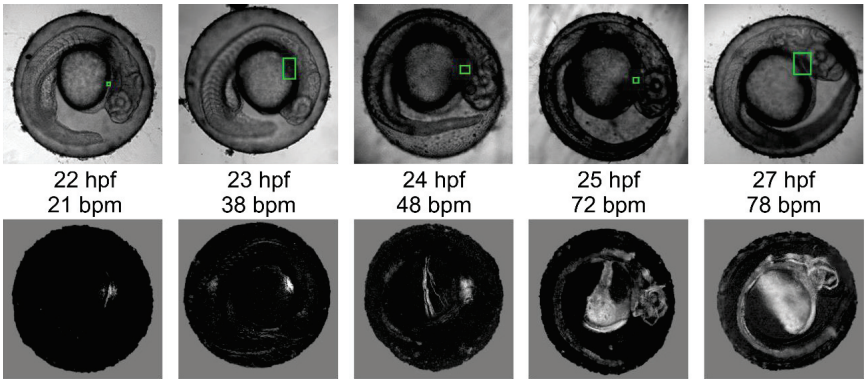

Figure 5. Calculated vessel images (green rectangles indicate the detected heart area).

4. Discussion

As a model biological system, the zebrafish possesses numerous advantages: rapid embryonic development, fully sequenced genome, low cost, etc. This organism also has a unique collection of features at pre-larval developmental stages: large size, optical transparency of the embryo's interior and relatively slow embryo movements inside the shell. This makes zebrafish an attractive model for in vivo study of the formation and functioning of its cardiovascular system using optical imaging techniques.

In this study, we have demonstrated that time-lapse bright-field microscopy and digital signal processing allow blood vessel imaging of a living embryo as well as heartbeat and blood flow velocity measurements without any anesthesia. In contrast to straightforward approaches based on image subtraction, the described pre-processing procedure enables the compensation of shifts and rotations between images and their pixel-to-pixel matching necessary for accurate quantitative characterization of cardiac activity.

The proposed algorithm is applicable for processing the images obtained by various microscope setups widely used for in vivo studies of zebrafish embryos. It can complement optical coherence tomography, acoustic microscopy and other imaging techniques by adding cardiac activity mapping capability.

5. Conclusions

The presented algorithm does not require the use of contrast agents and may be used to visualize cardiac morphology and measure dynamics in zebrafish embryos without anesthesia. We believe that it may help to shed light on the mechanisms by which the cardiovascular system's activity is initiated under natural conditions. Continuous study of the heart function and vessel structure transformation using the proposed algorithm may contribute to recognizing possible warning signs of developmental disorders at the very early stages and understanding the symptoms of various diseases, i.e., help to improve the techniques for their correct diagnosis and timely treatment.

Further development of this technique may include the interactive analysis of vessel structure and function in both normal and pathological condition at embryonic stages, as well as detecting and studying the changes in zebrafish cardiovascular system initiation, development and functioning induced by various environmental stressors.

6. Ethics

The authors confirm that all methods were carried out in accordance with relevant guidelines and regulations and were approved by the Lomonosov Moscow State University Bioethics Committee (Protocol #108-0).

7. Data Accessibility

The raw image sequence for the 26 hpf unhatched zebrafish embryo is available from Mendeley Data (http://dx.doi.org/10.17632/kj7mkcw8vn.1).

Supplementary Materials: Supplementary video presenting the locally matched images, blood flow images and a resulting vessel image is available from Mendeley Data (http://dx.doi.org/10.17632/kj7mkcw8vn.1).

Author Contributions: A.S.M. and A.B.B. conceived and designed the project; M.V.V. and D.D.K. acquired data; A.S.M., M.V.V. and A.V.P. analyzed data; A.S.M. drafted the article; and A.B.B., M.V.V. and D.D.K. revised it critically for important intellectual content. All authors gave final approval of the version to be published and agreed to be accountable for all aspects of the work. All authors have read and agreed to the published version of the manuscript.

Funding: This study is supported by the Ministry of Science and Higher Education of the Russian Federation (project 0069-2019-0010). Experiments were performed using the equipment of the Center for Collective Use of the Scientific and Technological Center of Unique Instrumentation of the Russian Academy of Sciences.

Acknowledgments: The experiments were carried out on the base of the Center for Collective Use of the Scientific and Technological Center of Unique Instrumentation of the Russian Academy of Sciences.

Conflicts of Interest: The authors declare no conflict of interests.

References

1. Kawasaki, T.; Maeno, A.; Shiroishi, T.; Sakai, N. Development and growth of organs in living whole embryo and larval grafts in zebrafish. *Sci. Rep. UK* **2017**, *7*, 16508. [CrossRef] [PubMed]
2. Yalcin, H.C.; Amindari, A.; Butcher, J.T.; Althan, A.; Yacoub, M. Heart function and hemodynamic analysis for zebrafish embryos. *Dev. Dynam.* **2017**, *246*, 868–880. [CrossRef] [PubMed]
3. Lawson, N.D.; Weinstein, B.M. Arteries and veins: Making a difference with zebrafish. *Nat. Rev. Genet.* **2002**, *3*, 674–682. [CrossRef] [PubMed]
4. Konno, M.; Asai, A.; Kitagawa, T.; Yabumoto, M.; Ofusa, K.; Arai, T.; Hirotsu, T.; Doki, Y.; Eguchi, H.; Ishii, H. State-of-the-Art Technology of Model Organisms for Current Human Medicine. *Diagnostics* **2020**, *10*, 392. [CrossRef]
5. Soroldoni, D.; Hogan, B.M.; Oates, A.C. Simple and efficient transgenesis with meganuclease constructs in zebrafish. *Methods Mol. Biol.* **2009**, *546*, 117–130. [CrossRef]
6. Foley, J.E.; Maeder, M.L.; Pearlberg, J.; Joung, J.K.; Peterson, R.T.; Yeh, J.R. Targeted mutagenesis in zebrafish using customized zinc-finger nucleases. *Nat. Protoc.* **2009**, *4*, 1855–1867. [CrossRef]

7. Hwang, W.Y.; Peterson, R.T.; Yeh, J.R. Methods for targeted mutagenesis in zebrafish using TALENs. *Methods* **2014**, *69*, 76–84. [CrossRef] [PubMed]
8. Du, X.; Xu, B.; Zhang, Y.; Du, J. A transgenic zebrafish model for in vivo long-term imaging of retinotectal synaptogenesis. *Sci. Rep. UK* **2018**, *8*, 14077. [CrossRef] [PubMed]
9. Marquart, G.D.; Tabor, K.M.; Brown, M.; Strykowski, J.L.; Varshney, G.K.; LaFave, M.C.; Mueller, T.; Burgess, S.M.; Higashijima, S.; Burgess, H.A. A 3D searchable database of transgenic zebrafish Gal4 and Cre lines for functional neuroanatomy studies. *Front. Neural Circuits* **2015**, *9*, 78. [CrossRef] [PubMed]
10. Mathias, J.R.; Perrin, B.J.; Liu, T.X.; Kanki, J.; Look, A.T.; Huttenlocher, A. Resolution of inflammation by retrograde chemotaxis of neutrophils in transgenic zebrafish. *J. Leukoc. Biol.* **2006**, *80*, 1281–1288. [CrossRef]
11. Ellett, F.; Pase, L.; Hayman, J.W.; Andrianopoulos, A.; Lieschke, G.J. mpeg1 promoter transgenes direct macrophage-lineage expression in zebrafish. *Blood* **2011**, *117*, e49–e56. [CrossRef] [PubMed]
12. Novoa, B.; Figueras, A. Zebrafish: Model for the study of inflammation and the innate immune response to infectious diseases. *Adv. Exp. Med. Biol.* **2012**, *946*, 253–275. [CrossRef] [PubMed]
13. Gabor, K.A.; Goody, M.F.; Mowel, W.K.; Breitbach, M.E.; Gratacap, R.L.; Witten, P.E.; Kim, C.H. Influenza A virus infection in zebrafish recapitulates mammalian infection and sensitivity to anti-influenza drug treatment. *Dis. Model. Mech.* **2014**, *7*, 1227–1237. [CrossRef]
14. Burgos, J.S.; Ripoll-Gomez, J.; Alfaro, J.M.; Sastre, I.; Valdivieso, F. Zebrafish as a new model for herpes simplex virus type 1 infection. *Zebrafish* **2008**, *5*, 323–333. [CrossRef]
15. Ding, C.B.; Zhang, J.P.; Zhao, Y.; Peng, Z.G.; Song, D.Q.; Jiang, J.D. Zebrafish as a potential model organism for drug test against hepatitis C virus. *PLoS ONE* **2011**, *6*, e22921. [CrossRef]
16. Prajsnar, T.K.; Cunliffe, V.T.; Foster, S.J.; Renshaw, S.A. A novel vertebrate model of Staphylococcus aureus infection reveals phagocyte-dependent resistance of zebrafish to non-host specialized pathogens. *Cell. Microbiol.* **2008**, *10*, 2312–2325. [CrossRef] [PubMed]
17. Bernut, A.; Dupont, C.; Sahuquet, A.; Herrmann, J.L.; Lutfalla, G.; Kremer, L. Deciphering and Imaging Pathogenesis and Cording of Mycobacterium abscessus in Zebrafish Embryos. *J. Vis. Exp.* **2015**, *103*, 53130. [CrossRef] [PubMed]
18. Brothers, K.M.; Wheeler, R.T. Non-invasive imaging of disseminated candidiasis in zebrafish larvae. *J. Vis. Exp.* **2012**, *65*, e4051. [CrossRef]
19. Voelz, K.; Gratacap, R.L.; Wheeler, R.T. A zebrafish larval model reveals early tissue-specific innate immune responses to Mucor circinelloides. *Dis. Models Mech.* **2015**, *8*, 1375–1388. [CrossRef]
20. Brown, D.R.; Samsa, L.A.; Qian, L.; Liu, J. Advances in the study of heart development and disease using zebrafish. *J. Cardiovasc. Dev. Dis.* **2016**, *3*, 13. [CrossRef]
21. Bakkers, J. Zebrafish as a model to study cardiac development and human cardiac disease. *Cardiovasc. Res.* **2011**, *91*, 279–288. [CrossRef]
22. Asnani, A.; Peterson, R.T. The zebrafish as a tool to identify novel therapies for human cardiovascular disease. *Dis. Models Mech.* **2014**, *7*, 763–767. [CrossRef] [PubMed]
23. Major, R.J.; Poss, K.D. Zebrafish heart regeneration as a model for cardiac tissue repair. *Drug Discov. Today Dis. Model.* **2007**, *4*, 219–225. [CrossRef] [PubMed]
24. Watkins, S.C.; Maniar, S.; Mosher, M.; Roman, B.L.; Tsang, M.; St Croix, C.M. High resolution imaging of vascular function in zebrafish. *PLoS ONE* **2012**, *7*, e44018. [CrossRef]
25. Mably, J.D.; Childs, S.J. Developmental physiology of the zebrafish cardiovascular system. *Fish Physiol.* **2010**, *29*, 249–287. [CrossRef]
26. Liu, J.; Stainier, D.Y. Zebrafish in the study of early cardiac development. *Circ. Res.* **2012**, *110*, 870–874. [CrossRef]
27. Giardoglou, P.; Beis, D. On zebrafish disease models and matters of the heart. *Biomedicines* **2019**, *7*, 15. [CrossRef] [PubMed]
28. Gut, P.; Reischauer, S.; Stainier, D.Y.R.; Arnaout, R. Little fish, big data: Zebrafish as a model for cardiovascular and metabolic disease. *Physiol. Rev.* **2017**, *97*, 889–938. [CrossRef]
29. Pylatiuk, C.; Sanchez, D.; Mikut, R.; Alshut, R.; Reischl, M.; Hirth, S.; Rottbauer, W.; Just, S. Automatic zebrafish heartbeat detection and analysis for zebrafish embryos. *Zebrafish* **2014**, *11*, 379–383. [CrossRef]
30. De Luca, E.; Zaccaria, G.M.; Hadhoud, M.; Rizzo, G.; Ponzini, R.; Morbiducci, U.; Santoro, M.M. ZebraBeat: A flexible platform for the analysis of the cardiac rate in zebrafish embryos. *Sci. Rep. UK* **2014**, *4*, 4898. [CrossRef]

31. Kang, C.P.; Tu, H.C.; Fu, T.F.; Wu, J.M.; Chu, P.H.; Chang, D.T. An automatic method to calculate heart rate from zebrafish larval cardiac videos. *BMC Bioinform.* **2018**, *19*, 169. [CrossRef] [PubMed]
32. Kimmel, C.B.; Ballard, W.W.; Kimmel, S.R.; Ullmann, B.; Schilling, T.F. Stages of embryonic development of the zebrafish. *Dev. Dynam.* **1995**, *203*, 253–310. [CrossRef] [PubMed]
33. Weber, M.; Huisken, J. In vivo imaging of cardiac development and function in zebrafish using light sheet microscopy. *Swiss. Med. Wkly.* **2015**, *145*, w14227. [CrossRef] [PubMed]
34. Chan, P.K.; Lin, C.C.; Cheng, S.H. Noninvasive technique for measurement of heartbeat regularity in zebrafish (*Danio rerio*) embryos. *BMC Biotechnol.* **2009**, *9*, 11. [CrossRef] [PubMed]
35. Machikhin, A.; Burlakov, A.; Volkov, M.; Khokhlov, D. Imaging photoplethysmography and videocapillaroscopy enable non-invasive study of zebrafish cardiovascular system functioning. *J. Biophotonics* **2020**, *13*, e202000061. [CrossRef]
36. Gierten, J.; Pylatiuk, C.; Hammouda, O.T.; Schock, C.; Stegmaier, J.; Wittbrodt, J.; Gehrig, J.; Loosli, F. Automated high-throughput heartbeat quantification in medaka and zebrafish embryos under physiological conditions. *Sci. Rep. UK* **2020**, *10*, 2046. [CrossRef] [PubMed]
37. Moraes, J.L.; Rocha, M.X.; Vasconcelos, G.G.; Vasconcelos Filho, J.E.; de Albuquerque, V.H.C.; Alexandria, A.R. Advances in photopletysmography signal analysis for biomedical applications. *Sensors* **2018**, *18*, 1894. [CrossRef]
38. Gore, A.V.; Monzo, K.; Cha, Y.R.; Pan, W.; Weinstein, B.M. Vascular development in the zebrafish. *Cold Spring Harb. Perspect. Med.* **2012**, *2*, a006684. [CrossRef]
39. Kunz, Y. *Developmental Biology of Teleost Fishes*; Springer: Dordrecht, The Netherlands, 2004. [CrossRef]
40. Isogai, S.; Horiguchi, M.; Weinstein, B.M. The vascular anatomy of the developing zebrafish: An atlas of embryonic and early larval development. *Dev. Biol.* **2001**, *230*, 278–301. [CrossRef]
41. Ibrahim, M.; Balakrishnan, A.; Prakash, S.; Lee, H.J. Effect of ethanol exposure on heart development in zebra fish (*Danio rerio*) embryos. *Int. J. Anat. Sci.* **2014**, *5*, 26–33.
42. Volkov, M.V.; Margaryants, N.B.; Potemkin, A.V.; Volynsky, M.A.; Gurov, I.P.; Mamontov, O.V.; Kamshilin, A.A. Video capillaroscopy clarifies mechanism of the photoplethysmographic waveform appearance. *Sci. Rep. UK* **2017**, *7*, 13298. [CrossRef]

diagnostics

MDPI

Article

Raman Spectroscopy of Changes in the Tissues of Teeth with Periodontitis

Elena Timchenko [1,*], Pavel Timchenko [1], Larisa Volova [2], Oleg Frolov [3], Maksim Zibin [4] and Irina Bazhutova [5]

1 Department of Laser and Biotechnical Systems, Samara National Research University, 443086 Samara, Russia; Timpavel@mail.ru
2 Research and Production Center "Samara Tissue Bank", Samara State Medical University, 443079 Samara, Russia; volovalt@yandex.ru
3 Department of Physics, Samara National Research University, 443086 Samara, Russia; owl-63@ya.ru
4 «DIAMANT» Dental Clinic, 443090 Samara, Russia; zybin_m.a@mail.ru
5 Department of Dentistry, Samara State Medical University, 443079 Samara, Russia; docba@mail.ru
* Correspondence: laser-optics.timchenko@mail.ru; Tel.: +7-927-7111-387

Received: 15 September 2020; Accepted: 20 October 2020; Published: 28 October 2020

Abstract: The results of experimental studies of the tissues of teeth with periodontitis, using the Raman spectroscopy method, are presented in this work. Spectral changes in the tissues of teeth with periodontitis were identified, and the results can be used for the correction of treatment of this disease in dental practice. Criteria for the noninvasive diagnosis of periodontitis, based on changes in tooth enamel spectral properties, were developed.

Keywords: raman spectroscopy; optical diagnostic; periodontitis; tooth tissues; biophotonics; calculus

1. Introduction

Chronic periodontitis is a serious and widespread periodontal pathology that causes significant impairment to dentoalveolar system functions, with damage to supporting tooth structures and the loss of teeth [1]. Periodontitis is mostly spread (60–65%) among people over age 30 [2]. However, the percentage of young patients with a severe form of chronic periodontitis has increased to 11.2%, and among people over age 65, it is 30% [3]. Current data indicate that periodontitis is a polyethiological disease [4]. Periodontitis is an insidious disease because the initial signs of inflammatory processes often remain unnoticed, and the chronic condition causes serious consequences not only for the dentoalveolar system, but for the patient as a whole.

Prompt diagnosis and prevention through the treatment of patients with periodontal diseases is essential. To improve this process and allow for a noninvasive diagnosis of periodontitis, it is necessary to identify the structural changes that occur in the tissues of teeth with this disease. Most studies that have investigated changes caused by this disease have not focused on changes in hard dental tissues, but have investigated the surrounding soft tissues [5,6], oral fluid [6–8], or osseous tissue regeneration during periodontitis treatment [9]. Few studies have focused on the tissues of teeth with periodontitis. The authors of [10] showed that the main structural change in the tissues of teeth with generalized periodontitis is dentin mineralization, and the process of root canal treatment of such teeth is recommended as an additional means of avoiding progression to dentin demineralization. The authors of [11] noted an increase in the micro-hardness of enamel in cases involving progression to periodontitis. Meanwhile, the authors of [10] showed that there are no apparent structural changes in the enamel in generalized periodontitis.

An analysis of the literature data showed that, for chronic periodontitis, the changes in hard dental tissues, especially in enamel, are unconfirmed, and having information about the changes in

the composition of tooth enamel could allow the development of a noninvasive method to diagnose this disease and provide a correct treatment plan. Therefore, research of the tissues of teeth with periodontitis is urgently needed.

Biochemical analysis, scanning electron microscopy [10], fluorescence [7], and spectroscopy [10] are well-known current methods used for tooth tissue research. Biochemical analysis and scanning electron microscopy (SEM) provide quality images of the tooth tissue microstructure and are the most widely used for assessing tooth structure, but they require destructive preparation of the sample [9,10,12,13]. Fluorescence diagnosis in dentistry is based on the analysis of the spectra of fluorescence of hard dental tissues. While the main studied substance is hydroxyapatite, of which teeth are composed, detailed analysis of the composition of teeth is not possible [7]. The limitations of these hard dental tissue research methods could be overcome with the use of Raman spectroscopy. This is a simple, noninvasive, and rapid way of assessing dental tissue [9,12,13].

In [12], with the use of traditional routine histological methods and Raman spectroscopy, comparative research on mineralized tissues of the human jaw was carried out, and it was shown that the joint use of these methods allows significantly more data about pathological processes in the mineralized tissues (in the case of caries) to be collected, as well as allowing the features of mineralization under the conditions of directed bone regeneration to be defined. The authors of [9] studied the processes of bone healing and regeneration in periodontitis treatment using Raman spectroscopy. In our previous work [13], we used Raman spectroscopy to analyze the structure of teeth compared with synthetic apatites. Spectral lines related to the hard and soft tissues of teeth that provide important data for understanding the chemical structural properties of dentin and enamel were discussed. In [6,14–16], attention was paid to the study of the periodontal ligament after the application of orthodontic force and gingival slit fluid in periodontal disease. The authors showed the possibility of using Raman spectroscopy to monitor the periodontal condition at the biochemical level in subjects undergoing orthodontic treatment.

The aim of this work is to study the changes in the tissues of teeth with periodontitis using the Raman spectroscopy method for early, rapid diagnosis and the correction of treatment.

2. Materials and Methods

A randomized study design was used. Forty-two teeth (molars, premolars, and canines) from European patients aged 35–70 of both genders, that were removed due to chronic periodontitis (26 teeth) or for orthodontic reasons (control group, 16 teeth), were used as the materials of the study. Diagnosis of periodontitis was done clinically and after cone beam computed tomography (CT) analysis (the code of the disease according to ICD-10 (1997)—K05.3). The teeth removed due to severe chronic periodontitis with periodontal pockets of at least 6 mm deep and pathologic tooth mobility of grades III–IV were selected for the main group of study. Computed tomography showed a decrease in the bone tissue around the roots of removed teeth of more than half of the root length.

The study was carried out in accordance with the Declaration of Helsinki. The protocol was approved by the Ethics Committee (extract 20.05.2020 No. 207 of minutes of the meeting of the Committee on Bioethics of Samara State Medical University). The samples were collected within a period of 2 months. Measurements were taken immediately after the sampling.

The surfaces of teeth in 5 different areas were studied: enamel (a), dentin (b), in longitudinal slices), cementum (c), and dental calculus localized in the outer part of the teeth. The degree of intensity of the surface formation of the studied teeth corresponded to distinct under-gum (e) and above-gum (d) calculus [17].

Three spectra were investigated (with subsequent averaging) in every studied area at 3–5 different points of the surface of every tissue of each tooth. Samples were divided into 2 main groups: the control group (Figure 1I) and the group with periodontitis (Figure 1II).

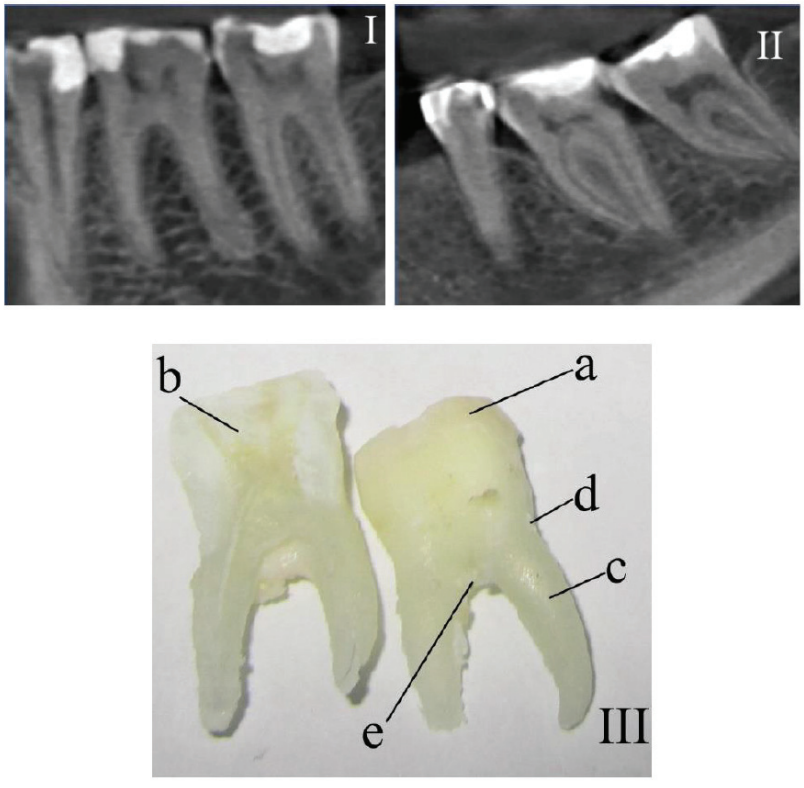

Figure 1. The fragments of teeth following computed tomography that were (**I**) healthy and (**II**) diagnosed with periodontitis. (**III**) Photo of a tooth with the researched areas indicated: a—enamel, b—dentin, c—cementum, d—above-gum dental calculus, and e—under-gum dental calculus.

An in vivo study of the enamel of 22 teeth (molars, premolars, and canines) of one female volunteer patient was also carried out. One of the patient's teeth was diagnosed with localized periodontitis (disease code according to ICD-10 (1997)—K05.3).

The study was carried out using Raman spectroscopy, implemented using the process described in detail in [18].

The experimental process included the use of a semiconductor laser (LML-785.0RB-04, California, USA), an optical module for Raman spectroscopy (RPB-785, Changchun, China), a spectrograph (Sharmrock SR-303i, www.andor.oxinst.com) with an integrated digital camera (ANDOR DV-420A-OE, www.andor.oxinst.com) that was cooled to −60 °C, and a computer.

The use of this spectrograph provided a wavelength resolution of 0.15 nm with a low level of inherent noise. The method of subtracting the fluorescence component of polynomial approximation with additional filtration of random noise effects was used to exclude autofluorescence from the Raman spectrum. Analysis of the Raman spectra was carried out in the range of 350–2200 cm^{-1} in this work. The power of the laser radiation, 400 mW, within the used exposure time (30 s) did not cause any changes to the samples. The optical probe, positioned over the subject at a distance of 7 mm, was used for Raman spectrum registration [19].

3. Results

We considered the characteristic average normalized Raman spectra of surface formations on teeth with this disease (Figure 2). This is often the reason for this disease.

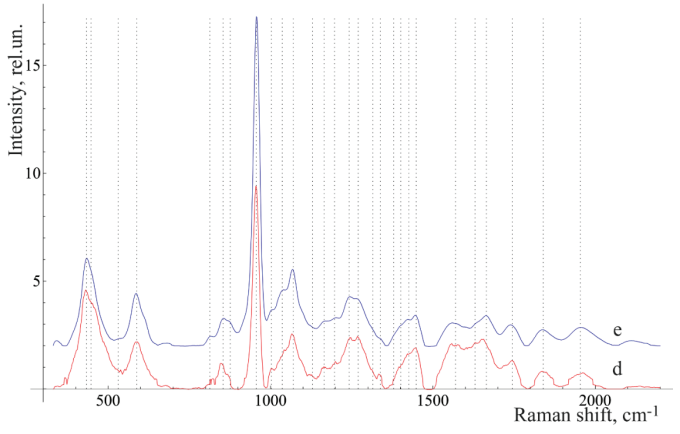

Figure 2. The average Raman spectra, normalized to the average intensity of the studied samples. d—above-gum dental calculus and e—under-gum dental calculus.

Figure 2 shows that the Raman spectra of the under-gum and above-gum calculi have certain spectral features that are apparently related to different periods of disease formation. In the initial stage of dental calculus formation, the above-gum calcareous deposits are composed primarily of organic components, as can be seen from the more intense lines in the ranges of 1550–1565 cm^{-1} (Amide II) and 1600–1665 cm^{-1} (Amide I) and the less intense line at 956 cm^{-1} (PO_4^{3-} (ν_1), hydroxyapatite), compared with the under-gum calculus spectrum. At the same time, the under-gum calculus spectrum is characterized by the explicit intensity of the lines of mineral components (PO_4^{3-} (ν_1), hydroxyapatite).

Figures 3 and 4 show the averaged spectra of the tissues of teeth with periodontitis and healthy teeth from the in vitro study (Figure 3) and the in vivo study (Figure 4).

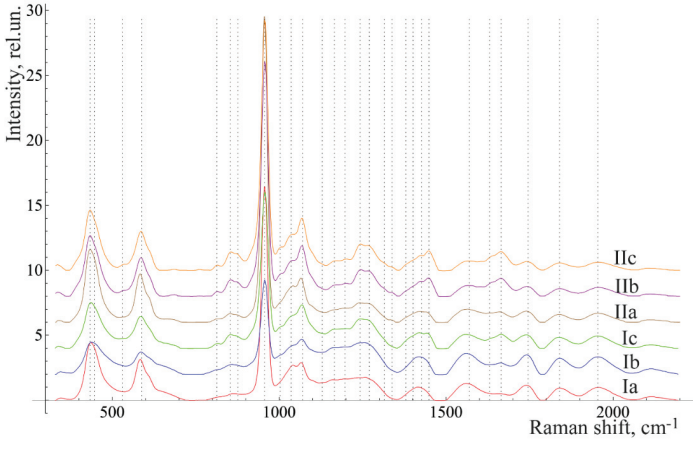

Figure 3. The average Raman spectra, normalized to the average intensity, for two groups of samples studied in vitro: a—enamel, b—denti and c—cementum. I = healthy, while II = diagnosed with periodontitis.

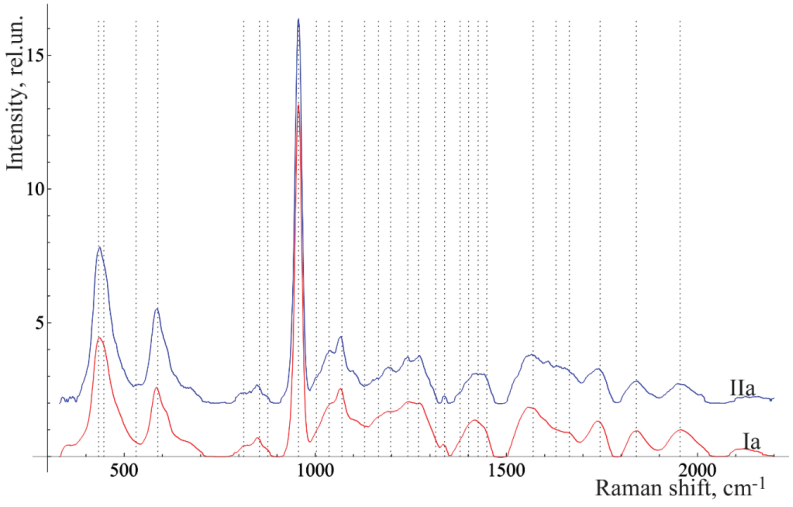

Figure 4. The average Raman spectra, normalized to the average intensity, of two in vivo studied groups of teeth of the volunteer: Ia—healthy enamel and IIa—enamel of the teeth with periodontitis.

The analysis of the healthy tooth tissues and the tissues of teeth with periodontitis showed that the main spectral features of tissues of teeth with periodontitis are changes in the intensity of organic compound lines at 852, 873 cm^{-1} (C–C stretching, proline, and hydroxyproline (collagen assignment)) [20], 1664 (Amide I), 1242 (Amide III) [21], and 1446 cm^{-1} (lipids and proteins) [22], as well as changes in the intensity of the lines of mineral compounds of the teeth at 956 cm^{-1} (P–O symmetrical valence fluctuation PO_4^{3-} (ν_1)) [23].

The comparative analysis shown in Figures 2–4 highlights many spectral changes in all tissues of teeth with periodontitis. These changes mainly occur in the same Raman lines as those related to calculus.

These spectral features are likely to be related to biochemical processes that take place during the formation of surface deposits during periodontitis (e.g., dental calculus and plaques), which affect all tooth tissues. The etiology of calculus formation is related to the mechanism of mineralization of the tooth surface deposits that consist of hydrocarbons and proteins (30% of each), as well as about 15% of lipids. The other components are extracellular bacterial products (plaques), remnants of their cytoplasm, and cell membranes (extracellular polysaccharides) [17].

To make the received Raman spectra more informative, a nonlinear regressive analysis of the Raman spectra was conducted, including an investigation of their spectral line decomposition. Figure 5 shows the results of decomposition of the spectral contours on the sum of distribution of the Gaussian lines. The Gaussian test function is described by the formula in [24].

The composition of the spectral lines was determined by literature analysis and multi-iteration modeling of 392 Raman spectra using MagicPlotPro 2.5.1 software. When modeling the spectral contours at the lines used as a template, the position x_0 and the width of the line (HWHM—half width at half) dx were fixed. Only the intensity of the line was selected when modeling. This allowed us to achieve highly stable results when modeling the contours. The amplitude of the lines a, which depended on the values of the independent regressors dx and x_0, as defined in the initial terms of the analysis, was used as a criterion variable.

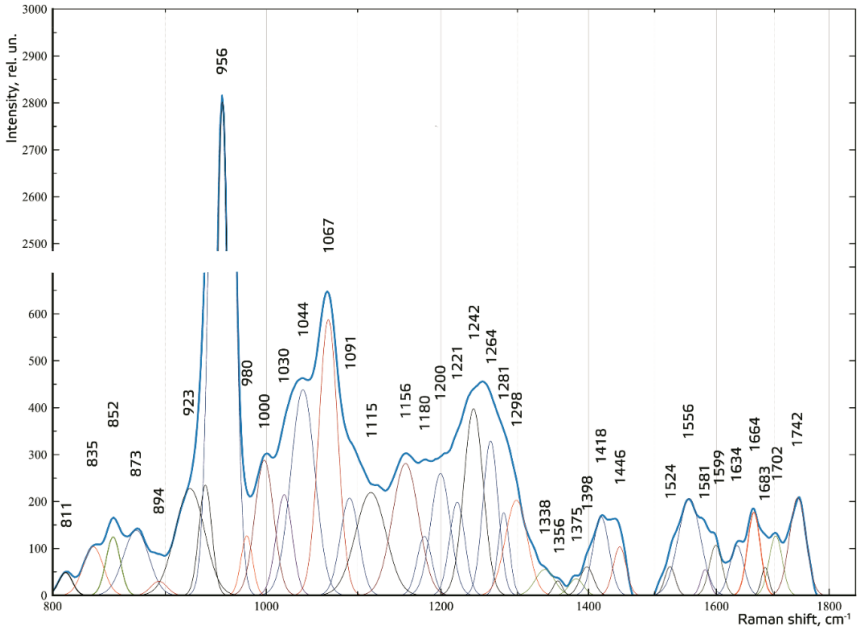

Figure 5. Spectral contour distribution of the enamel samples. The blue line is the original spectrum.

The average value of the coefficient of determination for the initial result spectrum in the range of 780–1780 cm^{-1} was $R^2 = 0.998$, the relative spectral line intensity assessment error a was less than 8%, the average standard deviation of the coordinate of a line x_0 was 1.4 cm^{-1}, and the average standard deviation of the width of the Gaussian line (HWHM) dx was 2.3 cm^{-1}.

For the relative quantitative analysis of the component composition, the relative coefficient k was introduced, where the Raman line of amide I ~1664 cm^{-1} was used as a denominator:

$$k_i = \frac{I_i}{I_{1664}}, \quad (1)$$

where I_i represents the values of intensity of the spectral lines of the analyzed components.

The analysis of the received data was done with IBM SPSS Statistics software through linear discriminant analysis (LDA).

The analysis of the relationships among groups with a pathology or relation to a certain tooth tissue is shown in Figure 6. It can be seen that most of the dispersion between the studied groups of samples can be described by the LD-1 function (58.5%). The common sampling size was 392 Raman spectra. The discriminant function LD-2 was able to describe 29.1% of the dispersion. This function has the physical meaning of the relationship of tooth tissue to the healthy group or to the group with periodontitis.

Positive values of LD-1 were found to mainly characterize the Raman spectra received from the enamel samples, and vice versa; the negative values characterized the samples of cementum, dentine, and dental calculus. The areas of the groups showed intersections, which influenced the rate of correctly classified subjects. The LD-1 function has the physical meaning of the difference between spectral compositions of tooth tissues. Positive values of LD-2 characterized the Raman spectra of the tooth tissue with periodontitis, and the negative values characterized the Raman spectra of healthy tooth tissue.

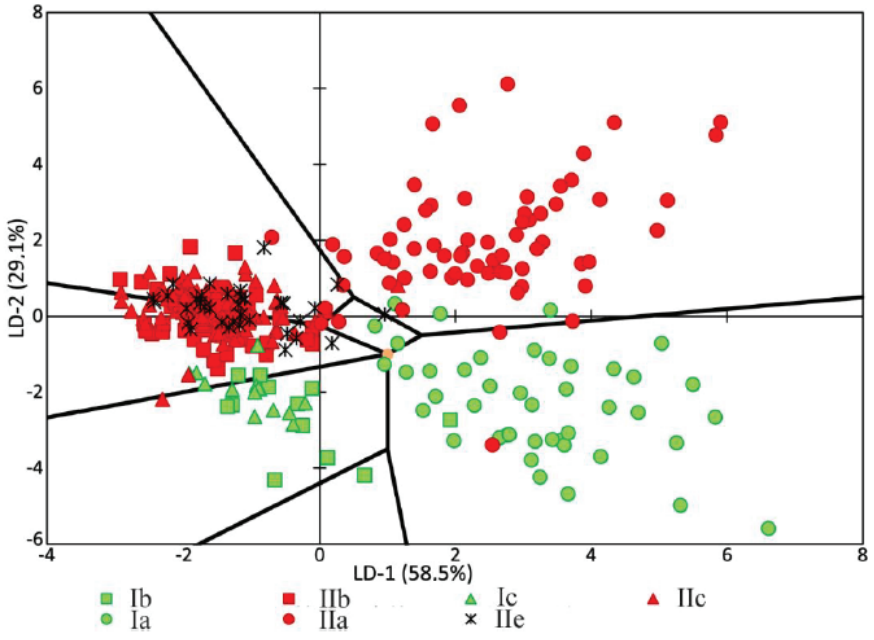

Figure 6. Chart of values showing the linear discriminant functions of the tooth tissue samples. a—enamel, b—dentin, and c—cementum. I = healthy tissue, II = tissue diagnosed with periodontitis.

Figures 6 and 7 show that the difference between healthy tissues and tissues with periodontitis can be described by the LD-2 function. It can be noted that the spectral composition of dental calculus showed similar changes to the spectra of dentin and cementum, which confirms the earlier hypothesis that calculus influences the internal structures of tooth tissue.

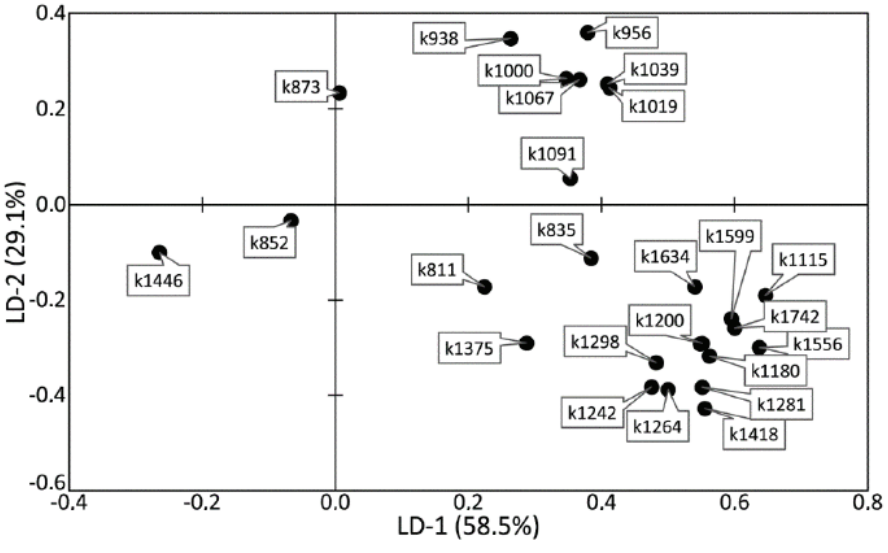

Figure 7. The values of factor structure coefficients for the tooth tissue samples.

High relative intensity values were observed for the lines ~1446 (CH_2 scissoring and CH_3 bending fluctuations of lipids and proteins), ~852 (C–C stretching benzene ring of proline), and ~873 cm^{-1} (C–C stretching benzene ring of hydroxyproline), with the rest of the lines having low spectral lines. These values characterize the tooth tissues—dentin, cementum with periodontitis, as well as calculus—compared with enamel, which indicates the differences in the organic–mineral compositions of these tissues.

Study of the changes in the enamel of teeth with periodontitis was further carried out. Figures 8 and 9 show a comparison of the LDA results of the enamel of healthy teeth and teeth with periodontitis. Sixty-seven spectra of the enamel of teeth with periodontitis and 43 Raman spectra of the enamel of healthy teeth were analyzed. The discriminant function LD-1 was able to describe 100% of the dispersion. Positive LD-1 values characterized the Raman spectra of the healthy enamel samples (the average LD-1 value of the group was 1.95, and the standard deviation was 0.912), and vice versa; negative values characterized the Raman spectra of the group of pathologic enamel samples (the average LD-1 value of the group was −1.25, and the standard deviation was 1.052). The areas of the groups had a minor intersection in the range of LD-1 = (−0.25; 2.25).

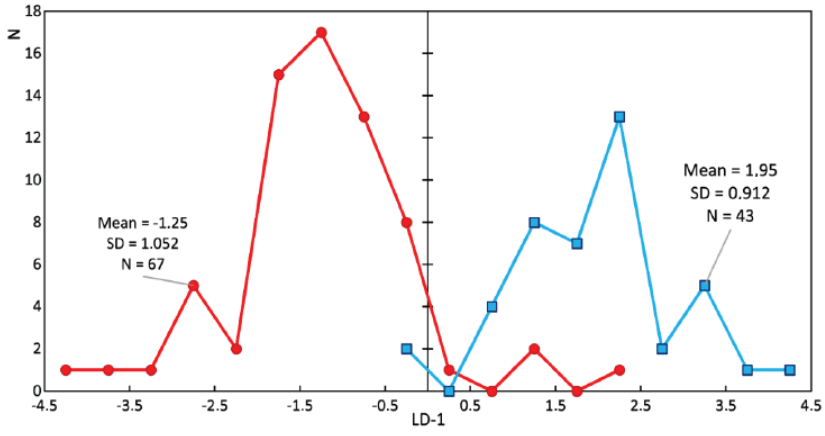

Figure 8. Chart of the linear discriminant function values of the enamel samples. The red line is the enamel of teeth with periodontitis (damaged enamel), and the blue line is the enamel of healthy teeth.

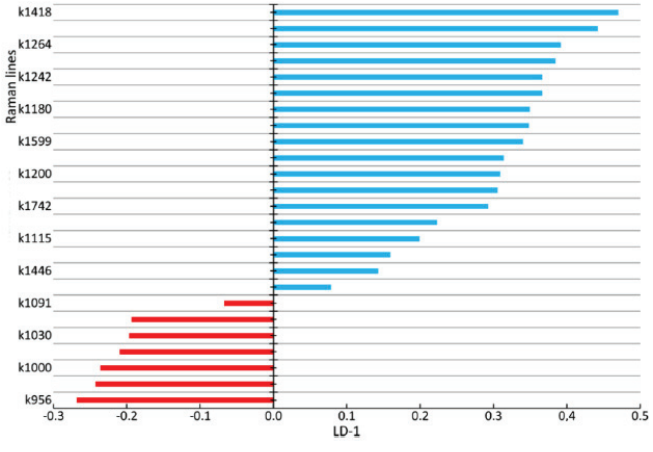

Figure 9. The values of factor structure coefficients for the enamel samples. Negative values are highlighted in red and positive values are highlighted in blue.

Figure 9 shows the coefficients of the factor structure matrix, with a correlation between the variables in the model and the discriminant function. In the analysis, these correlation coefficients were considered to be the factor loadings of the variables for each discriminant function.

The higher the absolute value of LD-1 for the variable is, the more strongly it determined the difference between the groups of samples in the received model of discriminant analysis. For example, the values of the introduced coefficients k873, k956, k1000, k1039, k1044, k1067, and k1091 were higher in the group of enamel samples with periodontitis, which indicates an increase in the relative intensity of the corresponding lines in tissue with periodontitis.

The increase in the relative intensity of the lines for hydroxyapatite 956 (P–O symmetrical valence fluctuation PO_4^{3-} (ν_1)), ~1044 (PO_4^{3-} (ν_3) (P–O asymmetrical valence fluctuation)), 1067 (C–O planar valence fluctuation CO_3^{2-} (ν_1) B-type substitution), and 1091 cm^{-1} (C–O planar valence fluctuation CO_3^{2-} (ν_1) A-type substitution) may be related to the presence of a water–mineral metabolism disorder in the tissues of teeth with periodontitis, which leads to more intensive substitution of the hydroxide ion OH by apatite ions CO_3^{2-} in the structure.

The change in the relative intensity of the lines at 1000 cm^{-1} and 1039 cm^{-1}, corresponding to fluctuations in the phenylalanine molecule, and 873 cm^{-1} (C–C stretching, proline and hydroxyproline (collagen assignment)) are apparently related to collagen synthesis disorder, which can also be seen in osteoporotic changes of bone tissues, as we showed earlier in [25].

We also observed a reduction in the relative intensity of the lines at ~1742 (phospholipids), ~1556 (Amide II Parallel/Antiparallel β-sheet structure), 1200–1300 (Amide III), ~1418, and ~1446 cm^{-1} (CH_2 scissoring and CH_3 bending fluctuations of lipids and proteins) in the tissues of teeth with periodontitis compared with healthy tissues. This effect may have been caused by the dehydration of peptide groups of amides that are sensitive to structural changes in the molecules of collagen [26].

In [6,16], chemical and structural changes were shown in the periodontal ligament after the application of orthodontic force and gingival slit fluid in teeth with periodontitis. Violation of the ligamentous apparatus leads to the development of periodontitis and changes in tooth tissues. Raman spectroscopy analysis of enamel can be used for the early diagnosis of periodontitis.

As a result of the discriminant analysis, we built a discriminant model of the enamel of healthy teeth and the enamel of teeth with periodontitis, taking into account characteristic changes in the relative intensity of the Raman lines. The number of true positive (*TP*) results was 64, while there were 3 false negative (*FN*) results. The number of true negative (*TN*) results was 41, and there were 2 false positive (*FP*) results.

The calculated sensitivity and specificity values of the method are

$$Sen = \frac{TP}{TP + FN} = \frac{64}{64 + 3} = 95.5\% \quad (2)$$

$$Spe = \frac{TN}{TN + FP} = \frac{41}{41 + 2} = 95.3\%. \quad (3)$$

Figure 10 shows the results of the receiver operator characteristic (ROC) analysis of the developed algorithm for diagnosing periodontitis. The discriminant adequacy of the method had an area under the curve (AUC) value of 0.983, which indicates the great quality of the diagnostic tool. The standard error (SE) was 0.01, and the 95% confidence interval of the AUC was in the range of 0.963–1. The optimal cut-off point for the presented algorithm, determined according to the condition of balance between sensitivity and specificity, was 0.55 (Figure 11). The values of sensitivity and specificity for the diagnostic model at that cut-off point were 95.5% and 95.3%, respectively.

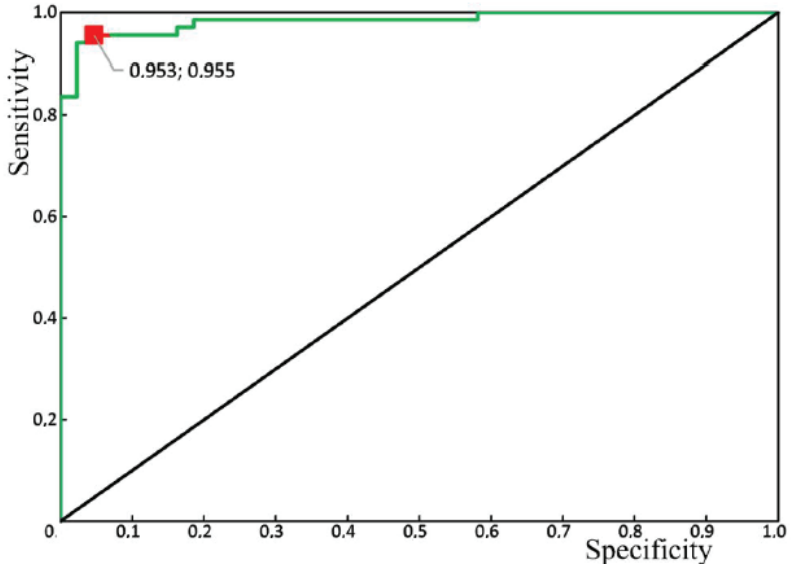

Figure 10. Receiver operator characteristic (ROC) analysis of the algorithm for periodontitis assessment, using the Raman spectroscopy method: green line—ROC-curve, the red square is the optimal cut-off point.

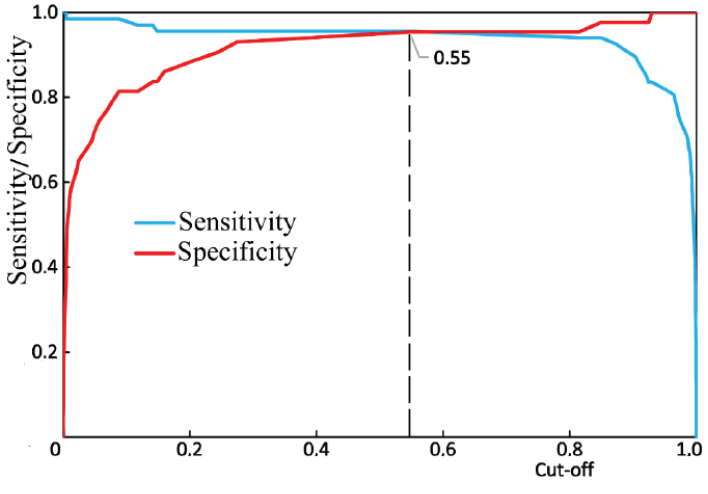

Figure 11. The balance point between sensitivity and specificity.

Therefore, if the received spectrum of enamel is classified as the spectrum of enamel with periodontitis, it could be a reason for including the patient in the at-risk group and may determine the treatment given.

4. Discussion

The main spectral changes in the tissues of teeth with periodontitis were identified in this work. The etiology of these changes is connected to the formation of calculus on the surface of teeth which, in turn, results in structural changes to all tooth tissues with periodontitis. These changes occur due to

the presence of a water–mineral metabolism disorder in the tooth tissues (intensive substitution of hydroxide ion OH by apatite ions CO_3^{2-} in the structure) or collagen synthesis disorder. Similar changes occur in bone tissues with osteoporosis, as we presented earlier in [25].

The spectral changes found in this work that occur in periodontitis do not occur in other widespread dental diseases (e.g., caries). We previously carried out studies [27] that showed a decrease in the concentration of ions $(PO_4)^{3-}$ in caries, as also shown in [28].

Diagnosing the spectral changes in tooth enamel, as well as developing an algorithm to identify enamel with periodontitis, will allow at-risk patients to be identified and treated with hydroxyapatite. The sensitivity and specificity values of the developed algorithm were 95.5% and 95.3%, respectively.

The received results are a prerequisite for creating an express device for the noninvasive (in vivo) assessment of periodontitis, based on changes in tooth enamel spectral values. These studies have already been carried out in vivo in this work and have shown good results, similar to the results of in vitro studies.

Author Contributions: Conceptualization, E.T. and L.V.; methodology, P.T. and L.V.; software, O.F. and P.T.; validation, P.T. and L.V.; formal analysis, P.T. and O.F.; investigation, O.F., M.Z. and I.B.; resources, E.T., L.V., M.Z. and I.B.; data curation, M.Z. and I.B.; writing—original draft preparation, E.T.; writing—review and editing, P.T. and L.V.; visualization, O.F. and P.T.; supervision, E.T., L.V. and I.V.B.; project administration, E.T.; All authors have read and agreed to the published version of the manuscript.

Funding: The study was made with financial support from Samara University (www.ssau.ru).

Conflicts of Interest: The authors declare no conflict of interest.

References

1. Epifanova:, Y.V.; Avanesov, A.M. The estimation of levels of bioamines in the blood cells at patients with parodontitis. *Electronniy Nauchno-Obraz. Vestnic Zdorovie i Obraz. v XXI veke-2012 [Electron. Sci. Educ. Bull. Health Educ. XXI Century—2012]* **2012**, *14*, 114–115.
2. Shashmurina, V.R.; Devlikanova, L.I.; Chumachenko, E.N. Biochemical characteristics of pulp removal in cases of periodontal diseases. *Ross. Stomatol. Vestn. [Russ. Dent. Bull.]* **2017**, *21*, 64–67. [CrossRef]
3. Papapanou, P.N.; Susin, C. Periodontitis epidemiology: Is periodontitis under-recognized, over-diagnosed, or both? *Periodontol. 2000* **2017**, *75*, 45–51. [CrossRef] [PubMed]
4. Cepov, L.M.; Cepova, E.L.; Cepov, A.L. Periodontitis: Local focus serious problems (literature review). *Parodontologiya* **2014**, *3*, 3–6.
5. Khaydar, D.A.; Kulchenko, A.G. Hypoxia of periodontium tissues with chronic periodontitis, Special issue. In Proceedings of the Materials of the XIX International Congress "Health and Education in the XXI Century", Moscow, Russia, 18–20 December 2017.
6. Camerlingo, C.; D'Apuzzo, F.; Grassia, V.; Perillo, L.; Lepore, M. Micro-Raman Spectroscopy for Monitoring Changes in Periodontal Ligaments and Gingival Crevicular Fluid. *Sensors* **2014**, *14*, 22552–22563. [CrossRef]
7. Sukhinina, A.V. The Methods of Optical Spectroscopy for Dental Disease Diagnosis. Ph.D Thesis, Abstract National Research Nuclear University MEPh, Moscow, Russia, 2014.
8. Gonchukov, S.; Sukhinina, A.; Bakhmutov, D.; Minaeva, S. Raman spectroscopy of saliva as a perspective method for periodontitis diagnostics. *Laser Phys. Lett.* **2011**, *9*, 73–77. [CrossRef]
9. Gatin, E.; Nagy, P.; Paun, I.; Dubok, O.; Bucur, V. Windisch Raman Spectroscopy: Application in Periodontal and Oral Regenerative Surgery for Bone Evaluation. *IRBM* **2019**, *40*, 279–285. [CrossRef]
10. Tsimbalistov, A.V.; Pikhur, O.L.; Dubova, M.A.; Sadikov, R.A.; Frank-Kamenetskaya, O.V.; Golovanova, O.A.; Belskaya, L.V. Morphology and Composition of Human Dental Hard Tissues and Dental Stones with the General Parodontite. *Vestn. St. -Peterbg. Univ. [St.-Petersburg Univ. Bull.]* **2006**, *11*, 128–135.
11. Remizov, S.M. Measuring microhardness for comparative assessment of dental tissues of human healthy and affected teeth. *Stomatologiya* **1965**, *3*, 33–37.
12. Minaeva, S.A.; Mikhaylovskiy, A.A.; Bukharova, T.B.; Antonov, E.N.; Goldshteyn, D.V.; Popov, V.K.; Volkov, A.V. Morphological study of hard tissues of facial skeleton using the Raman spectroscopy. *Ross. Stomatol.* **2005**, *1*, 3–10.

13. Ramakrishnaiah, R.; Rehman, G.U.; Basavarajappa, S.; Al Khuraif, A.A.; Durgesh, B.H.; Khan, A.S.; Rehman, I.U. Applications of Raman Spectroscopy in Dentistry: Analysis of Tooth Structure. *Appl. Spectrosc. Rev.* **2014**, *50*, 332–350. [CrossRef]
14. Kapoor, P.; Kharbanda, O.P.; Monga, N.; Miglani, R.; Kapila, S. Effect of orthodontic forces on cytokine and receptor levels in gingival crevicular fluid: A systematic review. *Prog. Orthod.* **2014**, *15*, 1–21. [CrossRef] [PubMed]
15. D'Apuzzo, F.; Perillo, L.; Delfino, I.; Portaccio, M. Monitoring early phases of orthodontic treatment by means of Raman spectroscopies. *J. Biomed. Opt.* **2017**, *22*, 1. [CrossRef]
16. Perillo, L.; d'Apuzzo, F.; Ilario, M.; Laino, L.; Di Spigna, G.; Lepore, M.; Camerlingo, C. Monitoring Biochemical and Structural Changes in Human Peridontal Ligaments during Orthodontic Treatment by Means of Micro-Raman Spectroscpy. *Sensors* **2020**, *20*, 497. [CrossRef]
17. Borodovitsina, S.I.; Saveleva, N.A.; Tabolina, E.S. *Dental Disease Prevention*; Ryazan State Medical University: Ryazan, Russia, 2019; p. 264.
18. Timchenko, E.V.; Timchenko, P.E.; Pisareva, E.V.; Vlasov, M.Y.; Volova, L.T.; Frolov, O.O.; Fedorova, Y.V.; Tikhomirova, G.P.; Romanova, D.A.; Daniel, M.A. Spectral Analysis of Rat Bone Tissue During Long Antiorthostostatic Hanging and at Introduction of Allogen Hydroxyapatitis. *Opt. Spectrosc.* **2020**, *128*, 989–997. [CrossRef]
19. Timchenko, E.V.; Timchenko, P.E.; Taskina, L.A.; Volova, L.T.; Miljakova, M.N.; Maksimenko, N.A. Using Raman spectroscopy to estimate the demineralization of bone transplants during preparation. *J. Opt. Technol.* **2015**, *82*, 153–157. [CrossRef]
20. Raghavan, M. Investigation of Mineral and Collagen Organization in Bone Using Raman Spectroscopy. Ph.D. Thesis, University of Michigan, Ann Arbor, MI, USA, 2011.
21. Ager, J.; Nalla, R.K.; Breeden, K.L.; Ritchie, R.O. Deep-ultraviolet Raman spectroscopy study of the effect of aging on human cortical bone. *J. Biomed. Opt.* **2005**, *10*, 034012. [CrossRef]
22. Gyeong Bok, J.; In Soon, K.; Young Ju, L.; Dohyun, K.; Hun-Kuk, P.; Gi-Ja, L.; Chaekyun, K. Label-free noninvasive characterization of osteoclast differentiation using raman spectroscopy coupled with multivariate analysis. *Curr. Opt. Photonics* **2017**, *1*, 412–420.
23. Ionita, I. Diagnosis of tooth decay using polarized micro-Raman confocal spectroscopy. *Rom. Rep. Phys.* **2009**, *61*, 567–574.
24. Motulsky, H.J.; Christopoulos, A. *Fitting Models to Biological Data Using Linear and Nonlinear Regression*; A practical guide to curve fitting; GraphPad Software Inc.: San Diego, CA, USA, 2003.
25. Timchenko, E.V.; Timchenko, P.E.; Pisareva, E.V.; Vlasov, M.Y.; Volova, L.T.; Fedotov, A.A.; Fedorova, Y.V.; Tyumchenkova, A.S.; Romanova, D.A.; Daniel, M.A.; et al. Optical analysis of bone tissue by Raman spectroscopy in experimental osteoporosis and its correction using allogeneic hydroxyapatite. *J. Opt. Technol.* **2020**, *87*, 161–167. [CrossRef]
26. Sukhodub, L.; Moseke, C.; Sulkio-Cleff, B.; Maleev, V.; Semenov, M.; Bereznyak, E.; Bolbukh, T. Collagen–hydroxyapatite–water interactions investigated by XRD, piezogravimetry, infrared and Raman spectroscopy. *J. Mol. Struct.* **2004**, *704*, 53–58. [CrossRef]
27. Timchenko, E.V.; Zherdeva, L.A.; Volova, L.T.; Burda, A.G.; Timchenko, P.E. Use of Raman spectroscopy for diagnosis of disease in dental tissue. *J. Opt. Technol.* **2016**, *83*, 313. [CrossRef]
28. Mandra, Y.V.; Ivashov, A.S.; Votjakov, S.L.; Kiseleva, D.V. Possibilities of Raman microspectrometry imaging for structural investigation of human enamel and dentin. *Eksperimentalnaya Klin. Stomatol.* **2011**, *1*, 24–28.

diagnostics

MDPI

Article

Machine Learning Aided Photonic Diagnostic System for Minimally Invasive Optically Guided Surgery in the Hepatoduodenal Area

Evgeny Zherebtsov [1,2,*], Marina Zajnulina [3], Ksenia Kandurova [1], Elena Potapova [1], Viktor Dremin [1,3], Andrian Mamoshin [1,4], Sergei Sokolovski [3], Andrey Dunaev [1] and Edik U. Rafailov [3]

1 Research and Development Center of Biomedical Photonics, Orel State University, 302026 Orel, Russia; kandkseniya@gmail.com (K.K.); e.potapova@oreluniver.ru (E.P.); v.dremin1@aston.ac.uk (V.D.); dr.mamoshin@mail.ru (A.M.); dunaev@bmecenter.ru (A.D.)

2 Faculty of Information Technology and Electrical Engineering, University of Oulu, Optoelectronics and Measurement Techniques Unit, 90570 Oulu, Finland

3 Aston Institute of Photonic Technologies, Aston University, Birmingham B4 7ET, UK; MZArea@hotmail.com (M.Z.); s.sokolovsky@aston.ac.uk (S.S.); e.rafailov@aston.ac.uk (E.U.R.)

4 Department of X-ray Surgical Methods of Diagnosis and Treatment, Orel Regional Clinical Hospital, 302028 Orel, Russia

* Correspondence: evgenii.zherebtsov@oulu.fi

Received: 28 August 2020; Accepted: 24 October 2020; Published: 27 October 2020

Abstract: Abdominal cancer is a widely prevalent group of tumours with a high level of mortality if diagnosed at a late stage. Although the cancer death rates have in general declined over the past few decades, the mortality from tumours in the hepatoduodenal area has significantly increased in recent years. The broader use of minimal access surgery (MAS) for diagnostics and treatment can significantly improve the survival rate and quality of life of patients after surgery. This work aims to develop and characterise an appropriate technical implementation for tissue endogenous fluorescence (TEF) and assess the efficiency of machine learning methods for the real-time diagnosis of tumours in the hepatoduodenal area. In this paper, we present the results of the machine learning approach applied to the optically guided MAS. We have elaborated tissue fluorescence approach with a fibre-optic probe to record the TEF and blood perfusion parameters during MAS in patients with cancers in the hepatoduodenal area. The measurements from the laser Doppler flowmetry (LDF) channel were used as a sensor of the tissue vitality to reduce variability in TEF data. Also, we evaluated how the blood perfusion oscillations are changed in the tumour tissue. The evaluated amplitudes of the cardiac (0.6–1.6 Hz) and respiratory (0.2–0.6 Hz) oscillations was significantly higher in intact tissues ($p < 0.001$) compared to the cancerous ones, while the myogenic (0.2–0.06 Hz) oscillation did not demonstrate any statistically significant difference. Our results demonstrate that a fibre-optic TEF probe accompanied with ML algorithms such as k-Nearest Neighbours or AdaBoost is highly promising for the real-time in situ differentiation between cancerous and healthy tissues by detecting the information about the tissue type that is encoded in the fluorescence spectrum. Also, we show that the detection can be supplemented and enhanced by parallel collection and classification of blood perfusion oscillations.

Keywords: liver cancer; endogenous fluorescence; laser Doppler flowmetry; blood perfusion; minimally invasive interventions; machine learning

1. Introduction

Abdominal cancer is a widely prevalent group of tumours with a high level of mortality if diagnosed at a late stage. Although the cancer death rates have in general declined over the past few decades, the mortality from tumours in the hepatoduodenal area specifically has increased in recent years [1]. Moving towards the broader use of minimally invasive techniques for diagnosis and treatment is promising to significantly improve the survival rate and quality of life of patients after surgery. Minimally invasive techniques require the use of reliable tools for real-time feedback to assist the surgeon. Usually, the manipulations in the operation field are conducted under ultrasound or X-ray control and visualisation. While the methods can provide an exceptional accuracy of the tool positioning, they hardly give sufficient information on the tissue type and, specifically, on the tumour borders. Various approaches have been put forward to solve this issue. The optical methods have been widely investigated in that respect and demonstrated high diagnostic potential in many applications [2–5]. Despite the gradual transition from the in vivo single-point measurements towards the in vivo imaging techniques, the use of fibre optical probes for the surgical guidance has great potential to compete with the costly techniques and to significantly improve the outcome of the routine procedures for cancer eradication. Most imaging approaches still need to address major issues concerning the motion artefacts, real time imaging processing and the trade-off between the parameters of resolution, frame rate and aperture diameter [6]. In particular, this set of limitations affects the minimally invasive surgical interventions as one deals with the tools of low outer diameters being applied in confined space of the abdominal cavity [7].

In recent years, there has been considerable interest in the measurements of the fluorescence parameters to be applied for the diagnostics in minimally invasive surgery [8]. The methods are based on the recording of the endogenous fluorescence. However, they often require the intravenous injection of fluorescence dyes or molecular fluorescence probes specifically binding to tumour cells [9,10]. The association between TEF emission and changes in tissue metabolism as well as the blood circulation and histological architecture offers a powerful diagnostic tool for direct monitoring of the malignancy of studied biotissues. TEF, based on autofluorescence spectra registration, can provide comprehensive information about the physiological or altered morphofunctional properties of cells and tissues, including ones caused by oncology [11]. Due to high proliferation, tumour cells have increased metabolic needs compared to normal ones [12], and tumour metabolism is associated with changes in relative concentrations of NADH and FAD [13]. These endogenous fluorophores of cells and tissues can serve as biomarkers for studying differences between tumour and non-tumour areas [14–18].

In the traditional approach, the TEF measurements were used to evaluate the changes in tissues based on the comparison of the absolute values of the related emission parameters in tumour and non-tumour areas. Nowadays, research tends to focus on machine learning (ML) approaches that combine input feature sets in one or several diagnostic classifiers [19]. One promising application of ML is MAS as the medical procedure commonly requires a high speed of the onsite decision making for the surgeon. More recent evidence shows that the diagnostic techniques based on the measurements of the intrinsic fluorescence aided with the machine learning algorithms can be used for distinguishing malignant and benign colorectal tissue [20].

To the best of our knowledge, the applicability of ML in fluorescence liver cancer diagnostics has not yet been studied thoroughly. The available published results in this research area either focus on the MRI or CT studies [21], are limited using tumour-targeting fluorescent labels [22] or reported results obtained ex vivo [23].

Recently, authors have published data on the evaluation of the liver tumours with the needle optical probe combining TEF and diffuse reflectance measurements [24]. Except for that, despite high interest and potential outcome, no one, to the best of our knowledge, has demonstrated results of the ML application for cancer diagnosis that deploys data obtained by optical probe in vivo and in situ in the hepatoduodenal area.

In this work, we present results of the ML techniques to facilitate optically guided surgery on tumours by the detection and classification of cancerous and healthy tissues. The data that we use in our studies was obtained in vivo and *in situ*. In particular, we focus on cancers of the liver and bile duct and collect and classify the data for TEF and blood perfusion. The focus on two types of data has the following reason: it is known that in vivo recorded fluorescence spectra are influenced by many factors such as the absorption by blood in the living tissue [25]. This blood-induced absorption attenuates and changes the shape of the fluorescence signal [26]. To mitigate this problem, we additionally analyse the parameters of the blood perfusion measured in living intact tissue (cf. [27]). For this, we deploy laser Doppler flowmetry (LDF). LDF provides a powerful tool for the blood perfusion measurements and analysis of rhythmic oscillations in the fine structure of microvascular blood flow. It was demonstrated that LDF is a highly informative method across a range of medical conditions and general physiological health monitoring applications. To record TEF and LDF blood perfusion parameters during MAS in patients with cancers of liver and bile duct, we implemented a flexible optical fibre probe capable of measurements in the hepatoduodenal area. We used ML techniques to detect the tumour borders by classification of healthy and cancerous tissues using the TEF and LDF data. The general aim of this work was to develop an appropriate technical implementation for TEF and LDF measurements and to assess the efficiency of ML methods for real-time diagnosis of liver cancer and tumours in the hepatoduodenal area.

2. Materials and Methods

2.1. Setup and In Situ Data Collection

The setup to collect data on TEF and LDF consists of a custom-built, flexible fibre-optical probe, two LED sources for fluorescence excitation (at 365 nm and 450 nm), a set of fluorescent filters, a CCD-based spectrometer and a laser Doppler flowmetry channel for blood perfusion measurements that utilises a single-mode laser at 1064 nm. The prototype of the fibre-optical probe (Figure 1) has two emitting fibres to excite TEF at wavelengths of 365 nm and 450 nm and a fibre to collect the fluorescence emission (all fibres are of 400 µm in diameter). Moreover, the probe is equipped with one emitting single-mode optical fibre and two multimode collecting fibres for the LDF channel. This configuration enables to register the fluorescence of all major endogenous fluorophores in living tissue, as well as to record the level of blood perfusion in the area of interest (Figure 2).

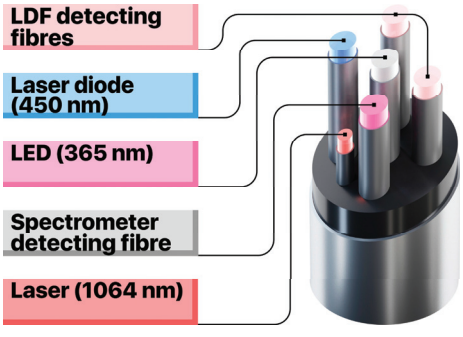

Figure 1. The configuration and measuring channels of the used fibre-optic probe.

The proposed setup was validated in the framework of limited tests in patients with obstructive jaundice caused by liver cancer. The patient cohort comprised of 27 volunteers. The measurements from the LDF channel were used as a sensor of the tissue vitality. The TEF spectra were recorded primarily in the areas of interest demonstrated a stable level of blood perfusion of about 15 a.u. Figure 3 (top panel) shows the exemplary records of blood perfusion registered in the intact bile duct and

in the cancer block. This procedure allowed us to avoid areas of necrosis and to decrease the TEF data variation associated with the variable blood volume fraction in the tissue. The measurements were performed during planned diagnostic and therapeutic interventions under ultrasound and X-ray examination. For every patient, 8–10 spectra were taken at the excitation wavelength of 365 nm and 450 nm. They were equally split between cancerous and intact tissues. In that way, 4–5 spectra were measured for each class in a patient. The measurement points were evenly distributed over the area of interest except for places with low blood perfusion prominent necrosis or covered with blood. Also, two 1 min long LDF recordings were made for places with apparent tumour and normal tissues respectively. The studies were conducted at the department of interventional radiology of Orel Regional Clinical Hospital (Orel, Russia) and were approved by the local Committee for Human Biomedical Research Ethics (record of the meeting No. 10 of 16.11.2017).

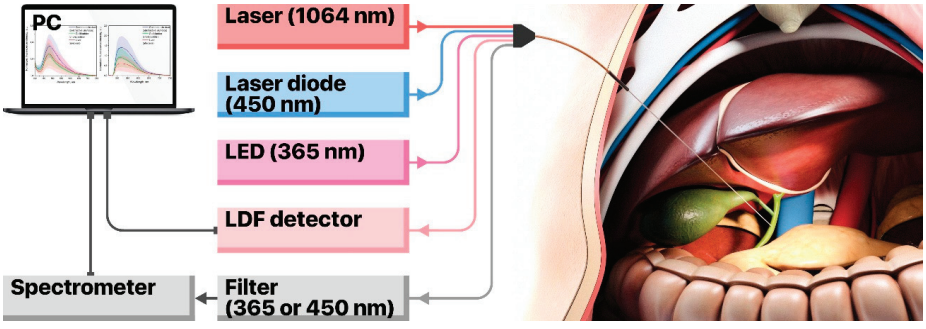

Figure 2. The components of measuring setup and probe placement in the region of interest.

2.2. Data Collection

The main challenge of the proposed technique lies in the collection of TEF data under the X-ray control directly during a surgical procedure. The imaging procedure, being realised with a radiopaque substance that fills the cavity of the bile duct, allows the surgeon to visualise the contour of the walls and the tumour block. In this case, the 2D radiological control is the only piece of feedback information about the probe position with respect to the bile duct and the tumour itself. Actually, this indirect approach might be sufficient for MAS as such. However, from the point of view of the data collection quality for ML, the indirect control might be insufficient for a precise localisation of the sampling point and, as a result, for a right labelling of the TEF spectrum. Thus, a spectrum coming from a healthy tissue can be falsely labelled as cancerous and vice versa. When used for training and testing of ML models, such spectra contribute towards a high value of the intrinsic lowest possible error (LPE) in classification and make it difficult to evaluate the performance of the ML models and to interpret their prediction results.

Besides the difficulty of the probe positioning due to the limitations of the available 2D X-ray visualisation (i), we identify three other sources of possible data mislabelling: (ii) the lack of ability to reliably visualise blood and bile in the field of view of the fibre-optical probe which significantly affects the quality of the collected fluorescence spectra; (iii) the uncertainty of the distribution of the cancer cells over the mucous surface; and (iv) the effects of the probe pressure on the tissues that manifests itself in the variable blood volume fraction in the tissue.

In the presented study, all patients were diagnosed with cancer and their samples were verified morphologically by biopsy. Nevertheless, regarding the challenges (i) and (iii), it should be noted that the allocation of the areas with cancer tissue significantly varies between the patients. The X-ray visualisation helps to identify the tumour block and the position of the probe. At the same time, in the vicinity of the tumour block, the malignant cells can belong to the primary tumour originated from the epithelial tissues of the bile duct or cells proliferated from the surrounding organs. Also, in some cases,

the cancer cells can be absent on the surface of the cancerous tissues. This happens when the tumour block compresses the healthy tissue where the probe is placed but does not permeate through the wall of the organ. These aspects further contribute to the increase of the system's LPE by leading to false labelling of spectra used for the training and testing of ML models.

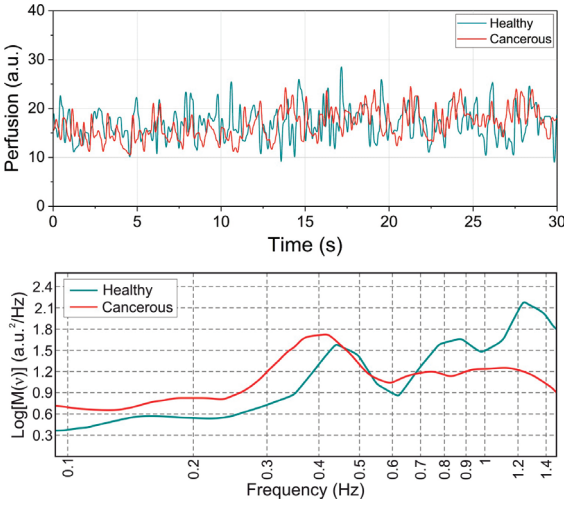

Figure 3. Exemplary blood perfusion records (upper panel) from the intact bile duct wall and the tumour located in the bile duct and the corresponding integrated wavelet spectra (IWS; bottom panel).

2.3. Machine Learning Method

In our experiments, the spectrometer for the TEF measurements covers the range between 346 nm and 816 nm sampled with 2100 pixels. To build and determine suitable machine learning models for classification of healthy and cancerous tissues, we consider the intensity spectra taken at 365 nm and 450 nm separately. For the purposes of classification, the following labels were used to label the spectra: "C" for cancerous tissues and "N" for healthy tissues. Figure 4 shows 5 arbitrary spectra and their labels for each channel. On the left side of each spectrum, we see a sharp excitation peak and to its right, a broad fluorescence spectrum. The information on whether a tissue is healthy or cancerous is encoded in the intensity of the fluorescence peak, its position in the spectrum and its shape. We use a Python-based library called Scikit-learn to pre-process and to classify the spectra automatically by ML methods.

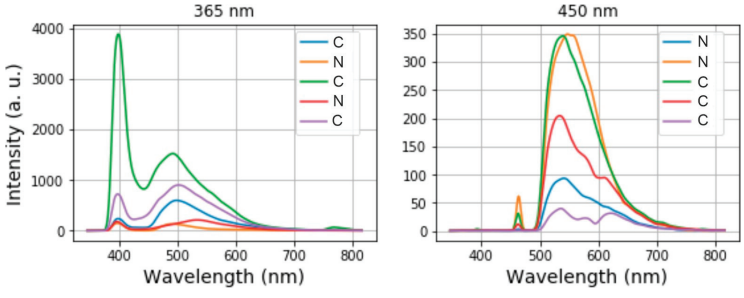

Figure 4. 5 arbitrary fluorescence spectra and their labels obtained at the excitation channel of 365 nm (**left**) and 450 nm (**right**). In these graphs, the label "N" denotes a normal tissue whereas "C" a cancerous tissue.

In terms of data pre-processing, we first removed the data samples where the noise floor overlapped with the actual fluorescence spectra. To further reduce the influence of noise, the remaining spectra were smoothed using a FIR filter. In the next step, noisy, not informative sections at the beginning (blue sides) of the spectra as well as at their (red) ends were cut off. This resulted in the reduced dimensionality of each spectrum of (1, 1920) instead of the initial dimension of (1, 2100) that was determined by the spectrometer pixel number.

The training and test sets were randomly split as follows: 199 samples for training and 40 samples for testing in the case of the 356 nm channel and 120 samples for training and 40 samples for testing in the case of the 450 nm channel. To increase the performance of our ML models, the data was standardised by subtracting the data mean value and dividing the result by the standard deviation.

To further reduce the dimensionality of our training and test data, we applied the principal component analysis (PCA) with 5 principal components. As Figure 5 shows, 5 principal components retain more than 90% of the information stored in the spectra. The first two components having the highest values carry the biggest part of this information. We interpret the first two components as the indicators of the fluorescence peak intensity and its position in the spectrum. After the PCA is performed, the dimension of each spectrum is only (1, 5). In our statistical experiments, we observe a variation of the first two PCA components values by ±3% and much smaller variation in other components. However, this variability does not prevent us from seeing a clear difference between the first and the second component.

Five classification models and their performance in differentiating between the healthy and cancerous tissues were considered for the TEF spectra of each channel as well as for the LDF blood flow oscillations. Those are the k-Nearest-Neighbours (KNN) algorithm [28], a Decision Tree (DT) [29], Support Vector Machines (SVM) [30] and such ensemble methods as the Random Forest (RF) [31] and AdaBoost [32]. In the blood perfusion analysis, the logistic regression model was applied instead of AdaBoost. A 10-fold validation was applied to evaluate the accuracy of each method. The accuracy denotes the ratio between the rightly classified values, and all considered ones and measures how close the predicted value of the class is to the true class label. Two further metrics that we used to evaluate the classifiers' performance are the sensitivity and the specificity. The sensitivity is the ratio between the true positives and the sum of true positives and false negatives, i.e., the portion of actual positives that are correctly predicted. The specificity measures the number of true negatives put into relation to the sum of true negatives and false positives, it is the portion of actual negatives that are correctly predicted [33]. The sensitivity is an important measure to accurately diagnose the cancerous tissues, whereas the specificity determines how well the system detects healthy tissues. In an ideal case, both sensitivity and specificity tend towards 100%. In the following, all three metrics (accuracy, sensitivity and specificity) are evaluated as an average of 10 statistical experiments for which the data was randomly shuffled each time.

When looking at Figure 3, we can assume that the information of the tissue type is encoded in the frequency components of the blood perfusion time series. The oscillations in the cancerous tissue are slower whereas the time series collected from healthy tissue exhibits more high-frequency components. To validate the assumption and extract this information, we pre-process the LDF data by means of the wavelet analysis with the Morlet wavelet taken as a mother function. We calculated the integrated wavelet spectra (IWS) using the signal analysis technique in the frequency domain. Examples of representative IWS for cancerous and normal tissues are presented in Figure 3 (bottom panel). The length of the recordings allowed us to calculate 3 spectral ranges of the oscillations in the fine structure of capillary blood flow corresponding to the cardiac (0.6–1.6 Hz), respiratory (0.2–0.6 Hz) and myogenic activities (0.2–0.06 Hz) [34]. The maximal amplitude of the oscillations in every spectral range was taken as a diagnostic parameter. One-Way ANOVA with Tukey's post hoc test was used to check the significance of the statistical variation between blood perfusion parameters measured in the tumour and the intact tissue. Only demonstrated statistically significant difference parameters of blood perfusion oscillations were used as the feature space for the ML methods.

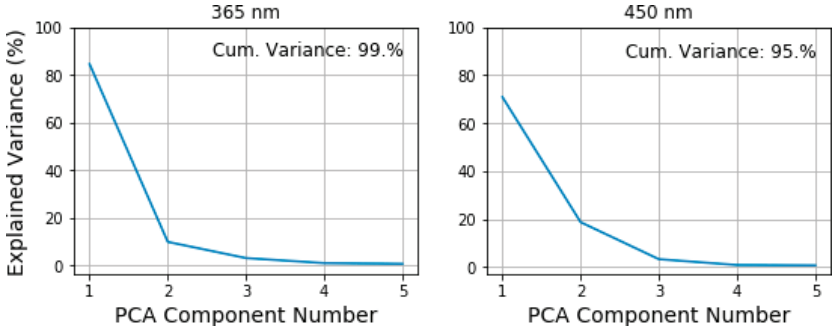

Figure 5. Example of percentage of explained variance at the excitation channel of 365 nm (**left**) and 450 nm (**right**) achieved by PCA.

3. Results

As in the case with data pre-processing, the data evaluation for TEF was done using the Scikit-learn library. The considered ML models underwent initial tuning in terms of the best prediction accuracy to pick the best possible hyperparameters. The resulting KNN classifier had 4 neighbours with distance weighting for both channels; also for both channels, the best maximum depth of the decision tree turned out to be only 1; the SVM model had a regularisation parameter of $Z = 0.1$ and a linear kernel for both 365 nm and 450 nm; the RF classifier for the 365 nm channel consisted of 5 estimators with a depth of 3; whereas the RF model for the 450 nm channel had 7 estimators with a depth of 3; the AdaBoost model consisted of 5 sub-estimators for each channel.

Tables 1 and 2 summarise the results for accuracy, sensitivity and specificity we achieved for 10 statistical experiments where the data used for training and testing was randomly shuffled each time. The results are presented as a mean value ± standard deviation in percent.

As Table 1 shows, the results of the TEF classification exhibit higher values for the 450 nm channel than for the 365 nm channel for all considered metrics. This suggests dropping the 365 nm channel in future which might considerably simplify the setup. Additionally, the dropping of the 365 nm channel would increase the in-field practicability of the suggested method. This is because the excitation radiation of 365 nm lying within the UV spectrum induces higher phototoxicity for living tissues than the light at 450 nm [35]. For TEF, the accuracy varies between 60% and 67% for the 365 nm channel and between 62% and 72% for the 450 nm channel.

Table 1. Achieved results of Accuracy and Specificity in % for each classifier and each excitation channel for TEF measurements.

Channel	*365 nm*			*450 nm*		
Model	**Accuracy**	**Sensitivity**	**Specificity**	**Accuracy**	**Sensitivity**	**Specificity**
KNN	60 ± 8	41 ± 21	73 ± 12	62 ± 6	46 ± 21	78 ± 8
Decision Tree	67 ± 7	28 ± 25	89 ± 9	67 ± 8	27 ± 37	94 ± 13
SVM	67 ± 8	15 ± 28	96 ± 6	72 ± 6	28 ± 35	99 ± 2
Random Forest	65 ± 8	27 ± 27	86 ± 11	64 ± 7	28 ± 28	88 ± 8
AdaBoost	65 ± 6	26 ± 26	87 ± 7	64 ± 5	37 ± 37	86 ± 16

As discussed in Section 2.2, we assume a high LPE implicating that several spectra were falsely labelled right at the beginning. We assume an LPE of around 15%. In this case, the accuracy is limited by this value, meaning that even a perfect classifier would not be able to achieve better accuracy results than around 85%. From this point of view, to achieve accuracy values up to 72% is highly promising.

In detail, from all considered values of accuracy, the SVM algorithm for the TEF data provides the best performance. Moreover, in terms of specificity, SVM shows the best results, going to 96–99%

well predicting the negative cases, i.e., the cases of healthy tissues. The second-best result is shown by the DT model. However, if you consider the sensitivity values, both SVM and DT perform poorly on the prediction of cancerous tissues, which is the most important aspect for in situ diagnosis. Taking into account the value of sensitivity, the best performance is shown by KNN for both channels and AdaBoost, specifically for the 450 nm channel. The considered Random Forest performs poorly in terms of all three metrics.

In general, we observe a high variety in sensitivity values that manifests itself in high values of standard deviation. This occurs due to the difficulties of the data collection described in Section 2.2 and poses the requirement to improve the data collection and labelling in further stages of the approach development.

As for LDF, the evaluated amplitudes of the cardiac and respiratory oscillation were significantly higher in intact tissues ($p < 0.001$) compared to the cancerous ones, while the myogenic oscillation did not demonstrate any statistically significant difference. The results on the statistical analysis of the differences in the oscillations in normal intact and cancerous tissues are presented in Figure 6. The reason for the observed distinction of the amplitude values in the healthy and cancerous tissues can lie in the mechanical properties of the tumour resulting in the dimming of the amplitude of the pulse that propagates through the microvessels within the cancerous tissue.

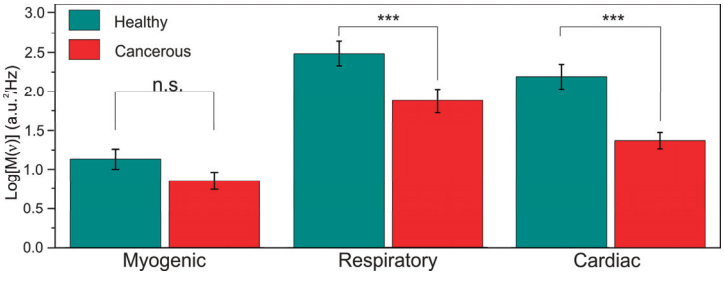

Figure 6. Results on the statistical analysis (One-Way ANOVA with Tukey's post hoc test, *** $p < 0.001$, n.s.: not significant, Mean ± SE) of the differences in the oscillations in normal intact and cancerous tissues in the hepatoduodenal area.

The results obtained by the ML models applied to the values of blood perfusion oscillations obtained from wavelet transform (Table 2) suggest that the parameters especially of the cardiac oscillations are of high a diagnostic value and can effectively supplement the TEF analysis and classification. However, more clinical research and better feature extraction as well as the fine-tuning of the ML models are needed to produce better prediction results and to correctly interpret them.

Table 2. Results of Accuracy and Specificity in % for each classifier for blood perfusion rhythmic oscillations.

Channel	*Cardiac Oscillations*			*Respiratory Oscillations*		
Model	**Accuracy**	**Sensitivity**	**Specificity**	**Accuracy**	**Sensitivity**	**Specificity**
KNN	58 ± 7	34 ± 26	82 ± 16	56 ± 10	35 ± 10	77 ± 18
Decision Tree	62 ± 7	61 ± 22	65 ± 24	55 ± 6	37 ± 20	72 ± 18
SVM	60 ± 9	26 ± 20	93 ± 8	59 ± 8	36 ± 19	81 ± 13
Random Forest	54 ± 15	57 ± 17	51 ± 30	58 ± 6	42 ± 14	73 ± 13
Logistic Regression	70 ± 7	52 ± 9	87 ± 9	64 ± 8	49 ± 11	79 ± 12

As Table 2 presents, the best results are achieved by logistic regression applied to classify the cardiac oscillations. This suggests focussing only on the data obtained for cardiac oscillations and to use logistic regression to evaluate it in future. Further, reliable evaluation of the blood perfusion

pulsations associated with the heart activity requires as much as twice shorter LDF recording duration than the one required for the respiratory oscillations. As a result, the duration of the LDF recording can be shortened.

4. Discussion

The challenge of more accurate data collection to significantly minimise the LPE still requires an appropriate solution. Further development of the proposed multimodal approach by equipping it with additional optical methods (e.g., diffuse reflectance spectroscopy or optical proximity sensor) can be an option to improve the accuracy of the probe placement. An approach based on the diffuse reflectance measurements might allow for a significant decrease in the influence of blood absorption on the recorded TEF spectra.

A non-contact proximity sensor embedded in the probe combined with the subsequent automation of the data collection at a fixed optimal distance might eliminate the negative effects of the sensor tip pressure on the soft tissues under study. Moreover, the saline delivery subsystem for the pus, mucus and blood removal from the tissue surface and optical probe cleaning during the procedure are also considered to be promising for the improvement of the quality of the data collection.

Based on the achieved results, we believe that the use of the 365 nm channel can be dropped in the further design development of the fibre-optic probe since it does not contribute to the overall performance. We see that TEF analysis and classification can be assisted by the analysis of the LDF data for cardiac oscillations. However, deeper-going studies with respect to the suitable feature extraction and ML model hyper-parameters are needed to effectively supplement the TEF classification with LDF classification. To improve the data quality and efficiency for the LDF analysis, the length of the blood perfusion recordings can be shortened from 1 min to 30 s as it is enough for the suggested analysis of the cardiac oscillations. As for the ML methods, AdaBoost and KNN models demonstrate the best results in terms of accuracy, specificity, and sensitivity and should be considered for classifying cancerous and noncancerous tissues in real-time in situ TEF diagnosis. The logistic regression is preferable for the classification based on the blood perfusion oscillations data.

5. Conclusions

Our results clearly demonstrate that a fibre-optic TEF probe accompanied with ML algorithms such as k-Nearest Neighbours or AdaBoost is highly promising for real-time in situ differentiation between cancerous and healthy tissues by detection the information about the tissue type that is encoded in the fluorescence spectrum. This detection can be supplemented and enhanced by parallel collection and classification of blood perfusion rhythmic data, especially the one that denote cardiac oscillations. Clearly, the data collection procedure as well as the design of the proposed fibre-optic probe have to be improved. Once it is done, we are convinced that the proposed fibre probe together with the elaborated ML techniques constitutes a highly promising device for a prompt and precise in situ decision-making and would allow to choose the optimal surgical tactics during the tumour resection.

As a next step, we will elaborate a procedure for the collection of data with much higher quality as well as improve the design of the fibre-optic probe by, for instance, dropping the 365 nm excitation channel and introducing a non-contact proximity sensor.

Author Contributions: Original draft preparation, data curation and processing, data acquisition software, E.Z.; data processing, draft preparation, M.Z.; measurements, methodology, data curation, E.P.; measurements, K.K.; data acquisition setup, methodology, V.D.; experiments at the Orel Regional Clinical Hospital, conceptualisation, A.M.; conceptualisation, S.S.; initiated and supervised the work, project administration, E.U.R.; funding acquisition, supervision, project administration, A.D.; all authors edited the manuscript. All authors have read and agreed to the published version of the manuscript.

Funding: This research received no external funding.

Acknowledgments: This study was supported by the Russian Science Foundation under project No. 18-15-00201 (development of experimental setup and data acquisition). Special thanks are extended to the patients of the Orel Regional Clinical Hospital who kindly agreed to take part in the studies in the framework of their planned

minimally invasive surgical intervention. M.Z. would like to acknowledge the funding received within the H2020-MSCA-IF-2017 scheme (grant No. 792421). E.Z. acknowledges the support of the Academy of Finland (grant No. 318281). V.D. acknowledges the funding received within the H2020-MSCA-IF-2018 scheme (grant No. 839888).

Conflicts of Interest: The authors declare no conflict of interest. The funders had no role in the design of the study; in the collection, analyses, or interpretation of data; in the writing of the manuscript, or in the decision to publish the results.

References

1. Siegel, R.L.; Miller, K.D.; Jemal, A. Cancer statistics, 2019. *CA Cancer J. Clin.* **2019**, *69*, 7–34. [CrossRef] [PubMed]
2. Tearney, G.; Brezinski, M.; Bouma, B.; Boppart, S.; Pitris, C.; Southern, J.; Fujimoto, J. In vivo endoscopic optical biopsy with optical coherence tomography. *Science* **1997**, *276*, 2037–2039. [CrossRef] [PubMed]
3. Sonn, G.A.; Jones, S.N.E.; Tarin, T.V.; Du, C.B.; Mach, K.E.; Jensen, K.C.; Liao, J.C. Optical biopsy of human bladder neoplasia with in vivo confocal laser endomicroscopy. *J. Urol.* **2009**, *182*, 1299–1305. [CrossRef] [PubMed]
4. Ladabaum, U.; Fioritto, A.; Mitani, A.; Desai, M.; Kim, J.P.; Rex, D.K.; Imperiale, T.; Gunaratnam, N. Real-time optical biopsy of colon polyps with narrow band imaging in community practice does not yet meet key thresholds for clinical decisions. *Gastroenterology* **2013**, *144*, 81–91. [CrossRef]
5. Wang, T.D.; Van Dam, J. Optical biopsy: A new frontier in endoscopic detection and diagnosis. *Clin. Gastroenterol. Hepatol.* **2004**, *2*, 744–753. [CrossRef]
6. Soulet, D.; Lamontagne-Proulx, J.; Aube, B.; Davalos, D. Multiphoton intravital microscopy in small animals: Motion artefact challenges and technical solutions. *J. Microsc.* **2020**, *278*, 3–17. [CrossRef]
7. Tonutti, M.; Elson, D.S.; Yang, G.Z.; Darzi, A.W.; Sodergren, M.H. The role of technology in minimally invasive surgery: State of the art, recent developments and future directions. *Postgrad. Med. J.* **2017**, *93*, 159–167. [CrossRef]
8. Nazeer, S.S.; Saraswathy, A.; Shenoy, S.J.; Jayasree, R.S. Fluorescence spectroscopy as an efficient tool for staging the degree of liver fibrosis: An in vivo comparison with MRI. *Sci. Rep.* **2018**, *8*, 10967. [CrossRef]
9. Zhao, M.; Dong, L.; Liu, Z.; Yang, S.; Wu, W.; Lin, J. In vivo fluorescence imaging of hepatocellular carcinoma using a novel GPC3-specific aptamer probe. *Quant. Imaging Med. Surg.* **2018**, *8*, 151–160. [CrossRef]
10. Sun, H.; Tan, W.; Zu, Y. Aptamers: Versatile molecular recognition probes for cancer detection. *Analyst* **2016**, *141*, 403–415. [CrossRef]
11. Buttemere, C.; Chari, R.; Anderson, C.; Washington, M.; Mahadevan-Jansen, A.; Lin, W. In vivo assessment of thermal damage in the liver using optical spectroscopy. *J. Biomed. Opt.* **2004**, *9*, 1018–1027. [CrossRef]
12. Gulledge, C.; Dewhirst, M. Tumor oxygenation: A matter of supply and demand. *Anticancer Res.* **1996**, *16*, 741.
13. Druzhkova, I.N.; Shirmanova, M.V.; Lukina, M.M.; Dudenkova, V.V.; Mishina, N.M.; Zagaynova, E.V. The metabolic interaction of cancer cells and fibroblasts–coupling between NAD (P) H and FAD, intracellular pH and hydrogen peroxide. *Cell Cycle* **2016**, *15*, 1257–1266. [CrossRef]
14. Liu, Q.; Grant, G.; Li, S.; Wilson, C.; Li, J.; Bigner, D.; Zhang, Y.; Hu, F.; Vo-Dinh, T.; Chen, K. Compact point-detection fluorescence spectroscopy system for quantifying intrinsic fluorescence redox ratio in brain cancer diagnostics. *J. Biomed. Opt.* **2011**, *16*, 037004. [CrossRef]
15. Palmer, S.; Litvinova, K.S.; Rafailov, E.U.; Nabi, G. Detection of urinary bladder cancer cells using redox 35ratio and double excitation wavelengths autofluorescence. *Biomed. Opt. Express* **2015**, *6*, 977–986. [CrossRef]
16. Awasthi, K.; Moriya, D.; Nakabayashi, T.; Li, L.; Ohta, N. Sensitive detection of intracellular environment of normal and cancer cells by autofluorescence lifetime imaging. *J. Photochem. Photobiol. B Biol.* **2016**, *165*, 256–265. [CrossRef] [PubMed]
17. Wang, M.; Long, F.; Tang, F.; Jing, Y.; Wang, X.; Yao, L.; Ma, J.; Fei, Y.; Chen, L.; Wang, G.; et al. Autofluorescence imaging and spectroscopy of human lung cancer. *Appl. Sci.* **2017**, *7*, 32. [CrossRef]
18. Kandurova, K.; Dremin, V.; Zherebtsov, E.; Potapova, E.; Alyanov, A.; Mamoshin, A.; Ivanov, Y.; Borsukov, A.; Dunaev, A. Fiber-optic system for intraoperative study of abdominal organs during minimally invasive surgical interventions. *Appl. Sci.* **2019**, *9*, 217. [CrossRef]

19. Zherebtsov, E.; Dremin, V.; Popov, A.; Doronin, A.; Kurakina, D.; Kirillin, M.; Meglinski, I.; Bykov, A. Hyperspectral imaging of human skin aided by artificial neural networks. *Biomed. Opt. Express* **2019**, *10*, 3545–3559. [CrossRef]
20. Ehlen, L.; Zabarylo, U.J.; Speichinger, F.; Bogomolov, A.; Belikova, V.; Bibikova, O.; Artyushenko, V.; Minet, O.; Beyer, K.; Kreis, M.E.; et al. Synergy of Fluorescence and Near-Infrared Spectroscopy in Detection of Colorectal Cancer. *J. Surg. Res.* **2019**, *242*, 349–356. [CrossRef]
21. Zhen, S.H.; Cheng, M.; Tao, Y.B.; Wang, Y.F.; Juengpanich, S.; Jiang, Z.Y.; Jiang, Y.K.; Yan, Y.Y.; Lu, W.; Lue, J.M.; et al. Deep learning for accurate diagnosis of liver tumor based on magnetic resonance imaging and clinical data. *Front. Oncol.* **2020**, *10*, 680. [CrossRef] [PubMed]
22. Pan, C.; Schoppe, O.; Parra-Damas, A.; Cai, R.; Todorov, M.I.; Gondi, G.; von Neubeck, B.; Bögürcü-Seidel, N.; Seidel, S.; Sleiman, K.; et al. Deep learning reveals cancer metastasis and therapeutic antibody targeting in the entire body. *Cell* **2019**, *179*, 1661–1676.e19. [CrossRef]
23. Lin, H.; Wei, C.; Wang, G.; Chen, H.; Lin, L.; Ni, M.; Chen, J.; Zhuo, S. Automated classification of hepatocellular carcinoma differentiation using multiphoton microscopy and deep learning. *J. Biophotonics* **2019**, *12*, e201800435. [CrossRef] [PubMed]
24. Dremin, V.; Potapova, E.; Zherebtsov, E.; Kandurova, K.; Shupletsov, V.; Alekseyev, A.; Mamoshin, A.; Dunaev, A. Optical percutaneous needle biopsy of the liver: A pilot animal and clinical study. *Sci. Rep.* **2020**, *10*, 14200. [CrossRef] [PubMed]
25. Dunaev, A.V.; Drernin, V.V.; Zherebtsov, E.A.; Rafailov, I.E.; Litvinova, K.S.; Palmer, S.G.; Stewart, N.A.; Sokolovski, S.G.; Rafailov, E.U. Individual variability analysis of fluorescence parameters measured in skin with different levels of nutritive blood flow. *Med. Eng. Phys.* **2015**, *37*, 574–583. [CrossRef]
26. Zherebtsov, E.; Dremin, V.; Zharkikh, E.; Zherebtsova, A.; Rafailov, I.; Dunaev, A.; Bazieva, N.; Rafailov, E. Fibre-Optic Probe for Fluorescence Diagnostics with Blood Influence Compensation. In Proceedings of the SPIE Conference on Dynamics and Fluctuations in Biomedical Photonics XV, San Francisco, CA, USA, 28–29 January 2018; Tuchin, V.V., Larin, K.V., Leahy, M.J., Wang, R.K., Eds.; SPIE: Bellingham, WA, USA, 2018; Volume 10493.
27. Lancaster, G.; Stefanovska, A.; Pesce, M.; Vezzoni, G.M.; Loggini, B.; Pingitore, R.; Ghiara, F.; Barachini, P.; Cervadoro, G.; Romanelli, M.; et al. Dynamic markers based on blood perfusion fluctuations for selecting skin melanocytic lesions for biopsy. *Sci. Rep.* **2015**, *5*, 12825. [CrossRef] [PubMed]
28. Cover, T.; Hart, P. Nearest neighbor pattern classification. *IEEE Trans. Inf. Theory* **1967**, *13*, 21–27. [CrossRef]
29. Podgorelec, V.; Kokol, P.; Stiglic, B.; Rozman, I. Decision trees: An overview and their use in medicine. *J. Med. Syst.* **2002**, *26*, 445–463. [CrossRef]
30. Vapnik, V.N. *Statistical Learning Theory*; Wiley-Interscience: Hoboken, NJ, USA, 1998.
31. Breiman, L. Random Forests. *Mach. Learn.* **2001**, *45*, 5–32. [CrossRef]
32. Freund, Y.; Schapire, R.; Abe, N.A. Short Introduction to Boosting. *J. Jpn. Soc. Artif. Intell.* **1999**, *14*, 1612.
33. Loong, T. Understanding sensitivity and specificity with the right side of the brain. *BMJ Br. Med. J.* **2003**, *327*, 716–719. [CrossRef] [PubMed]
34. Dremin, V.; Kozlov, I.; Volkov, M.; Margaryants, N.; Potemkin, A.; Zherebtsov, E.; Dunaev, A.; Gurov, I. Dynamic evaluation of blood flow microcirculation by combined use of the laser Doppler flowmetry and high-speed videocapillaroscopy methods. *J. Biophotonics* **2019**, *12*, e201800317. [CrossRef] [PubMed]
35. McKinlay, A.; Bernhardt, J.; Ahlbom, A.; Cesarini, J.; de Gruijl, F.; Hietanen, M.; Owen, R.; Sliney, D.; Soderberg, P.; Swerdlow, A.; et al. Guidelines on limits of exposure to ultraviolet radiation of wavelengths between 180 nm and 400 nm (incoherent optical radiation). *Health Phys.* **2004**, *87*, 171–186.

diagnostics

MDPI

Article

New Approaches in the Study of the Pathogenesis of Urethral Pain Syndrome

Olga Streltsova [1], Anton Kuyarov [1], Muhhamad Shuaib Abdul Malik Molvi [1], Svetlana Zubova [2], Valery Lazukin [3], Ekaterina Tararova [4] and Elena Kiseleva [5,*]

1 E.V. Shakhov Department of Urology, Privolzhsky Research Medical University, 10/1 Minin and Pozharsky Sq., 603950 Nizhny Novgorod, Russia; strelzova_uro@mail.ru (O.S.); kuyarov.anton@mail.ru (A.K.); msmolvi@mail.ru (M.S.A.M.M.)
2 N.A. Semashko Nizhny Novgorod Regional Clinical Hospital, 190 Rodionova St., 603126 Nizhny Novgorod, Russia; zubova.svetlana.65@yandex.ru
3 Department of Medical Physics and Informatics, Privolzhsky Research Medical University, 10/1 Minin and Pozharsky Sq., 603950 Nizhny Novgorod, Russia; valery-laz@yandex.ru
4 Nizhny Novgorod Regional Oncology Dispensary, 190 Rodionova St., 603126 Nizhny Novgorod, Russia; tararova-ea@mail.ru
5 Institute of Experimental Oncology and Biomedical Technologies, Privolzhsky Research Medical University, 10/1 Minin and Pozharsky Sq., 603950 Nizhny Novgorod, Russia
* Correspondence: kiseleva84@gmail.com; Tel.: +7-920-059-0536

Received: 25 September 2020; Accepted: 20 October 2020; Published: 22 October 2020

Abstract: Introduction: Urethral pain syndrome (UPS) is still a pathology in which the diagnosis is formulated as a "diagnosis of exclusion". The exact pathogenetic mechanisms are not yet fully understood and clear recommendations for the prevention and treatment of UPS are absent. Methods and Participants: A clinical and laboratory evaluation of 55 patients with established UPS included history taking, basic laboratory tests (e.g., complete blood count and clinical urine test), physical examination, uroflowmetry, and cystourethroscopy. Additionally, transvaginal ultrasound (TVUS) with compression elastography and cross-polarization optical tomography (CP OCT) were performed in 24 and 33 patients with UPS, respectively. The control group consisted of 14 patients with no complaints from the urinary system. Results: TVUS showed an expansion in the diameter of the internal lumen of the urethra, especially in the proximal region compared with the norm. Compression elastography revealed areas with increased stiffness (presence of fibrosis) in urethral and surrounding tissues. The performed CP OCT study showed that in UPS, the structure of the tissues in most cases was changed: trophic alterations in the epithelium (hypertrophy or atrophy) and fibrosis of underlying connective tissue were observed. The proximal fragment of the urethra with UPS underwent changes identical to those of the bladder neck. Conclusion: This paper showed that the introduction of new technology—CP OCT—in conjunction with TVUS will allow verification of structural changes in tissues of the lower urinary tract at the level of their architectonics and will help doctors understand better the basics of the UPS pathogenesis.

Keywords: cross-polarization optical coherence tomography (CP OCT); ultrasound; urethral pain syndrome; epithelial atrophy; epithelial hyperplasia; inflammation; fibrosis; image evaluation

1. Introduction

The most common reason for women to seek medical attention is dysuria, and it is believed that in 40% of cases urethritis and/or urethral syndrome are involved [1]. According to the US National Institutes of Health, one third of women with chronic pelvic pain (CPP) have urethral pain syndrome (UPS) [2,3]. The European Association of Urology defines UPS as the occurrence of chronic or recurrent

episodic pain lasting for more than 6 months, and felt in the urethra, in the absence of proven infection or other obvious local pathology. It is often associated with negative cognitive, behavioral, sexual or emotional consequences [4], as well as with symptoms suggestive of lower urinary tract, sexual, intestinal, or gynecological dysfunction [5].

The problem of pain in the urethra with unchanged urinalysis, the absence of any other clinical manifestations, and the absence of somatically explainable causes, is complex and ultimately remains unresolved, since the exact pathogenetic mechanisms are not yet fully understood [6–9]. Neither are there any clear recommendations for the prevention and treatment of UPS, as a result of which the only effective form of medical care today is symptomatic therapy—involving the continuing intake of strong pain medications, antidepressants, and anticonvulsants [4,9]. In the methodological recommendations on CPP, published under the auspices of the the Moscow Department of Health (dated 14 July 2016), it is noted that there is no specific accepted treatment for UPS [10]. The approach should be interdisciplinary and the treatment should be multimodal, with the general principles of chronic pain syndrome management being applied [11–13].

The close embryological relationship between the urethra and the bladder makes it likely that there are causes similar to ones connected with the development of painful bladder syndrome [14]. According to the classification of the International Association for the Study of Pain (IASP, 2019) the mechanism of CPP and possible causes of its occurrence may include vascular lesions, persistent inflammatory processes, or violation of the innervation of organs due to mechanical compression in the pelvic region, but often the reason is not clear [15].

The connective tissue matrix of organs plays a key role in the occurrence and persistence of pain, as shown by the number of studies [16,17]. It is believed that connective tissue, as well as performing its supporting, protective and trophic functions, acts as a network-wide mechanosensitive signaling system—as a global unifying network [16,18].

Thus, it can be surmised that the above reasons for the development of CPP could be associated with factors that affect the state of the connective tissue matrix of the lower urinary tract. However, there are currently no methods for adequate, appropriate study of the structure of urethral tissues. According to the standards for examination of patients with CPP when using the UPOINT (Urinary, Psychosocial, Organ Specific, Infection, Neurologic/Systemic, Tenderness of Skeletal Muscles) classification [19] in the urology domain, the recommended list of examinations includes keeping a urination diary, cystoscopy, and the use of ultrasound (US) and uroflowmetry, while for complaints involving the urethra, urethroscopy is recommended. These methods allow only indirect assessment of the urethral tissues. Objective evaluation and accurate diagnosis of a disease that does not cause any visual changes, and results from a "diagnosis of exclusion" when using standard instrumental diagnostic methods, is important for understanding the pathogenetic aspects of the disease. In this work, we used traditional diagnostic methods, including US and uroflowmetry, and the non-traditional methods of ultrasound elastography (USE) and cross-polarization optical tomography (CP OCT) to study changes in the functioning of organs and their structure in UPS in comparison with the norm, and assessed the role of background diseases in the development of UPS.

The USE is a medical imaging modality that measures tissue mechanical properties by monitoring the response of tissue to acoustic energy [20,21]. In clinical settings, USE is emerging as a powerful tool for imaging and quantitatively monitoring cancer and fibrosis [22]. It provides a rapid visualization of the tissue elasticity using color-coding mode, even in organs deep within the body. Recently, USE is applied especially on the breast and liver, but the technique has been increasingly used for other tissues including the thyroid, prostate, lymph nodes, gastrointestinal tract, kidney, spleen, pancreas, and the musculoskeletal and vascular systems [22,23]. There are several USE techniques used in clinical practice, but USE with strain (compression) being the most common one allowing real-time visualization of the elastographic map on the screen [24]. With regard to the study of the urethra in UPS, the method can be useful for detecting fibrous changes in the urethral wall and adjacent tissues.

In general, OCT is similar to the ultrasonic technique, except for using light instead of sound and is centered on interferometry in the near-infrared range of wavelength (700–1300 nm) [25,26]. It measures the time delay and amplitude of backscattered light. The aim of the OCT technology is to perform a real-time, in vivo, optic biopsy, with direct label-free visualization of the histological structure of the human tissues at the level of the general architectonics to a depth of 1.5 mm [27]. High spatial resolution (5–15 μm) and performance simplicity with minimal expertise are the main advantages of OCT in contrast to US. The endoscopic nature of OCT probes not only enhances patient comfort and safety but also makes it especially suitable for assessing narrow tubular organs as well as for using standard guidewires for examining deeply located objects in the body [28].

CP OCT is a functional extension of OCT that enables the detection of changes in the state of polarization of light caused by birefringence and coupling between two polarization states due to scattering in the random media (cross-scattering) [29]. As a result, two types of images are obtained simultaneously: in the initial (co-) polarization and orthogonal (cross-) polarization, which allow assessing isotropic (cells) and anisotropic (collagen and elastic fibers of connective tissue) structures separately [30,31]. This is important in cases when precise observation of only connective tissue structures is needed.

The goal of the study was to assess the condition of the tissue in the female urethra in UPS, by using non-traditional methods for this pathology—compression US and CP OCT.

2. Materials and Methods

2.1. Patients

In total, 69 female patients were enrolled in this study: 55 with established UPS ("UPS" group, aged from 21 to 66 years) and 14 with a healthy urethra as a control group ("Norm" group, aged from 24 to 62 years). Patients with UPS received treatment in the urology department of the N.A. Semashko Nizhny Novgorod Regional Clinical Hospital between 2014 and 2019.

Inclusion criteria for the UPS group consisted of: age 18 years and older; presence of recurrent episodic pain localized in the urethra lasting more than 6 months; absence of infectious lesion or obvious organ pathology [32]. Exclusion criteria for UPS group were: age under 18; the presence of inflammatory processes in the lower urinary tract; the presence of tumors of the pelvic organs; radiation damage to the pelvic organs; pregnancy; lactation. The control group included women whose age was 18 years and older, with no detected pathology and complaints from the lower urinary tract. Otherwise, people were excluded from the study.

This study was approved by the review board of the Privolzhsky Research Medical University (Protocol #6 from 28 April 2020). The research was carried out within the framework of the RFBR project #19-07-00395, agreements 1236/19 from 11 April 2019 and #1365/20 from 30 March 2020. Informed consent to participate in the study was obtained from the participants. All conducted studies and the number of patients included are presented in Table 1.

Table 1. Clinical and laboratory methods for patient's examination and number of included patients.

Type of Study	Purpose of the Study	Number of Patients in the UPS Group	Number of Patients in the Norm Group
1. History taking	identification of the presence of any previously transferred concomitant pathology	55	14
2. Laboratory tests of blood and urine	identification of inflammatory processes	55	14
3. Physical examination and palpation of the urethra and the walls of the vagina (on a gynecological chair)	assessment of the state of the external opening of the urethra, detection of the presence of any myofascial aspect in the disease	55	-
4. Uroflowmetry	assessment of the condition of the sphincters of the urethra and bladder	55	-
5. Transvaginal US/compression US	assessment of the size, shape, structure of the urethra and bladder neck/mapping of the urethral wall and surrounding tissues stiffness	24	6

Table 1. *Cont.*

Type of Study	Purpose of the Study	Number of Patients in the UPS Group	Number of Patients in the Norm Group
6. Cystoscopy	examination the inside of the bladder in detail; identification and recording of abnormal findings	33 *	14 [0]
7. CP OCT [#]	visualization of the internal structure of the bladder neck and urethral wall, evaluation the condition of epithelium and connective tissue layers	33	14

* carried out to exclude the presence of interstitial cystitis; [0] patients with stones of the upper urinary tract but without pyelonephritis who have been assigned cystoscopy; [#] performed in conjunction with cystoscopy.

2.2. Transvaginal US

Transvaginal US (TVUS) was performed using a Philips Epiq5 system (Philips Ultrasound., Inc., 22100 Bothell-Everett Highway, Bothell, Washington, 98021-8431, USA). The sensor was inserted directly into the vagina, allowing visualization of the state of the bladder neck and urethra (assessment of their structure, the condition of their walls, and the width of the internal lumen) and detecting abnormalities in the structure of the urethra compared with the norm. This was also the first study in which patients with UPS underwent compression elastography of the adjacent urethral tissues. Compression elastography is a technique that displays the relative deformation of tissues in the form of their color mapping in real time [33]. When the tissue is subjected to an external force (deformation), the harder/denser areas of the tissue exhibit relatively less compression than the softer areas [24]. In our study, on the USE images, the adjustment scale was set to display the harder areas in blue, with the softer areas appearing in red [34].

2.3. CP OCT Study and Image Analysis

Time-domain device "Polarization-sensitive optical coherence tomograph OCT-1300U" (BioMedTech LLC, Nizhny Novgorod, Russia) (Figure 1a), that provides two image acquisition in co- and cross-polarizations was used in the study [29,35]. The device is approved for clinical use (product license №FCP 2012/13479 of 30 May 2012) and is equipped with replaceable endoscopic probe (Figure 1b,c). It has the following characteristics: the radiation source is a superluminescent diode, of operating wavelength 1310 nm, spectrum width 100 nm, axial resolution 15 μm, lateral resolution 25 μm, and radiation power at the object 3 mW. OCT image size in each polarization is 1.8 × 1.3 mm (width × height), image acquisition time is 2 s. Due to the presence of a flexible endoscopic probe with an outer diameter of 2.7 mm, the examination of the urethral tissue could be carried out simultaneously with cystoscopy through a standard endoscope. Our group's application of the CP OCT method to the study of the female urethral wall in patients with UPS, is a global "first" [36].

From 4 to 13 images were obtained from each patient: of the bladder neck and three regions of the urethra (Figure 1d) at the 6 o'clock position corresponding to a conventional clockface, and, if possible, with other additional images of the urethra in the three directions (9, 12, and 3 h of the clockface).

In the "UPS"/"N" groups, 169/58 CP OCT images were obtained, which included 43/16 CP OCT images of the bladder neck, as the section closest to the urethra and therefore potentially involved in processes occurring in the proximal urethra and 126/42 CP OCT images of the urethra (its proximal 41/14, middle 40/12, and distal 45/16 regions) (Table 2).

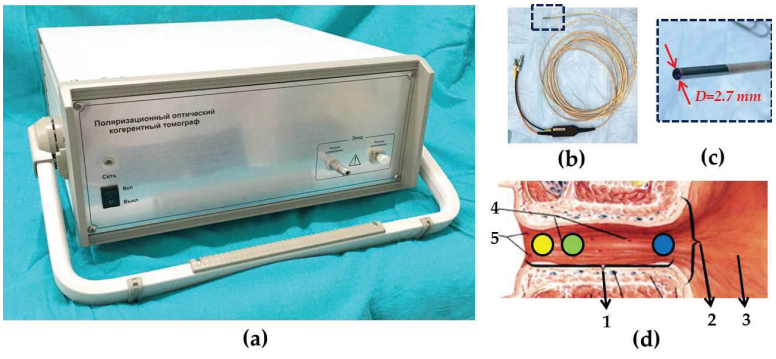

Figure 1. Cross-polarization optical tomography (CP OCT) device and areas under study shown on a diagram of the female urethra. (**a**) CP OCT device; (**b**) Flexible endoscopic forward-looking CP OCT probe; (**c**) Enlarged tip of the probe from (**b**). (**d**) Drawing of the urethra where it transitions to the bladder. Here, the circles indicate the locations from which CP OCT images were obtained in the proximal (blue), middle (green), and distal parts of the urethra (yellow) [37]. 1—urethra, 2—neck of urinary bladder, 3—triangle of urinary bladder, 4—lacunae and openings of urethral ducts, 5—openings of paraurethral Skene's ducts.

Table 2. Distribution of the CP OCT images by patient's groups and parts of the urethra.

Group	Number of Patients	Number of CP OCT Images	Average Number of CP OCT Images Created from 1 Patient	Number of CP OCT Images of Each Location			
				Bladder Neck	Distal Urethra	Medium Urethra	Proximal Urethra
UPS	33	169	5.12	43	41	40	45
Norm	14	58	4.14	16	14	12	16
Total	47	227	4.63	59	55	52	61

A visual assessment of the CP OCT images of the bladder neck and urethra was performed by two readers. The objects of interest were the epithelium and the state of the connective tissue structures of the urethra in patients with UPS, relative to the normal state of these structures. In the epithelium, the thickness was assessed as: normal, thickening (hyperplasia), or thinning (atrophy); in the connective tissue stroma, attention was paid to the presence of any element in the images corresponding to an inflammatory process or fibrosis. The CP OCT features of inflammation were: (1) lack of clarity of the border between the first (epithelial) and the second (connective tissue) layers, (2) the absence of horizontal ordering of the structures that are representative of the norm, and (3) the presence of any indistinctness in their images, which would correspond to cellular tissue infiltration. Significant thickening of the connective tissue layer, up to the lower border of the image with maintaining a high signal level was considered a sign of fibrosis [36,38]. Before qualitative evaluation of CP OCT images readers were trained by training test. After an independent blind visual assessment of the CP OCT images, the «UPS» group was divided into 2 age subgroups: patients under 50 and those over 50.

2.4. Statistical Analysis

The statistical analysis was performed using IBM SPSS Statistics software, V20 (IBM Corporation, Somers, NY, USA). The inter-reader reliability was calculated using the Fleiss' kappa (κ) coefficient: $\kappa > 0.8$—perfect agreement; $0.7 \leq \kappa < 0.8$—substantial agreement; $\kappa < 0.7$—poor agreement.

3. Results

3.1. The Role of Background Diseases in the Development of UPS

An analysis of concomitant pathology in patients with UPS, identified by their history is presented in Table 3. From Table 3 it follows that the predominant area of comorbidity was gynecological (70.9%). Hormonal abnormalities (94.8%) were found in 24 sexually active women in the pre-menopausal period, as well as in 13 women of the menopausal period; inflammatory diseases of the female genital area of bacterial and viral etiology were also present (76.9%).

Table 3. Concomitant pathology and the source of its occurrence in the group of patients with urethral pain syndrome (UPS) (n = 55).

Organ System with Pathology	n-Abs. (%)	Genesis of Pathology	n-Abs. (%)
1. Gynecological	39 (70.9)	Hormonal	37 (94.8)
		Inflammatory	30 (76.9)
		Surgical interventions on the pelvic organs	12 (30.7)
2. Respiratory	37 (67.2)	Upper (nose, nasal cavity, pharynx, larynx)	32 (86.4)
		Lower (trachea, bronchi, lungs)	5 (13.5)
		Psycho-emotional sphere	23 (41.8)
3. Neurological	35 (63.6)	Central nervous system	10 (18.2)
		Peripheral nervous system	42 (76.4)
		Psycho-emotional sphere	23 (41.8)
4. Urological	24 (43.6)	Inflammatory	10 (41.6)
		Non-inflammatory	17 (70.8)
5. Gastroenterological	18 (32.7)	Inflammatory diseases of the stomach, duodenum, biliary tract	38 (69.0)
		Bowel disease	21 (38.2)
6. Cardiovascular	9 (16.3)	Arterial hypertension	5 (55.5)
		Other	4 (44.5)
Total cases of pathology	162		

Anamnesis of upper respiratory tract pathology, more common in adolescence, was recorded in 67.2% of women, of whom the bulk of patients (64.9%) reported frequent viral diseases or herpes infection. The premorbid background in patients with UPS was neurological pathology (63.6%), and these are diseases associated with the involvement of the peripheral nervous system and as is important, with the state of the psycho-emotional sphere.

Each patient suffering from UPS had 2.94 (162/55) cases of comorbidity. Thus, the role of other factors in the presence of foci of chronic infection in the body, and a decrease in immune defense factors, as a comorbid background for the development of UPS, cannot be denied, since the presence in the patients' history of inflammatory diseases of the respiratory tract, gastrointestinal tract, urological and gynecological organs was revealed.

3.2. Results of Cystoscopic Examination

In 32.7% of cases (18 out of 55), clinical manifestations of UPS were combined with urinary pain syndrome. Low-volume (less than 300 mL) urination was reordered. The number of urinations exceeded 12 per day. Pains over the womb were present. During cystoscopy in patients of the "UPS" group, the bladder mucosa was unchanged—shiny, pale pink, while, in 16 cases (29.0%), there was a slight hyperemia in the bladder neck. A picture corresponding to interstitial cystitis—the presence of glomerulations in the mucous membrane of the bladder after the hydrodistension procedure, was found in 23.6% (n = 13).

3.3. Uroflowmetry Results

In 72.7% of cases (40 out of 55), there was a decrease in the urination rate to 13.7 ± 3.2 mL/s in combination with low-volume urination while the normal values of the urination rate for women are 23–32 mL/s [39]. The average volume of excreted urine was 172 ± 33 mL.

3.4. Results of TVUS Research

The results of TVUS studies showed that in the norm group in women, the urethra looks like a tube with a uniform lumen diameter without dilatations and contractions, which was 4.6 ± 0.6 mm, wall thickness 4.8 ± 1.1 mm. According to research by a group of authors [40], normally, the outer diameter of the urethra is 10.0 mm, the inner lumen of the urethra is closed during TVUS or 0.3 mm (Figure 2a,b). According to the authors [41], who conducted a study with an intraurethral sensor, the thickness of the urethra in the proximal section was normally 3.7 mm.

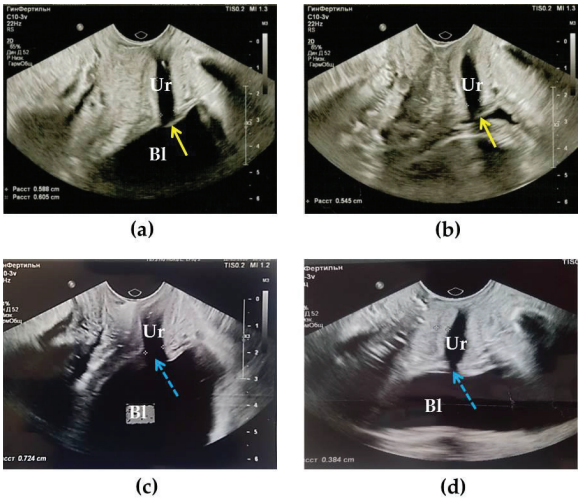

Figure 2. Transvaginal ultrasound (TVUS) of the urethra and adjacent tissues in normal conditions and with UPS. (**a**,**b**) A healthy woman 30 years of age before (**a**) and after (**b**) urination. The urethral tongue closes the opening to the urethra, as indicated by the yellow arrow; (**c**) Patient K., 30 years old, with a UPS disease duration of more than 10 years; (**d**) Patient Z., 38 years old, over 13 years of illness. In both cases, with UPS, the urethral tongue is indistinguishable and the gaping opening at the transition of the bladder into the urethra is indicated by the blue dashed arrows. Bl—bladder, Ur—urethra.

In women with UPS (n = 24), the structural features of the urethra were revealed: the urethra was funnel-shaped (Figure 2d), opening to the bladder. The internal lumen of the urethra in the proximal segment was expanded to 5.9 ± 2.1 mm. At the same time, 44% of patients had an expansion up to 7.5 ± 0.5 mm, in 56% up to 5.5 ± 0.5 mm. The thickness of the urethral walls in our study averaged 3.6 mm (from 2.4 to 6.0 mm). Thus, in all patients with UPS, an increase in the diameter of the internal lumen of the urethra, especially in the proximal region, was recorded.

In 7 (29.1%) cases, pathological changes were recorded in the urethral tongue, a cavernous structure that, as the bladder fills, normally increases in volume due to becoming engorged with blood and, together with the sphincter trigonalis, closes the exit from the bladder into the urethra. With the contraction of the urethra the posterior semicircle of the bladder neck is pressed against the anterior wall of the urethra and this closes its internal opening [42]. In patients with UPS, an absence of urethral tongue visualization (Figure 2c,d), or the absence of its adherence to the entrance to the urethra, was revealed. No residual urine was found in patients with UPS.

Compression US of the urethra and adjacent tissues of patients with UPS in the proximal and middle regions showed a significant predominance of areas colored blue, indicating tissue stiffness and rigidity (Figure 3b) compared to the norm, where no blue color was observed (Figure 3a). Thus, our studies confirm the presence of fibrosis of the tissues surrounding the urethra in UPS.

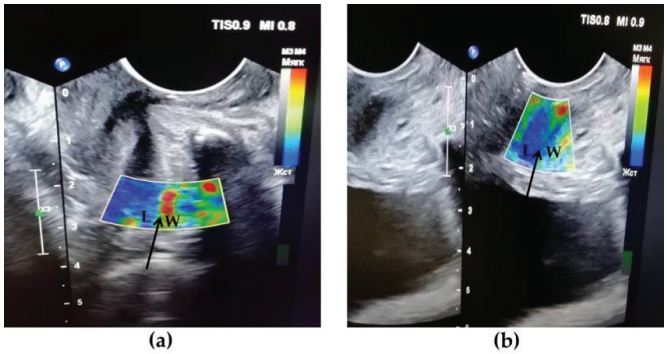

Figure 3. Compression ultrasound (US) in the normal condition (**a**) and in UPS (**b**). (**a**) Normally, the urethral wall is softer (red color) than in UPS (**b**) (predominance of green and blue colors). L—lumen of the urethra, W—urethral wall. The black arrow indicates the border between the lumen of the urethra and its wall.

3.5. Results of CP OCT Study

CP OCT images of all sections of the female urethra in the norm are structural. In co-polarization images (Figure 4a1–d1), the epithelium is clearly visualized in all areas of interest, its border contrasting with the underlying mucous layer. The epithelial layer and its thickness are marked in Figure 4a–d with dark blue rectangle. The signal from the connective tissue in the cross-polarization images (Figure 4a2–d2) is of medium intensity, has a horizontal orientation; in the middle and distal segments of the urethra, single, gland-like lacunas with clear contours can be determined. In cross-polarization, the OCT signal is determined mainly by the collagen fibers of the connective tissue layer, therefore, only this layer of the urethral wall is clearly visible in such images, and the epithelium and muscles are not visualized.

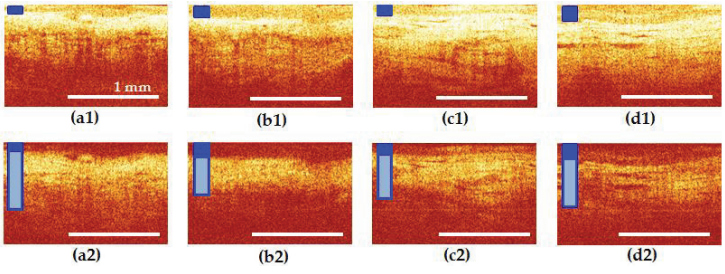

Figure 4. CP OCT images of the bladder neck (**a**) and three segments of normal urethra (**b**–**d**): (**b**) proximal; (**c**) middle; and (**d**) distal. The first row shows co-polarization images, the second row shows corresponding cross-polarization images. The first (epithelial) layer and its thickness are marked in all images with a dark blue rectangle. The second layer (connective tissue of lamina propria) in (**a2**–**d2**) is indicated by a vertical rectangle in light blue color: its height shows the average height of the layer and the blue color inside the frame indicates its normal condition.

In the normal group, there were no changes in the visible thickness in the zones of interest (Figure 4a1–d1). However, in women over 50 years old, a tendency of the epithelium to atrophy was revealed, which can be explained by the influence of hormonal changes. The connective tissue stroma generated approximately the same signal level in the cross-channel, without any extensive dark or bright areas and occupied 40–50% of the entire image height (Figure 4a2–d2), connective tissue is marked by vertical rectangle in light blue color: its height shows an average height of the layer and the light blue color inside the frame indicates its normal condition).

Visual analysis of CP OCT in the UPS group revealed that, in terms of the characteristics of the epithelium and connective tissue, the proximal part of the urethra was more similar to the bladder neck than to the middle and distal parts of itself. Examples are shown in Figures 5 and 6.

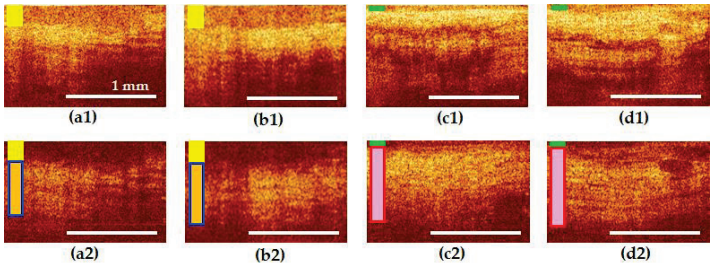

Figure 5. CP OCT images of the bladder neck (**a**) and three segments of the urethra (**b**–**d**) in patient I., 22 years old with UPS lasting 5 years. (**b**) Proximal; (**c**) middle; and (**d**) distal parts of the urethra. The first row shows co-polarization images, the second row shows corresponding cross-polarization images. (**a**,**b**) Epithelium hyperplasia is marked with yellow rectangle. Connective tissue in (**a2**,**b2**) have normal thickness (dark blue frame of vertical rectangle), but signs of inflammation (yellow color inside the rectangle); (**c**,**d**) Epithelial atrophy is marked with green rectangle. Connective tissue in (**c2**,**d2**) has increased thickness (red frame of vertical rectangle) and signs of fibrosis (pink color inside the rectangle).

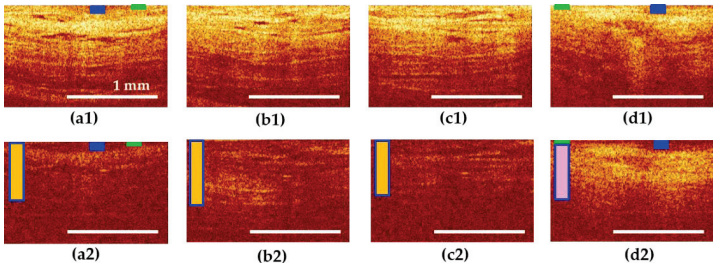

Figure 6. CP OCT images of the bladder neck (**a**) and three segments of the urethra (**b**–**d**) in patient E., 60 years old with UPS lasting 5 years. (**b**) proximal; (**c**) middle; and (**d**) distal parts of the urethra. The first row shows co-polarization images, the second row shows corresponding cross-polarization images. (**a**,**d**) Epithelium has signs of norm (blue rectangle), but mostly atrophic (green rectangle); (**b**,**c**) total epithelial atrophy is observed. (**a**–**c**) Connective tissue have normal thickness (dark blue frame of vertical rectangle), but signs of active inflammation (yellow color of vertical rectangle); (**d**) connective tissue has normal thickness (dark blue frame of vertical rectangle), but signs of fibrosis (pink color of vertical rectangle).

Figure 5 shows an example of patient I., 22 years old with UPS lasting 5 years. Epithelial hyperplasia is visible in the bladder neck and the proximal urethra (Figure 5a1,b1), the yellow rectangle), the border of the epithelium with the underlying connective tissue layer is blurred, indicating the presence of inflammatory processes in these tissues (Figure 5a1,b1). The signal from the connective tissue structures in cross-polarization has a noticeable local decrease in intensity caused by the shadows of dilated blood vessels and by tissue edema (Figure 5a2,b2), the vertical rectangle in yellow color shows tissue inflammation, dark blue frame indicates normal thickness of the layer). In the middle and distal parts of the urethra, by contrast, thinning of the epithelium is noticeable (Figure 5c1,d1), green rectangle), while in the middle part, the border with the underlying connective tissue layer is clear (Figure 5c1)).

The connective tissue layer is thickened (Figure 5c2,d2), the red frame of vertical rectangle indicates increased thickness of the layer, pink color indicates signs of tissue fibrosis and looks more

homogeneous in structure (Figure 5c2) than in the non-pathogenic case (Figure 4c2,d2). In this subgroup of patients, a thickening of the connective tissue layer in cross-polarization to occupy over 60% of the image height was observed in 44.4% (32 CP OCT images out of 72). In this case, an increase in the OCT signal was observed in all the images.

Figure 6 shows an example of patient E., 60 years old with UPS lasting 5 years. In the bladder neck and proximal urethra (Figure 6a1,b1), as well as in the rest of the urethra (Figure 6c1,d1), the epithelium is atrophic, and in places where it is partially preserved (Figure 6a,d, blue and green rectangle), the border of the epithelium with the underlying connective tissue layer is blurred (Figure 6a1,d1)). The signal from connective tissue structures in cross-polarization is weak, presumably due to severe tissue edema (Figure 6a2–c2), vertical rectangle in yellow color shows tissue inflammation, dark blue frame indicates normal thickness of the layer). In the distal urethra, on the other hand, the connective tissue layer exhibits cross-scattering, but appears homogeneous in structure (Figure 6d2), pink color of vertical rectangle indicates fibrosis) compared to normal (Figure 4d2). In this subgroup of patients, thickening of the connective tissue layer in cross-polarization to over 60% of the image height was observed in 46.7% (28 CP OCT images out of 60): 71.4% of them with an increase in the OCT signal (20 of 28), while 28.6% (8 out of 28) showed a weakening of the signal.

The inter-reader reliability in qualitative evaluation of CP OCT images was 0.93 that indicates high concordance between the two readers. Disagreements were observed in cases of focal epithelial atrophy (an example, Figure 6a,d): one of the readers rated the epithelium as atrophic, the other as normal. In other cases, the answers were completely the same.

The results of the incidence of the bladder neck + proximal conditions are presented in Table 4. 132 CP OCT images obtained at the '6 o'clock position' from 33 patients were analyzed.

Table 4. State of the epithelium of the bladder neck and the proximal region of the urethra compared with the epithelium of the middle and distal regions at the '6 o'clock position' in patients with UPS, depending on age.

Subgroup of Patients by Age, Years	Number of Patients	Number of CP OCT Images	Hyperplasia of the Bladder Neck + Proximal Urethra	Atrophy of the Bladder Neck + Proximal Urethra	Total Matches	% of Changes in the Bladder Neck + Proximal Urethra of the Total Number of Patients
≤49	18	72	4	4	8	44.4% (8/18)
50≥	15	60	7	7	14	93.3% (14/15)
Total (n = 33)	33	132	11	11	22	68.8% (22/33)

It was revealed that changes in the epithelium of the bladder neck and proximal urethra—hyperplasia or atrophy, which differed from the middle and distal segments of the urethra—coincided in 22 cases out of 33, representing 68.8%. Hyperplasia was identified in 34.4% of cases (n = 11) as well as atrophy in 34.4% of cases (n = 11). It is noteworthy that in women over 50 years of age (n = 15), changes in the analyzed area were more common—93.3%, compared with women of reproductive age (n = 18)—44.4%. It can be surmised that hormonal levels undoubtedly play a role in changing the state of the tissues of the bladder neck and urethra.

Of the 11 cases of hyperplasia detected in the proximal urethra, only in the case of the epithelium was there also thickening in the middle and distal urethra. In other situations, atrophy was recorded—our cases, while, in six the epithelium was of normal thickness. In the presence of atrophy in the proximal urethra (n = 11), atrophy was recorded in the underlying regions—five cases, while the epithelium was of normal thickness in six cases.

Thus, the CP OCT method allowed us non-invasively to determine the state of the epithelium and connective tissue structures of the bladder neck and urethra in vivo. It was shown that with UPS, the structure of the tissues in most cases is changed. In this case, the proximal fragment of the urethra with UPS undergoes changes identical to those of the bladder neck.

4. Discussion

UPS is still a pathology in which the diagnosis is formulated as a "diagnosis of exclusion". It is not specific for women, as it can also occur in men [43], but in this case, it is customary to speak about prostatic, scrotal, or penile chronic pelvic pain [8]. A large number of studies have been devoted to the study of UPS and chronic pelvic pain in men [44–48], while UPS in women has been studied significantly less [3,6]. Therefore, one of the motivations was to conduct research on the female urethra. In any case, the problems of correct and quick diagnosis and the appointment of effective treatment for UPS in men there remain the same [5]. An idea to diagnose male UPS by using ultrasound and CP OCT devices seems to be reasonable and appropriate.

Despite significant global use of OCT in many fields of medicine [49–53], in urology, our study demonstrated the first use of this technique for examining the urethra [36]. This paper shows that the introduction of new technology—CP OCT—in conjunction with TVUS allows verification of tissue changes and assessment of the structures of the connective tissue matrix of the lower urinary tract at the level of their architectonics.

According to TVUS, in our study, women with UPS had an enlarged internal lumen of the urethra in the proximal segment—on average of 5.9 ± 2.1 mm. According to the literature, with an intraurethral ultrasound study performed on sectioned material, the inner diameter of the proximal segment of the urethra at distances of 10, 15, and 20 mm from the neck was 3.73, 4.18, and 2.64 mm, respectively [41]. In another study, when measuring the internal diameter of the urethra using TVUS in women with urinary incontinence [54], the diameter in the middle third of the urethra in the control (healthy) group of patients was 4.7 ± 1.1 mm. Thus, we have recorded an increase in the diameter of the internal lumen of the proximal urethral segment in all patients with UPS. Normally, upon initiation of urination, the mechanism for opening the funnel-shaped depression in the bladder neck is associated with contraction of the muscles of the deep triangle and of muscles located anterior to the internal opening of the urethra, as well as with the simultaneous contraction of the longitudinal muscle fibers of the urethra [42]. This means, we can assume the presence of insufficiency of these muscle groups in UPS.

Trophic disorders recorded by CP OCT in the epithelium of the urethral neck and the proximal segment of the urethra were more common in women over 50 years of age—in 93.3%, indicating their dependence on the patient's hormonal background. The hormonal dependence of a number of urinary disorders is explained in [55,56]. In these works, it was shown that in the deep layers of the mucous membrane of the urethra there is a powerful venous plexus, and that this has a large number of anastomoses with the venous uterovaginal plexus. At the same time, the work of Petros et al. [57] indicated that the epithelium of the urinary system (urothelium) acts as a mechanoreceptor, using its sensitive nerve endings, and that it controls the activity of the afferent nerves, so this may contribute a pathogenetic component of chronic pelvic pain, and of urethral syndrome in particular.

Using the CP OCT method, we have previously shown that the thickness of the tissue of the urethral membrane in women is dependent on age [58]. The work reported that, with UPS, there are corresponding tendencies towards thinning of the epithelium and an increase in the thickness of the connective tissue matrix of the bladder neck, as occurs in women without pathology of the urological sphere, but that these processes proceed at a higher rate.

The recorded changes in the thickness of the epithelium are undoubtedly associated with the state of the connective tissue matrix of the subepithelium of the structural components. The compaction of the walls of the urethra and surrounding tissues that we have revealed using elastometry data, as well as in our earlier CP OCT data on the state of the connective tissue matrix of the urethra during UPS [36], indicate the presence of fibrosis processes both within the wall of the urethra and around it, the cause of which, at present, is not clear. Our studies have previously shown that the state of the urethral tissues in UPS is not normal, with changes in the urethral tissues occupying an intermediate place between the norm and the changes seen in chronic bacterial inflammatory processes [36].

Changes in the state of the connective tissue can lead to a decrease in the sensitivity of the stretch receptors at the base of the bladder, affecting the functionality results [57], in particular, influencing

the uroflowmetry data that we obtained. The results of the uroflowmetry allow us to assume the presence of functional disorders of the urethra in women with UPS. Considering the indices of the normal values of the urination rate for women, which are 23–32 mL/s [40], our results of uroflowmetry showing 13.7 ± 3.2 mL/s are likely to be associated with anatomical changes that are not detected in standard clinical studies, or with dysfunctional and/or obstructive urination due to an overactive urethra. However, it is known that the presence of symptoms of urinary disorders is not a reliable marker of pathological processes [40]. We are continuing our research in this direction.

There is reason to believe that the cause of the development of chronic inflammatory processes in UPS is located in the tissues of the urethra and, accordingly, this serves as an additional stimulus for the occurrence of disorders of the microcirculation, innervation, and functioning of the urethra, indirectly influencing the appearance of pain. Our anamnestic data on the presence of a prevailing gynecological pathology of inflammatory genesis suggest that the cause of such changes in the tissues of the bladder and urethra may be viral-bacterial associations in the tissues of the organs of the gynecological sphere. This aspect requires more detailed study. At present, the effect of the translocation of microorganisms in the tissues of the urinary system, vagina, and intestines has been proven in cases of upper urinary tract infection [59], although research in this area is ongoing. Analyses of the composition of the microflora of urine and of the large intestine in cases of infection of the lower urinary tract have also indirectly confirmed the presence of a translocation mechanism in microorganisms [59].

It is known that the close anatomical connection of the bladder, urethra, and vagina provides associated functional mechanisms for the urination process. A component of this mechanism is illustrated by the fact that in the distal urethra the circular fibers of the striated sphincter are transformed into loop structures, the ends of which are woven into the framework of the anterior vaginal wall [55]. According to the anamnesis, hormonal disorders, inflammatory diseases, and surgical interventions on the pelvic organs, which could result in dysfunction of the muscles of the urethra and vagina, were found in 70.9% of patients with UPS who were interviewed. At the same time, it is known that functional disorders, on their own, can generate pain [60]. The results of our study indicated that a reason for the development of pain and chronic dysuria in patients with UPS may be failure of the structures of the internal urethral sphincter. This sphincter is formed by the muscles of the external muscular layer of the bladder that pass into the urethra in the bladder neck region, forming spiral structures, occupying about 20% of its length. In the present study on TVUS, 29.1% of women were found to have an insufficiency of structures, namely the urethral tongue, in the area of this sphincter. This fact requires further research.

Thus, it has been shown that there are many factors that cause persistent long-term pain in the urethral region, or that contribute to the intensification of pain, some of which have yet to be studied. Given the non-obviousness of the causes of UPS, new research protocols and additional imaging and diagnostic methods are required for a comprehensive examination of such patients, without focusing only on their pathologies in the urological field.

The main shortcoming of our study was its retrospective nature and moderate patient number in the norm group. Therefore, our results are not definitive and require confirmation on a larger number of patients. However, we identified certain new patterns in patients with UPS compared with healthy women. We can suggest including our approach—the combined study of patients with UPS by TVUS/compression US and CP OCT—in the daily practice of urologists in order to undergo validation and prospective–comparative clinical trials.

Another drawback of our study was the lack of histological verification of CP OCT data. We proceeded from the results of our previous study [36], where the morphology of the female urethra was analyzed on cadaveric material and compared with CP OCT images. This fact and numerous studies on CP OCT visualization of mucous membranes in health and pathology [30,31,52,61,62] afford ground for confidence in the interpretation of CP OCT features, such as changes in the epithelium thickness and the state of connective tissue.

As soon as the limitations of the used methods are concerned, it is necessary to compare their imaging depth and resolution. With a fairly low resolution of TVUS, the advantage of the method is a sufficient imaging depth. The technique allows observing the entire urethra, estimating its size and shape, identifying concomitant pathologies in adjacent organs, and conducting a functional study (compare the state of the urethra and bladder before and after miction). In addition to the USE mode, which is used in this paper, the method also makes it possible to study the blood supply to the pelvic organs, which is an important part in the pathogenesis of UPS.

One of the limitations of the CP OCT method is the small depth of tissue visualization, namely, the inability to fully assess the muscle layer located deeper than the connective tissue. On the other hand, tissue imaging to a depth of 1–1.5 mm is an advantage over urethroscopy, which allows the assessment of the urethral mucosa only from the surface. The forward-looking CP OCT probe used in this study allows visualizing the urethral wall in a certain place, while it would be optimal to study the urethral mucosa along its entire length, for example, when using rotary or needle OCT probes with manual scanning [28]. Despite this, the advantage of CP OCT is the rapid assessment of the urethral wall structure at the tissue level: the high resolution of the method (5–15 μm) is sufficient for the rapid assessment of epithelium and connective tissue—structures that play a key role in the emergence of UPS [63].

As a prospect, we intend to continue research on the pathogenesis of UPS by adding neurophysiological methods for diagnosing lesions of the pudendal nerve and sacral pathways, assessing the hormonal status of women, and studying the microflora of the tissues of the urethra and the bladder neck.

5. Conclusions

For the first time in the case of UPS, the layered structure of the urethral wall was investigated in vivo using CP OCT to assess some of the pathogenetic aspects of the development and progression of this disease. The CP OCT method covers the range of possibilities of traditional cystoscopy and allows information to be obtained about the state of the urethral tissues that cannot be adequately assessed during cystoscopic examination alone. The predominant changes in the tissues of the urethra are fibrosis of the subepithelial structures and trophic changes in the epithelial layer. In 68.8% of cases, the "behavior" of the tissues of the proximal segment of the urethra coincided with changes in the bladder neck. The importance of the in vivo acquisition and operative analysis possible with CP OCT in combination with TVUS/compression US data in patients with UPS is beyond doubt.

Deep objective analysis of tissues can reveal the basis of pathogenesis. Real-time visualization of structural changes in the tissues of the urethra (epithelium, connective tissue, muscle layer, vasculature, and paraurethral glands) is important because it influences the final diagnosis, understanding of the pathogenesis of the disease and treatment tactics. An analysis of the comorbidities of patients with UPS showed that inflammatory gynecological diseases can become a premorbid background/one of the triggering mechanisms for the development of UPS.

Author Contributions: Conceptualization, O.S. and E.K.; methodology, E.T.; software, M.S.A.M.M. and V.L.; investigation, O.S., A.K., M.S.A.M.M., S.Z., and E.T.; data curation, V.L.; writing—original draft preparation, O.S., A.K., E.K., and S.Z.; writing—review and editing, O.S., A.K., and E.K.; funding acquisition, O.S. All authors have read and agreed to the published version of the manuscript.

Funding: This research was funded by Russian Foundation for Basic Research, grant number 19-07-00395.

Acknowledgments: The authors would like to thank Grigory V. Gelikonov and Valentin M. Gelikonov (Institute of Applied Physics of the RAS, Russia) for the provision of the CP OCT device and its technical support during the research.

Conflicts of Interest: The authors declare no conflict of interest. The funders had no role in the design of the study; in the collection, analyses, or interpretation of data; in the writing of the manuscript, or in the decision to publish the results.

References

1. Rothberg, M.B.; Wong, J.B. All dysuria is local a cost-effectiveness model for designing site-specific management algorithms. *J. Gen. Intern. Med.* **2004**, *19*, 433–443. [CrossRef] [PubMed]
2. Cho, S.T. Urethral pain syndrome really part of bladder pain syndrome? *Urogenit. Tract Infect.* **2017**, *12*, 22–27. [CrossRef]
3. Phillip, H.; Okewole, I.; Chilaka, V. Enigma of urethral pain syndrome: Why are there so many ascribed etiologies and therapeutic approaches? *Int. J. Urol.* **2014**, *21*, 544–548. [CrossRef] [PubMed]
4. Piontek, K.; Ketels, G.; Albrecht, R.; Schnurr, U.; Dybowski, C.; Brünahl, C.A.; Riegel, B.; Löwe, B. Somatic and psychosocial determinants of symptom severity and quality of life in male and female patients with chronic pelvic pain syndrome. *J. Psychosom. Res.* **2019**, *120*, 1–7. [CrossRef] [PubMed]
5. Passavanti, M.B.; Pota, V.; Sansone, P.; Aurilio, C.; De Nardis, L.; Pace, M.C. Chronic pelvic pain: Assessment, evaluation, and objectivation. *Pain Res. Treat.* **2017**, *2017*, 9472925. [CrossRef] [PubMed]
6. Kaur, H.; Arunkalaivanan, A.S. Urethral pain syndrome and its management. *Obstet. Gynecol. Surv.* **2007**, *62*, 348–351. [CrossRef]
7. Elsenbruch, S.; Häuser, W.; Jänig, W. Visceral pain. *Schmerz* **2015**, *29*, 496–502.
8. Fall, M.; Baranowski, A.P.; Elneil, S.; Engeler, D.; Hughes, J.; Messelink, E.J.; Williams, A.D.C. EAU guidelines on chronic pelvic pain syndrome. *Europ. Urol.* **2010**, *57*, 35–48. [CrossRef]
9. Dreger, N.; Degener, S.; Roth, S.; Brandt, A.S.; Lazica, D. Urethral pain syndrome: Fact or fiction—An update. *Urol. A* **2015**, *54*, 1248–1255. [CrossRef]
10. Zaitsev, A.V.; Sharov, M.N.; Pushkar, D.Y.; Khodyreva, L.A.; Dudareva, A.A. *Chronic Pelvic Pain Methodical Recommendations № 20*; LLC Publishing House ABV-Press: Moscow, Russia, 2006; p. 46.
11. Flor, H.; Fydrich, T.; Turk, D.C. Efficacy of multidisciplinary pain treatment centers: A meta-analytic review. *Pain* **1992**, *49*, 221–230. [CrossRef]
12. Jarrell, J.F.; Vilos, G.A.; Allaire, C.; Burgess, S.; Fortin, C.; Gerwin, R.; Lapensée, L.; Lea, R.H.; Leyland, N.A.; Martyn, P.; et al. Chronic pelvic pain working group; society of obstetricians and gynaecologists of canada. consensus guidelines for the management of chronic pelvic pain. *J. Obstet. Gynaecol. Can.* **2005**, *27*, 869–910. [PubMed]
13. Grinberg, K.; Sela, Y.; Nissanholtz-Gannot, R. New insights about chronic pelvic pain syndrome (CPPS). *Int. J. Environ. Res. Public Health* **2020**, *17*, 3005. [CrossRef] [PubMed]
14. Persu, C.; Cauni, V.; Gutue, S.; Blaj, I.; Jinga, V.; Geavlete, P. From interstitial cystitis to chronic pelvic pain. *J. Med. Life* **2010**, *3*, 167–174.
15. Aziz, Q.; Giamberardino, M.A.; Barke, A.; Korwisi, B.; Baranowski, A.P.; Wesselmann, U.; Treede, R.D. The IASP Classification of Chronic Pain for ICD-11: Chronic secondary visceral pain. *Pain* **2019**, *160*, 69–76. [CrossRef] [PubMed]
16. Stecco, C. *Functional Atlas of the Human Fascial System*, 1st ed.; Elsevier Health Sciences: London, UK, 2014; p. 384.
17. Muiznieks, L.D.; Keeley, F.W. Molecular assembly and mechanical properties of the extracellular matrix: A fibrous protein perspective. *Biochim. Biophys. Acta.* **2013**, *1832*, 866–875. [CrossRef]
18. Langevin, H.M. Connective tissue: A body-wide signaling network? *Med. Hypotheses* **2006**, *66*, 1074–1077. [CrossRef]
19. Shoskes, D.A.; Nickel, J.C.; Kattan, M.W. Phenotypically directed multimodal therapy for chronic prostatitis/chronic pelvic pain syndrome: A prospective study using UPOINT. *Urology* **2010**, *75*, 1249–1253. [CrossRef]
20. Wells, P.N.; Liang, H.D. Medical ultrasound: Imaging of soft tissue strain and elasticity. *J. R. Soc. Interface* **2011**, *8*, 1521–1549. [CrossRef]
21. Bamber, J.; Cosgrove, D.; Dietrich, C.F.; Fromageau, J.; Bojunga, J.; Calliada, F.; Cantisani, V.; Correas, J.M.; D'Onofrio, M.; Drakonaki, E.E.; et al. EFSUMB guidelines and recommendations on the clinical use of ultrasound elastography. Part 1: Basic principles and technology. *Ultraschall Med.* **2013**, *34*, 169–184. [CrossRef]
22. Cosgrove, D.; Piscaglia, F.; Bamber, J.; Bojunga, J.; Correas, J.M.; Gilja, O.H.; Klauser, A.S.; Sporea, I.; Calliada, F.; Cantisani, V.; et al. EFSUMB guidelines and recommendations on the clinical use of ultrasound elastography. Part 2: Clinical applications. *Ultraschall Med.* **2013**, *34*, 238–253.

23. Lupsor-Platon, M. *Ultrasound Elastography*; IntechOpen: London, UK, 2020; p. 146.
24. Sigrist, R.; Liau, J.; Kaffas, A.E.; Chammas, M.C.; Willmann, J.K. Ultrasound elastography: Review of techniques and clinical applications. *Theranostics* **2017**, *7*, 1303–1329. [CrossRef] [PubMed]
25. Huang, D.; Swanson, E.A.; Lin, C.P.; Schuman, J.S.; Stinson, W.G.; Chang, W.; Hee, M.R.; Flotte, T.; Gregory, K.; Puliafito, C.A.; et al. Optical coherence tomography. *Science* **1991**, *254*, 1178–1181. [CrossRef] [PubMed]
26. Drexler, W.; Liu, M.; Kumar, A.; Kamali, T.; Unterhuber, A.; Leitgeb, R.A. Optical coherence tomography today: Speed, contrast, and multimodality. *J. Biomed. Opt.* **2014**, *19*, 071412. [CrossRef] [PubMed]
27. Lamirel, C. Optical Coherence Tomography. In *Encyclopedia of the Neurological Sciences*, 2nd ed.; Aminoff, M.J., Daroff, R.B., Eds.; Academic Press: Waltham, MA, USA, 2014; pp. 660–668.
28. Gora, M.J.; Suter, M.J.; Tearney, G.J.; Li, X. Endoscopic optical coherence tomography: Technologies and clinical applications [Invited]. *Biomed. Opt. Express* **2017**, *8*, 2405–2444. [CrossRef] [PubMed]
29. Gelikonov, V.M.; Gelikonov, G.V. New approach to cross-polarized optical coherence tomography based on orthogonal arbitrarily polarized modes. *Laser Phys. Let.* **2006**, *3*, 445–451. [CrossRef]
30. Gladkova, N.; Kiseleva, E.; Robakidze, N.; Balalaeva, I.; Karabut, M.; Gubarkova, E.; Feldchtein, F. Evaluation of oral mucosa collagen condition with cross-polarization optical coherence tomography. *J. Biophotonics* **2013**, *6*, 321–329. [CrossRef]
31. Kiseleva, E.; Kirillin, M.; Feldchtein, F.; Vitkin, A.; Sergeeva, E.; Zagaynova, E.; Gladkova, N. Differential diagnosis of human bladder mucosa pathologies in vivo with cross-polarization optical coherence tomography. *Biomed. Optic. Express* **2015**, *6*, 1464–1476. [CrossRef]
32. Abrams, P.; Cardozo, L.; Fall, M.; Griffiths, D.; Rosier, P.; Ulmsten, U.; van Kerrebroeck, P.; Victor, A.; Wein, A. Standardisation Sub-Committee of the International Continence Society. The standardisation of terminology in lower urinary tract function: Report from the standardisation sub-committee of the International Continence Society. *Urology* **2003**, *61*, 37–49. [CrossRef]
33. Prado-Costa, R.; Rebelo, J.; Monteiro-Barroso, J.; Preto, A.S. Ultrasound elastography: Compression elastography and shear-wave elastography in the assessment of tendon injury. *Insights Imaging* **2018**, *9*, 791–814. [CrossRef]
34. Zahran, M.H.; El-Shafei, M.M.; Emara, D.M.; Eshiba, S.M. Ultrasound elastography: How can it help in differentiating breast lesions? *Egypt. J. Radiol. Nucl. Med.* **2018**, *49*, 249–258. [CrossRef]
35. Gelikonov, V.M.; Gelikonov, G.V. Fibreoptic methods of cross-polarisation optical coherence tomography for endoscopic studies. *IEEE J. Quantum Electron.* **2008**, *38*, 634–640.
36. Kiseleva, E.B.; Moiseev, A.A.; Kuyarov, A.S.; Molvi, M.A.; Gelikonov, G.V.; Maslennikova, A.V.; Streltsova, O.S. In vivo assessment of structural changes of the urethra in lower urinary tract disease using cross-polarization optical coherence tomography. *J. Innov. Opt. Health Sci.* **2020**, *13*, 2050024-1-16.
37. Netter, F.H. *Atlas of Human Anatomy*, 6th ed.; Elsevier Inc.: Philadelphia, PA, USA, 2014; pp. 339–400.
38. Kiseleva, E.; Gladkova, N.; Streltzova, O.; Kirillin, M.; Maslennikova, A.; Dudenkova, V.; Sergeeva, E. Cross-polarization OCT for in vivo diagnostics and prediction of bladder cancer. In *Bladder Cancer—Management of NMI and Muscle-Invasive Cancer*; Ather, M., Ed.; InTech: Rijeka, Croatia, 2017; pp. 43–61.
39. Afraa, T.A.; Mahfouz, W.; Campeau, L.; Corcos, J. Normal lower urinary tract assessment in women: I. Uroflowmetry and post-void residual, pad tests, and bladder diaries. *Int. Urogynecol. J.* **2012**, *23*, 681–685.
40. Makrushina, N.V.; Fastykovskaya, E.D. Ultrasound diagnosis of pelvic floor muscle insufficiency in women. *Sib. Med. J. Tomsk* **2012**, *27*, 91–96.
41. Schaer, G.N.; Schmid, T.; Peschers, U.; Delancey, J.O. Intraurethral ultrasound correlated with urethral histology. *Obstet. Gynecol.* **1998**, *91*, 60–64. [PubMed]
42. Jung, J.; Ahn, H.K.; Huh, Y. Clinical and functional anatomy of the urethral sphincter. *Int. Neurourol. J.* **2012**, *16*, 102–106.
43. Cakici, Ö.U.; Hamidi, N.; Ürer, E.; Okulu, E.; Kayigil, O. Efficacy of sertraline and gabapentin in the treatment of urethral pain syndrome: Retrospective results of a single institutional cohort. *Cent. European J. Urol.* **2018**, *71*, 78–83. [PubMed]
44. Nickel, J.C. Clinical evaluation of the man with chronic prostatitis/chronic pelvic pain syndrome. *Urology* **2002**, *60*, 20–22.

45. Trinchieri, A.; Magri, V.; Cariani, L.; Bonamore, R.; Restelli, A.; Garlaschi, M.C.; Perletti, G. Prevalence of sexual dysfunction in men with chronic prostatitis/chronic pelvic pain syndrome. *Arch. Ital. Urol. Androl.* **2007**, *79*, 67.
46. Juan, Y.-S.; Shen, J.-T.; Jang, M.-Y.; Huang, C.-H.; Li, C.-C.; Wu, W.-J. Current Management of Male Chronic Pelvic Pain Syndromes. *Urol. Sci.* **2010**, *21*, 157–162.
47. Smith, C.P. Male chronic pelvic pain: An update. *Indian J. Urol.* **2016**, *32*, 34–39. [CrossRef] [PubMed]
48. Archambault-Ezenwa, L.; Markowski, A.; Barral, J.-P. A comprehensive physical therapy evaluation for Male Chronic Pelvic Pain Syndrome: A case series exploring common findings. *J. Bodyw. Mov. Ther.* **2019**, *23*, 825–834. [CrossRef]
49. Wang, Y.; Liu, S.; Lou, S.; Zhang, W.; Cai, H.; Chen, X. Application of optical coherence tomography in clinical diagnosis. *J. X-ray Sci. Technol.* **2019**, *27*, 995–1006. [CrossRef]
50. Carrasco-Zevallos, O.M.; Viehland, C.; Keller, B.; Draelos, M.; Kuo, A.N.; Toth, C.A.; Izatt, J.A. Review of intraoperative optical coherence tomography: Technology and applications. *Biomed. Opt. Express* **2017**, *8*, 1607–1637. [CrossRef]
51. Freund, J.E.; Buijs, M.; Savci-Heijink, C.D.; de Bruin, D.M.; de la Rosette, J.J.; van Leeuwen, T.G.; Laguna, M.P. Optical coherence tomography in urologic oncology: A comprehensive review. *SN Compr. Clin. Med.* **2019**, *1*, 67–84. [CrossRef]
52. Kirillin, M.Y.; Motovilova, T.; Shakhova, N.M. Optical coherence tomography in gynecology: A narrative review. *J. Biomed. Opt.* **2017**, *22*, 121709. [CrossRef]
53. Olsen, J.; Holmes, J.; Jemec, G.B.E. Advances in optical coherence tomography in dermatology—A review. *J. Biomed. Opt.* **2018**, *23*, 040901. [CrossRef]
54. Oliveira, F.R.; Ramos, J.G.L.; Martins-Costa, S. Translabial ultrasonography in the assessment of urethral diameter and intrinsic urethral sphincter deficiency. *J. Ultrasound Med.* **2006**, *25*, 1153–1158. [CrossRef] [PubMed]
55. Petros, P.P.E.; Ulmsten, U.I. An integral theory and its method for the diagnosis and management of female urinary incontinence. *Scand. J. Urol. Nephrol. Suppl.* **1993**, *153*, 1–93. [PubMed]
56. Petros, P.E.P.; Ulmsten, U.I. An integral theory of female urinary incontinence: Experimental and clinical considerations. *Acta Obstet. Gynecol. Scand. Suppl.* **1990**, *153*, 7–31. [CrossRef]
57. Petros, P. *The Female Pelvic Floor. Functions, Dysfunctions and Their Treatment in Accordance with the Integral Theory*, 3rd ed.; Springer: Berlin/Heidelberg, Germany, 2010; p. 352.
58. Streltsova, O.S.; Kiseleva, E.B.; Molvi, M.A.; Lazukin, V.F. Structural features of the urethra in patients with urethral pain syndrome. *Exper. Clin. Urol.* **2019**, *3*, 170–177. [CrossRef]
59. Naboka, Y.L.; Gudima, I.A.; Dzhalagoniya, K.T.; Chernitskaya, M.L.; Ivanov, S.N. Urine and colon microbiota in patients with recurrent uncomplicated lower urinary tract infection. *Urol. Herald.* **2019**, *7*, 59–65. [CrossRef]
60. Crofford, L.J. Chronic pain: Where the body meets the brain. *Trans. Am. Clin. Climatol. Assoc.* **2015**, *126*, 167–183.
61. Bibas, A.G.; Podoleanu, A.G.; Cucu, R.G.; Bonmarin, M.; Dobre, G.M.; Ward, V.M.M.; Odell, E.; Boxer, A.; Gleeson, M.J.; Jackson, D.A. 3-D optical coherence tomography of the laryngeal mucosa. *Clin. Otolaryngol.* **2004**, *29*, 713–720. [CrossRef] [PubMed]
62. Di Stasio, D.; Lauritano, D.; Iquebal, H.; Romano, A.; Gentile, E.; Lucchese, A. Measurement of oral epithelial thickness by optical coherence tomography. *Diagnostics* **2019**, *9*, 90. [CrossRef]
63. Parsons, C.L. The role of a leaky epithelium and potassium in the generation of bladder symptoms in interstitial cystitis/overactive bladder, urethral syndrome, prostatitis and gynecological chronic pelvic pain. *BJU Int.* **2011**, *107*, 370–375. [CrossRef]

diagnostics

MDPI

Article

Design of Liver Functional Reserve Estimation Technique Based on Optical Densitometry

Ekaterina Savchenko [1,*], Ilya Kolokolnikov [1], Elena Velichko [1], Victor Osovskikh [2], Lyubov Kiseleva [2] and Zhyldyz Musakulova [3]

[1] Institute of Physics, Nanotechnology and Telecommunications, Peter the Great St. Petersburg Polytechnic University, 195251 St. Petersburg, Russia; kin_kolin@mail.ru (I.K.); velichko-spbstu@yandex.ru (E.V.)
[2] Department of Anesthesiology and Resuscitation Russian Research Center for Radiology and Surgical Technologies, 197758 St. Petersburg, Russia; osoff@mail.ru (V.O.); luba_kiseleva@mail.ru (L.K.)
[3] Computer Information Systems, International University of Kyrgyzstan, Bishkek 720007, Kyrgyzstan; mjyldyz@rambler.ru
* Correspondence: savchenko-spbstu@mail.ru; Tel.: +7-999-245-77-86

Received: 14 July 2020; Accepted: 13 August 2020; Published: 16 August 2020

Abstract: This work is aimed at creating a modified invasive technique for assessing the liver's functional reserves. A study of the degree of hepatodepression is carried out by measuring the plasma elimination of indocyanine green using the method of optical densitometry. This paper presents test results for an aqueous solution and an albumin solution, as well as the results of measurements of plasma elimination of indocyanine green for patients with liver disease. Perfecting the proposed method will make an important scientific contribution to modern diagnostic medicine. Diagnosing the stages in the progression of the disease and its developing complications can make it possible to rapidly correct the patient's treatment algorithm, achieving positive outcomes in medical practice.

Keywords: optical densitometry; liver diagnosis; indocyanine green; liver functional reserve; optical density; plasma disappearance rate

1. Introduction

One of the pressing issues in modern hepatology is assessing the degree of hepatic depression [1–5]. As of 2019, 325 million people worldwide have been infected with viral hepatitis B or C, and 1.4 million people die from it every year, while the need for resection occurs in 80% of cases in patients with hepatitis C and B [2].

Liver disease can be divided into diffuse and focal. The underlying pathophysiological mechanisms of the progression of diffuse liver disease are inflammation, vascular insufficiency, or abnormal accumulation of substances. Chronic liver failure is most frequently caused by viral hepatitis and fatty degeneration of hepatocytes of alimentary origin. Fulminant liver failure is mainly caused by hepatitis viruses and xenobiotics (including drugs). Diffuse liver disease is traditionally treated by hepatologists. The progression of chronic liver failure naturally raises the question about a radical method of treatment that is liver transplantation. Unfortunately, the existing clinical criteria for prediction are not perfect, which means that patients are not placed on the waiting list for transplantation in a timely manner. In the case of focal lesions (primary tumor, metastases, parasitic cyst, and abscess), the surgical strategy consists of removing pathological lesions while ensuring sufficient function of remaining organ volume. Experimental data indicate that the mass of liver tissue sufficient to meet the needs of the body is about 1% of body weight. However, this refers to fully functional tissue. In case of combined focal and diffuse lesions, such estimates will be low. Another branch of medicine where functional assessment of the liver plays a crucial role is treatment of organ failure in patients in critical condition. It is known that the hepatic component is the most difficult to control.

The study of the functional status of the liver currently includes the parameters of synthesis (prothrombin, cholesterol, and albumin), cellular integrity (transaminase), detoxification (ammonia) excretion, and cholestasis (bilirubin, alkaline phosphatase, and gamma-glutamyl transpeptidase) in combination with various imaging techniques. These "static" tests of hepatic function have limitations, especially when it comes to prognosis of survival or liver function tests in patients in critical condition [6]. Currently, only dynamic tests based on studies of the clearance of exogenously introduced substances can give a global picture of organ function [7]. Some tests can be used repeatedly within a limited time frame, for example, allowing to determine the limit of resection more thoroughly in conditions of temporary vascular isolation of the organ.

Dozens of substances were proposed as dynamic markers (both natural participants of metabolic reactions, and xenobiotics), along with methods for their detection. Only a few have reached widespread clinical use. One of the markers that has become firmly rooted in the practice of hepatology is indocyanine green (ICG) [8]. It is a water-soluble non-toxic fluorescent dye used for diagnostics of the cardiovascular system since 1956 [9]. After indocyanine green is administered intravenously, it is distributed only to the intravascularly space, binding to plasma proteins, and is removed from the blood only by hepatocytes. ICG refers to exogenous markers with rapid hepatic elimination, respectively, the rate of excretion depends on the function of hepatocytes and the hepatic blood flow rate.

The gold standard for determining the rate of ICG elimination is the method of sequential samples. Blood samples taken at regular intervals after the introduction of ICG are centrifuged, and the plasma is subjected to photometry (spectrophotometry) at a wavelength of 805 nm [10,11]. The disadvantages of sequential sampling are the long times it takes, and the additional personnel required. Thanks to the unique physical characteristics of indocyanine green, determination of ICG elimination rate by pulse densitometry was first introduced in the late 1990s. While a large number of publications confirm a high correlation of invasive and non-invasive techniques, there are certain problems related to pulse densitometry [10–14]. In particular, impaired capillary blood flow [15,16], obesity, and tremor of the extremities prevent obtaining reliable data [14]. This problem is especially important) in patients in critical condition. If non-invasive measurements fail, not only are expensive drugs lost, but new measurements are inevitably delayed to ensure that the previous dose of the indicator has been eliminated. Unfortunately, the technique for non-invasive determination of absolute ICG concentration and the related opportunities for calculating the circulating blood volume have also not been developed any further.

To solve this problem, we propose to use a combination of invasive and non-invasive methods for determining the rate of dye elimination on a single platform, with the possibility of post-processing the data obtained by pulse densitometry. The goal of this work is to develop the first stage, namely, an invasive method for measuring the plasma elimination of indocyanine green for diagnosing hepatic function.

2. Experimental Setup of Optical Densitometry

An experimental setup that we developed (Figure 1) was used to conduct measurements of plasma elimination of indocyanine green for diagnostics of hepatic function.

Light emitted from diode (**1**) passes though the test solution. Part of the radiation is absorbed, and part of the radiation is backscattered [17,18]. The emitting diode has an emission spectrum narrower than the peak absorption spectrum of the dye in the near infrared region; therefore, a monochromatic filter in the circuit is not required. The prepared solution of known concentration of indocyanine green is placed in cuvette (**2**). Photodetector (**3**) is used to detect the transmitted radiation. The distance between the emitting diode and the photodetector is 100 mm. Measured at this distance, the intensity of light passing through the cuvette with water without dye is 100 μW. The cuvette with the solution is placed 50 mm from the emitting diode. Measurements are made every 0.4 s.

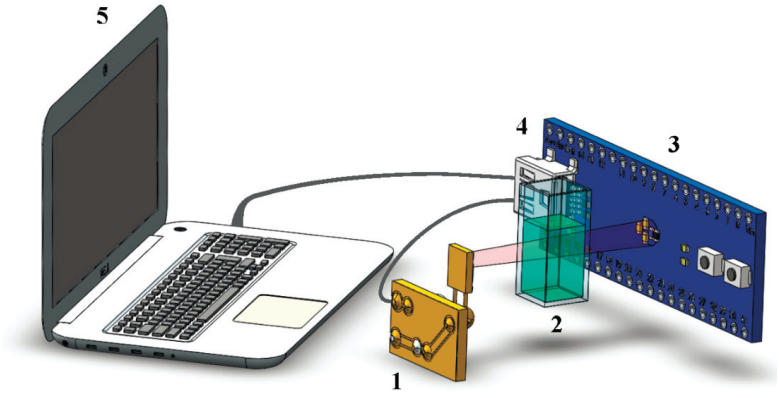

Figure 1. Experimental setup: (**1**) emitting diode, (**2**) sample cell, (**3**) photodetector, (**4**) microcontroller, and (**5**) computer.

Microcontroller (**4**) controls the collection of data by the Serial Peripheral Interface bus. The emitting diode is powered by the MCU pins and has only two modes: on and off. Communication with the photodetector is performed through the I2C interface. Data from the microcontroller for further processing are displayed on user device (**5**), which is a personal computer or an android device via USB.

The signal fluctuations of the medium optical density occur during the measurements. Their deviation from the average value, as a rule, does not reach 0.5% [19,20]. Fluctuations in optical density can be conditioned by fluctuations of dye concentration, intensity measurement error is mostly determined by photodetector quantization error. Figure 2 presents an example of the received signal.

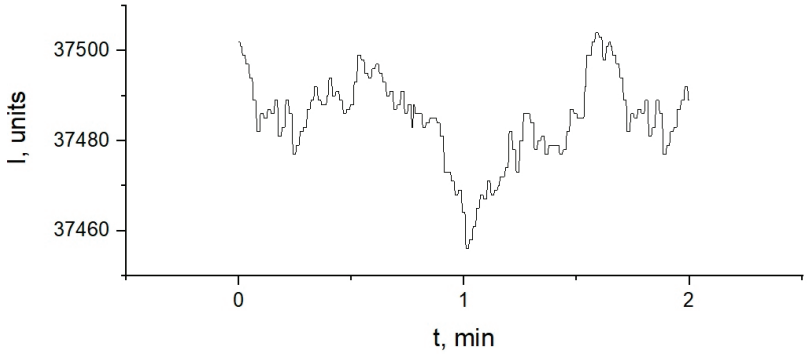

Figure 2. Example of time dependence of intensity of the light transmitted by 20% albumin solution without dye: I–the intensity of the light transmitted, t–recording time of the signal.

The developed experimental setup has several advantages compared with other photometric methods.

- Small dimension: The size of the experimental setup is 15 × 7 × 5 cm. The number of elements in this installation is minimized.
- Noise immunity: To improve the noise immunity, the Butterworth low pass filter and median filter were used.
- Cost-effectiveness: Optimized device design allows using cheaper optical elements. Emitting diode with 810 nm was used as a light source. (Which is cheaper than deuterium and tungsten sources)

- Simplicity of use: This experimental setup does not require additional training of users for carrying out experimental studies.
- Quick real-time presentation of the results: Processing of experimental studies takes up to several minutes.

3. Results and Discussion

This paper presents test measurements of the developed experimental setup and the proposed software. Solutions of the indocyanine green dye with water and with albumin were used as test samples.

At the first stage, measurements were made for an aqueous solution of indocyanine green at a low dye concentration. These samples were prepared by adding small portions of the dye with a known concentration in distilled water. Figure 3 shows a graph of the obtained experimental results for measuring the concentration of an aqueous solution of green indocyanine at a low dye concentration and their approximation by the exponent. The measurement result is calculated by averaging the signal values. The error bars marked on the graph reflect the value of the random experimental error calculated by estimation of the mean value (10 measurements), and confidence interval with a confidence level of 95%.

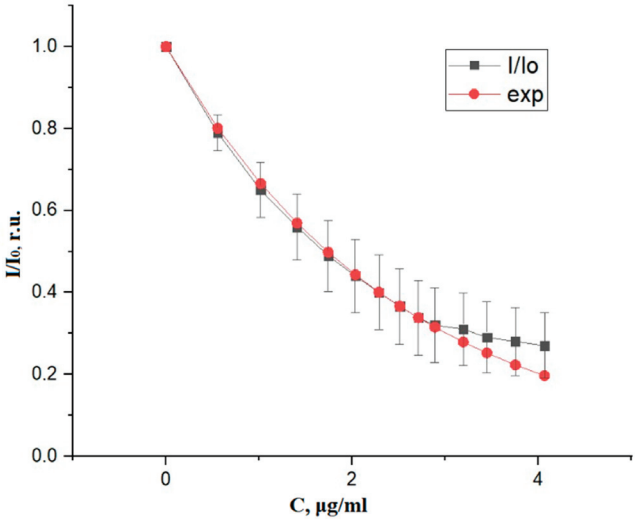

Figure 3. Ratio of intensity (I) of the light transmitted by aqueous solution of green indocyanine at low dye concentration (C) to intensity (I_0) of the light transmitted by water, and its approximation by an exponential function (exp).

Measurements at a low dye concentration are approximated by an exponent with a selected coefficient.

To test the operability of the developed experimental setup, we also performed experiments for a 20% albumin solution, gradually adding the dye to the test medium. The experimental results of measurements with low concentrations of indocyanine green in a 20% albumin solution and their exponential approximation are presented in Figure 4.

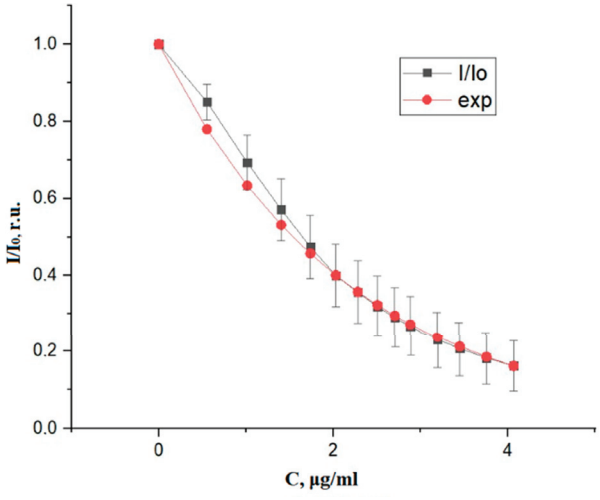

Figure 4. Ratio of the intensity of the light transmitted by dye albumin solution to intensity of light transmitted by solution of albumin and its approximation by an exponential function.

An experiment with a 20% albumin solution in the dye concentration range showed agreement with the theoretical data. However, in contrast to the experiment with water, it was not possible to choose an exponent that could approximate the beginning of the graph at a concentration near zero.

At the second stage of the measurements, we studied blood plasma samples from patients with liver pathology. Plasma samples were taken from 23 patients with liver pathology as part of routine ICG serial blood testing at the department of anesthesiology and intensive care of Russian Research Center of Radiology and Surgical Technologies. Plasma samples form a series each consisting of a set of measurements during the study of one patient. We have studied the samples taken before administering the dye, which are used to determine the optical density of the blood plasma itself. The intensity I_0 of the light passing through the plasma without dye allows to calculate the relative concentration of the dye in subsequent samples:

$$C_{rel} = -\ln\left(\frac{I}{I_0}\right). \quad (1)$$

In addition, plasma samples taken 2, 7, 12, and 17 min after dye administration were investigated. Figure 5 shows the results for a plasma sample from one of the patients with liver pathology.

Experiments with plasma allowed us to estimate the rate of dye elimination in the blood of patients. By calculating the relative concentration of the dye in these samples and comparing them, we can estimate the PDR (plasma disappearance rate) parameter by approximating a series of concentrations with an exponent with a selected coefficient for the argument. Measurements of the concentration ratio in the samples taken after 2 and 17 min determine the value of the PDR parameter, defined as the percentage by which the dye concentration decreases in 15 min. Figure 6 presents the results of experiments with plasma aimed at assessing the rate of elimination of the dye in the blood of patients.

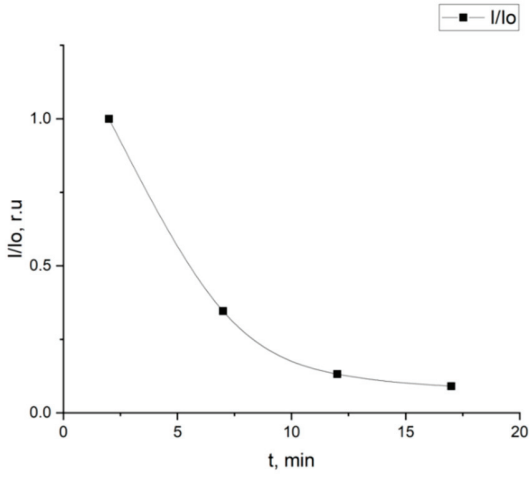

Figure 5. Ratio of intensity of the light transmitted by the dye blood plasma solution to the intensity of light transmitted by blood plasma solution from the time the plasma was taken from the patient.

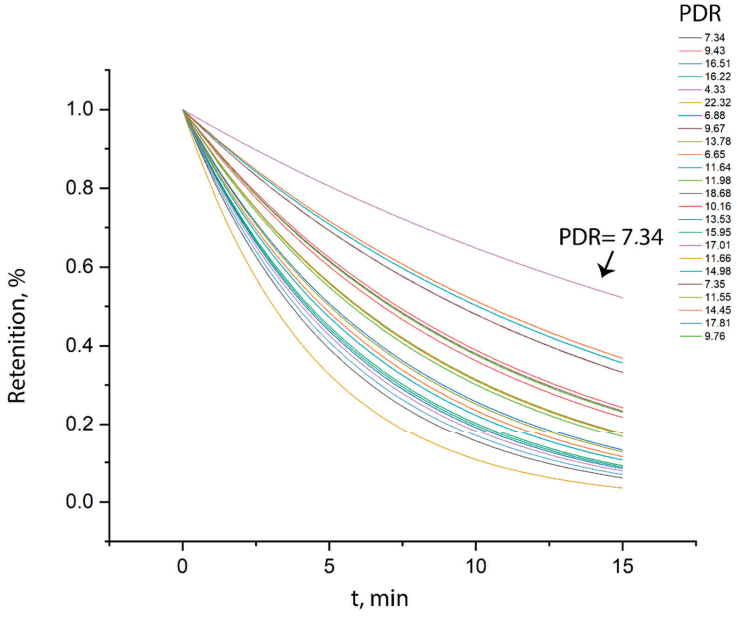

Figure 6. Plasma dye elimination curves corresponding to individual series.

The metabolic function of the liver of patients can be assessed based on these results. The faster the liver removes the dye from the circulatory system, the lower the ratio of the concentration in the subsequent sample to the concentration in the previous one after the same period. The liver of those patients whose curves are located lower purifies the blood better than the liver of those whose curves are higher.

To compare the results obtained by evaluating the concentration of the dye in the plasma, parallel studies were carried out by the method of sequential sampling on a commercial DU® 800 UV/Visible

Spectrophotometer. Figure 7 shows the relationship between the optical densities of the samples measured using a spectrophotometer (D_2) and the optical densities of the samples measured using our experimental setup (D_1).

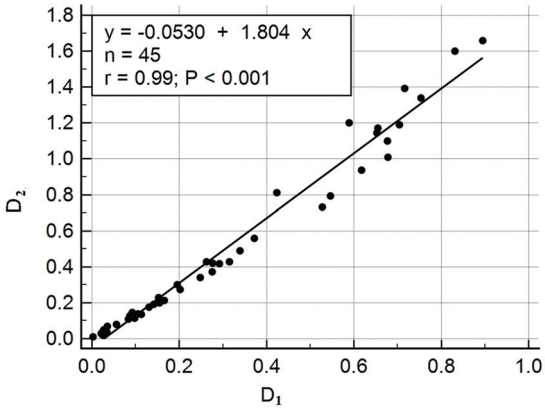

Figure 7. Comparison of the optical densities, D, obtained by two methods: D_2–the optical densities of the samples measured using a spectrophotometer and D_1–the optical densities of the samples measured using our experimental setup.

PDR values were also calculated by two methods. The comparison of the results is shown in Figure 8.

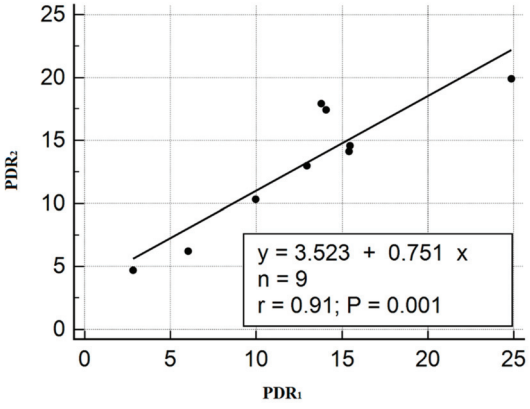

Figure 8. Comparison of plasma disappearance rate (PDR) parameters calculated from the measurements obtained with DU® 800 UV/Visible Spectrophotometer at the Department of Anesthesiology and Intensive Care of Russian Research Center for Radiology and Surgical Technologies (PDR_2), and with our experimental setup (PDR_1).

Figures 7 and 8 show that there is a correlation between the two measurement methods. The preliminary results obtained for assessing the concentration of indocyanine green in various liquids can be the basis for further studies [21]. This development can be included in the smart medical autonomous distributed system for diagnostics based on machine learning technology [22].

4. Conclusions

In this study, we developed an experimental setup, a program for collecting and displaying data, and an experimental technique for assessing the concentration of green indocyanine in various solutions. The experimental studies involved measurements with an aqueous dye, an albumin solution, and blood plasma correlated with the data from a commercial DU® 800 UV/Visible spectrophotometer. The main (advantages) of a device are cost-effectiveness, simplicity of use and quick real-time presentation of the results. The developed system will make it possible to diagnose liver function and predict its recovery with higher accuracy compared with existing approaches.

Author Contributions: Funding acquisition, supervision, E.V.; methodology, formal analysis, V.O.; investigation, I.K.; experiment in Russian Research Center for Radiology and Surgical Technologies, L.K.; writing—original draft preparation, E.S. and I.K.; and machine learning consultation and data evaluation, Z.M. All authors have read and agreed to the published version of the manuscript.

Funding: This research work was supported by Peter the Great St. Petersburg Polytechnic University in the framework of the Program "5-100-2020".

Acknowledgments: We express our gratitude to the Russian Research Center for Radiology and Surgical Technologies for providing biological samples, to S.V. Ermak for comprehensive assistance and valuable scientific advice, and to E.K. Nepomnyashchaya for illustration design.

Conflicts of Interest: The authors declare no conflict of interest. The funders/sponsors had no role in the design of the study; in the collection, analyses, or interpretation of data; in the writing of the manuscript, or in the decision to publish the results.

References

1. Rosen, H.R. Chronic hepatitis C infection. *N. Engl. J. Med.* **2011**, *364*, 2429–2438. [CrossRef] [PubMed]
2. World Health Organization. Available online: https://www.who.int/campaigns/world-hepatitis-day/2019 (accessed on 3 July 2020).
3. Williamson, R.M.; Price, J.F.; Glancy, S.; Perry, E.; Nee, L.D.; Hayes, P.C. Prevalence of and risk factors for hepatic steatosis and nonalcoholic fatty liver disease in people with type 2 diabetes: The Edinburgh Type 2 Diabetes Study. *Diabetes Care* **2011**, *34*, 1139–1144. [CrossRef] [PubMed]
4. Aijaz, A.; Perumpail, R.B.; Harrison, S.A. High prevalence of hepatic fibrosis in the setting of coexisting diabetes and hepatic steatosis: A case for selective screening in the general population? *Hepatology* **2016**, *63*, 20–22.
5. Mueller, A.R.; Platz, K.P.; Kremer, B. Early postoperative complications following liver transplantation. *Best Pract. Res. Clin. Gastroenterol.* **2004**, *18*, 881–900. [CrossRef]
6. Bonfrate, L.; Grattagliano, I.; Palasciano, G.; Portincasa, P. Dynamic carbon 13 breath tests for the study of liver function and gastric emptying. *Gastroenterol. Rep.* **2014**, *3*, 12–21. [CrossRef] [PubMed]
7. Sakka, S.G. Assessing liver function. *Curr. Opin. Crit. Care* **2007**, *13*, 207–214. [CrossRef] [PubMed]
8. Kunikowska, A.J.; Wildgruber, M.; Schulte-Frohlinde, E.; Lahmer, T.; Schmid, R.M.; Huber, W. Liver function assessment using indocyanine green plasma disappearance rate in a young male with icteric leptospirosis: A case report. *BMC Infect. Dis.* **2019**, *19*, 473. [CrossRef] [PubMed]
9. Slakter, J.S.; Yannuzzi, L.A.; Guyer, D.R.; Sorenson, J.A.; Orlock, D.A. Indocyanine-green angiography. *Curr. Opin. Ophthalmol.* **1995**, *6*, 25–32. [CrossRef] [PubMed]
10. Haruna, M.; Kumon, K.; Yahagi, N.; Watanabe, Y.; Ishida, Y.; Kobayashi, T.; Aoyagi, T. Blood Volume Measurement at the Bedside Using ICG Pulse Spectrophometry. *Anesthesiology* **1998**, *89*, 1322–1328. [CrossRef] [PubMed]
11. Osamu, O.; Tetsuya, K.; Hiroyuki, S.; Soichiro, I.; Shin, T.; Akimasa, N. ICG Pulse Spectrophotometry for Perioperative Liver Function in Hepatectomy. *J. Surg. Res.* **2002**, *103*, 109–113.
12. Kovac, N.; Peric, M. Liver function assessment by indocyanine green plasma disappearance rate in patients with intra-abdominal hypertension after "non-hepatic" abdominal surgery. *Curr. Med. Res. Opin.* **2018**, *34*, 1741–1746. [CrossRef] [PubMed]

13. Mayr, U.; Fahrenkrog-Petersen, L.; Batres-Baires, G.; Herner, A.; Rasch, S.; Schmid, R.M.; Lahmer, T. Largevolume paracentesis effects plasma disappearance rate of indocyanine green in critically ill patients with decompensated liver cirrhosis and intraabdominal hypertension. *Ann. Intensive Care* **2018**, *8*, 1–10.
14. Pantanali, C.A.; Gonzalez, D.E.; D'Albuquerque, L.A.; Andraus, W.; Barzallo, P.; Asperti, A.M. Lessons Learned with the LiMON Method of Indocyanine Green Elimination. *EC Gastroenterol. Dig. Syst.* **2018**, *5*, 297–304.
15. Li, H.-m. Microcirculation of liver cancer, microenvironment of liver regeneration, and the strategy of Chinese medicine. *Chin. J. Integr. Med.* **2016**, *22*, 163–167. [CrossRef] [PubMed]
16. Tian, H.; Qi, W. Quantitative analysis of microcirculation blood perfusion in patients with hepatocellular carcinoma before and after transcatheter arterial chemoembolisation using contrast-enhanced ultrasound. *Eur. J. Cancer* **2016**, *68*, 82–89. [CrossRef] [PubMed]
17. Davydov, R.V.; Antonov, V.I.; Yushkova, V.V.; Grebenikova, N.M.; Dudkin, V.I. A new algorithm for processing the absorption and scattering signals of laser radiation on a blood vessel and human tissues. *J. Phys. Conf. Ser.* **2019**, *1236*, 012079. [CrossRef]
18. Bisyarin, M.A.; Kotov, O.I.; Hartog, A.H.; Liokumovich, L.B.; Ushakov, N.A. Influence of a variable Rayleigh scattering-loss coefficient on the light backscattering in multimode optical fibers. *Appl. Opt.* **2017**, *56*, 4629. [CrossRef] [PubMed]
19. Kotov, O.; Chapalo, I. Signal-to-noise ratio for mode-mode fiber interferometer. In *Optical Measurement Systems for Industrial Inspection X*; SPIE Optical Metrology: Munich, Germany, 2017.
20. Liokumovich, L.B.; Kostromitin, A.O.; Ushakov, N.A.; Kudryashov, A.V. Method for Measuring Laser Frequency Noise. *J. Appl. Spectrosc.* **2020**, *86*, 1106–1112. [CrossRef]
21. Privalov, V.E.; Rybalko, A.V.; Charty, P.V.; Shemanin, V.G. Effect of noise and vibration on the performance of a particle concentration laser meter and optimization of its parameters. *Tech. Phys.* **2007**, *52*, 352–355. [CrossRef]
22. Velichko, E.; Nepomnyashchaya, E.; Baranov, M.; Galeeva, M.A.; Pavlov, V.A.; Zavjalov, S.V.; Savchenko, E.; Pervunina, T.M.; Govorov, I.; Komlichenko, E. A Concept of Smart Medical Autonomous Distributed System for Diagnostics Based on Machine Learning Technology. In *Internet of Things, Smart Spaces, and Next Generation Networks and Systems*; Springer: Cham, Switzerland, 2019; pp. 515–524.

diagnostics

MDPI

Article

Identification of Human Ovarian Adenocarcinoma Cells with Cisplatin-Resistance by Feature Extraction of Gray Level Co-Occurrence Matrix Using Optical Images

Chih-Ling Huang [1,*], Meng-Jia Lian [2], Yi-Hsuan Wu [3], Wei-Ming Chen [2] and Wen-Tai Chiu [4]

1 Center for Fundamental Science, Kaohsiung Medical University, Kaohsiung 807, Taiwan
2 School of Dentistry, College of Dental Medicine, Kaohsiung Medical University, Kaohsiung 807, Taiwan; sy2es93103@gmail.com (M.-J.L.); bill321cm1@gmail.com (W.-M.C.)
3 Department of Medicinal and Applied Chemistry, College of Life Science, Kaohsiung Medical University, Kaohsiung 807, Taiwan; qoo860724@gmail.com
4 Department of Biomedical Engineering, National Cheng Kung University, Tainan 701, Taiwan; wtchiu@mail.ncku.edu.tw
* Correspondence: chihling@kmu.edu.tw; Tel.: +886-7-312-1101 (ext. 2245#12)

Received: 18 May 2020; Accepted: 7 June 2020; Published: 9 June 2020

Abstract: Ovarian cancer is the most malignant of all gynecological cancers. A challenge that deteriorates with ovarian adenocarcinoma in neoplastic disease patients has been associated with the chemoresistance of cancer cells. Cisplatin (CP) belongs to the first-line chemotherapeutic agents and it would be beneficial to identify chemoresistance for ovarian adenocarcinoma cells, especially CP-resistance. Gray level co-occurrence matrix (GLCM) was characterized imaging from a numeric matrix and find its texture features. Serous type (OVCAR-4 and A2780), and clear cell type (IGROV1) ovarian carcinoma cell lines with CP-resistance were used to demonstrate GLCM texture feature extraction of images. Cells were cultured with cell density of 6×10^5 in a glass-bottom dish to form a uniform coverage of the glass slide to get the optical images by microscope and DVC camera. CP-resistant cells included OVCAR-4, A2780 and IGROV and had the higher contrast and entropy, lower energy, and homogeneity. Signal to noise ratio was used to evaluate the degree for chemoresistance of cell images based on GLCM texture feature extraction. The difference between wile type and CP-resistant cells was statistically significant in every case ($p < 0.001$). It is a promising model to achieve a rapid method with a more reliable diagnostic performance for identification of ovarian adenocarcinoma cells with CP-resistance by feature extraction of GLCM in vitro or ex vivo.

Keywords: chemoresistance; cisplatin; gray-level co-occurrence matrix; ovarian adenocarcinoma

1. Introduction

Ovarian cancer is the most malignant of all gynecological cancers [1]. A challenge that deteriorates with ovarian adenocarcinoma in neoplastic disease patients has been associated with the chemoresistance of cancer cells. Cisplatin (CP) is a platinum-containing compound, which belongs to the first-line chemotherapeutic agents for the treatment of human ovarian cancer [2]. Therefore, it would be beneficial for cancer therapy to identify various chemoresistance for human ovarian adenocarcinoma cells, especially CP-resistance.

Ovarian carcinomas consist of at least five distinct diseases: high-grade serous, low-grade serous, clear cell, endometrioid, and mucinous [3]. High-grade serous ovarian cancer is responsible for approximately 80% of ovarian cancer cases and two-thirds of ovarian cancer deaths. OVCAR-4 ranked as one of the highest matches to high-grade serous ovarian cancer, a cell-line collected from a 42-year-old

ovarian cancer patient and found to be resistant to combination chemotherapy [4]. A2780 is serous carcinoma cell line with platinum sensitivity [5]. IGROV1 is human clear cell type ovarian carcinoma cell line. It has the propensity to float as clusters isolated from tumor tissue and ascites [6].

Gray level co-occurrence matrix (GLCM) characterizes the texture of images by calculating from a numeric matrix [7], which was defined by Haralick et al. [8]. It can be used to analyze the medical imaging from magnetic resonance imaging or ultrasonography and find the potential relationship with tumor malignancies [9], such as brain tumor detection [10], liver tumors [11], and histopathological images [12].

In general, it is not easy to take images of ovarian cancer, but ovarian cancer cells can be extracted from ascites of patients. The cells can be cultured mono-layered to dissolve the problem for the image taken. In our previous study, detection of various characteristics of cancer cells by feature extraction of GLCM can be applied in real clinical cases for metastatic cancer cells [13] or biopsy [14] images which were successfully taken from camera.

In search of novel mechanisms that may lead to CP chemoresistance, scientists used a lot of cells and subtractive hybridization to identify differentially expressed genes [15]. However, chemoresistance happens in cells where equivalent effects of various expressed genes is expressed outside of cell imaging. In this study, we proposed a promising method based on GLCM image processing model to achieve a rapid method with a more reliable diagnostic performance for various chemoresistance for CP of human ovarian adenocarcinoma cells by feature extraction of GLCM.

2. Materials and Methods

The optical image system used in this study comprised a microscope (BX-53 OLYMPUS, Tokyo, Japan) and DVC camera (Model: 1500M-T1-GE S/N 3797) with an image capture software (DVC View™). The different images (1392 × 1040 pixels) of the samples were obtained. The diameter of a cell was approximately 10–20 pixels in obtained images and the processing image was 150 × 150 pixels with 256 gray level for extracting the characteristic texture feature of cells [13].

GLCM was used to calculate contrast, energy, entropy, and homogeneity to analyze the images texture features. The variable C (i, j) expressed in Equations (1)–(4) refer to the value at the (i, j) position in a GLCM. These four indexes corresponded to the disorder in cell images and indicate the surface characteristic of cancer cells. For example, contrast displayed the edges and three-dimensional (3D) structures of cell; energy represented the orderliness; homogeneity represented the smoothness of the distribution for gray level and entropy showed the disorder degree.

$$\text{Contrast}: \sum_{ij=1}^{G} C_{ij}(i-j)^2 \tag{1}$$

$$\text{Energy}: \sum_{ij=1}^{G} {C_{ij}}^2 \tag{2}$$

$$\text{Homogeneity}: \sum_{ij=1}^{G} \frac{1}{1+\left|i-j\right|} C_{ij} \tag{3}$$

$$\text{Entropy}: -\sum_{ij=1}^{G} C_{ij} \log C_{ij} \tag{4}$$

Due to ovarian cancer being the most malignant of all gynecological cancers its chemoresistance was challenging the first-line chemotherapeutic agents for the treatments. High-grade serous ovarian cancer is responsible for approximately 80% of ovarian cancer cases so we selected human serous type ovarian adenocarcinoma cell lines (OVCAR-4 and A2780), and human clear cell type ovarian carcinoma cell line (IGROV1) to demonstrate the GLCM texture feature extraction and analysis of images. Furthermore, wild type (WT) human ovarian adenocarcinoma cell lines and that with chemoresistance for CP were used. All cells were maintained in RPMI1640 medium solution (Gibco)

containing 10% fetal calf serum and incubated at 37 °C with 5% CO_2. A2780 were cultured in PMI1640 medium with non-essential amino acids, glutamine, and 0.5 units insulin.

Before acquiring the images, cells were cultured with cell density of 6×10^5 in a glass-bottom dish. A silicone separator (Culture-Insert 2 Well, iBidi, Martinsried, Germany) was placed to trap cells to form a uniform coverage of the glass slide and create a clear region as the blank. Samples were incubated for 48 h and then washed twice in a phosphate buffered saline solution (PBS, 0.1 M, pH = 7.4).

To evaluate the reliability of the detection method, the statistical differences were evaluated using a one-way analysis of variance (ANOVA) technique. In evaluating the test results, a * p value of <0.05 was statistically significant, a ** p value of <0.01 was very statistically significant, and a *** p value of <0.001 was highly statistically significant.

3. Results and Discussion

Figure 1 shows cell images for serous cell type of OVCAR-4, A2780, and clear cell type IGROV1 of WT and CP-resistantance of ovarian adenocarcinoma cells. Under the optical microscope, little morphological differences could be observed between the WT ovarian adenocarcinoma cells (Figure 1a–c) and its CP-resistant counterpart (Figure 1d–f). However, chemoresistance is a very complex phenomenon, and it involves multiple interconnected mechanisms [16]. CP is localizing to the nucleus and binding to DNA, and then it gives rise to intrastrain DNA adducts. Subsequently, cancer cells apoptosis was caused by triggering G2 cell cycle arrest [17]. In a previous study, ovarian adenocarcinoma cells with CP-resistance recovered a normal proliferation state after a treatment with 5 μg/mL CP for 41 days. At confluence, the cell layer displayed some morphological differences and cells were becoming able to pile and to form three dimensional spherical structures [18]. It means that the cells with chemoresistance were tending to form stereoscopic structures and this characteristic can be analyzed by GLCM texture feature extracting of images. It will be promising and potentially detect chemoresistance before the new therapeutics.

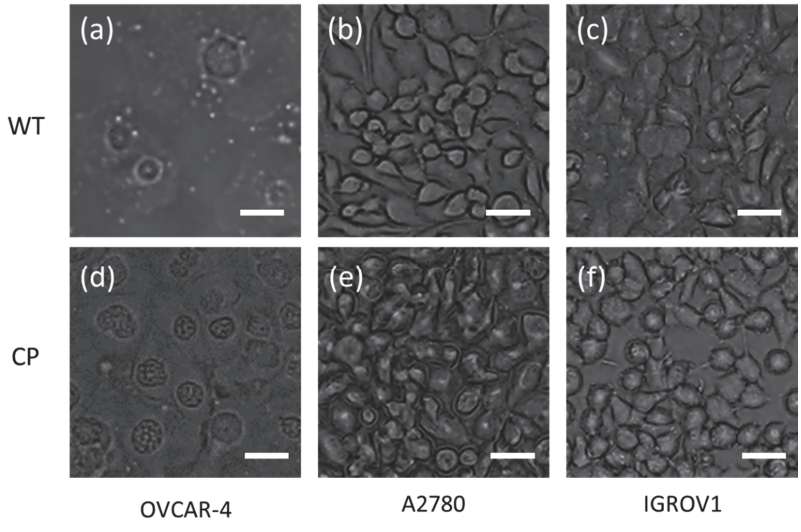

Figure 1. Cell images for serous cell type (**a**) OVCAR-4, (**b**) A2780, and (**c**) clear cell type IGROV1 of wild type (WT) ovarian adenocarcinoma cells and (**d**–**f**) which were cisplatin-resistant (CP). (Scale bar: 20 μm)

Figure 2 shows GLCM texture features of energy, contrast, homogeneity, and entropy for serous type (OVCAR-4) of ovarian adenocarcinoma cells with various interpixel distance with chemoresistance for CP and WT cells. The inflection points of texture feature can be found in Figure 2 around interpixel

distances of 10–20 pixels. The size of the image used for processing is 150 × 150 pixels and the diameter of ovarian adenocarcinoma cells is approximately 10–20 pixels, which implies that the characteristic texture feature commonly occurs in the boundary of cells, and that we can set up the interpixel distance as a specific value (e.g., 10 pixels) around the cell diameter to obtain the typical texture features. The ovarian adenocarcinoma cells with CP-resistance exhibit more 3D structures with characteristic rough surfaces. These structures enhance the optical scattering effect and it is difficult to observe the cells in the same focus plane and enhance the margins of cells. These characteristics indicate that the images of ovarian adenocarcinoma cells with CP-resistance have lower energy and homogeneity but higher contrast and entropy due to the morphologies. These four texture features can be used to predict the ability for CP-resistance of ovarian adenocarcinoma cells.

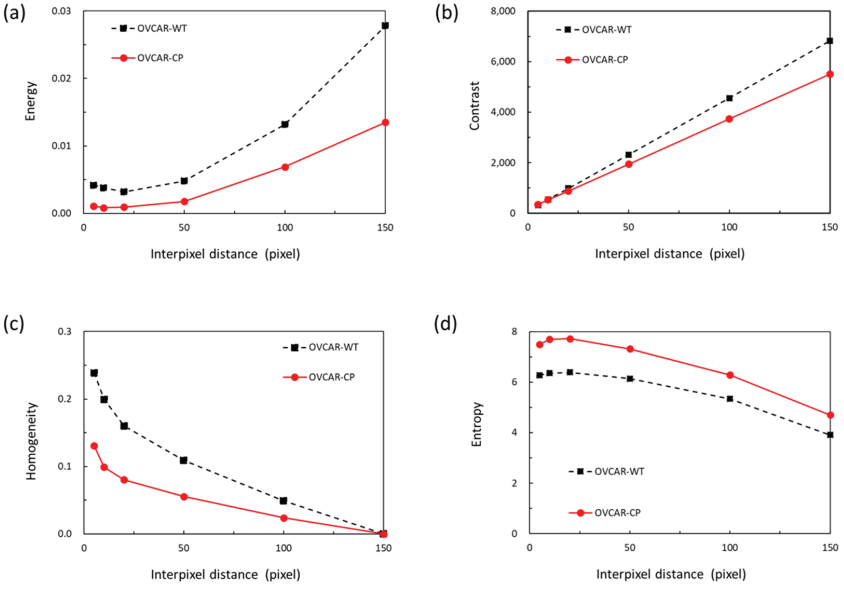

Figure 2. Gray level co-occurrence matrix (GLCM) texture feature: (**a**) energy, (**b**) contrast, (**c**) homogeneity, and (**d**) entropy for serous type (OVCAR-4) of ovarian adenocarcinoma cells with various interpixel distance with wild type (WT) and chemoresistance for cisplatin (CP).

Texture feature of GLCM extracting for WT and CP-resistant ovarian adenocarcinoma cell images are shown in Table 1. The texture features of WT ovarian adenocarcinoma cells were used as the benchmark and statistically compared with those of the CP-resistant cells for OVCAR-4, A2780, and IGROV-1, respectively. In general, the results show that for each of the cell lines, the CP-resistant ovarian adenocarcinoma cells have a higher contrast and entropy than the WT. Figure 3 shows GLCM texture features of WT and CP-resistant ovarian adenocarcinoma cells for OVCAR-4, A2780, and IGROV1. Table 1 and Figure 3 show that almost the differences in these four GLCM texture features of CP-resistant and WT cells were statistically significant in every case ($p < 0.01$ or $p < 0.001$). In other words, it provides the means to reliably differentiate between WT and CP-resistant cells for all three cell lines.

Table 1. Gray level co-occurrence matrix (GLCM) texture features for wild type (WT) and cisplatin-resistant (CP) of ovarian adenocarcinoma cells.

Cell	Feature	WT	CP	*p*-Value
OVCAR-4	Contrast ($\times 10^3$)	0.54 ± 0.08	0.53 ± 0.07	0.86
	Entropy ($\times 10^0$)	6.36 ± 0.22	7.70 ± 0.26	***
	Energy ($\times 10^{-3}$)	3.80 ± 0.84	0.83 ± 0.32	***
	Homogeneity ($\times 10^{-1}$)	1.99 ± 0.18	0.99 ± 0.10	***
A2780	Contrast ($\times 10^3$)	0.91 ± 0.13	1.35 ± 0.19	**
	Entropy ($\times 10^0$)	8.23 ± 0.21	8.85 ± 0.11	***
	Energy ($\times 10^{-3}$)	0.45 ± 0.11	0.20 ± 0.03	***
	Homogeneity ($\times 10^{-1}$)	0.60 ± 0.08	0.40 ± 0.03	**
IGROV1	Contrast ($\times 10^3$)	0.74 ± 0.15	1.32 ± 0.09	***
	Entropy ($\times 10^0$)	7.92 ± 0.21	9.41 ± 0.06	***
	Energy ($\times 10^{-3}$)	0.61 ± 0.12	0.18 ± 0.01	***
	Homogeneity ($\times 10^{-1}$)	0.71 ± 0.09	0.33 ± 0.01	***

Note: GLCM sampling offset was (10.0) and compare to WT and * $p < 0.05$, ** $p < 0.01$, and *** $p < 0.001$.

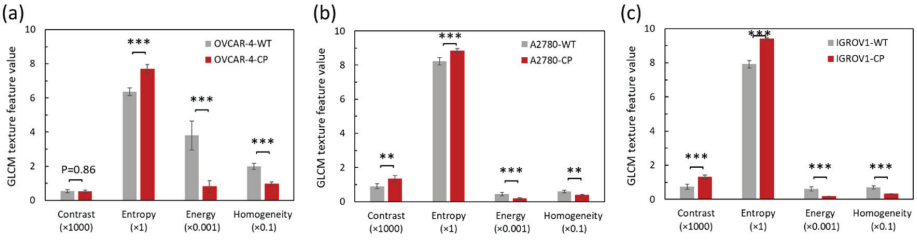

Figure 3. Gray level co-occurrence matrix (GLCM) texture feature of wild type (WT) and cisplatin (CP)-resistant ovarian adenocarcinoma cells for (**a**) OVCAR-4, (**b**) A2780, and (**c**) IGROV1.

Due to the multi-factor analysis being complex, signal-to-noise (S/N) ratios of these four GLCM texture features for WT and CP-resistant ovarian adenocarcinoma cells were calculated and shown in Table 2. The basic concept was according to Taguchi method [19]. In this study, S/N ratio was meaning the degree of the images influenced by the various factors. It was calculated by equations from the Taguchi method. Taguchi method was used to improve the qualities of products efficiently with parameters designed in engineering fields. S/N ratio was meaning the degree of the product influenced by the various factors. In this study, the various GLCM texture features can be the parameter of cell images. For CP-resistant type cells, two of the four GLCM texture features were for smaller-is-better (i.e., energy and homogeneity) and two for larger-is-better (i.e., contrast and entropy). It was same as the basic concept of Taguchi method, so we used it for multi-factor calculation. S/N ratio was calculated by Equations (5) and (6) [20]:

$$\text{Smaller-is-better}: \ \text{S/N ratio} = -10\log\left(\frac{1}{n}\sum y_i^2\right) \tag{5}$$

$$\text{Larger-is-better}: \ \text{S/N ratio} = -10\log\left(\frac{1}{n}\sum \frac{1}{y_i^2}\right) \tag{6}$$

S/N ratio can be referred to the degree for chemoresistance of cells based on GLCM texture feature extraction. The higher S/N ratio means the cell images were more like CP-resistant type. In Table 2, the S/N ratio of WT of ovarian adenocarcinoma cells were 17.93 ± 0.59, 23.37 ± 0.42, and 22.81 ± 0.43 for OVCAR-4, A2780 and IGROV1, respectively. The S/N ratio of CP-resistant ovarian adenocarcinoma cells were 21.76 ± 0.50, 24.44 ± 0.17, and 25.09 ± 0.07 for OVCAR-4, A2780 and IGROV1, respectively.

The differences in these cells were statistically significant in every case ($p < 0.001$). Compared to Table 1, the results of false positive CP were eliminated using multi-factor calculation. In this study, S/N ratio was meaning the degree of the images influenced by the various factors. Moreover, multi-factors included the tumor heterogeneity caused by different cell types in vivo.

Table 2. Signal-to-noise (S/N) ratio of gray level co-occurrence matrix (GLCM) texture feature for wild type (WT) and cisplatin-resistant (CP) ovarian adenocarcinoma cells.

Cells	WT	CP	*p*-Value
OVCAR-4	17.93 ± 0.59	21.76 ± 0.50	***
A2780	23.37 ± 0.42	24.44 ± 0.17	***
IGROV1	22.81 ± 0.43	25.09 ± 0.07	***

Note: GLCM sampling offset was (10.0) and compare to WT and * $p < 0.05$, ** $p < 0.01$, and *** $p < 0.001$.

The main factors which limit treatment efficiency are recurrence and progressive acquisition of chemoresistance. Chemoresistance is a complex process involving many stages. As a result, there is an urgent requirement for low-cost, high-throughput methods for assessing the risk of chemoresistance in a timely and quantitative manner. Accordingly, this study has proposed an optical method for chemoresistance detection based on GLCM texture features extraction. The feasibility of the proposed approach has been demonstrated using three pairs of ovarian adenocarcinoma cells, namely OVCAR-4, A2780, and IGROV1. Notably, the proposed method enables physical characterization of ovarian adenocarcinoma cells even in the case where the size and morphologies of the CP-resistant cells are very similar to those of WT.

Optical images could be used to study biophysical processes in living systems and to monitor morphological and physiological changes such as precancerous or cancerous conditions [21]. In a previous study, it has been indicated that epithelial-mesenchymal transition (EMT) contributes to chemoresistance acquisition [22] and indeed CP-resistant cell images result in the formation of dense 3D structures with characteristic rough surfaces compared to wild type cells. These cell structures enhance the higher contrast and entropy, and lower energy and homogeneity in GLCM texture feature of images.

The proposed method in this study has many advantages over in vitro tests, including a faster optical detection, a lower cost, a larger sample size, and a greater throughput. Most importantly, it provides the means to obtain a quantitative evaluation of the chemoresistance risk and therefore reduces the reliance on the practical skill and experience of the practitioner. Figure 4 shows the sketch of this promising model to achieve a rapid method with a more reliable diagnostic performance for identification of ovarian adenocarcinoma cells with cisplatin-resistance by feature extraction of GLCM in vitro or ex vivo. In the same time, machine learning was rapidly developing as the artificial intelligence technique [23]. The proposed method in this study was based on computer aided diagnosis [24] and it can be combined with the support vector machine [25] to train the model for proceeding the mass identification of chemoresistance risk for cancer cells. According to our previous study [13,14], more than ten cancer species were selected for feature extraction using optical images and we get positive results for various identification. It has potential for other cancer cells due to their equivalent effect for epithelial-mesenchymal transition expressed in cell imaging. However, it was required for the high throughput platform and combined with machine learning to train the model for proceeding the mass identification of chemoresistance risk for more cancer species. It provides a highly promising solution for physical characterization of ovarian adenocarcinoma cells with chemoresistance in vitro. Even for clinical practice, multiple invasive biopsies also can be used to analyze for feature extraction using optical images, but it was required to use scanned laser pico-projection system (SLPP) which has the narrower bandwidth compared to traditional white light to enhance the contrast and entropy of images for analysis [14].

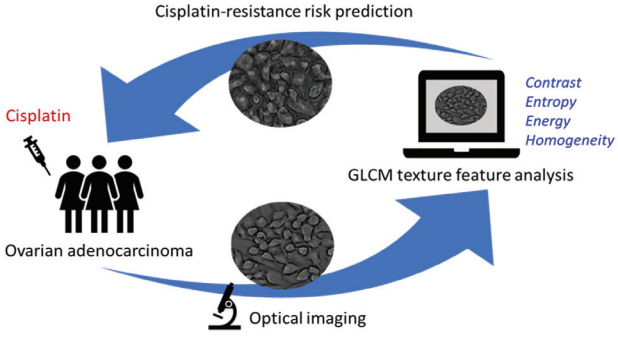

Figure 4. Sketch of the proposed promising model to achieve a rapid method with a more reliable diagnostic performance for identification of ovarian adenocarcinoma cells with cisplatin-resistance by feature extraction of GLCM in vitro or ex vivo.

4. Conclusions

Serous type ovarian adenocarcinoma cells with chemoresistance have more obvious edges and 3D structures, and the images were respected to have the higher contrast and entropy, lower energy and homogeneity. This provides the means to obtain a quantitative evaluation of the chemoresistance risk. It is a promising model to achieve a rapid method with a more reliable diagnostic performance for identification of ovarian adenocarcinoma cells with cisplatin-resistance by feature extraction of GLCM in vitro or ex vivo. In the future, the cells of the same patient could be taken from various stages of treatments to monitor morphological and physiological changes for cancerous conditions. It provides a quantitative evaluation of chemoresistance risk for chemotherapeutic agents in the next treatments. It can help to detect chemoresistance of cancer cells before the new therapeutics.

Author Contributions: Conceptualization, C.-L.H. and W.-T.C.; investigation, M.-J.L., Y.-H.W. and W.-M.C.; supervision, C.-L.H. All authors have read and agreed to the published version of the manuscript.

Funding: This research was funded by College Student Research Scholarship of Ministry of Science and Technology (MOST) in Taiwan under grant no. (107-2813-C-006-179-B) and sponsored by the Ministry of Education in Taiwan.

Acknowledgments: The authors would like to thank the financial support provided to this study by College Student Research Scholarship of Ministry of Science and Technology (MOST) in Taiwan under grant no. (107-2813-C-006-179-B) and sponsored by the Ministry of Education in Taiwan.

Conflicts of Interest: The authors declare no conflict of interest.

References

1. Janda, M.; McGrath, S.; Obermair, A. Challenges and controversies in the conservative management of uterine and ovarian cancer. *Best Pract. Res. Clin. Obstet. Gynaecol.* **2019**, *55*, 93–108. [CrossRef] [PubMed]
2. Jendželovský, R.; Jendželovská, Z.; Hiľovská, L.; Kovaľ, J.; Mikeš, J.; Fedoročko, P. Proadifen sensitizes resistant ovarian adenocarcinoma cells to cisplatin. *Toxicol. Lett.* **2016**, *243*, 56–66. [CrossRef] [PubMed]
3. Anglesio, M.S.; Wiegand, K.C.; Melnyk, N.; Chow, C.; Salamanca, C.; Prentice, L.M.; Senz, J.; Yang, W.; Spillman, M.A.; Cochrane, D.R.; et al. Type-specific cell line models for type-specific ovarian cancer research. *PLoS ONE* **2013**, *8*, e72162. [CrossRef] [PubMed]
4. Shaw, S.K.; Schreiber, C.L.; Roland, F.M.; Battles, P.M.; Brennan, S.P.; Padanilam, S.J.; Smith, B.D. High expression of integrin αvβ3 enables uptake of targeted fluorescent probes into ovarian cancer cells and tumors. *Bioorg. Med. Chem.* **2018**, *26*, 2085–2091. [CrossRef] [PubMed]
5. Rivard, C.; Geller, M.; Schnettler, E.; Saluja, M.; Vogel, R.I.; Saluja, A.; Ramakrishnan, S. Inhibition of epithelial ovarian cancer by Minnelide, a water-soluble pro-drug. *Gynecol. Oncol.* **2014**, *135*, 318–324. [CrossRef] [PubMed]

6. Carduner, L.; Picot, C.R.; Leroy-Dudal, J.; Blay, L.; Kellouche, S.; Carreiras, F. Cell cycle arrest or survival signaling through αv integrins, activation of PKC and ERK1/2 lead to anoikis resistance of ovarian cancer spheroids. *Exp. Cell Res.* **2014**, *320*, 329–342. [CrossRef] [PubMed]
7. Lloyd, K.; Rosin, P.L.; Marshall, D.; Moore, S.C. Detecting violent and abnormal crowd activity using temporal analysis of grey level co-occurrence matrix (GLCM)-based texture measures. *Mach. Vis. Appl.* **2017**, *28*, 361–371. [CrossRef]
8. Haralick, R.; Shanmugam, K.; Dinstein, I.H. Textural features for image classif. *IEEE Trans. Ind. Electron.* **1973**, *3*, 610–621. [CrossRef]
9. Molina, D.; Pérez-Beteta, J.; Martínez-González, A.; Martino, J.; Velásquez, C.; Arana, E.; Pérez-García, V.M. Influence of gray level and space discretization on brain tumor heterogeneity measures obtained from magnetic resonance images. *Comput. Biol. Med.* **2016**, *78*, 49–57. [CrossRef] [PubMed]
10. Vallabhaneni, R.B.; Rajesh, V. Brain tumour detection using mean shift clustering and GLCM features with edge adaptive total variation denoising technique. *Alex. Eng. J.* **2018**, *57*, 2387–2392. [CrossRef]
11. Xian, G.-M. An identification method of malignant and benign liver tumors from ultrasonography based on GLCM texture features and fuzzy SVM. *Expert Syst. Appl.* **2010**, *37*, 6737–6741. [CrossRef]
12. Öztürk, Ş.; Akdemir, B. Application of Feature Extraction and Classification Methods for Histopathological Image using GLCM, LBP, LBGLCM, GLRLM and SFTA. *Procedia Comput. Sci.* **2018**, *132*, 40–46. [CrossRef]
13. Lian, M.-J.; Huang, C.-L. Texture feature extraction of gray-level co-occurrence matrix for metastatic cancer cells using scanned laser pico-projection images. *Lasers Med. Sci.* **2019**, *34*, 1503–1508. [CrossRef] [PubMed]
14. Lian, M.-J.; Huang, C.-L.; Lee, T.-M. Automation Characterization for Oral Cancer by Pathological Image Processing with Gray-Level Co-occurrence Matrix. *J. Image Graph.* **2018**, *6*, 80–83. [CrossRef]
15. Solár, P.; Sytkowski, A.J. Differentially expressed genes associated with cisplatin resistance in human ovarian adenocarcinoma cell line A2780. *Cancer lett.* **2011**, *309*, 11–18. [CrossRef] [PubMed]
16. Ji, X.; Lu, Y.; Tian, H.; Meng, X.; Wei, M.; Cho, W.C. Chemoresistance mechanisms of breast cancer and their countermeasures. *Biomed. Pharmacother.* **2019**, *114*, 108800. [CrossRef] [PubMed]
17. Kawahara, B.; Ramadoss, S.; Chaudhuri, G.; Janzen, C.; Sen, S.; Mascharak, P.K. Carbon monoxide sensitizes cisplatin-resistant ovarian cancer cell lines toward cisplatin via attenuation of levels of glutathione and nuclear metallothionein. *J. Inorg. Biochem.* **2019**, *191*, 29–39. [CrossRef] [PubMed]
18. Villedieu, M.; Deslandes, E.; Duval, M.; Héron, J.F.; Gauduchon, P.; Poulain, L. Acquisition of chemoresistance following discontinuous exposures to cisplatin is associated in ovarian carcinoma cells with progressive alteration of FAK, ERK and p38 activation in response to treatment. *Gynecol. Oncol.* **2006**, *101*, 507–519. [CrossRef] [PubMed]
19. Rezania, A.; Atouei, S.A.; Rosendahl, L. Critical parameters in integration of thermoelectric generators and phase change materials by numerical and Taguchi methods. *Mater. Today Energy* **2020**, *16*, 100376. [CrossRef]
20. Avikal, S.; Nithin Kumar, K.C.; Singh, A.R.; Jain, R. Grey based Taguchi optimization for multi-lobe bearing. *Mater. Today Proc.* **2020**. [CrossRef]
21. Duran-Sierra, E.; Cheng, S.; Cuenca-Martinez, R.; Malik, B.; Maitland, K.C.; Lisa Cheng, Y.S.; Wright, J.; Ahmed, B.; Ji, J.; Martinez, M.; et al. Clinical label-free biochemical and metabolic fluorescence lifetime endoscopic imaging of precancerous and cancerous oral lesions. *Oral Oncol.* **2020**, *105*. [CrossRef] [PubMed]
22. Hoshiba, T. An extracellular matrix (ECM) model at high malignant colorectal tumor increases chondroitin sulfate chains to promote epithelial-mesenchymal transition and chemoresistance acquisition. *Exp. Cell Res.* **2018**, *370*, 571–578. [CrossRef] [PubMed]
23. Waring, J.; Lindvall, C.; Umeton, R. Automated machine learning: Review of the state-of-the-art and opportunities for healthcare. *Artif. Intell. Med.* **2020**, *104*. [CrossRef] [PubMed]
24. Raghavendra, U.; Gudigar, A.; Rao, T.N.; Ciaccio, E.J.; Ng, E.Y.K.; Rajendra Acharya, U. Computer-aided diagnosis for the identification of breast cancer using thermogram images: A comprehensive review. *Infrared Phys. Technol.* **2019**, *102*. [CrossRef]
25. Wang, G.; Zhang, G.; Choi, K.-S.; Lam, K.-M.; Lu, J. Output based transfer learning with least squares support vector machine and its application in bladder cancer prognosis. *Neurocomputing* **2020**, *387*, 279–292. [CrossRef]

diagnostics

MDPI

Review

Scattering of Light from the Systemic Circulatory System

Sidra Batool [1,*], Mehwish Nisar [1,2], Fabio Mangini [3], Fabrizio Frezza [1] and Eugenio Fazio [2]

[1] Department of Information Engineering, Electronics and Telecommunications, Sapienza University of Rome, Via Eudossiana 18, 00184 Rome, Italy; mehwish.nisar@uniroma1.it (M.N.); fabrizio.frezza@uniroma1.it (F.F.)
[2] Department of Fundamental and Applied Sciences for Engineering, Sapienza University of Rome, Via A. Scarpa 16, 00161 Rome, Italy; eugenio.fazio@uniroma1.it
[3] Department of Information Engineering, University of Brescia, Via Branze 59, 25123 Brescia, Italy; fabio.mangini@uniroma1.it
* Correspondence: sidra.batool@uniroma1.it

Received: 19 October 2020; Accepted: 23 November 2020; Published: 30 November 2020

Abstract: There are many factors of methodological origin that influence the measurement of optical properties of the entire circulatory system which consists of blood as the basic component. The basic idea of this review article is to provide the optical properties of the circulatory system with all those factors of influence that have been employed in biomedical optics for different applications. We begin with the available optical properties, i.e., absorption, scattering and, reduced scattering coefficient, in general for any tissue inside the human body and prominent scattering theories (e.g., light, X-rays, neutrons) that are helpful in this regard. We have reviewed and compiled already available formulas and their respective available data for different human tissues for these optical properties. Then we have descended to the blood composition and to different scattering techniques available in the literature to study scattering and light propagation inside blood. We have reviewed both computational and theoretical scattering techniques.

Keywords: optical properties; scattering theories; circulatory system

1. Introduction

When light interacts with the human body, several phenomena take place depending on the type of tissue and on its biological composition [1], such as reflection, refraction, absorption, scattering or even emission. The different optical properties of the tissues influence the interaction with light and consequently the various diagnostic and therapeutic applications. The heterogeneity of the tissues increases the complexity of the analysis of interactions with light; therefore, following a methodological approach for further study, it is useful to first analyse the factors that influence the average optical properties on a macroscopic scale and then deal with the microscopic effects related to the heterogeneity of the individual structures. The optical properties that mainly describe the transport of light in the tissues are absorption and scattering. The absorption of light is due to the electronic transitions that can occur in the molecules that make up the tissues and whose selectivity, consequently, gives colour to the tissues (often the coloration of the fabric is identified with that part of the molecule responsible for absorption called chromophore, a word coming from the Greek term "chroma" which means colour) [2–5]. Electronic transitions typically have energies of the order of electronvolts and therefore occur in the optical band, i.e., partly in the UV, in the visible and partly in the IR too where the molecular transitions (rotations/vibrations/roto-vibrations) have more their characteristic energies. The scattering of light is instead due to fluctuations and discontinuities in the refractive index of the optical tissue due to the presence of cells, membranes, microstructures and

sub-cellular components [6]. The most used technique for the characterization of the optical properties of matter is optical spectroscopy, with which it is possible to determine the light absorption and emission absorption properties. It is possible to carry out both absorption spectroscopy, revealing the spectral components of the sent light which have been absorbed or diffused due to absorption or scattering, and emission spectroscopy, in which case, given a high energy excitation, the spectral components of the radiation emitted by the material are measured [7–10]. In the next section, we shall describe the scattering and absorption of light by biological tissues.

2. Fundamental Optical Properties of Tissues

Tissues are generally characterized by structural inhomogeneities of very different dimensions, from tenths of nanometers to hundreds of micrometers [11]. For this reason, many different techniques are used for the microscopic and macroscopic characterization of the optical properties of the tissues, as shown in Figure 1 [12–15], and many different simulation models have been implemented to highlight the specific behaviour of the materials and the propagation of the light inside them. The light scattering from spherical particles is mainly described by the Rayleigh and Mie theories. The Rayleigh scattering indicates scattering by small particles or mass density variation much smaller than the wavelength of light, while the Mie scattering indicates the scattering by particles comparable to or larger than the wavelength of light [16–22]. One of the simplest and most used models for light scattering by biological tissues implements a Mie scattering procedure. Such a model represents a biological tissue as a mixture of particles of varying sizes dispersed within a host matrix with a different refractive index [23,24]. Mie scattering is defined as when the size of the object is larger than the wavelength of light. This type of model is certainly effective even, if the idealization of the sphericity of the scattering centers leads to results sometimes different from the real behaviours. An alternative approach to Mie scattering is represented by the continuum model, in which a tissue is modeled as a continuous medium where there are fluctuations in density and therefore in the refractive index, which can be described through an autocorrelation function [25]. The Wiener–Khintchine theorem, in general, relates the autocorrelation function to the corresponding spectrum of the scattered power [26].

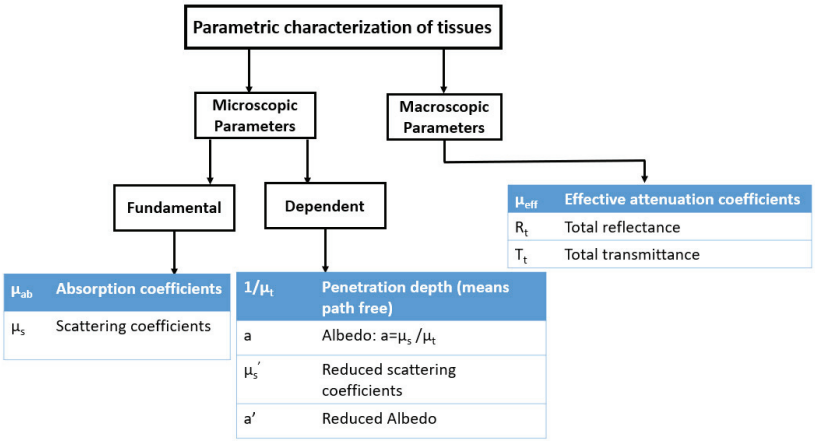

Figure 1. Parametric characterization of tissues on microscopic and macroscopic levels [27].

The popular scattering theories that have been employed in many fields of biomedical optics are Rayleigh and Mie scattering theories. The Rayleigh scattering indicates scattering by small particles or mass density variation much smaller than the wavelength of light, and Mie scattering indicates the scattering by particles comparable to or larger than the wavelength of light.

2.1. Absorption Coefficient

The absorption of light by an optimum volume of identical molecules can be expressed in terms of the absorption coefficient, which represents the probability that a photon is absorbed with respect to the medium according to its required path-length. Let us consider a homogeneous medium composed by absorbing molecules. The absorption coefficient is defined as the product between the probability that a photon is absorbed by a molecule (i.e., the cross-section a) and the density of the molecules present in the volume:

$$\mu_a = \rho_a \sigma_a \tag{1}$$

The absorption cross section measures the rate at which the photon energy is being absorbed from the light wave [27].

2.2. Scattering Coefficient

Similarly to absorption, the elastic scattering for single events (i.e., not for multiple scattering processes) in a certain medium can still be represented by a scattering coefficient s, that describes the probability of photon to be scattered during a unitary path-length. The reciprocal of s is called the scattering length of the object and denoted as the average distance traveled by a photon between consecutive scattering events (photon mean-free-path). Furthermore, the scattering coefficient may be defined as [28] as the product between the probability that a photon is diffused by a scattering center (i.e., the cross section s) and the density s of scatterers in the volume:

$$\mu_s = \rho_s \sigma_s \tag{2}$$

The scattering cross-section area is defined as the rate with which the power is removed from the initial S' direction towards the new S direction compatible with the medium, as shown in Figure 2. The probability that a photon is scattered within a certain solid angle is defined by the phase function p:

$$p = \frac{1}{\sigma_s} \frac{d\sigma_s}{d\Omega} \tag{3}$$

where the term $\frac{d\sigma_s}{d\Omega}$ represents the differential scattering cross section [29]. Both the scattering and the absorption coefficients depend on the light wavelength [30,31].

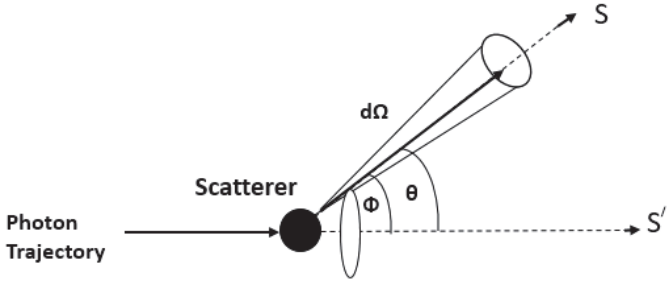

Figure 2. A photon initially traveling from S' is scattered into a differential solid angle $d\Omega$ along S. Here ϕ corresponds to the azimuthal angle from the scattered trajectory, and θ corresponds to the polar angle from the initial trajectory.

2.3. Reduced Scattering Coefficient

Instead of using the whole scattering theories, often an equivalent reduced scattering coefficient is used to describe both Mie and Rayleigh regimes. This reduced coefficient can effectively describe the dispersion properties of the main six different groups of tissues such as skin, breast, brain, bones,

fibrous and fatty tissues. All of them are a set of small and large scatterers that act simultaneously. Its expression refers to the scattering efficiency at a reference visible wavelength 0 (usually the green @500 nm) according to the following wavelength-dependent expression:

$$\mu_s' = a\left(\frac{\lambda}{500\,(\mathrm{nm})}\right)^{-b} \tag{4}$$

where a is the $\mu_s{}'$ value at the reference wavelength and b is the characteristic power dependence. A more explicit expression of the scattering coefficient separates the Rayleigh and the Mie contributions keeping the same wavelength-type dependence:

$$\mu_s' = a'\left(f_{Ray}\left(\frac{\lambda}{500\,\mathrm{nm}}\right)^{-4} + (1 - f_{Ray})\left(\frac{\lambda}{500\,\mathrm{nm}}\right)^{-b_{Mie}}\right) \tag{5}$$

where f_{Ray} and f_{Mie} represent the fraction of small and large scatterers, respectively and satisfy the conservation rule:

$$f_{Ray} + f_{Mie} = 1 \tag{6}$$

In Figure 3 the explicit expressions and values of $\mu_s^{'}$ are reported for different tissues. All of them, as shown by the previous analytical expressions illustrated in Tables 1 and 2, have a hyperbolic decreasing dispersion increasing the wavelength, in the VIS-NIR spectral range [32–35].

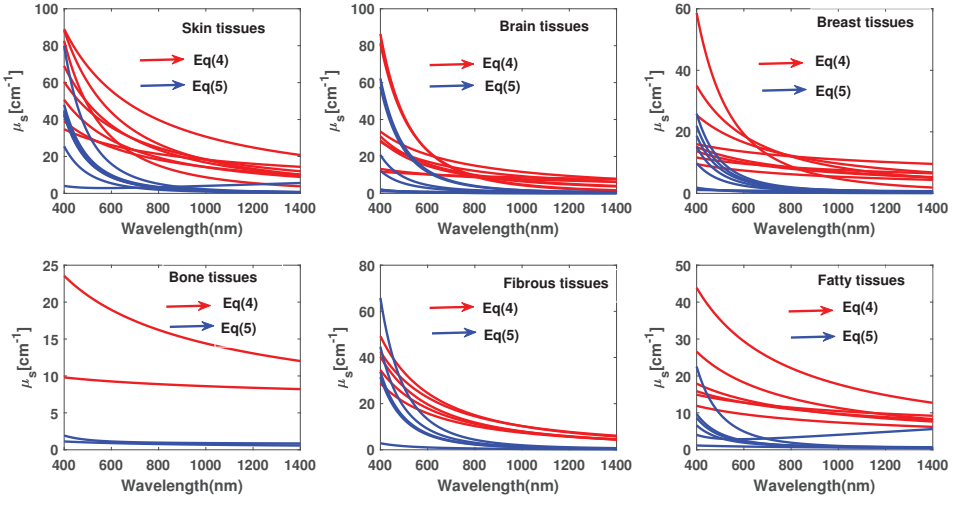

Figure 3. In the review literature, some measurement expressing the optical properties of tissues [27].

Table 1. Represents the different tissues (e.g., skin, brain, breast, bone) description using scattering parameters, where a is the μ_s' value at the reference wavelength and b is the characteristic power dependence and f_{Ray} or f_{Mie} demonstrated the fraction of small and large scatterers, respectively.

#	a	b	a′	f_{Ray}	f_{Mie}	Tissue Description	Ref
				Skin			
1	48.9	1.548	45.6	0.22	1.184	skin	[36]
2	47.8	2.453	42.9	0.76	0.351	skin	[35]
3	37.2	1.39	42.6	0.4	0.919	skin	[37]
4	60.1	1.722	58.3	0.31	0.919	skin	[38]
5	29.7	0.705	36.4	0.48	0.22	skin	[39]
6	45.3	1.292	43.6	0.41	0.562	dermis	[40]
7	68.7	1.161	66.7	0.29	0.689	epidermis	[40]
				Brain			
8	40.8	3.059	40.8	0	3.088	brain	[41]
9	10.9	0.334	13.3	0.36	0	cortex (frontal lobe)	[42]
10	11.6	0.601	15.7	0.53	0	cortex (temporal lobe)	[42]
11	20	1.629	29.1	0.81	0	astrocytoma of optic nerve	[42]
12	25.9	1.156	25.9	0	1.156	normal optic nerve	[42]
13	21.5	1.629	31	0.82	0	cerebellar white matter	[42]
14	41.8	3.254	41.8	0	3.254	medulloblastoma	[42]
15	21.4	1.2	21.4	0	1.2	brain	[25]
				Breast			
16	31.8	2.741	31.8	0	2.741	breast	[41]
17	11.8	0.775	15.2	0.58	0	breast	[41]
18	24.8	1.544	24.8	0	1.544	breast	[41]
19	20.1	1.054	20.2	0.18	0.638	breast	[41]
20	14.6	0.41	18.1	0.41	0	breast	[43]
21	12.5	0.837	17.4	0.6	0.0076	breast	[44]
22	8.3	0.617	11.2	0.54	0.009	breast	[44]
23	10.5	0.464	10.5	0	0.473	breast	[45]
				Bone			
24	9.5	0.141	9.7	0.04	0.116	skull	[42]
25	20.9	0.537	20.9	0	0.537	skull	[46]

Table 2. Represents the different tissues (e.g., fibrous and fatty) description using scattering parameters, where a is the μ_s' value at the reference wavelength and b is the characteristic power dependence and f_{Ray} or f_{Mie} demonstrated the fraction of small and large scatterers, respectivelypectively.

#	a	b	a′	f_{Ray}	f_{Mie}	Tissue Discription	Ref
Fibrous tissue							
26	33.6	1.712	37.3	0.72	0	tumor	[41]
27	30.1	1.549	30.1	0.02	1.521	prostate	[47]
28	27.2	1.768	29.7	0.61	0.585	glandular breast	[48]
29	24.1	1.618	25.8	0.49	0.7845	fibrocystic breast	[48]
30	20.7	1.487	22.8	0.6	0.327	carcinoma breast	[48]
Fatty tissues							
31	13.7	o.385	14.7	0.16	0.250	Subcutaneous fat	[37]
32	10.6	0.520	11.2	0.29	0.089	Adipose breast	[48]
33	15.4	0.680	15.4	0.00	0.680	Subcutaneous adipose	[39]
34	35.2	0.988	34.2	0.26	0.567	Subcut. fat	[40]
35	21.6	0.930	21.1	0.17	0.651	Subcut. adipocytes	[40]
36	14.1	0.530	na	na	na	Adipose	[49]

3. Scattering of Light from Nerves, Veins, and Arteries

The polarization of light contributes to the observed appearance of the skin and its relative colour, since the reflection/refraction/diffraction of the light on it depends strictly on the degree of polarization of the light used. Since on some chromatic bands the absorption is very high and on others much less, the observed effects can be either superficial or deep, with light penetrations in the underlying layers either limited to a few microns or extended to several centimeters [50–52].

Based on conventional tissue staining protocols, pathological understanding of arterial diseases is mainly attributable to observations that have been reported in the literature [53]. A new venue for visualizing pathological changes in the extracellular matrix caused by the progression of atherosclerosis is the emerging development of Nonlinear Optical Microscopy (NLOM), especially in second-harmonic generation, two-photon excited fluorescence and, coherent Raman scattering. In general, these techniques can offer rapid three-dimensional imaging in the biomedical sector. In this review, we look at recent progress in applications related to arterial disease imaging using various forms of NLOM [53,54].

During internal propagation, the light undergoes both scattering, due to the strong inhomogeneity of the biological tissue (formed by dispersed micro and nanostructures, filamentous proteins, cells, fibres, successive layers of dermis, fat, veins and capillaries, etc.), and absorption, due to the presence of many chromophores (the main ones being haemoglobin and melanin [39,55,56]. The melanin function is essentially the absorption of light radiation on some spectral bands, for example, the erythemal UV between 290 and 320 nm, which could be harmful to the body). Through the skin, the veins are also visible and with them the blood circulating inside, being able to make remote measurements in a non-invasive and non-bloody way. Focusing attention on it, the absorption spectrum of oxygenated (HbO_2) and deoxygenated haemoglobin (Hb) is shown in Figure 4 [57].

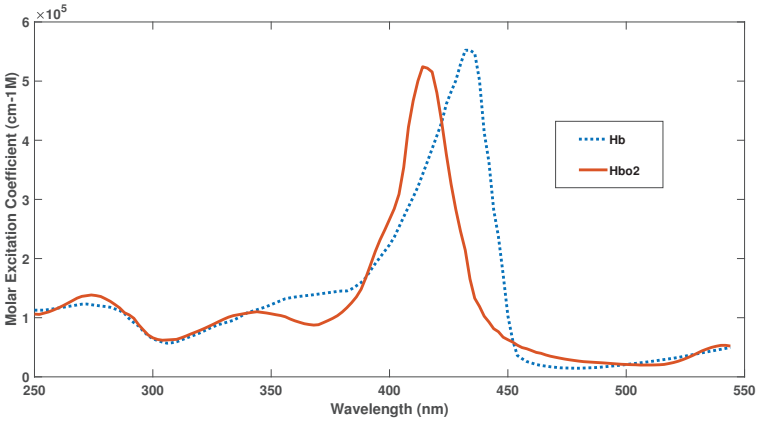

Figure 4. The graph shows the best-estimated spectrum of *Hb* and HbO_2 from the various sources by Scott Prahl Data [57].

Color	Wavelength Interval	Frequency Interval
Violet	430–380 nm	700–790 THz
Blue	500–430 nm	600–700 THz
Cyan	520–500 nm	580–600 THz
Green	565–520 nm	530–580 THz
Yellow	590–565 nm	510–530 THz
Orange	625–590 nm	480–410 THz
Red	740–625 nm	405–480 THz

Figure 5. White light spectrum with its corresponding wavelength and frequency interval.

3.1. Haemoglobin Absorption

As you can see, the two forms, *Hb* and HbO_2, have absorption peaks posted with respect to each other. Therefore, by making differential absorption measurements on the different peaks, it is possible to control the level of oxygenation with great precision [58]. This different absorption also influences the observed colour of the blood: oxygenated blood, within arteries, has a cherry red colour while the deoxygenated blood, present in the veins, is dark red (but through the skin it looks blue). The absorption rate of light is higher in the blue band than in the red band, because dark red deoxygenated venous blood has a higher absorption coefficient than cherry red oxygenated arterial blood in the human body [59]. However, the arteries are generally brighter than the veins. This is because they have thick vessel walls as they have to withstand high pressures due to heart beating. The arterial walls are typical of elastic and sometimes muscular tissues, which dilate and contract both to withstand the large pressures induced by heart pulses and to regulate and control the resistance of the flow in the capillary network. The veins, on the other hand, are used only for the transport of low oxygen blood to the organs used for its purification, lungs, and liver. For this reason, venous blood appears very dark to the eye [60,61]. Arteries and veins have different dispositions within the human body too: the arteries travel deep and are difficult to see and not accessible from the outside; the veins, on the other hand, are typically superficial and therefore can be easily monitored with non-invasive imaging techniques. However, it is possible to make non-bloody and non-invasive measurements also on the arteries by monitoring the retinal one: in fact, in the retina, there is a network of arterial capillaries between cones and rods of the retina. The central artery of the retina, through the dural

sheath of the optic nerve, reaches the optic papilla, where it divides first into an ascending and descending branch and then, subsequently, into lateral and medial branches. In this way, a dense network of small vessels is formed that never anastomose and that is easily accessible for observation by intraocular retinal imaging techniques. For many medical applications, it is of great importance to measure blood pressure and check for abnormal changes in veins and arteries that could be analyzed in depth using these retinal imaging techniques. In fact, many diseases cause an abnormal ratio between the length, diameter, and cross-linking of arteries and veins. For example, in diabetic patients the veins are abnormally wide, while pancreatic diseases lead to a narrowing of the wall of the vessels which generates an increase in blood pressure [5,62]. Minhaj et al. have shown that by combining together the optical density ratio (ODR) and the tracking of blood vessels (BVT) it is possible to make and characterize the map of the vessels, both arteries and veins. This is often traced starting from the source nodes and uses the curvature and the angle to derive the whole network. This measurement technique, despite being qualitative, has an accuracy of 97.06% in identifying veins and arteries [63]. Furthermore, the different response of oxygenated and deoxygenated hemoglobin to electromagnetic excitation finds application in functional magnetic resonance [64].

3.2. Optical Properties of Human Blood and Its Composition

Normal human blood consists of red blood cells (RBCs or erythrocytes, $\pm 4500 \times 103/\mu L$ blood), white blood cells (leukocytes, $\pm 8 \times 103/\mu L$ blood), platelets (thrombocytes, $\pm 300 \times 103/\mu L$ blood) and blood plasma that mainly contains water, electrolytes, plasma proteins, carbohydrates, lipids and various extracellular vesicles. The major portion of RBCs consists of haemoglobin. In healthy human adults, the haemoglobin concentration in blood is 140 g/L in women and 155 g/L in men on average.

Scattering and absorption of light in the blood is largely conducted by red blood cells for many reasons. Firstly, it should be remembered, that the quantity of red blood cells is about 4000 times greater, than that of white blood cells and therefore, they constitute the largest mass fraction. In humans, red blood cells have the typical shape of flexible biconcave discs, 6–8 μm in diameter, and 2.5 μm thick [58,65,66]. They dominate blood light scattering over any other component of the blood both for their large size and for the contrast index of refraction between the red blood cells and the surrounding blood plasma. In fact, their refractive index has a value of approximately between 1.40 and 1.42 [67], due to the combination of HbO_2 (1.615) and water (1.333) [68], while the refractive index of plasma (and serum) ranges from 1.36 (@400 nm) to 1.34 (@800 nm) [69]. Absorption is instead dominated by hemoglobin, in the two deoxygenated *Hb* and oxygenated HbO_2 forms (Figure 5). Flow cytometric light scattering measurements are helpful to determine the concentration of RBCs and their volume fraction, the hemoglobin concentration, and to discriminate the health of blood cells, as for example thalassaemic vs normal RBCs [70–73].

4. Computational Techniques in Literature

Many numerical models are used to describe the propagation of light within diffusive environments such as for example liquid suspensions of red blood cells. It is the most used, the Monte Carlo (MC) method is one of the most used statistical methods to describe multivariable dynamic systems. It is based on the dynamic simulation of the propagation of a population of elements which in our case are photons. By imposing the rules of absorption and diffusion of light passing through a suspension of RBCs, the MC method analyses in parallel the propagation of a set of photons statistically independent through the suspension. At each iteration a single photon may (1) not suffer anything and continue straight or (2) be absorbed or (3) be diffused. Statistically reconstructing the evolution of the entire population is initially possible to estimate the behaviour of light when passing through an RBCs suspension. The MC method is accessible to record the transmission and reflection coefficients from the tissues; from a comparison of the numerical results with the experimental data, it is possible to identify the micro topologies developed, the succession of the tissue layers, the properties of the materials, and the efficiencies of absorption and scattering [74,75].

The finite differences in time domain (FDTD) is a method of solving the electromagnetic wave equation using a step integration (finite differences) in the time domain. The method, in principle conceptually simple, is based on the definition of a derivative as a ratio of finite and not infinitesimal increments. This approximation is very delicate and leads to converging results if the rules defined by the Nyquist–Shannon sampling theorem [in the book Advances in FDTD Computational Electrodynamics] are respected [76]. Subsequent versions of the model have been developed over the years to decrease the error resulting from sampling using more complex definitions of the derivative as a ratio of symmetrical increments with respect to the calculation point. The FDTD method is general and flexible in terms of implementation of the full-wave techniques used to solve complex biological scattering problems [77]. It is suitable for the numerical simulation of scattering from non-homogeneous objects of arbitrary forms, as it numerically solves Maxwell's equations and it can calculate the angular dispersion of the scattered light [78,79]. For readers interested in the FDTD method, the book by Taflove [76] is recommended for further information. An effective method of optimizing the scattering results produced by FDTD simulations takes advantage of the Rytov approximation, and is often applied in tomography. Starting from the phase mapping of the scattered light and comparing it with the experimental data, the method exercises an iterative process of convergence to optimize the distribution of the scattering centers [80,81]. The Discrete Dipole Approximation (DDA) is closely related to the method of moments applicable for multiple scattering from RBCs. The working principle of this method is based on the decomposition of the volume into infinitesimal elements, each represented as a dipole. The electromagnetic field is calculated as the superposition of the injected field with the secondary ones emitted by the induced dipole sources [82]. Jiangping et al. performed a comparison of these methods, finding that the Rytov approximation is less accurate than DDA and FDTD methods [80].

5. Theoretical and Experimental Techniques in the Literature

There has been a considerable amount of consequence in applying polarization properties of light to biomedical imaging usage, in the recent years. Optical polarization imaging is examining to be a popular convenient non-invasive technique for the detection of biological structures. The ultimate goal is the detection of millimeter-sized small tissues in the biological texture. A few of the research that used polarization principles for biomedical imaging were expressed in the following section. Demos et al. reported that the techniques regarding polarization principles for non-invasive surface imaging of biological systems [83,84]. Polarization discrimination of the scattered photons were precisely used employing a non-rotating retarder polarimetric configuration to enhance the visualness of the subsurface textures. Jacques et al. [85] used the simple polarization principle for visualizing superficial layers of tissue such as skin, breast, brain, bones, connective tissue and fat. The study gives the detailed information on the transition of linearly polarized light into randomly polarized light using the light propagation through tissues. Results from the study demonstrated that the polarized light imaging of skin yields images based on backscattered photon from apparent epidermal and initial papillary dermis however, the birefringent dermal collagen immediately irregular polarized light.

Sankaran et al. [86] described the light propagates through tissue phantoms with densely packed scatterers show the changes in the properties of polarization. To study the increase and decrease in linear and circular polarization were used polystyrene microspheres suspended in an aqueous solution. This study was playing a vital role in designing and optimizing polarimetric techniques for tissue imaging and diagnostics. Shamaraj et al. [87,88] reported the study of scattered polarized light from highly scattering media are helpful for an analytical model and material characterization techniques. This study might be described in understanding the techniques for imaging tissues and hidden objects, which can be, used for the treatment of malignant diseases and diagnostics. Kari et al. [89] investigated the use of polarized light reflections to image tissues such as wood fibers. The components of the reflected light from the wood fibers contained information regarding the structure of the tissue.

They described the wood-fiber absorption, scattering cross sections, and scattering matrices in the ray-optics approximation. They computed the complicated internal structure of the wood fibers.

5.1. Fundamentals of Polarized Light Scattering

An incident of polarized light on an object can be described as two orthogonal linear polarization components of the incident light field parallel $\mathbf{E_{i||}}$ and perpendicular $\mathbf{E_{i\perp}}$ to the scattering plane shown in Figure 6.

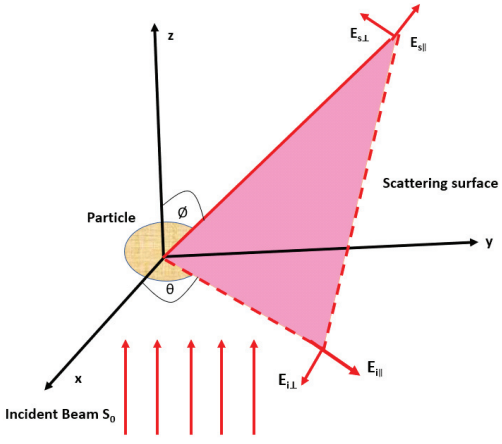

Figure 6. Geometry represents the scattering of light by an object located at the origin.

This figure represents the geometry of the scattering of light by an object (a particle representing the primary components of a biological structure). Here, the incident light beam $\mathbf{S_0}$ is parallel to the $z-axis$, θ and ϕ are the scattering angles in the scattering plane and in the plane perpendicular to the scattering plane, respectively. The detecting plane located at a distance r from the origin along the vector $\mathbf{S_1}$. two orthogonal polarization components, $\mathbf{E_{s\perp}}$ and $\mathbf{E_{s||}}$ of the scattered light formed a specific state of polarization depending on the amplitudes and phase shifts between components. The linear relationship between incident and scattered components can be described by the transformation of an arbitrarily polarized light (linear, circular, or elliptical) [90,91].

$$\begin{bmatrix} \mathbf{E_{s||}} \\ \mathbf{E_{s\perp}} \end{bmatrix} = \frac{e^{-ik(r-z)}}{-ikr} \begin{bmatrix} S_1 & S_2 \\ S_3 & S_4 \end{bmatrix} \begin{bmatrix} \mathbf{E_{i||}} \\ \mathbf{E_{i\perp}} \end{bmatrix} \tag{7}$$

where $k = \frac{2\pi}{\lambda}$ is a wave number, $\iota = \sqrt{-1}$, r represents the distance from the scatterer to the detector, z is the position coordinate of the scatterer. The matrix elements from $\mathbf{S_1}$ to $\mathbf{S_4}$ are described the amplitude of the scattering matrix (S-matrix) or Jones matrix. Each element depends on an elevation and azimuthal angles θ and ϕ, which contain information regarding the scatterer. Both phase and amplitude must be measured to evaluate the amplitude scattering matrix. The Jones matrix elements of transparent optical materials without sign ambiguity can be determined by using polarimetric methods.

5.2. Polarimetric Imaging

Polarimetry is the technique of measuring polarization state and interaction of polarized light with the target object always returns the change in the state of polarization of the interacting light. Weakly scattered light retains its polarization state easily, meanwhile strongly scattered light does not retain its polarization state [92]. Investigating the state of polarization of light interaction with the target results in a better imaging procedure to extract useful information from the target.

5.3. Stokes Parameter

The polarization state of light can be adequately demonstrated by the four Stokes parameters as shown below.

$$I = \mathbf{E}_x^2 + \mathbf{E}_y^2 \tag{8}$$

$$Q = \mathbf{E}_x^2 - \mathbf{E}_y^2 \tag{9}$$

$$U = 2\mathbf{E}_x\mathbf{E}_y \cos\delta \tag{10}$$

$$V = 2\mathbf{E}_x\mathbf{E}_y \sin\delta \tag{11}$$

where $\mathbf{E}_x$ and $\mathbf{E}_y$ describes the maximum amplitudes of the optical components of the field in x and y directions, respectively, and δ describes the phase difference between the optical components of the field.

I expresses the total intensity of light;

Q expresses the amount of linear horizontal or vertical polarization;

U expresses the amount of linear $+45^\circ$ or -45° polarization;

V expresses the amount of right or left circular polarization contained in the light beam. The Stokes matrix may be written as:

$$\mathbf{S} = \begin{bmatrix} I \\ Q \\ U \\ V \end{bmatrix} = \begin{bmatrix} I_H + I_V \\ I_H - I_V \\ I_P - I_M \\ I_R - I_L \end{bmatrix} \tag{12}$$

where I_H and I_V are light intensities measured with horizontally and vertically oriented linear polarizers, I_P and I_M are measured with $+45^\circ$ and -45° oriented linear polarizers, I_R and I_L are measured with right circularly and left circularly oriented linear polarizers in front of a detector, respectively.

5.4. Mueller Matrix

When light comes in contact with the object, the polarization state of the light beam changes with respect to the medium. Eventually, the incident and exciting beam will have a different state of polarized light. The polarization of the scattered light from an object in far field shown in Figure 1. is investigated the Stokes vector S_s associated with the Stokes vector of the incident light S_i connected by the matrix equation S_s = M S_i, where M is the normalized scattering matrix (Mueller matrix) [93,94].

$$\begin{bmatrix} I_s \\ Q_s \\ U_s \\ V_s \end{bmatrix} = \begin{bmatrix} M_{11} & M_{12} & M_{13} & M_{14} \\ M_{21} & M_{22} & M_{23} & M_{24} \\ M_{31} & M_{32} & M_{33} & M_{34} \\ M_{41} & M_{42} & M_{43} & M_{44} \end{bmatrix} \begin{bmatrix} I_i \\ Q_i \\ U_i \\ V_i \end{bmatrix} \tag{13}$$

Elements of the Mueller matrix depends on the scattering angle the wavelength of light, and the optical parameters of the object with the corresponding geometries. Element M_{11} tell us the information of the incident light is unpolarized, and scattered light is a function of the moving angles, it allows long-range structure rather than the other light scattering matrix elements. Element M_{12} is access by measuring the total scattered field intensity for a horizontally linearly polarized incoming light and subtracting the total scattered field intensity for a vertically linearly polarized incoming light. Element M_{22} refers to the ratio of depolarized light to the total scattered light. M_{34} refers to the transformation of the 45° obliquely polarized incident light to circularly polarized scattered light.

The elements M_{33} and M_{44} also displays the accurate measurement of the scattering beam from the object [95–97].

6. Conclusions

In this article, we have reviewed and compiled the optical properties of human tissues and the circulatory system with the main focus on blood. From this literature review, one of the main conclusions is that there are numerous factors of physical and methodological origin that are responsible for the study of the optical properties that anyone should aware of before performing own optical properties measurements. We have pointed out the main factors that influence absorption spectra of whole blood and hence influence optical properties. Revision of available polarimetric techniques can be helpful for the reader in the practice of biomedical optics. From this, we hope that we have provided the reader with a set of optical property spectra for whole blood and different polarimetric techniques that can be used in the practice of biomedical optics.

Author Contributions: The authors S.B. conceived the presented idea. S.B. developed the formulation or evolution of overarching research goals and aims. and performed the computations. Following co-authors (M.N., F.M., F.F., E.F.) encouraged first author to investigate a specific aspect and supervised the findings of this work. All authors provided critical feedback and helped in equal contribution to the formation of the research article. All authors have read and agreed to the published version of the manuscript.

Funding: This research received no external funding.

Conflicts of Interest: The authors declare no conflict of interest.

References

1. Tang, J.; Fu, C. Preliminary experimental research on skin reflection, transmission and absorption of light rays. *Chin. J. Lasers* **1987**, *7*, 1-14.
2. Lister, T.; Wright, P.A.; Chappell, P.H. Optical properties of human skin. *J. Biomed. Opt.* **2012**, *17*, 090901. [CrossRef] [PubMed]
3. Cuccia, D.J.; Bevilacqua, F.P.; Durkin, A.J.; Ayers, F.R.; Tromberg, B.J. Quantitation and mapping of tissue optical properties using modulated imaging. *J. Biomed. Opt.* **2009**, *14*, 024012. [CrossRef] [PubMed]
4. Beck, G.C.; Akgun, N.; Ruck, A.; Steiner, R. Design and characterisation of a tissue phantom system for optical diagnostics. *Lasers Med. Sci.* **1998**, *17*, 160–171. [CrossRef]
5. Tuchin, V.V.; Maksimova, I.L.; Zimnyakov, D.A.; Kon, I.L.; Mavlyutov, A.H.; Mishin, A.A. Light propagation in tissues with controlled optical properties. *J. Biomed. Opt.* **1997**, *2*, 401–418. [CrossRef]
6. Kim, M.K. Principles and techniques of digital holographic microscopy. *SPIE Rev.* **2010**, *1*, 018005. [CrossRef]
7. Yodh, A.; Chance, B. Spectroscopy and imaging with diffusing light. *Phys. Today* **1995**, *3*, 34–41. [CrossRef]
8. Hardy, J.D.; Hammel, H.T.; Murgatroyd, D. Spectral transmittance and reflectance of excised human skin. *J. Appl. Physiol.* **1956**, *2*, 257–264. [CrossRef]
9. Papadopoulos, M.G.; Sadlej, A.J.; Leszczynski, J. *Non-Linear Optical Properties of Matter*; Springer: Dordrecht, The Netherlands, 2006.
10. Asahara, A.; Nishiyama, A.; Yoshida, S.; Kondo, K.I.; Nakajima, Y.; Minoshima, K. Dual-comb spectroscopy for rapid characterization of complex optical properties of solids. *Opt. Lett.* **2016**, *41*, 4971–4974. [CrossRef]
11. Lin, S.P.; Wang, L.; Jacques, S.L.; Tittel, F.K. Measurement of tissue optical properties by the use of oblique-incidence optical fiber reflectometry. *Appl. Opt.* **1997**, *1*, 136–143. [CrossRef]
12. Wilson, B.C.; Patterson, M.S.; Flock, S.T. Indirect versus direct techniques for the measurement of the optical properties of tissues. *Photochem. Photobiol.* **1987**, *46*, 601–608. [CrossRef] [PubMed]
13. Schmitt, J.M.; Knuttel, A.; Bonner, R.F. Measurement of optical properties of biological tissues by low-coherence reflectometry. *Appl. Opt.* **1993**, *32*, 6032–6042. [CrossRef] [PubMed]
14. Batool, S.; Nisar, M.; Mangini, F.; Frezza, F.; Fazio, E. Polarization Imaging for Identifying the Microscopical Orientation of Biological Structures. In Proceedings of the URSI GASS Conference, Rome, Italy, 29 August 2020.
15. Frezza, F.; Mangini, F.; Muzi, M.; Stoja, E. In silico validation procedure for cell volume fraction estimation through dielectric spectroscopy. *J. Biol. Phys.* **2015**, *41*, 223–234. [CrossRef] [PubMed]

16. Frezza, F.; Mangini, F.; Tedeschi, N. Introduction to electromagnetic scattering: Tutorial. *JOSA A* **2018**, *35*, 163–173. [CrossRef]
17. Frezza, F.; Mangini, F.; Tedeschi, N. Introduction to electromagnetic scattering, part II. tutorial. *JOSA A* **2020**, *37*, 1300–1315. [CrossRef]
18. Batool, S.; Frezza, F.; Mangini, F.; Xu, Y.L. Scattering from multiple PEC sphere using Translation Addition Theorems for Spherical Vector Wave Function. *J. Quant. Spectrosc. Radiat. Transf.* **2020**, *248*, 106905. [CrossRef]
19. Batool, S.; Naqvi, Q.A.; Fiaz, M.A. Scattering from a cylindrical obstacle deeply buried beneath a planar non-integer dimensional dielectric slab using Kobayashi potential method. *Opt. Int. J. Light Electron Opt.* **2018**, *153*, 95–108. [CrossRef]
20. Prieve, D.C.; Walz, J.Y. Scattering of an evanescent surface wave by a microscopic dielectric sphere. *Appl. Opt.* **1993**, *32*, 1629–1641. [CrossRef]
21. Frezza, F.; Mangini, F. Vectorial spherical-harmonics representation of an inhomogeneous elliptically polarized plane wave. *JOSA A* **2015**, *32*, 1379–1383. [CrossRef]
22. Batool, S.; Benedetti, A.; Frezza, F.; Mangini, F.; Xu, Y.L. Effect of Finite Terms on the Truncation Error of Addition Theorems for Spherical Vector Wave Function, PhotonIcs. In Proceedings of the IEEE Electromagnetics Research Symposium-Spring (PIERS Spring), Rome, Italy, 17–20 June 2019; pp. 2795–2801.
23. Bassan, P.; Kohler, A.; Martens, H.; Lee, J.; Byrne, H.J.; Dumas, P.; Gazi, E.; Brown, M.; Clarke, N.; Gardner, P. Resonant Mie scattering (RMieS) correction of infrared spectra from highly scattering biological samples. *Analyst* **2010**, *135*, 268–277. [CrossRef]
24. Graaff, R.; Aarnoudse, J.G.; Zijp, J.R.; Sloot, P.M.; De Mul, F.F.; Greve, J.; Koelink, M.H. Reduced light-scattering properties for mixtures of spherical particles: A simple approximation derived from Mie calculations. *Appl. Opt.* **1992**, *31*, 1370–1376. [CrossRef]
25. Yi, J.; Backman, V. Imaging a full set of optical scattering properties of biological tissues by inverse spectroscopic optical coherence tomography. *Opt. Lett.* **2012**, *37*, 4443–4445. [CrossRef]
26. Fung, A.K. A note on the Wiener-Khintchine theorem for autocorrelation. *Proc. IEEE* **1967**, *55*, 594–595. [CrossRef]
27. Jacques, S.L. Optical properties of biological tissues: A review. *Phys. Med. Biol.* **2013**, *11*, 37–61. [CrossRef]
28. Jacques, S.L.; Prahl, S.A. *ECE532 Biomedical Optics*; Oregon Graduate Institute: Washington, DC, USA, 1998.
29. Gazdaru, D.; Chilom, C.; Calin, M.A.; Geanta, C.; Popescu, A. Laser radiation propagation and heat transfer into cells and tissues. *Rom. J. Biophys.* **2008**, *18*, 73–85.
30. Schmidt, F.E. Development of a Time-Resolved Optical Tomography System for Neonatal Brain Imaging. Ph.D. Thesis, University of London, London, UK, 2000.
31. Grossweiner, L.I.; Grossweiner, J.B.; Rogers, B.G. *The Science of Phototherapy: An Introduction*; Springer: Dordrecht, The Netherlands, 2005.
32. Johns, M.; Giller, C.A.; German, D.C.; Liu, H. Determination of reduced scattering coefficient of biological tissue from a needle-like probe. *Opt. Express* **2005**, *13*, 4828–4842. [CrossRef]
33. Yariv, I.; Duadi, H.; Fixler, D. Optical method to extract the reduced scattering coefficient from tissue: Theory and experiments. *Opt. Lett.* **2018**, *43*, 5299–5302. [CrossRef]
34. Mourant, J.R.; Fuselier, T.; Boyer, J.; Johnson, T.M.; Bigio, I.J. Predictions and measurements of scattering and absorption over broad wavelength ranges in tissue phantoms. *Appl. Opt.* **1997**, *36*, 949–957. [CrossRef]
35. Jacques, S.L. Origins of tissue optical properties in the UVA, visible, and NIR regions. *OSA TOPS Adv. Opt. Imaging Photon Migr.* **1996**, *1*, 364–371.
36. Anderson, R.R.; Parrish, J.A. *Optical Properties of Human Skin*; Springer: Berlin/Heidelberg, Germany, 1982; pp. 147–194.
37. Simpson, C.R.; Kohl, M.; Essenpreis, M.; Cope, M. Near-infrared optical properties of ex vivo human skin and subcutaneous tissues measured using the Monte Carlo inversion technique. *Phys. Med. Biol.* **1998**, *43*, 2465. [CrossRef]
38. Saidi, I.S.; Jacques, S.L.; Tittel, F.K. Mie and Rayleigh modeling of visible-light scattering in neonatal skin. *Appl. Opt.* **1995**, *34*, 7410–7418. [CrossRef]
39. Bashkatov, A.N.; Genina, E.A.; Tuchin, V.V. Optical properties of skin, subcutaneous, and muscle tissues: A review. *J. Innov. Opt. Health Sci.* **2011**, *4*, 9–38. [CrossRef]
40. Salomatina, E.V.; Jiang, B.; Novak, J.; Yaroslavsky, A.N. Optical properties of normal and cancerous human skin in the visible and near-infrared spectral range. *J. Biomed. Opt.* **2006**, *11*, 064026. [CrossRef]

41. Sandell, J.L.; Zhu, T.C. A review of in vivo optical properties of human tissues and its impact on PDT. *J. Biophotonics* **2011**, *4*, 773–787. [CrossRef]
42. Bevilacqua, F.; Berger, A.J.; Cerussi, A.E.; Jakubowski, D.; Tromberg, B.J. Broadband absorption spectroscopy in turbid media by combined frequency-domain and steady-state methods. *Appl. Opt.* **2000**, *39*, 6498–6507. [CrossRef] [PubMed]
43. Spinelli, L.; Torricelli, A.; Pifferi, A.; Taroni, P.; Danesini, G.M.; Cubeddu, R. Bulk optical properties and tissue components in the female breast from multiwavelength time-resolved optical mammography. *J. Biomed. Opt.* **2004**, *9*, 1137–1143. [CrossRef]
44. Cerussi, A.E.; Berger, A.J.; Bevilacqua, F.; Shah, N.; Jakubowski, D.; Butler, J.; Holcombe, R.F.; Tromberg, B.J. Sources of absorption and scattering contrast for near-infrared optical mammography. *Acad. Radiol.* **2001**, *8*, 211–218. [CrossRef]
45. Durduran, T.; Choe, R.; Culver, J.P.; Zubkov, L.; Holboke, M.J.; Giammarco, J.; Chance, B.; Yodh, A.G. Bulk optical properties of healthy female breast tissue. *Phys. Med. Biol.* **2002**, *47*, 2847. [CrossRef]
46. Firbank, H.; Hiraoka, M.; Essenpreis, M.; Delpy, D.T. Measurement of the optical properties of the skull in the wavelength range 650–950 nm. *Phys. Med. Biol.* **1993**, *38*, 503–510. [CrossRef]
47. Newman, C.; Jacques, S.L. Laser penetration into prostate for various wavelengths. *Lasers Surg. Med.* **1991**, *3*, 75.
48. Peters, V.G.; Wyman, D.R.; Patterson, M.S.; Frank, G.L. Optical properties of normal and diseased human breast tissues in the visible and near infrared. *Phys. Med. Biol.* **1990**, *35*, 1317. [CrossRef] [PubMed]
49. Alexandrakis, G.; Rannou, F.R.; Chatziioannou, A.F. Tomographic bioluminescence imaging by use of a combined optical-PET (OPET) system: A computer simulation feasibility study. *Phys. Med. Biol.* **2005**, *50*, 4225. [CrossRef] [PubMed]
50. Brinchmann, H.O.; Heier, H. Theoretical relations between light streak characteristics and optical properties of retinal vessels. *Acta Ophthalmol.* **1986**, *64*, 33–37. [CrossRef]
51. Fitzgerald, A.J.; Berry, E.; Zinovev, N.N.; Homer, V.S.; Miles, R.E.; Chamberlain, J.M.; Smith, M.A. Catalogue of human tissue optical properties at terahertz frequencies. *J. Biol. Phys.* **2003**, *29*, 123–128. [CrossRef]
52. Gerken, M.; Faris, G.W. Frequency-domain immersion technique for accurate optical property measurements of turbid media. *Opt. Lett.* **1999**, *24*, 1726–1728.
53. Ko, A.C.; Ridsdale, A.; Mostaco, G.L.B.; Major, A.; Stolow, A.; Sowa, M.G. Nonlinear optical microscopy in decoding arterial diseases. *Biophys. Rev.* **2012**, *4*, 323–334. [CrossRef]
54. Hu, J.J.; Humphrey, J.D.; Yeh, A.T. Characterization of engineered tissue development under biaxial stretch using nonlinear optical microscopy. *Tissue Eng. Part A* **2009**, *15*, 1553–1564. [CrossRef]
55. Bashkatov, A.N.; Genina, E.A.; Kochubey, V.I.; Tuchin, V.V. Optical properties of human skin, subcutaneous and mucous tissues in the wavelength range from 400 to 2000 nm. *J. Phys. D Appl. Phys.* **2005**, *15*, 2543–2554. [CrossRef]
56. Troy, T.L.; Thennadil, S.N. Optical properties of human skin in the near infrared wavelength range of 1000 to 2200 nm. *J. Biomed. Opt.* **2001**, *2*, 167–177. [CrossRef]
57. Gareau, D.S.; Gratzer, W.B.; Kollias, N. *Personal Communication from Gratzer*; Med. Res. Council Labs: Holly Hill, SC, USA; London, UK; N Kollias, Wellman Laboratories, Harvard Medical School: Boston, MA, USA. Available online: http://omlc.ogi.edu/spectra/hemoglobin/ (accessed on 10 October 2020).
58. Roggan, A.; Friebel, M.; Dorschel, K.; Hahn, A.; Mueller, G.J. Optical properties of circulating human blood in the wavelength range 400–2500 nm. *J. Biomed. Opt.* **1999**, *4*, 36–47. [CrossRef]
59. Kienle, A.; Lilge, L.; Vitkin, I.A.; Patterson, M.S.; Wilson, B.C.; Hibst, R.; Steiner, R. Why do veins appear blue? A new look at an old question. *Appl. Opt.* **1996**, *35*, 1151–1160. [CrossRef]
60. Bosschaart, N.; Edelman, G.J.; Aalders, M.C.; Van Leeuwen, T.G.; Faber, D.J. A literature review and novel theoretical approach on the optical properties of whole blood. *Lasers Med. Sci.* **2014**, *29*, 453–479. [CrossRef] [PubMed]
61. Hammer, M.; Roggan, A.; Schweitzer, D.; Muller, G. Optical properties of ocular fundus tissues-an in vitro study using the double-integrating-sphere technique and inverse Monte Carlo simulation. *Phys. Med. Biol.* **1995**, *40*, 963. [CrossRef] [PubMed]
62. Kondermann, C.; Kondermann, D.; Yan, M. Blood vessel classification into arteries and veins in retinal images. *Int. Soc. Opt. Eng.* **2007**, *12*, 651247.

63. Alam, M.; Son, T.; Toslak, D.; Lim, J.I.; Yao, X. Combining ODR and Blood Vessel Tracking for Artery/Vein Classification and Analysis in Color Fundus Images. *Transl. Vis. Sci. Technol.* **2018**, *2*, 1–23. [CrossRef] [PubMed]
64. Mangini, F.; Dinuzzo, M.; Maugeri, L.; Moraschi, M.; Mascali, D.; Cedola, A.; Frezza, F.; Giove, F.; Fratini, M. Numerical simulation of the blood oxygenation level-dependent functional magnetic resonance signal using finite element method. *Int. J. Numer. Methods Biomed. Eng.* **2020**, *36*, 3290. [CrossRef]
65. Shvalov, A.N.; Soini, J.T.; Chernyshev, A.V.; Tarasov, P.A.; Soini, E.; Maltsev, V.P. Light-scattering properties of individual erythrocytes. *Appl. Opt.* **1998**, *38*, 230–235. [CrossRef]
66. Borovoi, A.G.; Naats, E.I.; Oppel, U.G. Scattering of light by a red blood cell. *J. Biomed. Opt.* **1998**, *3*, 364–372. [CrossRef]
67. Kinnunen, M.; Kauppila, A.; Karmenyan, A.; Myllyla, R. Effect of the size and shape of a red blood cell on elastic light scattering properties at the single-cell level. *Biomed. Opt. Express* **2011**, *2*, 1803–1814. [CrossRef]
68. Mazeron, P.; Muller, S.; El Azouzi, H. Deformation of erythrocytes under shear: A small-angle light scattering study. *Biorheology* **1997**, *34*, 99–110. [CrossRef]
69. Liu, S.; Deng, Z.; Li, J.; Wang, J.; Huang, N.; Cui, R.; Zhang, Q.; Zhou, W.M.; Zhang, C.; Ye, Q.; et al. Measurement of the refractive index of whole blood and its components for a continuous spectral region. *J. Biomed. Opt.* **2019**, *24*, 035003. [CrossRef]
70. Tycko, D.H.; Metz, M.H.; Epstein, E.A.; Grinbaum, A. Flow-cytometric light scattering measurement of red blood cell volume and hemoglobin concentration. *Appl. Opt.* **1985**, *9*, 1355–1365. [CrossRef]
71. Yurkin, M.A.; Semyanov, K.A.; Tarasov, P.A.; Chernyshev, A.V.; Hoekstra, A.G.; Maltsev, V.P. Experimental and theoretical study of light scattering by individual mature red blood cells by use of scanning flow cytometry and a discrete dipole approximation. *Appl. Opt.* **2005**, *25*, 5249–5256. [CrossRef]
72. Amer, J.; Goldfarb, A.; Fibach, E. Flow cytometric measurement of reactive oxygen species production by normal and thalassaemic red blood cells. *Eur. J. Haematol.* **2003**, *2*, 84–90. [CrossRef]
73. Altendorf, E.; Zebert, D.; Holl, M.; Yager, P. Differential blood cell counts obtained using a microchannel based flow cytometer. *Proc. Int. Solid State Sens. Actuators Conf.* **1997**, *1*, 531–534.
74. Sakota, D.; Takatani, S. Quantitative analysis of optical properties of flowing blood using a photon-cell interactive Monte Carlo code: Effects of red blood cells orientation on light scattering. *J. Biomed. Opt.* **2012**, *5*, 1–12. [CrossRef]
75. Friebel, M.; Roggan, A.; Muller, G.J.; Meinke, M.C. Determination of optical properties of human blood in the spectral range 250 to 1100 nm using Monte Carlo simulations with hematocrit-dependent effective scattering phase functions. *J. Biomed. Opt.* **2006**, *3*, 21–34. [CrossRef]
76. Taflove, A. *Computational Electrodynamics: The Finite Difference Time-Domain Method*; Artech House: Norwood, MA, USA, 1995.
77. Lu, J.Q.; Yang, P.; Hu, X.H. Simulations of light scattering from a biconcave red blood cell using the finite-difference time-domain method. *J. Biomed. Opt.* **2005**, *10*, 024022. [CrossRef]
78. Brock, R.S.; Hu, X.H.; Yang, P.; Lu, J.Q. Evaluation of a parallel FDTD code and application to modeling of light scattering by deformed red blood cells. *Opt. Express* **2005**, *14*, 5279–5292. [CrossRef]
79. Brock, R.S.; Hu, X.H.; Weidner, D.A.; Mourant, J.R.; Lu, J.Q. Effect of detailed cell structure on light scattering distribution: FDTD study of a B-cell with 3D structure constructed from confocal images. *J. Quant. Spectrosc. Radiat. Transf.* **2006**, *1*, 25–36. [CrossRef]
80. He, J.; Karlsson, A.; Swartling, J.; Andersson-Engels, S. Light scattering by multiple red blood cells. *JOSA A* **2004**, *10*, 1953–1961. [CrossRef] [PubMed]
81. Karlsson, A.; He, J.; Swartling, J.; Andersson-Engels, S. Numerical simulations of light scattering by red blood cells. *IEEE Trans. Biomed. Eng.* **2005**, *1*, 13–18. [CrossRef] [PubMed]
82. Wriedt, T.; Hellmers, J.; Eremina, E.; Schuh, R. Light scattering by single erythrocyte: Comparison of different methods. *J. Quant. Spectrosc. Radiat. Transf.* **2006**, *1*, 444–456. [CrossRef]
83. Demos, S.G.; Alfano, R.R. Optical polarization imaging. *Appl. Opt.* **1997**, *36*, 150–155. [CrossRef] [PubMed]
84. Demos, S.G.; Radousky, H.B.; Alfano, R.R. Deep subsurface imaging in tissues using spectral and polarization filtering. *Opt. Express* **2000**, *7*, 23–28. [CrossRef]
85. Jacques, S.L.; Roman, J.R.; Lee, K. *Imaging Superficial Tissues with Polarized Light*; Wiley Interscience: New York, NY, USA, 1999.

86. Sankaran, V.; Walsh, J.T.; Maitland, D.J. Polarized light propagation through tissue phantoms containing densely packed scatterers. *Opt. Lett.* **2000**, *25*, 239–241. [CrossRef]
87. Firdous, S.; Ikram, M. Polarized Laser Beam Scattering through Turbid Medium for Application in Tissue Imaging. *Sci. Asia* **2005**, *31*, 167–172. [CrossRef]
88. Anderson, R.R. Polarized light examination and photography of the skin. *Arch. Dermatol.* **1991**, *127*, 1000–1005. [CrossRef]
89. Saarinen, K.; Muinonen, K. Light scattering by wood fibers. *Appl. Opt.* **2001**, *40*, 06477. [CrossRef]
90. Mischenko, M.I.; Hovenier, J.W.; Travis, L.D. *Light Scattering by Nonspherical Particles Theory Measurement and Applications*; Academic Press: Cambridge, MA, USA, 2000.
91. Mishchenko, M.I.; Travis, L.D.; Lacis, A.A. *Scattering Absorption and Emission of Light by Small Particles*; Cambridge University Press: Cambridge, UK, 2002.
92. Giakos, G.C. Multispectral, multifusion laser polarimetric imaging principles. *IEEE Int. Workshop Imaging Syst. Tech.* **2004**, *4*, 54–59.
93. Khos, O.T.; Munkhbaatar, P.; Yang, B.K.; Kim, H.W.; Kim, J.S.; Kim, M.W. Polarimetric measurement of Jones matrix of a twisted nematic liquid crystal spatial light modulator. *J. Opt. Soc. Korea* **2012**, *16*, 443–448. [CrossRef]
94. Jiao, S.; Wang, L.V. Jones-matrix imaging of biological tissues with quadruple-channel optical coherence tomography. *J. Biomed. Opt.* **2002**, *7*, 1083–3668. [CrossRef]
95. Layden, D.; Ghosh, N.; Vitkin, A. Quantitative polarimetry for tissue characterization and diagnosis. *Adv. Biophotonics Tissue Opt. Sect.* **2013**, *5*, 73–108.
96. Arteaga, O.; Freudenthal, J.; Wang, B.; Kahr, B. Mueller matrix polarimetry with four photoelastic modulators theory and calibration. *Appl. Opt.* **2012**, *28*, 6805–6817. [CrossRef]
97. Pezzaniti, J.L.; Chipman, R.A. Mueller matrix imaging polarimetry. *Opt. Eng.* **1995**, *34*, 1558–1569. [CrossRef]

MDPI
St. Alban-Anlage 66
4052 Basel
Switzerland
Tel. +41 61 683 77 34
Fax +41 61 302 89 18
www.mdpi.com

Diagnostics Editorial Office
E-mail: diagnostics@mdpi.com
www.mdpi.com/journal/diagnostics

MDPI
St. Alban-Anlage 66
4052 Basel
Switzerland

Tel: +41 61 683 77 34
Fax: +41 61 302 89 18

www.mdpi.com

ISBN 978-3-0365-1618-9